Evaporation at microscopic scale and at high heat flux

Vladislav Janecek

THÈSE DE DOCTORAT
DE L'UNIVERSITÉ PIERRE ET MARIE CURIE

Spécialité : Physique

École doctorale : « La physique, de la particule au solide »

réalisée

Laboratoire de Physique et Mécanique des Milieux Hétérogènes,
École Supérieure de Physique et de Chimie Industrielles
et Service des Basses Températures, CEA-Grenoble

présentée par

Vladislav JANEČEK

pour obtenir le grade de :

DOCTEUR DE L'UNIVERSITÉ PIERRE ET MARIE CURIE

Sujet de la thèse :

Evaporation à l'échelle microscopique et à haut flux thermique

soutenue le 17 décembre 2012

devant le jury composé de :

M^{me}	Catherine Colin	Rapportrice
M.	Pierre Colinet	Rapporteur
M.	Frédéric Doumenc	Examinateur
M.	Christophe Josserand	Examinateur
M.	Laurent Limat	Examinateur
M.	Vadim S. Nikolayev	Directeur de thèse
M.	Lev Truskinovsky	Examinateur

Acknowledgments

First, I want to thank Vadim Nikolayev, the supervisor, for his availability, help and patience during my thesis.

I also take this opportunity to sincerely thank the following people directly or indirectly involved in the present work: Bruno Andreotti, Lev Truskinovsky, Daniel Beysens, Yves Garrabos, Carole Lecoutre, Bernard Zappoli, Catherine Colin, Pierre Colinet, Alexey Rednikov, Dalibor Pražák, Tomáš Bárta, Benoît Mathieu, Didier Jamet, R. Peralta-Fabi, Denis Chatain, Jean Hare and Isabelle Schuster.

This thesis was done at the Laboratory of physics and mechanics of heterogeneous media (PMMH, ESPCI) in cooperation with the Division of cryogenics of the French Atomic Energy and Alternative Energies Commission (SBT, CEA). The hospitality of both institutions as well as French National Centre for Scientific Research (CNRS) is gratefully acknowledged. I thank to José Eduardo Wesfreid (former director of PMMH), Philippe Petitjeans (actual director of PMMH) and Alain Girard (director of SBT) for giving me the opportunity to be a part of their institutions. I thank all members of Laboratory PMMH, with who I had an opportunity to spend last three years for creating friendly and stimulating research environment.

I would also like to thank to Frédérique Auger, Amina Mialet and Michèle Moucot for help with bureaucratic issues.

Special thanks are due to my wife and my two sons for their support and amazing patience. I thank my parents as well as my close friends for their support, help and kindness during these three years.

Contents

Nomenclature

$\vec{e}$	unit vector directed along an axes
$\vec{m}$	horizontal unit vector normal to the contour and external to the integration area
$\vec{n}$	normal vector to the interface
$\vec{u}$	velocity vector, $\vec{u} = [u, v]$
$\vec{Z}$	vector of unknowns
A	Hamaker constant, [J]; vapor-liquid interface or its area (section 3.3), [m^2]
D	solid heater thickness, [m]
e	specific energy, [J/(kg)]
f	accommodation coefficient
g	gravity acceleration, [m/s^2]
H	latent heat, [J/kg]
J	mass evaporation flux, [$kg/(m^2 s)$]
j	volume heat supply, [W/m^3]
K	curvature, [1/m]
k	thermal conductivity [W/(m·K)]
L	bubble contour half length, [m]
M	molar mass, [g/mol]
N_A	Avogadro constant ($6.02214129 \cdot 10^{23}$, [1/mol])
Q	integrated heat flux, [W/m]
R	bubble radius, [m]
r	radius, [m]
R^i	interfacial thermal resistance, [(K m^2)/W]
R_g	universal gas constant (8.3144), [J/(mol K)]
s	curvilinear coordinate, [m]
t	time, [s]
T_S	wall temperature, [K]
U	volume flux, [m^3/s]
u	velocity, [m/s]; local slope of the liquid-gas interface = dh/dx
V	bubble 2D half volume, [m^2]; bubble volume (section 3.3), [m^3]
x, y	cartesian coordinates, [m]
Bo	Bond number
Ca	Capillary number
Fo	Fourier number
Ja	Jakob number

Abbreviations

BC	Boiling Crisis, Boundary Condition
BEM	Boundary Element Method
CHF	Critical Heat Flux
CL	Contact Line
CP	Critical Point
FVM	Finite Volume Method
HTC	Heat Transfer Coefficient
ONB	Onset of Nucleate Boiling

Greek symbols

α	thermal diffusivity, [m^2/s]
β	parameter related to slip length or interface thermal resistance
Δp	pressure jump, [Pa]
ΔT	wall superheating, [K]
Δt	time step, [s]
δ	arc length, [m]; modified capillary number in sec. 2.4
ε	small parameter (dimensionless superheating $\Delta T/T_{sat}$)
Γ	contact line or its length, [m]
γ	Marangoni coefficient ($\gamma = \partial\sigma/\partial T$), [N/(K·m)]
κ	exponent
Λ	total thermodynamics potential, [N·m]
μ	dynamic viscosity, [Pa·s]; chemical potential (in Chapiter 1)
Ω	contour of a domain; length of a contour (section 3.3), [m]
ϕ	local slope angle of the liquid-gas interface
Π	disjoining pressure, [$J/m^3 = Pa$]
Ψ	stream function
ψ	reduced temperature
ρ	density, [kg/m^3]
σ	surface tension, [N/m]
τ	characteristic time [s]
θ	contact angle
φ	polar angle, [rad]
ϱ	Euler Mascheroni constant (0.5772156649)
$\vec{\omega}$	vorticity
ξ	reduced curvilinear coordinate
ζ	reduced heat flux

Subscripts and superscripts

ad	adsorbed film
app	apparent
d	dry
eq	equilibrium
i	interface
$init$	initial
L	liquid
l	lower
max	maximal
$micro$	microscopic
mol	molecular
n	node
$prev$	previous
r	recoil
sat	saturation
u	upper
V	vapor, Voinov
w	wall
Y	Young

Chapter 1

Introduction

Contents

1.1 Evaporation as a multiscale problem

The evaporation in the vicinity of the triple gas-liquid-solid contact line (CL) is of high importance in many natural and technological processes (e.g. boiling, drying of paint, etc.). While this phenomenon was intensively studied last decades, many questions still remain unsolved. The main issue that complicates understanding of the heat and mass transport processes lies in their strong localization in the vicinity of the CL. This complicates on one hand experimental measurements and on the other, the mathematical and numerical modeling. Indeed, one has to deal with a system exhibiting singular-like behavior of various macroscopic quantities (e.g. shear rate, local heat flux, evaporation flux etc.). One also has to mention that although the transport processes occur at a scale smaller than several hundreds of nm (microregion) it is necessary to consider also a coupling with the macroscopic problem (macroregion), see Fig. 1.1. The problem is thus multiscale. The microregion provides boundary conditions to macroscopic problem statement.

In general the wedge-shaped liquid layer confined between the heated substrate and the gas-liquid interface at small scales near the liquid-gas-solid CL is extremely important for at least two reasons:

- A substantial part of the evaporative mass transfer occurs there [1–3],
- A strong meniscus curvature that occurs in this region leads to the apparent contact angle θ_{app} (angle at the border of microregion) larger than its actual microscopic value [2–7], see Fig. 1.1.

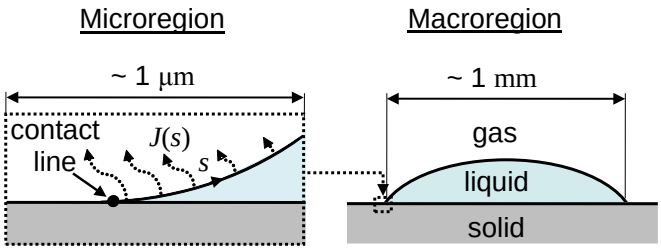

Figure 1.1: Geometry of the problem, microregion and macrorgion (volatile liquid drop).

These two aspects are key arguments which show the necessity of the careful microregion consideration.

There are two main regimes that may occur when dealing with the evaporation in the vicinity of CL. Both have similar features due to common geometry but it is important to distinguish them since evaporation is driven by different mechanism in each case. In the first of them, the evaporation is controlled by the diffusion of liquid vapor into another gas (e.g. drying of water drop surrounded by air). Such type of evaporation, controlled by processes in gas phase, is not a main objective of this thesis. However due to conceptual relevance and to the wide interest to this regime the situation in this field is briefly described. Up to now, many experimental and theoretical approaches have been developed [8, 9]. Particular field where the diffusion controlled evaporation is of crucial importance is a deposit formation during drying of colloidal suspensions extensively studied since the work of Deegan *et al.* [10]. Its authors proposed solving the diffusion problem in gas phase using an analogy with the electrostatics. With such a strategy they were theoretically able to show , that intensive evaporation appears in the vicinity of the CL. More precisely, the local mass evaporation flux J scales in the vicinity of CL as $J \propto s^{-\lambda}$, where s is the coordinate along the liquid-vapor interface, see Fig. 1.1. The exponent λ depends on the contact angle. For contact angle smaller than 90°, $\lambda \in (0, \pi/2)$ and J thus diverges at the CL. Such a situation induces a liquid flow towards the CL, which explains the formation of a ring shaped deposit of coffee particles, coffee stain problem. A significant effort has been made to understand and treat such a problem. Two main strategies were used to relax J singularity: 1) mathematical relaxation of divergent form of J e.g. by using an exponential cut-off near the CL [11], 2) a precursor film account [12, 13], which restricts applications to the complete wetting case. Recently, in the frame of the latter approach a full coupling of the liquid and vapor phase has been performed [12, 14]. However on a hydrophobic substrate, the precursor film is not expected and a proper treatment of this situation is lacking. The evaporation in combination with moving CL is treated e.g. in [13, 15–17].

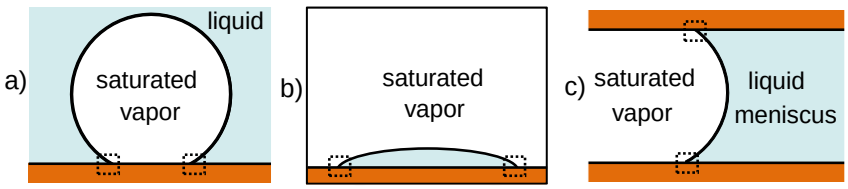

Figure 1.2: Industrially relevant geometries to the thermally controlled evaporation in the vicinity of CL: a) vapor bubble during boiling, b) sessile drop evaporation during the spray cooling, c) evaporation of liquid menisci in capillaries.

The second regime of evaporation, addressed in this thesis, is the evaporation of liquid into the atmosphere of its pure vapor controlled by the heat supplied from the liquid side and spent to compensate the latent heat of vaporization. Unlike the previous regime, evaporation is controlled by the processes in the liquid and solid phases. Such a regime occurs in many industrially relevant situations with different macroscopic geometry. Generally one distinguishes three of them: 1) bubble growth on the heater at boiling, 2) sessile drop evaporation during the spray cooling, 3) evaporation of liquid menisci in capillaries of the heat pipes, see Fig. 1.2.

The heat pipe application is not directly discussed in this thesis, however as this application is very close to the author, it is at least shortly mentioned in the following. There are several different kinds of heat pipes, with different geometry and a mechanism of fluid transport. The oldest (dates back to 1942) and simplest are the conventional heat pipes. It is a passive two-phase heat transfer device capable of transferring large quantities of heat with minimal temperature drop. The heat pipe consists of evaporator and condenser connected by the adiabatic section. The heat is consumed at evaporator, where the working fluid is vaporized. The vapor condenses in the condenser. During the phase change, the fluid takes or releases latent heat of vaporization/condensation. The liquid returns to the evaporator through the capillary structure from the condenser to the evaporator driven by capillary force. Many heat pipes are designed in a way to maximize the total length of contact line (e.g. evaporation in porous media), this increases the evaporative heat transport. This is the feature that links the heat pipe application to the contact line evaporation research and thus to this thesis. A large amount of literature on this topic is available [18, 19].

In the present thesis the emphasis will be put on the boiling application as it was the author's primary motivation for this work. A separate and more concrete introduction to thermally controlled evaporation microregion models is given at the end of this section.

1.2 Heater dryout

Boiling process is a complex and crucially important phenomenon which is used in many engineering but also natural and everyday life applications, e.g. transfer of thermal energy, mixing of fluids, sterilization, distillation, changing of surface properties, etc. Undoubtedly, the most important application of boiling for modern society is the transfer of heat in energy industry (e.g. power plant steam generators). In such applications the boiling process is used to transfer high amounts of heat. However, the boiling heat transfer is limited by a threshold value of heat flux q_{CHF} (the Critical Heat Flux, CHF), at which the nucleated vapor bubbles on the heating surface form abruptly a film that thermally insulates the heater from the bulk liquid. The heat transfer is suddenly blocked and the temperature of the heater rapidly grows (if the source of heat is not immediately suspended) and consequent burnout of the heater may appear. This phenomenon is known under names of "boiling crisis" (BC), "heater dryout" or "transition to film boiling". As a consequence the heater temperature can rise so high that it exceeds the melting temperature of heater, which causes its destruction, see e.g. Fig. 1.3. This phenomenon is of particular importance for the nuclear power platns where the burnout causes a severe nuclear accident. The critical heat flux must never be reached at any place of the nuclear core, to preventing melting; it is one of the design requirements of nuclear reactors. The heater dryour may also occur in the grooves of heat pipes that are widely used as cooling systems in electronics. Such a situation leads to the loss of the efficiency or functionality of the evaporator and possibly to the damage of the electronic component.

In spite of the fact that boiling and BC have been extensively studied for several decades, the

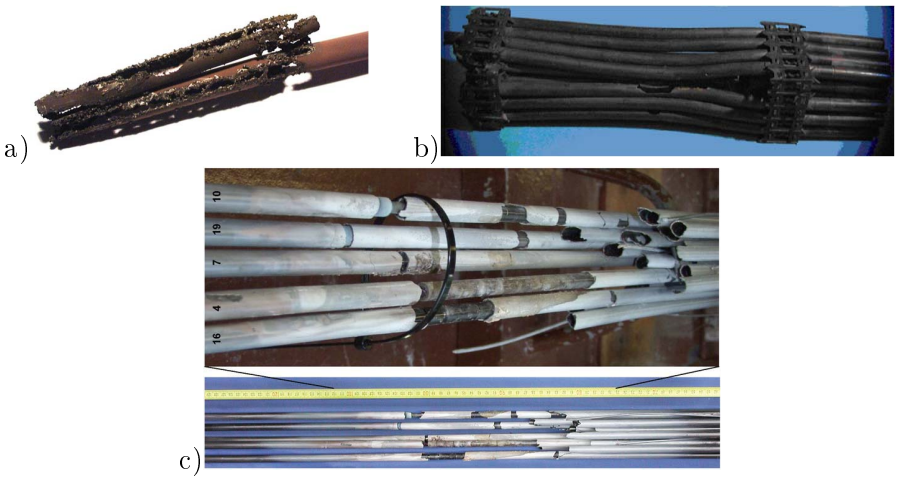

Figure 1.3: Examples of destruction caused by BC in nuclear power applications. Photos: a, b) Simulated burnout of the fuel rods, CEA/DEN; c) Severe fuel damage experiment QUENCH-15 at Karlsruhe Institute of Technology [20].

basic theory of boiling is still incomplete. This is mainly because of the violence of fluid motion (e.g. water under the ambient pressure) that on the one hand conceals the mechanisms of bubble growth from detailed observation, and on the other hand strongly complicates direct numerical simulations. There are many unanswered questions concerning the close vicinity of the heating surface, down to the scale of bubbles nucleation and growth heater surface.

1.2.1 Theoretical background

In this section, a theoretical basis related to boiling and BC phenomena are briefly introduced.

The boiling and BC are demonstrated here by referring to the boiling curve. It is a plot of the heat flux q from the heater vs. the average heater temperature for conditions of interest (pressure, gravity level, etc.), see Fig. 1.4. The rate of the heat transfer from the heater to the liquid is characterized by the slope of the boiling curve called HTC. The boiling curve was introduced nearly 80 years ago by Shiro Nukiyama in the pioneering paper [21]. This paper essentially started the "run" towards the full understanding of the boiling heat transfer. Numerous researchers discovered a lot on this run but still at the current stage we must state that the general theory of boiling is still far from being completed. Here a schematic representation of the pool boiling curve is presented in Fig. 1.4. The pool boiling means that there is no externally imposed fluid flow (stagnant fluid) and the relative motion of fluid near the heated surface is primary due to the rising vapor bubbles. The main regimes of pool boiling are indicated here schematically, for more detailed discussion on boiling curve see e.g. [22]. In the following, we assume that the bulk liquid surrounding the horizontal heater is at the saturation temperature for the ambient pressure. The associated average wall superheat is thus defined as $\Delta T = T_w - T_{sat}$.

- Natural convection regime: When the heat load is small, heat may be transferred from the surface to ambient liquid by natural convection and diffusion. The HTC associated with this regime is relatively low.

- Natural convection regime: At larger heat flux, when the superheat becomes large enough to initiate vapor bubble nucleation at some of the cavities on the surface. Such an event is called onset of nucleate boiling (ONB) and from this moment on, the boiling process started.

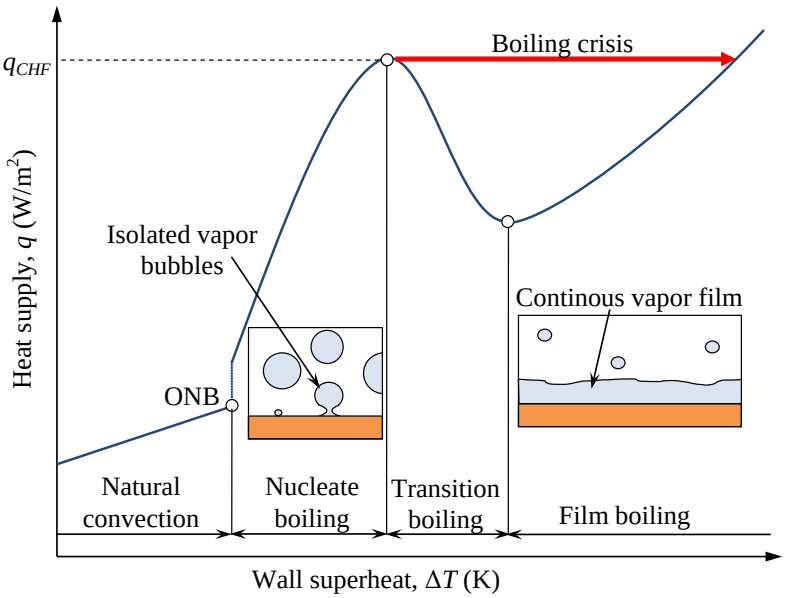

Figure 1.4: Boiling curve

Once such a situation appeared a further increase of heat load causes an intensification if the boiling process (higher bubble departure frequency) and increase of number of active nucleation sites. Separate vapor bubbles that grow at the heater and depart from it under the action of lift off forces (e.g. buoyancy), see [23]. In this regime the heat transfer is very large due to both phase change (latent heat of evaporation) and the fact that the superheated liquid is carried away from the heating surface by the departing vapor bubbles. Therefore the boiling curve slope (HTC) is much larger than for the convection regime.

- Transition boiling (boiling crisis): Increasing further the heat load produces an increase in the vapor production. When the superheat still increases and exceeds a critical value (called Critical Heat Flux, CHF), the vapor bubbles on the heating surface covers a significant fraction of the solid heater. This regime is characterized by rapid and considerable fluctuations in the local heat flux or temperature values. This causes unstable dry regions, appearing very rapidly at a given location before collapsing (i.e., bubble departing from the solid substrate), allowing the surface to be rewetted (rapidly cooled by the bulk liquid). Note that this part of the boiling curve is difficult to reach as the red line in Fig. 1.4 is usually followed when increasing the imposed heat flux. However it is well accessible when the boiling curve is followed from the opposite direction e.g. during the quench experiments[1][24]. This signifies abrupt formation of a vapor film that thermally insulates the heater from the liquid and the efficiency of heat transfer decreases drastically.

- Film boiling: In this case the liquid phase does not wet the solid wall. In this regime heat flux monotonically increases as the superheat increases. This trend is a consequence of increased conduction, and convection. At high wall superheating radiative heat transport across the vapor layer may be also important.

[1] The hot object is immersed in to the liquid bath. If the temperature of the object is high enough, the film boiling regime can be achieved.

1.2.2 State of the art

An overview of several important experimental and theoretical publications related to nucleate boiling and boiling crisis are presented in this section. For more detailed overview of all important publications on boiling heat transfer and BC, the reader is referred to review articles e.g. [25, 26].

Nucleate boiling has been debated over many decades resulting in several competing or mutually exclusive physical models. Han and Griffith [27] opened a discussion on different heat transfer mechanisms involved during bubble boiling. In their work, two main heat transfer mechanisms were distinguished: 1) the bulk convection mechanism which describes the convective heat flow towards the bulk liquid caused by vapor bubble dynamics (growth, departure), 2) the natural convection mechanisms which describes the heat transfer from heating surface to bulk liquid by usual convection process in a continues manner[2]. Later, based on experimental measurements, Cooper *et al.* [28][3] distinguished another fundamental heat transfer mechanism based on the existence of a thin liquid layer underneath each growing vapor bubble (microlayer). Due to its small thickness (and thus small thermal resistance) the heat transfer is very significant. This heat transfer mechanism can be considered as a predecessor of the microregion modeling presented in this thesis. Mikic *et al.* [30], identified another mechanism called "transient conduction" by him, related to a transient process of rewetting of the dry spot after vapor bubble departure. In addition, they proposed a model describing a fraction of the total heat flux associated with this mechanism. These are some important historical studies which gave an important insight to the theoretical background of nucleate boiling. During the last decades such ideas were more developed, reflecting more precise measurement techniques and increased possibilities of numerical treatment of the problem. Recent classification of heat transfer mechanisms was recently reviewed by Kim [31]. Generally, four basic mechanisms that contribute to total pool boiling heat flux are distinguished [32] in up to date publications:

- Transient conduction. Includes the heat transfer at the area of influence of a bubble growing at a nucleation site.
- Evaporation at the liquid-vapor interface. Only a fraction which may be added in the transient conduction is meant here. The evaporation in the vicinity of the CL is included here.
- Enhanced natural convection. The convective contribution in the vicinity of the growing vapor bubble is meant here.
- Natural convection. This contribution covers a natural convection from regions that has no active nucleation site and are completely uninfluenced by grooving vapor bubbles.

The contribution of each of these mechanisms to the overall heat transfer depends on the input heat load, fluid used and the geometrical configuration of the system.

During the last decades very large amount of correlations for the boiling heat transfer coefficient were developed, see e.g. [22]. Most of these correlations rely heavily on empirical parameters, and are valid only for limited range of system parameters, certain fluids and system geometrical configurations. These correlations are still heavily used to design the thermal devices.

The experimental observation and measurements are very useful tools to get insight into the boiling phenomenon. Very frequent experimental technique lies in using optical cameras to

[2] Note that in the original work [27] such classification was based on identification of two areas of heating surface, the bulk convection area (including the impact of growing and departing vapor bubble) and the natural convection area (not influenced by existence vapor bubbles).

[3] However first who suggested this mechanism for evaporation were Snyder and Edwards [29]

capture growing vapor bubble shape evolution. Such measurements are however very difficult to perform with high precision because of fast motion of the liquid-gas interfaces and temperature gradients that cause strong optical aberrations [33]. This is because there is an index of refraction gradient within the thermal boundary layer which creates a parallax effect. Snapshots of the vapor bubbles evolution can provide information on e.g. vapor bubble shape, bubble departure diameter, nucleation side density, apparent contact angle, etc. Optical measurements providing the detailed information on the vicinity of CL are very rare [34]. Optical experimental observation of the bubble boiling regime at low heat loads was performed e.g. by Son *et al.* [32, 35], and successfully compared with the results of their numerical simulation.

In order to obtain information concerning local temperature and heat fluxes, another kind of experiments needs to be performed. Considerable effort was done recently in miniaturization of experimental sensors. The time and length scales resolved have thus become smaller. The most relevant to this thesis measured quantities are the instantaneous local quantities at the vapor bubble foot such as the wall superheating or transferred heat flux. Very frequently used techniques to measure these quantities are the thermochromic liquid crystals (TCLs) [36] or high speed infrared thermography [37, 38]. Another approach that allows to obtain information on

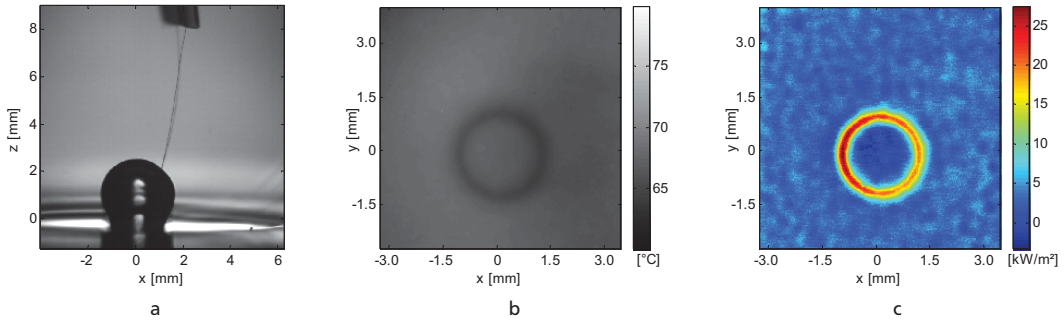

Figure 1.5: Infrared camera measurement of temperature distribution on the backside of a 20 μm thick stainless steel heater during microgravity boiling experiment. The fluid used was n-Perfluorohexane, t_{sat} = 42.32°, the electrical heating power q=3865 W/m^2. a) bubble shape, b) temperature, and c) calculated heat flux distribution. The figure taken from [38], p. 78.

the local heat flux or temperature at the foot of growing vapor bubble is the use of micro heater arrays to impose constant temperature or constant heat flux boundary conditions [31]. The main conclusion from the local measurements during the nucleate boiling is that there is a very high heat flux and temperature variation in the vicinity of the CL, see Fig. 1.5. The local heat flux measured at the bubble foot can be of several orders higher than its value averaged over the heater surface. However note that the reality might be even more striking as due to limited resolution the measured values are still averaged over several tens of micrometers which is much larger than the overall typical size of the microrgion ($\sim$ 1 μm). In addition, most of publications indicate [31] that the mircoregion heat flux contribution to overall heat transfer from the solid heater is about 30 %. This is a rather high value when considering that the area over which such an energy is transferred is very small (proportional to the overall CL length). It needs to be taken into account in the modeling of boiling. In addition, the microregion is important also due to its impact on vapor bubble geometry and naturally its influence on bubble departure event [39]. The microregion is thus significant for the global vapor bubble dynamic evolution during bubble boiling.

One of first studies dealing with simulation of nucleate boiling was made by Stephan and

Hammer [1] who attempted to determine the heat transfer coefficient. In this publication, an implementation of microregion model for complete wetting (briefly described in section 1.3.2) was proposed and applied to 2D numerical simulation of single spherical vapor bubble growth on heated surface. In the macroregion liquid domain, the hydrodynamics was completely neglected. A quasi stationary heat conduction was solved in liquid and solved domains. No bubble departure was considered.

More recent research work of the same group concerns the numerical simulation of the bubble boiling [40, 41]. The significant progress with respect to [1] was made. The volume-of-fluid (VOF) solver of the OpenFOAM package was used to simulate repetitive bubble growth and detachment from the heated wall. Full Navier-Stokes equations in the vapor and liquid domain were solved in three dimensional space. The correlated values of the microregion model [1] were used. The apparent contact angle was used to determine the surface tension adhesion force, playing the major role in vapor bubble departure. Relatively low heat fluxes corresponding the nucleate boiling regime were applied.

Nowadays, there are many numerical studies of boiling phenomenon available e.g. [32, 42–47], treating the problem at various level of complexity with various computational approaches (VOF, Level-Set method, Lattice Boltzmann method, etc.) and interface tracking method. However to perform full simulation of boiling in complex geometries is still far from being feasible with any of existing codes.

The previously mentioned studies targeted the nucleate boiling as it is a usual working regime of the industrial heat exchangers. Obviously, it is of high importance to study the limiting phenomena of nucleate boiling as it determines the maximal possible heat loads transferable within the device. It is important to predict the CHF value for given system configuration. Such a task requires clear understanding of the physical phenomenon that triggers it.

Concerning the boiling crisis, several dozens of existing models are available, see [48, 49]. Several mechanisms are considered to be generally important [50], for instance: 1) breakdown of stability in macroscopic hydrodynamics [51], 2) rapid vapor blanketing due to the heterogeneous spontaneous nucleation [52], 3) contact line instability due to the vapor recoil effect [53, 54], etc. The first mentioned, Zuber model [25, 51, 55] is the only one that can be considered as a theory, the others being mainly empirical or semi-empirical. According to Zuber's model, vapor columns form at the nucleation sites on the heater. The vapor moves upwards while the liquid moves to the bottom of the column where evaporation occurs. This counter-flow motion induces the Kelvin-Helmholtz instability, which is supposed to cause destabilization of the whole system and formation of a vapor film on the heater. This transition occurs when the vapor velocity exceeds the Kelvin-Helmholtz threshold [55] resulting in the following CHF (Zuber-Kutateladze) expression,

$$q_{CHF} \sim H[\sigma g(\rho_L - \rho_V)/\rho_V^2]^{1/4}, \tag{1.1}$$

where H is the latent heat, ρ_L (ρ_V) is the density of the liquid (gas) phase, σ is the surface tension, and g is the gravity acceleration. While this expression fits a number of experimental data sets, the underlying physics is questionable. Indeed, the vapor column morphology of boiling is quite rarely observed while the BC occurs inevitably for all morphologies of boiling, for pool as well as for flow boiling. Besides, many experimental results, in particular those obtained in low gravity [56], cannot be fitted by Eq. (1.1). Other physical phenomena should then be responsible for the triggering of BC. A strong dependence of CHF on the wetting properties and the surface state of the heater [25] suggests a phenomenon at the level of the triple (vapor-liquid-solid) contact line rather than a phenomenon related to the bulk hydrodynamics [55, 57]. It is important to identify this small-scale phenomenon that triggers the BC and thus defines

its threshold. Either the dry spots under individual vapor bubble begin to grow independently and coalesce later or many neighboring bubbles begin to coalesce thus creating a growing dry spot. A thorough analysis [58] of this second scenario has shown a necessity of the repetitive (at least 30 – 40 times) formation of aggregates of 2 – 3 coalesced bubbles at the same neighboring nucleation spots. This is not a likely event because in order to coalesce: 1) the bubbles need to grow close to each other, which is prohibited by their thermal interaction [59, 60], and 2) the strong lubrication forces between their interfaces need to be overcome [61], which means that either the bubbles are densely crowded or strongly pinned at their nucleation sites. More recent experimental studies [62, 63] corroborate these considerations.

In the present thesis we consider the scenario based on the spreading of the dry spot under a vapor bubble, suggested theoretically in [53]. The reasoning was based on the vapor recoil force, a force originated from intensive evaporations at the CL (see section 1.25), neglecting completely the hydrodynamics. Such a reasoning has been confirmed by observation of growth of individual dry spots through the transparent heater [64, 65]. To our knowledge, the dynamics of BC that clearly showed its progression was observed only at nearly critical pressure (near the liquid-gas critical point) where the weak heat diffusion slowed down the bubble growth and where the CHF value become very small [66, 67]. Such experiments had to be performed in the reduced gravity. The reason for this is that close to the critical point the surface tension is very low (vanishing at the critical point), which cause a strong bubble interface deformation when experiment done at terrestrial conditions. In such a way, it has been shown that the spreading of dry spots under individual bubbles precedes their coalescence which gives rise to the fast heater temperature rise. Recently, very fine experiments dedicated to study of boiling crisis near the vapor-liquid critical

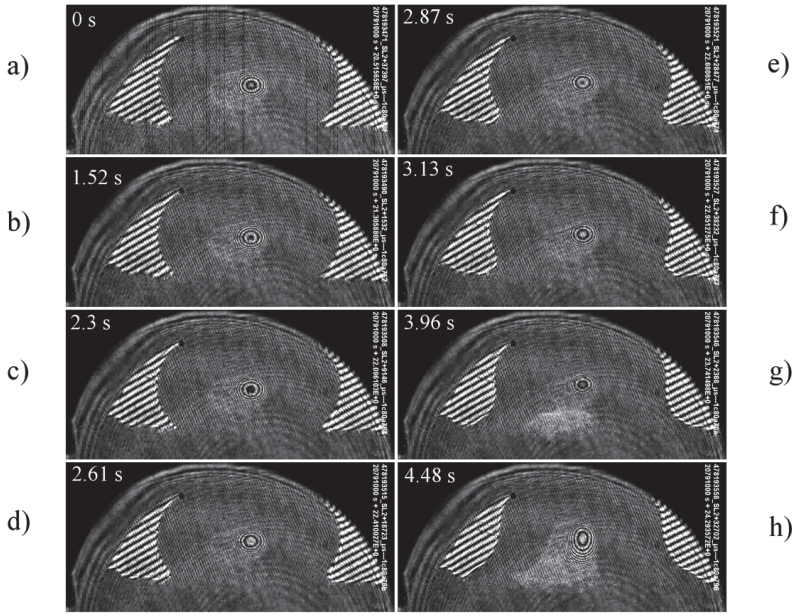

Figure 1.6: Preliminary results from DECLIC experiment [66]. The side view snapshots of the bubble on the solid heater are shown. The system is heated by initial short pulse heat generation in the heater ($t = 0$). The time evolution shows the deformation of the liquid-vapor interface in the vicinity of the CL.

point were performed on board of the International space station in the facility developed by CNES and managed by NASA, DECLIC. Some details on DECLIC can be found in Appendix A. Representative preliminary results [68] are shown in Fig. 1.6. In this figure, sevaral side

view snapshots of the bubble on the solid heater are shown. The flattened shape of the bubble is caused by the geometry of the experimental cell (zero gravity environment). The system is heated by initial ($t = 0$) short pulse heat generation in solid. The time evolution shows the deformation of the liquid-vapor interface in the vicinity of the CL. The apparent contact angle increases in time. Such an experiment shows that the vapor spreading process is caused by heating and the contact line region is enormously important for the bubble growth dynamics.

1.3 Hydrodynamics in the vicinity of contact line

In the previous section, we showed the importance of the vicinity of the contact line. In this section, the hydrodynamics in the vicinity of CL is discussed in more detail.

1.3.1 Theoretical background

In this section, the theoretical basis related to the contact line modeling is discussed.

1.3.1.1 Slip length

Slip length is a parameter related to the slip boundary condition which, contrary to the no-slip boundary condition, allows nonzero liquid velocity at the solid wall. The necessity of relaxing the no-slip boundary condition is typical in several situations such as gas flow in microchannels, flows of non-Newtonian fluids and in problems related to the contact line. In order to demonstrate its necessity let us consider purely isothermal CL dynamic situation ($v_{CL} \neq 0$) with conventional no-slip boundary condition $v_x = 0$ at solid wall, see Fig. 1.7.

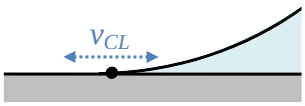

Figure 1.7: Geometry of isothermal dynamic CL situation.

This exactly demonstrates co called viscous stress singularity, which was pointed out first by Huh and Scriven .

$v_{CL} \neq 0$ dictates that the liquid-vapor interface moves with respect to the solid liquid interface. Since CL belongs to both interfaces, its velocity is then ambiguous, which is well known to produce logarithmically divergent total drag force on solid substrate [69], which is not physically acceptable. The oldest and simplest way to overcome such a difficulty is to employ the slip length. The simplest expression that involves the slip length l_s is the Navier slip condition

$$v_x = l_s \frac{\partial v_x}{\partial y}.$$

From the modeling point of view, the slip boundary condition is a suitable candidate, which provides a satisfactory description for the significant features of the motion. Satisfactory means that the system admits a simple mathematical description, which can be solved with given boundary conditions (finite slope and zero thickness of liquid-vapor interface at CL). Nevertheless, a logarithmically divergent hydrodynamics pressure (although integrable) at the CL is nonphysical.

One needs to mention that the slip of liquid along the solid substrate is well confirmed experimentally, see e.g. [70, 71], and recent measurements permit to determine hydrodynamic slip lengths up to 10 nm accuracy [72]. Another approach supporting the concept of the slip length

is the molecular dynamic simulations [73, 74]. More detailed discussion on this phenomenon may be found in the review articles [71, 74]. In general, all these studies showed that the no-slip boundary condition should be replaced in the vicinity of the CL.

1.3.1.2 Kelvin effect

The Kelvin effect (sometimes also called the Gibbs-Thomson effect) is a dependence of the saturation temperature on pressure. Such a phenomenon is topic covered by most of textbooks on fluid physics. Here, the books [75] and [76] are followed.

Let us consider a large volume of liquid separated by a flat interface from its vapor, where the pressure is p_{sat}^{∞}. The liquid contains a vapor bubble at equilibrium, see Fig. 3.1. The pressure is constant within each phase. The pressures in each phase satisfy the equation $\mu_V(p_V, T^i) = \mu_L(p_L, T^i)$. A similar expression can be written for the flat liquid-vapor interface, $\mu_V(p_{sat}^{\infty}, T^i) = \mu_L(p_{sat}^{\infty}, T^i) \equiv \mu$, where μ is the common value of the two chemical potentials. In order to obtain each of the pressures, let us subtract two latter equations

$$\mu_V(p_V, T^i) - \mu_V(p_{sat}^{\infty}, T^i) = \mu_L(p_L, T^i) - \mu_L(p_{sat}^{\infty}, T^i). \tag{1.2}$$

The pressure in the phases may be different, because of the bubble interface curvature or other

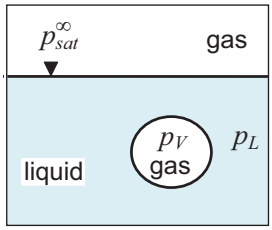

Figure 1.8: Vapor bubble in bulk liquid, isothermal system.

reasons

$$p_V - p_L = \Delta p, \tag{1.3}$$

where Δp is the pressure jump.

For small differences $\delta p_V = p_V - p_{sat}^{\infty}$, $\delta p_L = p_L - p_{sat}^{\infty}$ one expands (1.2) in terms of $\delta p_{V,L}$ [76], and gets

$$\frac{\delta p_V}{\rho_V} = \frac{\delta p_L}{\rho_L}. \tag{1.4}$$

Using this formula together with (1.3), written however for pressure differences ($\delta p_V - \delta p_L = \Delta p$), one obtains for the vapor bubble surrounded by liquid

$$p_V - p_{sat}^{\infty} = \Delta p \frac{\rho_V}{\rho_L - \rho_V}, \quad p_L - p_{sat}^{\infty} = \Delta p \frac{\rho_L}{\rho_L - \rho_V}. \tag{1.5}$$

In order to get an expression for the equilibrium temperature of interface (dependent on the pressure jump), we use the assumption $\rho_L \gg \rho_V$. For (1.5b) we get $p_L \sim p_{sat}(T^i) - \Delta p$ and (1.5a) reduces to

$$p_V \sim p_{sat}(T^i) - \Delta p \frac{\rho_V}{\rho_L}. \tag{1.6}$$

The Clausius-Clapeyron equation

$$\left.\frac{dp}{dT}\right|_{sat} = \frac{H \rho_L \rho_V}{T_{sat}(p_V)(\rho_L - \rho_V)} \tag{1.7}$$

leads to

$$\frac{p_{sat}(T^i) - p_V}{T^i - T_{sat}(p_V)} = \frac{H\rho_V}{T_{sat}(p_V)}. \tag{1.8}$$

When combining (1.6, 1.8) one obtains the expression for the equilibrium interface temperature as a function of pressure jump

$$T^i = T_{sat}\left(1 + \frac{\Delta p}{H\rho_L}\right). \tag{1.9}$$

The interface temperature thus depends on the pressure jump across the liquid-vapor interface. This phenomenon is hereafter referred as the Kelvin effect.

In the microregion description, the vapor pressure p_V is considered to be spatially homogeneous ("one-sided" description [1–3, 5, 6, 77]). The interface temperature is however allowed to vary following the pressure in the liquid phase p_L, which needs to be determined from the hydrodynamic part of the problem. Eq. (1.9) is used in this case under the hypothesis of local equilibrium.

1.3.1.3 Interfacial thermal resistance

This phenomenon is considered mainly due to extremely high local heat fluxes at the liquid-vapor interface in the vicinity of the contact line. It is related to the question of maximal theoretical evaporation flux and its limitation due to molecular kinetic aspect (motion of vapor molecules in the vicinity of the interface during the phase change). Here the phenomenon is briefly introduced, detailed description can be found in books [22, 78] or in more recent publications on this topic [79, 80].

From the molecular kinetics theory, the following expression [22] can be derived for heat flux at the interface

$$q^i = \frac{2f}{2-f}\frac{H}{\sqrt{2\pi R_g/M}}\left(\frac{p_V^i}{\sqrt{T^i}} - \frac{p_V}{\sqrt{T_{sat}(p_V)}}\right), \tag{1.10}$$

where f is the accommodation coefficient taking into account molecular effects such as reflection or emission of molecules from the liquid-vapor interface. The main assumptions used for its derivation: Maxwell velocity distribution of particles in gaseous phase, the flux of molecules of each phase is determined by corresponding temperature and pressure, ideal gas law, small rate between the average molecular velocity (in the bulk) and characteristic velocity of molecules $q^i(\rho_V H)^{-1}/\sqrt{2R_g T_V/M} \ll 1$. p_V is the pressure of the bulk vapor and p_V^i the pressure in the vapor phase at the interface.

There are several ways to simplify Eq. (1.10), see [22, 81]. We follow the approach of Stephan *et al.* [1, 41], who proposed to reduce the expression (1.10) by considering a negligible difference between the interfacial temperature and the saturation temperature compared to their absolute values for the case of a flat interface $p_V^i = p_{sat}(T^i)$

$$q^i = \frac{2f}{2-f}\frac{H(p_{sat}(T^i) - p_V)}{\sqrt{2\pi R_g T_{sat}/M}}. \tag{1.11}$$

By using the linearized form of Clausious-Clapeyron equation (1.8), one can get an expression describing the deviation of interface temperature from the value given by the bulk vapor pressure

$$T^i = T_{sat}(p_V) + R^i q^i, \tag{1.12}$$

where R^i is defined as

$$R^i = \frac{2-f}{2f}\frac{T_{sat}\sqrt{2\pi R_g T_{sat}/M}(\rho_L - \rho_V)}{H^2\rho_L\rho_V}, \tag{1.13}$$

The value of accommodation coefficient is quite unsure quantity [82] (experimentally obtained data scatter over two orders of magnitude). For simplicity, similarly to [1], f is set to unity here.

1.3.1.4 Surface forces at partial wetting

This phenomenon enters the problem when the length scale of interest in the vicinity of CL is comparable to the length scale of interaction between the molecules [83]. Let us first consider a thin liquid film of a homogeneous thickness h on a solid substrate at equilibrium, see Fig. 1.9. The liquid is surrounded by its gas and the system is at the saturation temperature T_{sat} given by

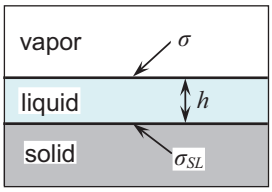

Figure 1.9: Isothermal liquid film on solid.

the bulk vapor pressure. The excess free energy W (appearing due to the presence of interfaces) per unit area is

$$W(h) = \sigma_{SL} + \sigma + P(h), \tag{1.14}$$

where the first two terms in the right side are the tensions of the solid-liquid and gas-liquid interfaces, respectively. The term $P(h)$ is the energy of the surface (or thin film) forces [83, 84]. It appears because the molecules of the solid "feel" the gas-liquid interface. It is a contribution of the differential (proportional to difference of liquid and vapor density) interaction energy of the molecules of the liquid and of the gas with those of the solid. The h scale at which $P(h)$ matters depends mainly on the combination of materials in the given system. Obviously, $P(h \to \infty) = 0$.

The limit $h \to 0$ may be attained at partial wetting. It is evident that $W(h \to 0)$ has to be finite in this case. It has been postulated by [85] that

$$W(h \to 0) = \sigma_{SG}, \tag{1.15}$$

which corresponds to the energy of the dry (bare) solid-gas interface. Equations (1.14), (1.15) then lead to the constraint $P(h \to 0) = S$, where

$$S = \sigma_{SG} - \sigma_{SL} - \sigma \tag{1.16}$$

is the spreading coefficient. A more general case [86, 87] $P(h \to 0) \geq S$ is adopted here. The inequality can be justified by the existence of a monolayer of fluid molecules that may modify the surface energy so that $W(h \to 0) > \sigma_{SG}$.

Consider next the wedge-like geometry appearing at partial wetting (when contact angle is small), again at equilibrium. At large scales, the meniscus and the substrate make the contact angle θ_Y (see Fig. 1.12) defined by the Young formula $\cos\theta_Y = 1 + S/\sigma$ where $S < 0$. At the scale of molecular size, the meniscus forms a contact angle θ_{micro}. By minimizing the free energy functional in statics [86], it can be shown that θ_{micro} needs to satisfy the equation [87]

$$\cos\theta_{micro} = 1 + \frac{S - P(h \to 0)}{\sigma}. \tag{1.17}$$

One finds out easily that

$$\cos\theta_{micro} = \cos\theta_Y - \frac{P(h\to 0)}{\sigma}. \tag{1.18}$$

Note that the assumption (1.15) results in $\theta_{micro} = 0$; $\theta_{micro} \geq 0$ in a more general case considered here.

The above approach has been developed in the "local" approximation, where P is assumed to be independent of the spatial variation of h (i.e., on its spatial derivatives). The non-local approach, e.g. [88–90] (where P is considered to be a functional of $h(x)$) gives a correction to (1.18) and (1.19) at large θ_Y. In particular, $\theta_{micro} \neq 0$ even for $P(h\to 0) = S$. For small angles, the results of the local and non-local approaches are essentially similar. The meniscus shape is calculated from the normal stress balance at the interface,

$$\Delta p = K\sigma + \Pi(h), \tag{1.19}$$

where K is the interface curvature and Π is the disjoining pressure related to P via

$$\Pi = -\frac{\partial P}{\partial h}. \tag{1.20}$$

In general, the disjoining pressure includes contributions from dispersion, electrical double layers, electrostatic and structural forces [84]. For simplicity, only the dispersion component (Π_a) is considered here in spite of the fluid choice (water, for which the electrostatic and structural forces are important). For $h \gtrsim 10$ nm (neglecting the retardation effect),

$$\Pi_a(h) = A/(6\pi h^3). \tag{1.21}$$

The Hamaker constant A is positive for the "high-energy" metal or oxidized surfaces, and its value is $A \sim 10^{-20} - 10^{-19}$ J. When the interface extends up to the solid surface ($h \to 0$), $\Pi_a \to \infty$ and a difficulty appears while solving Eq. (1.19) with $\Pi = \Pi_a$. There are several solutions to this problem at equilibrium [91] or out of it [6]. Choosing a particular shape of Π, finite as $h \to 0$ is adopted here, see discussion associated with Fig. 1.12.

1.3.1.5 Vapor recoil

Every fluid molecule evaporated from the liquid interface causes a recoil force analogous to that created by the gas emitted by a rocket engine. It pushes the interface towards the liquid side in the normal direction. This force appears because the fluid necessarily expands while transforming from liquid to gas phase. Obviously, the stronger the evaporation rate, the larger is the vapor recoil force.

Let us consider a portion of the liquid-vapor interface of area $\mathrm{d}A$, see Fig. 1.10. During the time $\mathrm{d}t$, the liquid of the mass $\mathrm{d}m$ is evaporated. This mass can be expressed as

$$\mathrm{d}m = \rho_V \mathrm{d}V_V = \rho_L \mathrm{d}V_L, \tag{1.22}$$

where $\mathrm{d}V_L(\mathrm{d}V_V)$ and $\rho_L(\rho_V)$ are the volume and the density of the evaporated liquid (created vapor). As a consequence, the interface moves towards the liquid side $\mathrm{d}\vec{l} = -\vec{n}\mathrm{d}V_L/\mathrm{d}A$, where $\vec{n}$ is the unit vector to the interface.

The conservation of momentum for the portion of the fluid shown in Fig. 1.10 is

$$(\vec{v}_V + \vec{v}^{\,i})\mathrm{d}m + \vec{p}_r \mathrm{d}t\mathrm{d}A = 0, \tag{1.23}$$

where $\vec{p}_r$ is the vapor recoil pressure, $\vec{v}^i = \mathrm{d}\vec{l}/\mathrm{d}t$ is the velocity of the interface and $\vec{v}_V = \vec{n}\mathrm{d}V_V/(\mathrm{d}A\mathrm{d}t)$ is the velocity of the vapor with respect to the interface. When using the expression for $\vec{v}_V$ and Eq. (1.22), Eq. (1.23) can be rewritten as

$$\vec{p}_r = -\vec{n}J^2\left(\frac{1}{\rho_V} - \frac{1}{\rho_L}\right), \tag{1.24}$$

where $J = \mathrm{d}m/(\mathrm{d}A\mathrm{d}t)$ is the mass evaporation flux. Note that $\vec{p}_r$ is always directed towards the

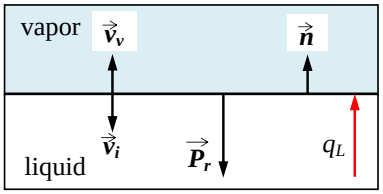

Figure 1.10: Control part of the interface

liquid. Similarly to the disjoining pressure term, the vapor recoil pressure enters the pressure balance equation like $K\sigma = \Delta p + p_r$ [53], where $p_r = J^2(\rho_V^{-1} - \rho_L^{-1})$. The counter part expression to (1.9, 1.12) reflecting the impact of the vapor recoil on the interface temperature (its influence might be important at large heat fluxes) is

$$T^i = T_{sat} + \frac{T_{sat}J^2}{2H}\left(\frac{1}{\rho_V^2} - \frac{1}{\rho_L^2}\right), \tag{1.25}$$

see [92, 93] for its derivation and discussion.

1.3.2 State of the art

Present understanding of the processes related to the evaporation in the vicinity of CL is based on the approach originally developed by Wayner [2, 94] for the evaporation from the continuous liquid meniscus. This approach assumes a continuous adsorbed film (see Section 1.3.1.4) that covers the solid surface and does not evaporate because of the attractive surface forces, see Fig. 1.11. Small interface slopes are usually considered and thus the hydrodynamics is described within the lubrication approximation. The key essence of the model in [2] was the implementation of the disjoining pressure (1.21) and the interfacial resistance. The system was heated by imposing constant temperature of the heater increased with respect to saturation temperature by ΔT, called superheating. The numerical solution of such a problem was proposed (orthogonal collocation method), imposing perturbed flat adsorbed film of the thickness h_{ad} at the border of the microrgeion corresponding to $x \to -\infty$, see Fig. 1.11. Such a solving strategy was followed by majority of researchers modeling this problem, in the the regime of complete wetting e.g. [1, 3, 5]. The authors showed that the evaporation in the contact line region induces a considerable liquid flow towards the adsorbed liquid film. This necessarily impose a pressure drop induced curvature variation. In practice it means that the slope of the free interface, zero at $x \to -\infty$ may considerably differ at the opposite limit $x \to \infty$. The latter slope is associated with the so called apparent contact angle, observable at macroscopic scale (cf. Fig. 1.11).

The microregion model of Moosman & Homsy [3] was based on previous research results of Wayner, including disjoining pressure, Kelvin effect, interface resistance, and gravity force. They have made an attempt to solve the problem analytically by perturbation about the isothermal conditions in perturbation series with respect to the superheating. Due to inclusion of gravity

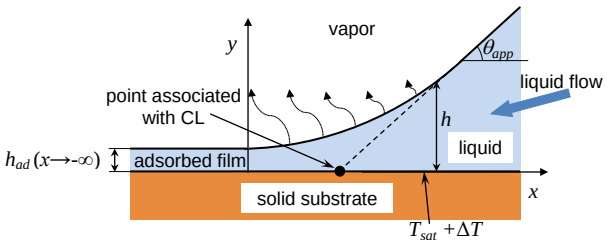

Figure 1.11: Geometry of the complete wetting evaporation problem. The actual CL is in fact nonexistent and is usually associated with a point where the extended shape of the macroscopic part of the meniscus intersects the solid surface.

term directed towards the solid wall, the isothermal liquid-vapor interface profile (for $\Delta T = 0$, zero order solution) deviated from flat film. Note that when gravity is excluded, the solution for an isothermal case is nonexistent when zero curvature of interface far from CL is imposed. The first order mathematical problem statement was too difficult to be solved by the authors. They thus solved it numerically. Such a work inspired the author of this thesis to perform similar analysis, obtaining the solution in a closed analytical form up to the first order.

Another publication that should be highlighted in this context is the research paper of Stephan *et al.* [1]. They presented a stationary contact line evaporation model based on [2, 3], including the disjoining pressure, interface resistance and Kelvin effect. The model equations are presented below, as the model represents the starting point of this thesis

$$\frac{d}{dx}\left(\frac{h^3}{3}\frac{d\Delta p}{dx}\right) = -\mu\frac{q_L^i}{H\rho_L}, \tag{1.26}$$

$$\sigma\frac{d^2h}{dx^2}\frac{1}{\sqrt{\left(1+\left(\frac{dh}{dx}\right)^2\right)^3}} = \Delta p - \Pi, \tag{1.27}$$

where $\Delta p(x)$ is the pressure jump and Π the disjoining pressure (1.21). The local heat flux at the free interface (from the liquid side) is expressed as

$$q_L^i(x) = \frac{\Delta T - \Delta p T_{sat}/(H\rho_L)}{R^i + h/k_L}. \tag{1.28}$$

The equations (1.26, 1.27) are of the forth order and thus four boundary conditions are necessary. Two of them are supplied from the definition of complete wetting and knowing that the interface is flat (curvature K vanishes) for $\pm\infty$:

$$h|_{x\to-\infty} = h_{ad}, \quad \left.\frac{dh}{dx}\right|_{x\to-\infty} = 0, \quad K|_{x\to\infty} = 0, \quad K|_{x\to-\infty} = 0. \tag{1.29}$$

The thickness of the liquid film can be easily obtained as the existence of nontrivial solution to (1.26 - 1.29) requires $q_L^i(-\infty) = 0$ ($\Delta T - \Pi_a T_{sat}/(H\rho_L) = 0$, $\Pi_a = A/(6\pi h_{ad}^3)$) and one directly gets $h_{ad} = (\rho_l H\Delta T/A)^{-1/3}$. The numerical solution of the model was obtained with the Runge-Kutta method. Note however that the numerical treatment of this problem is relatively difficult since true CL is nonexistent, the solution domain extends from $-\infty$ to ∞. One has to impose some finite size in numerical treatment and to choose some small perturbation for one (or two) initial conditions to avoid flat film solution[4] and shoot for the boundary condition at the opposite

[4]Note however that, in [1] slightly different boundary conditions were used: $\Delta p_{ad}|_{x\to-\infty} = A/(6\pi h_{ad}^3)$, which is in principle equivalent to (1.29d). $q_L^i|_{x\to-\infty} = 0$ was used as shooting parameter to satisfy (1.29c).

side of the domain. The results were in the macroscopic vapor bubble problem simulation to determine the overall heat transfer coefficient in boiling. This model is in its essence similar to the model developed and presented in this thesis, however significantly differs in several aspects e.g. CL treatment (absent in [1]), the implementation of surface forces or solution method.

Morris [5, 95] revisited the complete wetting microregion model (1.26 - 1.28) including dispersion component of disjoining pressure, Kelvin effect and interface resistance. He subjected this model to various studies, including the effect of substrate conductivity. He considered the problem as multiscale and formulated it in the inner and outer regions. θ_{app} was determined in the inner region contributing, by a negligible fraction of total evaporation. The total transferred heat was mainly given by its contribution at larger scales defined by conduction in a wedge defined by θ_{app}. A numerical and an approximate asymptotic results were presented. Morris first suggested that the apparent contact angle scales as $\Delta T^{1/4}$. The weak part of his work seems to be an attempt to validate his results experimentally as experimental data [96] were obtained for very small (and not explicitly measured during the experiment) solid surface superheating ΔT (several mK). Morris made an attempt to estimate a value of superheating from the experimental results using his microregion model. Results obtained by such a procedure seem to be implausible.

Recently three research groups represented by Wayner, Stephan and Kim joined their efforts and provided experimental measurements [4] of the apparent contact angle of evaporating droplets. Though authors assume that the liquid (FC-72) completely wets the solid substrate (copper) they measured the equilibrium contact angle $\theta_Y = 8°$. This fact is in contradiction to the mathematical modeling in the frame of the complete wetting performed by them for comparison (cf. Eq. 1.29b). The microregion model used was in its core identical to that presented in [1] (Eqs. 1.26 - 1.29), enhanced for the vapor recoil pressure[5]. The measured apparent contact angle has been shown to be much larger (up to $\Delta\theta \sim 35°$) with respect to θ_Y due to the applied wall superheating.

Another recent and significant research publication on this topic is that of Rednikov & Colinet [6], which is a continuation of their previous mathematically based analysis [97] of the CL microstructure (called microregion here). Their model under study is similar to that of Morris [5] Eqs. (1.26 - 1.29). The advancement with respect to previous existing studies lies in consideration of the spreading coefficient as an additional independent parameter. They argued that the regime with truncated microfilm (film ending by dry solid) is preferred if the spreading coefficient is smaller than a positive (i.e., corresponding to complete wetting) critical value dependent upon the solid superheating. Some comment was also made on the negative spreading parameter, stating that in this case the liquid film is always truncated. The authors however did not treat the microregion for $h \to 0$ as the problem related to the divergence of the used form of disjoining pressure (1.21) appears. Instead, they used a "truncated film" solution of Eq. (1.19) (see Fig. 1.12), which was used before at equilibrium [91] or more recently e.g. for diffusive evaporation modeling [15]. It has an asymptotics $h \sim \sqrt{x}$ as $x \to 0$. Such type of a solution can only be obtained in the small slope approximation where $K \approx \partial^2 h/\partial x^2$. However the solution is not coherent with the approximation precisely at $x \to 0$. When a full expression for K is used, such type of the solution is absent. To make the mathematical theory coherent, one needs either to exclude the vicinity $h \to 0$ from the consideration [89, 91] (one notes that the truncated film then describes the solution at some intermediate range of h, see Fig. 1.12) or use a more sophisticated expression for Π modified at $h \to 0$. An exhaustive asymptotic analysis of contact line models based on asymptotic $h \sim \sqrt{x}$ was presented by Colinet & Rednikov in [98].

[5] Which by the way might be important in the case of FC-72, though not discussed by authors (see Fig. 2.33 and to it associated discussion).

In the recent publication [99] authors also pointed out the importance of the disjoining pressure together with the Kelvin effect in complete wetting microregion modeling.

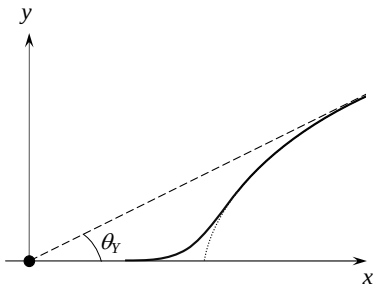

Figure 1.12: Interface shape in the vicinity of the contact line at partial wetting according to different modeling approaches. Dashed line: surface forces are neglected. Dotted line: truncated film; only attractive intermolecular interaction is considered [6, 98]. The solid line represents a solution when both attractive and repulsive intermolecular interactions are considered [85]. Such an approach is adopted here.

Majority of above mentioned studies targeted primarily the complete wetting situation. The complete wetting case is unfortunately not often seen in real applications (in fact it is quite difficult to achieve a situation in which liquid completely wets solid substrate [8]). The liquid-solid-vapor system exhibits usually a finite contact angle under isothermal conditions. Treating this situation is rather difficult in the mathematical description developed within the complete wetting modeling approach, relying on the presence of disjoining pressure term. Such an attempt was made (including CL motion) in [7], where the choice of the disjoining pressure of nonmonotonous shape resulted in isothermal interface shape exhibiting finite slope far from CL ($x \to \infty$ when microregion decoupled from the macroregion problem) and adsorbed film at the opposite end of the microregion domain $x \to -\infty$. Such a situation corresponds to "pseodo partial" wetting [83], which leads to a physical model, necessarily containing microscopic parameters related to surface forces, which are nowadays still practically impossible to measure or reliably theoretically estimate. Second alternative is the approach already mentioned in the previous paragraph using the leading order behavior $h \sim \sqrt{x}$. The contact angle enters the system through the spreading coefficient [91, 98]. The asymptotic $h \sim \sqrt{x}$ thus results in dry solid substrate for $x < 0$.

In our opinion, the simplest and most natural way of treating a partial wetting case is imposing directly the contact angle characterizing the equilibrium slope of the liquid-vapor interface at the solid substrate a part of which is dry at the CL. Such a situation is primarily addressed in this thesis. The list of publications related to such a situation in the context of evaporation is small. The research in this frame was initiated by Anderson and Davis [100], first studying the local fluid flow and heat transfer near CL and analyzing the associated singularities with the straight wedge approximation. In their next publication [101] they studied theoretically the evaporation of a two-dimensional volatile liquid drop on uniformly heated horizontal substrate. The drop was described within the lubrication approximation. The physical model included the slip length[6], interface resistance and thermocapillary terms. Their study concerned both unsteady and stationary regimes. Without any justification, they imposed the slope at the contact line dependent upon the CL velocity. The stationary evaporation regime was achieved by introducing the liquid injector in the drop base. Such a source was considered to compensate exactly the evaporated mass.

[6] Note that the slip length was recently accounted for in the complete wetting CL modeling [102].

The latter study encouraged Hocking [103] to publish a theoretical asymptotic study of stationary drop evaporation (using in principle identical model as in [100]), giving an explicit relation for the corresponding apparent contact angle $\sim \Delta T^{1/4}$. In both studies the hydrodynamic singularity was relaxed by using the slip length and thermal interface resistance. The mass evaporation flux was limited at the CL by considering the interface thermal resistance.

The publication which is directly related to the present thesis is a numerical study of nonstationary volatile liquid drop evaporation performed by Nikolayev [104]. This paper deals similarly to [101] with essentially nonstationary liquid drop evaporation. Some new features were introduced. First, the dependence of interface temperature on liquid pressure (Kelvin effect) was included. Second, the dynamic CL motion was solved in a self consistent way. This means that no *a priori* relation between dynamic contact angle and CL velocity was applied. The microscopic contact angle (angle at which liquid-vapor interface meets solid surface) was considered to be independent of evaporation and CL motion. Such an assumption was also made earlier for the spreading of a drop [105] or, as already mentioned, for stationary drop evaporation e.g. [101, 103], but never considered in combination (evaporation and CL motion). The semi infinite conductive heater was used. The physical model proposed by Nikolayev served as a departure point for this thesis. Here the detailed physical analysis of the importance of its individual physical constituents is performed and the CL relaxation mechanism analyzed. The main purpose is to develop a physically justified and reasonably simple microregion model which can be used for macroscopic modeling purposes. The favored macroregion application which we target here is the boiling process.

The present thesis also touches at some limited extend the CL motion. The case of isothermal CL dynamics is a special topic with numerous applications in industrial but also natural processes. Only several publications related to the present thesis are discussed below. For more complete overview, see the review articles [8, 91]. Similarly to the evaporation case, the CL singularity needs to be relaxed [69] (see also section 1.3.1.1, related to the slip length). Most research publications dealing with the analytical description of the problem restrict the consideration to small capillary number $Ca = U\mu/\sigma \leq 0.1$, perfect surfaces (with no contact angle hysteresis, or pinning) and small interface slopes so that the lubrication approximation can be used. The problem is multiscale. Voinov [106] gave an analytical solution of the problem at intermediate scale from CL where the viscous stress is balanced by the capillary force. The particular solution provided by Voinov is obtained for the vanishing curvature at $x \to \infty$. The slope of interface varies logarithmically with the distance to the CL. Such a solution thus diverges at the CL. There were several propositions to overcome this difficulty, from which the most frequent is an introduction of the slip boundary condition [71, 105, 107, 108] or precursor wetting film [91, 109] at small scales. In the thesis, another mechanism of CL singularity relaxation is proposed, based on evaporation or condensation [110, 111]. Such an idea was previously suggested by Pomeau [112, 113], however in a rather general frame, without any suggestion of the mechanism that would link the CL motion and phase change.

1.4 The objectives of the thesis

The main goal of the present thesis is a development of the contact line model that can be used to simulate various macroscopic heat transfer problems, relevant to the described above technological applications. The primary requirement on the microregion model is an implementation of the partial wetting conditions, which in its essence requires to put stress on the asymptotic behavior and singularity relaxation at the CL. The impact of surface forces is also studied, as

such analysis was not performed before. The focus of the thesis lies on the numerical as well as analytical solution of the proposed microregion model. The microregion model is intended to be a research tool which can be used to gain a more detailed insight into the processes related to evaporation in the vicinity of the CL.

Second purpose of the present thesis is to demonstrate usage of the developed microregion evaporation CL model in a simulation of the single growing vapor bubble during the pool boiling using the Boundary Element Method (BEM). For this purpose the high slopes of the liquid-vapor interface are necessary to be treated and attention is addressed to enhance the lubrication approximation in its standard form applicable only to small interface slopes. A possibility of triggering the boiling crisis originating in processes at the microregion is discussed.

Another goal lies in an attempt to apply the evaporation/condensation to the treatment of the viscous singularity for the contact line dynamics.

In summary, the goals of the thesis are the development, implementation and analysis of the microregion model for partial wetting that overcomes limitations of other existing models. Further, the model is used to simulate a single vapor bubble growth during the boiling process with the aim to study of possibility of the microregion triggered boiling crisis.

Chapter 2

Contact line modeling at partial wetting and evaporation

Contents

In the previous chapter, the importance of the contact line (CL) region was pointed out. In this chapter that contains a key part of the thesis, the CL modeling at partial wetting and evaporation is discussed. The main purpose is to develop a microregion (i.e., contact line vicinity) model suitable for the description of industrially important problems such as the vapor bubble growth.

First, the governing equations of the microregion model are described. The major assumptions leading to simplification of the problem with corresponding arguments are discussed. The geometrical singularity at the CL requires to perform an asymptotic analysis (section 2.3). This leads to clarification of boundary conditions to be imposed. With the help of asymptotic analysis, the minimal complexity problem statement is identified, analyzed and solved for small superheating. The governing length scales of the problem are identified. Next, the moving contact line problem and its multiscale nature is addressed. The full microregion model is described and solved numerically. The impact of surface forces, interface resistance, slip length, solid surface conductivity and CL motion is studied. In the last section, an extension of the microregion model for large slopes of free interface (and large superheating) is presented and discussed.

2.1 Physical background of the model

In order to solve the problem in the vicinity of CL (i.e., in microregion), it is in principle necessary to solve full free-interface hydrodynamics in the liquid and vapor phases together with the thermal part of the problem in liquid, vapor and solid phases in 3-dimensions. The vapor is considered to be of the corresponding liquid. Such a problem is described by the complete set of the Navier-Stokes equations [114]:

$$\frac{D\rho}{Dt} = -\rho\nabla\cdot\vec{u}, \tag{2.1}$$

$$\rho\frac{D\vec{u}}{Dt} = -\nabla p + \mu\nabla^2\vec{u} + f, \tag{2.2}$$

$$\rho\frac{De}{Dt} = -p\nabla\cdot\vec{u} + \nabla\cdot(k\nabla T) + \Phi, \tag{2.3}$$

where

$$\Phi = \lambda\left(\frac{\partial u_k}{\partial x_k}\right)^2 + \mu\left(\frac{\partial u_i}{\partial x_j} + \frac{\partial u_j}{\partial x_i}\right)\frac{\partial u_j}{\partial x_i}$$

is the dissipation function, f represents external forces such as gravity and the operator D/Dt is the material derivative defined as $D/Dt = \partial/\partial t + \vec{u}\cdot\nabla$. The problem represented by Eqs. (2.1 - 2.3) has to be closed by the equation of state and accompanied by the relevant boundary conditions. Solving such a problem is a rather challenging task mainly due to its multi-scale nature. We approach this problem as previous research groups (e.g. [1, 2]) with following simplifications:

- The fluid is considered to be incompressible. This issue can be discussed essentially in two contexts: (1) related to the non-stationary macroscopic problem statement, (2) related to the density variation due to the pressure change. In the first context it is necessary to realize that the characteristic size (volume) of the microregion is very small ~ 1 μm, in considered applications (vapor bubble growth, liquid menisci in heat pipe). The associated acoustic time scales (liquid ~ 1 ns, gas ~ 10 ns) are much smaller than characteristic time scale of the macroscopic problem e.g. vapor bubble growth (~ 1 μs). The induced pressure perturbations (pressure waves) are thus nearly instantaneously equilibrated within the microregion.

  In the second case the justification of the assumption of incompressible fluid is less evident and it is necessary to say that some more attention should be addressed to this issue in futures studies. For situation far from the liquid-gas critical point (CP) the compressibility of usual fluids is negligibly small and even though the pressure jump in the CL vicinity is high, the impact of pressure on density is often neglected. This is consistent with usual assumption of constant material parameters, determined at vapor pressure [3, 5, 7, 97].

- One-sided approximation for the gas-liquid interface. (vapor side stress variation and heat flux are neglected). Arguments that lead to such an assumption are two. First, the ratio of thermal conductivity of vapor and liquid is very small ($k_V/k_L \ll 1$). Second argument follows from the thinness of the liquid layer. Its low thermal resistance leads to an extremely high local heat flux along the liquid-vapor interface (from the liquid side). The vapor domain on the contrary, can be considered as bulk, confined only by macroscopic geometrical configuration, of which characteristic length scale is much larger than the characteristic size of the microregion ($L_{micro} \sim 1$ μm). The expected thermal gradient (heat conducted to the vapor phase) in the vapor phase can be thus expected to be very small. The vapor viscosity being small, it equilibrates the pressure very quickly so that vapor pressure can be considered to be homogeneous.

- Small slope of the gas-liquid interface. This assumption allows us to simplify Eqs. (2.1, 2.2 - 2.3) with the standard lubrication approximation. Such an assumption is justified when the liquid-vapor interface meets solid surface at small microscopic contact angle and the slope of the interface within the microregion domain does not exceeds $\sim 35°$. Such an assumption will be violated in the microregion model implemented in the bubble growth simulation as high slopes of the interface are conceptually necessary. A correction to standard lubrication approach will be discussed in chapter 3.1.2.

- External forces such as gravity or inertial forces are neglected. They are proportional to the mass and are neglected due to smallness of the considered domain.

- Convective terms in (2.2) and (2.3) are neglected. The natural convection transport is neglected by the same reason. The advection terms in Eqs. (2.1, 2.2) and (2.3) are dropped due to small microregion characteristic size which results in small Reynolds and Rayleigh numbers ($Re \ll 1$, $Ra \ll 1$).

- Ideal solid substrate. The solid substrate is considered to be smooth and chemically homogeneous, with no defects (no CL pinning, no contact angle hysteresis).

- Two dimensional microregion domain. The curvature of the vapor-liquid interface in the plane parallel to the CL is neglected with respect to the curvature K in the perpendicular plane.

- Continuum description is valid up to subatomic scale. Such an issue is related to the fact that liquid layer merges solid substrate at CL. This geometric feature necessarily results in a region where the thickness of the liquid layer h vanishes ($h(x \to 0) \to 0$) and the continuum description may break down. Such an issue is however inevitable feature of the CL models in general. The continuum approach is generally justified when the size of the domain is at least several times larger than characteristic size of liquid molecules. Molecular dynamics simulations for the Couette and Poiseuille flows of the Lennard-Jones liquids [74] for channels whose width was larger than 10 molecular diameters showed that the macroscopic liquid properties such as velocity or stress field agreed completely with the solution of the Navier-Stokes equations. One needs to mention that the molecular level simulations [115–121] are far from being able to provide needed macroscopic variables for practical applications. In case of complete wetting, the continuum description seems to be more solid as the adsorbed liquid film is considered. However the film thickness is typically very small, see Fig. 2.1. What can justify such an approach is the fact that the contribution of "hydrodynamic pressure" from molecular length scale part of microregion is negligibly small. What is crucial is the asymptotic behavior of calculated quantities such as pressure or heat flux, they have to be bounded or at least integrable as $x \to 0$.

  Some discussion on justification of continuum CL models with ultra-thin films can be found in [122], reasoning in terms of averaging over sufficiently large area, time and agreement with experimental data, which is also our argument justifying meaningfulness of our approach. The only known comparison between the molecular dynamic simulation [123] and continuous microregion model of [1] shows a satisfactory agreement.

  Some features of molecular scale phenomena may be accounted for the disjoining pressure, interface thermal resistance or slip length. Their influence is studied in sections 2.5, below.

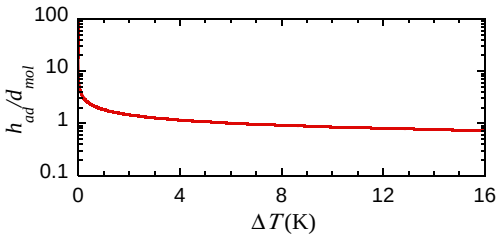

Figure 2.1: The thickness of the adsorbed liquid film h_{ad} scaled by the estimated characteristic diameter of the FC-72 molecule $d_{mol} = (3MN_A/(4\rho_L\pi))^{1/3}$ vs. wall superheating ΔT. The range of ΔT is chosen to be the same as presented in [4], p. 8, Fig. 6.

By considering mentioned simplifications, the problem defined by Eqs. (2.1, 2.2) and (2.3) is massively reduced. On the other hand there are several aspects which in addition need to be considered due to small scale geometrical configuration.

- Thin film forces. In the vicinity of the CL the liquid-vapor and solid liquid interface meet. When thickness of the liquid layer is less than 100 nm [83], additional forces originating from molecular interactions need to be considered [84].

- Liquid-vapor interface temperature varies along the interface. The geometrical singularity at the CL leads to high values of heat flux and pressure jump across the interface. This impacts the local thermodynamic equilibrium and results in a change of local interface temperature with respect to the saturation temperature given by the vapor pressure.

- No-slip boundary condition might be violated near CL. Similarly to CL dynamic case, high shear stress in the vicinity of CL due to flow caused by evaporation might require relaxation of the hydrodynamic singularity. Usually the Naiver slip boundary condition is used.

In the following, the microregion model equations describing the heat transfer problem, hydrodynamics, and interface shape are derived.

2.2 Microregion description

In this chapter the equations governing a stationary evaporation CL problem at partial wetting are presented. We limit ourselves to a case where the gas is a pure vapor corresponding to the liquid; the evaporation dynamics is then controlled by the supplied heat flux spent mainly to compensate the latent heat of vaporization. The heat stored the thin liquid layer is neglected compared to the heat transferred by evaporation. In the wedge-like geometry, a stationary regime can be attained: the liquid can be supplied to the meniscus to compensate exactly the evaporation losses. The stationary regime was studied both theoretically [1, 101, 103] and experimentally [4, 37]. Its immense benefit is a possibility of calculating the quantities needed for matching to the macroscopic problem (i.e., apparent contact angle θ_{app} and the total heat transferred through microregion Q_{micro}) as time independent functions of external parameters. The effect of the contact line velocity can be studied in this geometry by assuming that the liquid wedge is steady but the substrate is moving.

2.2.1 Heat transfer in the microregion

In order to demonstrate the specificity of the microregion heat transfer, let us first approach the problem naively, with a standard macroscopic approach [124]. Both liquid-vapor and liquid-solid interfaces are assumed to be isothermal. The background argument for this would be that the temperature of vapor-liquid interface T^i is generally homogeneous and equal to the saturation temperature T_{sat} corresponding to the given bulk vapor pressure. The surface of the metal heater can be assumed for isothermal due to its high thermal conductivity. In order to maintain evaporation of liquid, the heater surface temperature T_S must be higher than T_{sat}, see Fig. 2.2. The temperature at CL is thus ambiguous as at this point both interfaces merge, which causes

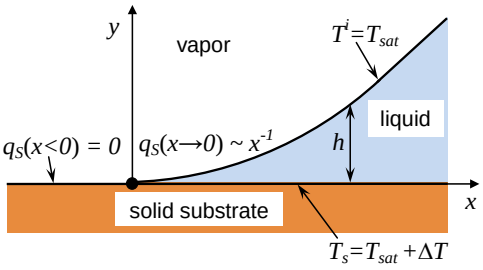

Figure 2.2: The oversimplified CL situation that leads to the singular heat flux.

a nonintegrable divergence of heat flux at the vapor-liquid interface $q_L^i(x) \sim 1/x$ [100], which indicates an inconsistency in the integral energy balance. Note that in addition, the singular heat flux at CL results, similarly to the CL dynamic case, to a viscous stress singularity at CL. Such an issue will be discussed later in more detail.

A more complicated modeling approach, in which temperature is allowed to vary along at least one of the interfaces, is necessary. One possibility is to allow the solid heater temperature to

vary due to its finite conductivity. Such an approach leads to regularization of the heat flux singularity at CL, but does not cure the problem completely as extremely high heat fluxes [54, 100] (approaching a theoretical maximum possible evaporation flux derived from molecular kinetic theory [22], used e.g. in [54] as a limiting value) appears in the vicinity of CL, overestimating the total heat transferred through microregion by factor of at least 3.5 [95]. Based on such a reasoning, one has to relax also the condition of the isothermal liquid-vapor interface. A phenomena causing the interface temperature to differ from saturation temperature corresponding to bulk vapor pressure were introduced in the section 1.3.1. The gas-liquid interface temperature T^i including the effects of the interfacial pressure jump Δp (Kelvin effect), interface resistance and vapor recoil pressure is

$$T^i = T_{sat}\left[1 + \frac{\Delta p}{H\rho_L} + \frac{J^2}{2H}\left(\frac{1}{\rho_V^2} - \frac{1}{\rho_L^2}\right)\right] + R^i q_L^i. \tag{2.4}$$

$\Delta p(x)$ needs to be determined from the hydrodynamic part of the problem, see below. Note that including the Kelvin effect into thermal part of the problem is the key feature, which couples the thermal and hydrodynamic parts of the problem. Such a link was absent in previous works dealing with CL evaporation under partial wetting [101, 103]. The vapor recoil contribution was derived in [93]. It is assumed hereafter that $\rho_L \gg \rho_V$ and $1/\rho_L^2$ can be neglected in the vapor recoil term. The heat conduction in the vapor in neglected; the enthalpy balance at the interface states that all heat brought from the liquid is consumed as latent heat at the interface

$$JH = q_L^i. \tag{2.5}$$

The same assumption causes the heat flux to the vapor domain to be zero

$$q_S(x < 0) = 0, \tag{2.6}$$

where q_S is the heat flux at the substrate surface. The heat is then transferred by conduction in solid and liquid domains. In the frame of the small slope approximation, a linear in y temperature variation in the liquid domain is assumed. The heat flux is then independent of y so that the following equation is valid for $x \geq 0$:

$$q_S = q_L^i = k_L \frac{T_S - T^i}{h}. \tag{2.7}$$

By combining (2.4, 2.5) and (2.7), one obtains the expression

$$J^2 \frac{T_{sat}}{2H\rho_V^2} + JH\left(R^i + \frac{h}{k_L}\right) + \frac{T_{sat}\Delta p}{H\rho_L} - \Delta T = 0, \tag{2.8}$$

which describes the heat transfer problem in the liquid phase. The first term is the effect of vapor recoil on the liquid vapor interface temperature, the second term covers the effect of conductivity of liquid layer and interface thermal resistance and the third term covers the impact of liquid pressure on the temperature of the liquid-vapor interface (Kelvin effect). $\Delta T = T_S - T_{sat}$ is the heater surface superheating, positive in the case of evaporation (negative for condensation). For a moderate heat load, the vapor recoil contribution in (2.8) is small and the mass evaporation flux at the liquid-gas interface may be developed as

$$J = \frac{q_L^i}{H} = \frac{1}{H}\frac{\Delta T - \Delta p T_{sat}/(H\rho_L)}{R^i + h/k_L} + \frac{T_{sat}}{2H^4\rho_V^2}\frac{(\Delta T - \Delta p T_{sat}/(H\rho_L))^2}{(R^i + h/k_L)^3}. \tag{2.9}$$

Expressions (2.8 - 2.9) contain the superheating of the solid heater surface, which of course crucially depends on the considered solid heat transfer problem. Only several researchers [45, 95] considered the conductive solid heater within the microregion formulation. It was shown in [95] that for the small conductivity ratio k_L/k_S, it is a good approximation to assume a uniform wall temperature. The argument was that the temperature of the conductive solid varies at a scale much larger than that at which the apparent contact angle is established. This seems to be a reasonable argument for metal solid heaters. The isothermal heater was used in the most of previous studies [1, 2, 43, 97]. If not mentioned explicitly in the text, the isothermal heater is considered in this chapter. The extended version of the microregion including infinite (along x) conductive heater of thickness D is addressed in section 2.7.2.

2.2.2 Hydrodynamics in the microregion

When CL moves, the liquid-vapor interface is curved due to the induced liquid motion and the associated liquid pressure variation along the wedge. In case of evaporation, the situation is analogous, the evaporated liquid needs to be supplied to CL and thus it is essential to solve the hydrodynamic part of the problem. Similarly to [1, 2, 43, 97, 101, 103], the lubrication approximation [125, 126] can be applied in the vicinity of the CL where the interface slope is small. For the convenience of the reader, the employed equations are re-derived here.

The key points of the lubrication approximation are:

- It is assumed that the velocity along the liquid film is much larger than that in the perpendicular direction ($v_x \gg v_y$),
- The v_x variation across the liquid layer is assumed to be much larger than along it: $\partial v_x/\partial y \gg \partial v_y/\partial x$.

Under such additional assumptions (to these mentioned at the beginning of this chapter) Eqs. (2.2) reduce to

$$\frac{\partial p_L}{\partial x} = \mu \frac{\partial^2 v_x}{\partial y^2}, \tag{2.10}$$

$$\frac{\partial p_L}{\partial y} = 0. \tag{2.11}$$

One can easily verify that the solution of Eqs. (2.10, 2.11) is $v_x = a + by + cy^2$, where a, b and c are constants. They are to be determined from the boundary conditions and the volume conservation law:

- Slip boundary condition. The Naiver slip condition for the tangential velocity $v_x(y)$ at the solid surface $y = 0$ is used. The slip phenomenon is discussed in more detail in section 1.3.1.1. Here the relation between the tangential velocity and shear stress is repeated for convenience of the reader

  $$v_x = l_s \frac{\partial v_x}{\partial y}, \tag{2.12}$$

  that involves the slip length l_s reviewed in detail in [71].

- Viscous stress boundary condition at the free interface. Viscous stress at the liquid-vapor interface is defined by the gradient of the surface tension:

  $$\mu \frac{\partial v_x}{\partial y} = \frac{\partial \sigma}{\partial x}. \tag{2.13}$$

The latter may be induced by the concentration or thermal effect. The thermocapillary effect will be considered here since only single-component fluids are discussed.

- Liquid volume conservation law. The volume flux U flowing through the liquid film of thickness h at a given position x

$$U = \int_0^h v_x(y)dy \tag{2.14}$$

serves as the third equation for the three unknowns a, b, c. The U value is defined below.

By using the boundary conditions (2.14 - 2.12) three constants in the expression for velocity $v_x(y)$ can be determined. The back substitution of the solution into (2.10) written at the vapor-liquid interface results in the following expression:

$$U = \frac{1}{\mu}\left[\frac{\partial\sigma}{\partial x}\left(\frac{h^2}{2} + l_s h\right) - \left(\frac{h^3}{3} + h^2 l_s\right)\frac{\partial p_L}{\partial x}\right]. \tag{2.15}$$

By using the fluid volume conservation, U can also be expressed via the component v_n of the liquid velocity normal to the vapor-liquid interface:

$$U = \int_0^s v_n(s)ds \approx \int_0^x v_n(x)dx, \tag{2.16}$$

where s is the coordinate along the free interface. Eq. (2.16) can be rewritten as

$$v_n = \frac{\partial U}{\partial x}, \tag{2.17}$$

where v_n is related to the mass evaporation flux at the interface J (assumed positive at evaporation), via the mass conservation law

$$J = (v^i - v_n)\rho_L. \tag{2.18}$$

The normal interface velocity v^i is considered to be positive if directed inside the liquid (as the vector $\vec{n}$ in Fig. 2.28).

By injecting (2.18) and (2.15) into (2.17), and using the the identity $\partial\Delta p/\partial x = -\partial p_L/\partial x$ one arrives finally at the expression

$$\frac{\partial}{\partial x}\left[h\left(\frac{h}{2} + l_s\right)\frac{\partial\sigma}{\partial x} + h^2\left(\frac{h}{3} + l_s\right)\frac{\partial\Delta p}{\partial x}\right] = \mu\left(v^i - \frac{J}{\rho_L}\right), \tag{2.19}$$

where the interface velocity $v^i = v^i(x)$ is

$$v^i = v_{CL}\frac{\partial h}{\partial x}, \tag{2.20}$$

v_{CL} is the imposed CL velocity along x axis. $v_{CL} > 0$ corresponds to the displacement of the substrate to the left in Fig. 2.2 (i.e., to the substrate dewetting). CL remains immobile in this reference frame. The linear dependence of the surface tension on the temperature is assumed. Thus the thermocapillary stress

$$\frac{\partial\sigma}{\partial x} = -\gamma\frac{\partial T^i}{\partial x}, \tag{2.21}$$

where $\gamma = -d\sigma/dT$ is constant. Note that γ is generally positive for pure fluids.

2.2.3 Interfacial pressure balance

The microregion interface is free and is defined by the normal interface stress balance [2, 7, 43, 104]

$$K\sigma = \Delta p + p_r - \Pi, \tag{2.22}$$

where K is the interface curvature, $p_r = J^2(\rho_V^{-1} - \rho_L^{-1})$ is the differential vapor recoil pressure and the last term in the right side is the disjoining pressure term covering the effect of surface forces. The curvature full expression can be approximated in the frame of lubrication approximation as

$$K = \frac{\partial^2 h}{\partial x^2}\frac{1}{(1+u^2)^{3/2}} \approx \frac{\partial^2 h}{\partial x^2}, \tag{2.23}$$

where $u = \partial h/\partial x$.

2.2.4 Governing equations and boundary conditions

In the previous sections the heat transfer and hydrodynamic parts of the contact line evaporation problem together with interface pressure balance equation, were presented. In this section the extended microregion model given by Eqs. (2.9, 2.19) and (2.22) is summarized, including the boundary conditions.

The governing equations of the evaporation contact line model:

- Interface force balance equation (2.22)

$$\sigma\frac{\partial^2 h}{\partial x^2} = \Delta p + \frac{J^2}{\rho_V} - \Pi, \tag{2.24}$$

- Pressure jump equation (2.19)

$$\frac{\partial}{\partial x}\left[h^2\left(\frac{h}{3}+l_s\right)\frac{\partial \Delta p}{\partial x} - h\left(\frac{h}{2}+l_s\right)\gamma\frac{\partial T^i}{\partial x}\right] = \mu\left(v_{CL}\frac{\partial h}{\partial x} - \frac{J}{\rho_L}\right), \tag{2.25}$$

  where mass evaporation flux (2.9) is

$$J = \frac{q_L^i}{H} = \frac{1}{H}\frac{\Delta T - \Delta p T_{sat}/(H\rho_L)}{R^i + h/k_L} + \frac{T_{sat}}{2H^4\rho_V^2}\frac{(\Delta T - \Delta p T_{sat}/(H\rho_L))^2}{(R^i + h/k_L)^3}.$$

- The interface temperature is given by Eq. (2.4)

$$T^i = T_{sat}\left[1 + \frac{\Delta p}{H\rho_L} + \frac{J^2}{2H\rho_V^2}\right] + R^i q_L^i. \tag{2.26}$$

  where the interface thermal resistance (1.13)

$$R^i = \frac{2-f}{2f}\frac{T_{sat}\sqrt{2\pi R_g T_{sat}/M}(\rho_L - \rho_V)}{H^2\rho_L\rho_V}.$$

The differential Eqs. (2.24, 2.25) are both of the second order, four boundary conditions need to be specified. Following [103, 104, 127], we consider the microscopic contact angle to be unchanged by the fluid motion. This assumption is corroborated also by an analogy with the study [128] where the boundary conditions were derived together with the equation of motion from variational principles. The equilibrium contact angle boundary condition (Young's law;

the surface forces were neglected there) has been recovered there in dynamics. The boundary conditions at the CL (at $x = 0$) are thus given by two expressions,

$$h = 0, \tag{2.27}$$

$$u = \theta_{micro}. \tag{2.28}$$

In case the thin film forces are not considered ($\Pi = 0$), the microscopic contact angle equals to Young equilibrium contact angle ($\theta_{micro} = \theta_Y$) to provide the same macroscopic equilibrium shape as for $\Pi \neq 0$ case. Another boundary condition for the semi-infinite wedge geometry is given by zero curvature $K(x \to \infty) = 0$ that implies

$$\Delta p = 0 \tag{2.29}$$

at $x \to \infty$ (where $\Pi(h \to \infty) = 0$).

The fourth boundary condition is missing. It is shown below that in fact it stems from the other conditions.

The described model is hereafter refereed as the full microregion model.

2.3 Asymptotic analysis of microregion model

In this section the asymptotic analysis of the microregion model is presented. Most of its content is the original author contribution, some parts were done in collaboration with B. Andreotti, D. Pražák and T. Bárta, which is mentioned in the appropriate sections. First, an important question of singularity relaxation is addressed. Next, I formulate the minimal complexity microregion model, describing thermal and hydrodynamic aspects of evaporation in CL vicinity. The asymptotic analysis of this model is performed in order to obtain the asymptotic behavior of the system variables in the vicinity of CL. This analysis provides the missing boundary condition for its numerical solution. At the next step, the minimal complexity model is solved numerically but also analytically by using regular perturbation method. The governing length scales of the problem are identified and used to find a universally valid law describing the apparent contact angle. The isothermal CL motion is also addressed.

2.3.1 Missing boundary condition at contact line

In the previous section the three boundary conditions used to solve the set of governing equations (2.9, 2.19) and (2.22) were presented. The fourth, missing boundary condition is derived here. It belongs to author's original contribution to the problem, presented in [129].

In a theoretical treatment of the microregion problem, apart from (2.27 - 2.29), the fourth condition is imposed automatically by the requirement of the finiteness of the solution (in particular that for the temperature) or by the argument based on the geometry of partial wetting (see section 2.3.3). In the numerical solution, a finite value x_{max} needs to be used instead of infinity and the fourth condition needs to be chosen in coherency with the equations of the problem. Its definition is somewhat delicate. A condition valid at a "theoretical" domain border $x = 0$ or $x \to \infty$ may lead to the absence of the solution when applied at some nonzero or finite x value, respectively. E.g. the condition $J = 0$ valid at $x \to \infty$ but applied at $x = x_{max}$ leads to an evident incoherency in Eq. (2.9) if used together with the condition (2.29). The $J = 0$ condition is however useless as a boundary condition and is discussed here for the sake of clarity.

To obtain the fourth boundary condition, one may proceed similarly to the complete wetting case ($v_{CL} = 0$), where the pressure boundary condition

$$\Delta p(x \to -\infty) = \frac{H\rho_L}{T_{sat}}\Delta T \tag{2.30}$$

is recovered at the left domain limit ($x \to -\infty$ in that case) because of the existence of a wetting film assumed to be flat [2]. Because of its flatness, it is in equilibrium with the vapor; the condition $J = 0$ is satisfied and Eq. (2.30) stems from Eq. (2.9). Note that the pressure boundary condition is not given by some extra assumption but derived from the geometrical boundary condition at the left domain border. A similar derivation can be carried out for the partial wetting case, see section 2.3.3. In the following, the reasoning based on the requirement of temperature continuity is followed.

In the partial wetting case considered here the pressure boundary condition at $x \to 0$ may be obtained directly from Eq. (2.26). When temperature continuity $T^i = T_h$ is considered it directly implies that at the CL,

$$\Delta p(x \to 0) = \frac{H\rho_L}{T_{sat}}\left[\Delta T - HR^i J(x \to 0) - \frac{J^2(x \to 0)}{2H\rho_V^2}\right]. \tag{2.31}$$

However the value of $J(x \to 0)$ is *a priori* unknown. To obtain it, let us integrate Eq. (2.25) from 0 to x and then tend x to 0 asymptotically so that h can be replaced by $\theta_{micro}x$. This results in the equation

$$-\gamma\frac{\partial T^i}{\partial x} + h\frac{\partial \Delta p}{\partial x} = \frac{\mu}{l_s\theta_{micro}}\left(\theta_{micro}v_{CL} - \frac{J}{\rho_L}\right), \tag{2.32}$$

The T^i derivative can be obtained by developing Eq. (2.7) into the Taylor series around $h \to 0$:

$$\frac{\partial T^i}{\partial x} = -\frac{H\theta_{micro}}{k_L}J. \tag{2.33}$$

Its substitution into Eq. (2.32) results in the expression

$$x\frac{d\Delta p}{dx} = \frac{\mu}{l_s\theta_{micro}}\left[v_{CL} - J\left(\frac{1}{\theta_{micro}\rho_L} + \frac{l_sH\theta_{micro}}{\mu k_L}\gamma\right)\right]. \tag{2.34}$$

By injecting the value of J from Eq. (2.9) into Eq. (2.34), one obtains a differential equation for Δp.

$$x\frac{d\Delta p}{dx} = \frac{\mu}{l_s\theta_{micro}}\left[v_{CL} - \left(\frac{1}{\theta_{micro}\rho_L} + \frac{l_sH\theta_{micro}}{\mu k_L}\gamma\right)\frac{\Delta T - \Delta p T_{sat}/(H\rho_L)}{H(R^i + \theta_{micro}x/k_L)}\right]. \tag{2.35}$$

In the asymptotic limit $x \to 0$ one neglects $\theta_{micro}x/k_L$ with respect to R^i and the differential equation takes the form

$$x\frac{d\Delta p}{dx} = b\Delta p - a, \tag{2.36}$$

where a and $b > 0$ may be easily deduced from Eq. (2.35). The general solution of Eq. (2.36) is

$$\Delta p = \frac{a}{b} - cx^b, \tag{2.37}$$

obtained with the separation of variables method; c is the integration constant and a/b value is given in fact by Eq. (2.31). Such an expression shows that $\Delta p(x \to 0) \to a/b$. The asymptotic

solutions for some other cases are shown in sections 2.3.3 and 2.3.4. They are obtained with more rigorous approach but lead in all cases to the same final conclusion.

From (2.37) one easily deduces that Δp saturates at $x \to 0$ so that

$$x \frac{d\Delta p}{dx}\bigg|_{x\to 0} = 0. \tag{2.38}$$

This result is in entire agreement with Eq. (2.31). Note that such a behavior is different from the isothermal CL dynamics [130] where the pressure boundary condition cannot be written and the limit (2.38) is nonzero. Finally, Eqs. (2.34, 2.38) result in

$$J(x \to 0) = \frac{v_{CL}}{\frac{1}{\theta_{micro}\rho_L} + \frac{l_s H \theta_{micro}}{\mu k_L}\gamma}. \tag{2.39}$$

The evaporation flux at the CL is proportional to v_{CL}. In particular, $J(h \to 0)$ becomes zero when the CL is immobile. This behavior is similar to the complete wetting case where $J(x \to -\infty)$ also vanishes. When the contact line advances ($v_{CL} < 0$), the heat flux at the CL is negative. It means that $J(x)$ changes sign and condensation occurs in the vicinity of the CL. This effect was considered for the complete wetting case [131]. The regularization of the viscous stress singularity by the Kelvin effect in the CL motion will be further considered in section 2.4. In the numerical treatment the condition (2.31) is not however used as the boundary condition. The reason is that the pressure jump approaches the value given by (2.31) quite slowly following the slow powerlaw (2.37) when $x \to 0$ (when R^i and l_s is included). Since in the numerical algorithm used to solve the problem one needs to impose the boundary condition at some small distance from the contact line, the numerical error might be important if the condition (2.31) were used. The boundary condition on pressure (2.38) is applied. It is discussed in section related to numerical treatment of the problem.

In this section the asymptotic analysis of the full microregion model including slip length, interface resistance, vapor recoil pressure, thermocapillary flow and contact line motion was performed. The asymptotic value of the pressure jump and mass evaporation flux was given, Eqs. (2.31, 2.39). The main conclusion is that the pressure jump, for microregion model under study, attains a finite value at the contact line. When $v_{CL} = 0$, this value coincides with the condition derived for the complete wetting system (Eq. (2.30)), written however for $x = 0$. When contact line motion is considered, the mass evaporation flux $J(x \to 0) \neq 0$ and depends on the CL velocity.

2.3.2 Existence of a regular solution for the microregion model including only the Kelvin effect and v_{CL}

The following section contains the original research work made in collaboration with D. Pražák and T. Bárta from Department of Mathematical Analysis, Charles University in Prague. The viability of the singularity relaxation in Eqs. (2.24, 2.25) is analyzed. Only the Kelvin effect, superheating and contact line motion terms are considered.

For clarity, the system under study is rewritten here:

$$\frac{d}{dx}\left[\frac{h^3}{3}\frac{d\Delta p}{dx}\right] = \mu\left(v_{CL}\frac{dh}{dx} - \frac{k_L}{H\rho_L}\frac{\Delta T - \Delta p T_{sat}/(H\rho_L)}{h}\right), \tag{2.40}$$

$$\Delta p = \sigma \frac{d^2 h}{dx^2}, \tag{2.41}$$

Four boundary conditions are needed in order to close the problem. Three boundary conditions (2.27 - 2.29) can be used. To verify the legitimacy of the usage of the fourth boundary condition (2.31) by mathematically rigorous method is in principle the main goal of this section.

In the following, the length scale $l_l = \sigma/(H\rho_L)$, the pressure scale $H\rho_L$ and superheating T_{sat} are used to make Eqs. (2.40 - 2.41) dimensionless

$$\frac{d}{d\hat{x}}\left[\frac{\hat{h}^3}{3}\frac{d\hat{p}}{d\hat{x}}\right] = Ca\frac{d\hat{h}}{d\hat{x}} + N_l\frac{\hat{p}}{\hat{h}}, \tag{2.42}$$

$$\Delta\hat{p} = \frac{d^2\hat{h}}{d\hat{x}^2}, \tag{2.43}$$

and

$$\hat{h}(\hat{x}\to 0) = 0, \qquad u(\hat{x}\to 0) = \theta_{micro}, \tag{2.44}$$

where hat means the corresponding dimensionless quantity, $\hat{p} = \Delta\hat{p} - \varepsilon$, $u = d\hat{h}/d\hat{x}$, $Ca = \mu v_{CL}/\sigma$ capillary number, $N_l = \mu k_L T_{sat}/\sigma^2$ is the parameter related to evaporation and $\varepsilon = \Delta T/T_{sat}$ is the reduced superheating. Note that only the boundary conditions related to the vicinity of CL (the condition (2.29) is not essential to the analysis) are rewritten. We aim to show that the conditions (2.31, 2.39) that reduce to

$$\hat{p}(\hat{x}\to 0) = 0 \tag{2.45}$$

stem from (2.42 - 2.44).

We are interested in the properties of the system (2.42 - 2.43) in the vicinity of the contact line. The partial wetting conditions force the liquid wedge to approach the solid substrate at a slope corresponding to θ_{micro}. From this condition, it follows that the leading order term of $\hat{h}(\hat{x}\to 0)$ is a straight wedge. $\hat{h}(\hat{x}\to 0)$ in (2.42) can thus be replaced by $\hat{x}\theta_{micro}$ and

$$\frac{d}{d\hat{x}}\left[\hat{x}^3\frac{d\hat{p}}{d\hat{x}}\right] = A + B\frac{\hat{p}}{\hat{x}}, \tag{2.46}$$

where we group the parameters as $A = 3Ca/\theta_{micro}^2$ and $B = 3N_l/\theta_{micro}^4$.

In the following, let us consider differential equation (2.46), where $B > 0$. The purpose of the following is to show that there exists a solution $\hat{p}$ such that $\lim_{\hat{x}\to 0}\hat{p}(\hat{x}) = 0$.

First, with substitutions $s = B/(4\hat{x}^2)$, $q = 2\sqrt{B}\hat{p}/A$ Eq. (2.46) reduces to

$$q'' - \frac{q}{s} = \frac{1}{s^{3/2}}, \tag{2.47}$$

and CL $x = 0$ corresponds to $s\to\infty$. The task now is to show that Eq. (2.47) has a solution with $\lim_{s\to\infty} q(s) = 0$.

Second, let us apply formally the *inverse* Laplace transform to (2.47),

$$q(s) = \int_0^\infty f(t)e^{-st}dt, \tag{2.48}$$

which results in

$$t^2 f(t) - \int_0^t f(r)dr = at^{1/2}, \tag{2.49}$$

where $a = 2/\sqrt{\pi}$. We will show that the equation (2.49) has a solution which is Laplace transformable, which means that the integral in (2.48) is finite for any $s > 0$. It follows from Lebesgue

Dominated Convergence Theorem [132] (Satz 3.6.1) that if the Laplace transform $q(s)$ exists, it satisfies the condition $\lim_{s\to\infty} q(s) = 0$.

Let us introduce $F(t) = \int_0^t f(r)dr$ that reduces (2.49) to

$$F'(t) - \frac{F(t)}{t^2} = at^{-3/2}. \tag{2.50}$$

Eq. (2.50) can be easily solved,

$$F(t) = Ce^{-1/t} + ae^{-1/t}\int_1^t e^{1/r}r^{-3/2}dr, \tag{2.51}$$

where C is the integration constant. We will show next that $F(t \to 0+) = 0$. The first term obviously vanishes at $t \to 0+$. The l'Hospital rule can be applied to the second term,

$$\lim_{t\to 0+}\frac{\int_1^t e^{1/r}r^{-3/2}dr}{e^{1/t}} = \lim_{t\to 0+}\frac{e^{1/t}t^{-3/2}}{-t^{-2}e^{1/t}} = 0. \tag{2.52}$$

As the function $F(t)$ is obviously bounded for $t \to \infty$, the integral

$$\int_0^\infty e^{-st}f(t)dt \tag{2.53}$$

exists for every $s > 0$ by Dirichlet convergence criterion, which means that $f(t)$ is Laplace transformable, and its Laplace transform $q(s)$ solves (2.47). We therefore conclude that this solution of Eq. (2.46) verifies the boundary conditions (2.44, 2.45).

Note that the family of the solutions corresponding to Eq. (2.51) is incomplete: it has only one arbitrary constant while Eq. (2.46) is of the second order. From the above analysis one may conclude that the other part of the solutions is not inverse Laplace transformable and thus diverge at $\tilde{x} \to 0$. This means that the boundary conditions (2.44) cannot be satisfied for them.

In this section, it has been proven mathematically that the boundary condition (2.31) follows from the geometrical boundary condition at CL.

2.3.3 Asymptotics near contact line for $l_s = R^i = \gamma = v_{CL} = 0$

In the previous sections 2.3.1, 2.3.2, the pressure boundary condition for the extended microregion model was derived. Here, the reduced microregion model ($l_s = R^i = \gamma = v_{CL} = 0$) is introduced. Another alternative way of deriving the condition (2.31) for this model is shown.

We look for a minimal complexity problem, keeping only the term essential for regularization of CL singularity. Next, the immobile CL is considered, the slip length, vapor recoil pressure, surface forces, Marangoni effect and the interfacial resistance are excluded from consideration. Keeping the same notation as in [129], l_h, σ/l_h and T_{sat} (where $l_h = \sigma/(H\rho_L)$ are used to make lengths, pressure jump and temperature in the Eqs. (2.25 - 2.24) dimensionless. The reduced set of Eqs. (2.29 - 2.24) then reads in dimensionless variables

$$\frac{\partial}{\partial\hat{x}}\left(\frac{\hat{h}^3}{3}\frac{\partial\Delta\hat{p}}{\partial\hat{x}}\right) = N_l\frac{\Delta\hat{p} - \Delta\hat{T}}{\hat{h}}, \tag{2.54}$$

$$\frac{\partial^2\hat{h}}{\partial\hat{x}^2} = \Delta\hat{p}, \tag{2.55}$$

$$\hat{h}|_{\hat{x}=0} = 0, \tag{2.56}$$

$$u|_{\hat{x}=0} = \theta_{micro}, \tag{2.57}$$

$$\Delta\hat{p}|_{\hat{x}\to\infty} = 0, \tag{2.58}$$

where $u = \partial\hat{h}/\partial\hat{x}$ and $N_l = \mu k_L T_{sat}/\sigma^2$ is the only parameter that characterizes evaporation. The hat means the corresponding dimensionless quantity. The CL microregion model described by Eqs. (2.54 - 2.55) is hereafter referred as simplified microregion model or minimal complexity problem.

The partial wetting condition requires that the liquid-vapor interface makes finite microscopic contact angle with solid substrate (Eqs. (2.56 - 2.57)). At the CL the leading order solution for h is a straight wedge. We are looking for a solution of the problem (2.54) - (2.55) for $\hat{x} \to 0$ for which following substitution can be used $\hat{h} \sim \hat{x}\theta_{micro}$. By using this substitution in Eq. (2.54) one can easily check that the equation has a form of modified Bessel's equation with the general solution for $\Delta\hat{p}$:

$$\Delta\hat{p}(\hat{x}) = \Delta\hat{T} + C_1\frac{K_1(A/\hat{x})}{\hat{x}} + C_2\frac{I_1(A/\hat{x})}{\hat{x}}, \tag{2.59}$$

where K_1, I_1 are the modified Bessel functions, C_1, C_2 are integration constants and $A = \sqrt{3N_l}/\theta^2_{micro}$. The asymptotic limit of Eq. (2.59) for $\hat{x} \to 0$ (at the CL) is

$$\Delta\hat{p}(\hat{x}) = \Delta\hat{T} + C_1\sqrt{\frac{\pi}{2A\hat{x}}}\exp\left(-\frac{A}{\hat{x}}\right) + C_2\sqrt{\frac{\pi}{2A\hat{x}}}\exp\left(\frac{A}{\hat{x}}\right). \tag{2.60}$$

Since I_1 in (2.59) diverges for $\hat{x} \to 0$, the finitness of T^i requires the finiteness of Δp and thus $C_2 = 0$.

The asymptotic development of Eq. (2.59) for $\hat{x} \to 0$ is thus

$$\Delta\hat{p} = \Delta\hat{T} + C_1\sqrt{\frac{\pi}{2A\hat{x}}}\exp\left(-\frac{A}{\hat{x}}\right). \tag{2.61}$$

By differentiating Eq. (2.61), it is easy to find that $\partial\Delta\hat{p}/\partial\hat{x}(\hat{x} \to 0)$ is zero and

$$\Delta\hat{p}(\hat{x} \to 0) = \Delta\hat{T}, \tag{2.62}$$

which is the boundary condition equivalent to (2.31) for the considered case.

Note that similarly to complete wetting case one can also reason purely in terms of geometrical constraint imposed by partial wetting and justify the choice $C_2 = 0$ directly from Eqs. (2.56), (2.57). Let us integrate Eq. (2.60) once to get an asymptotic solution for the interface slope $\hat{u}$

$$\begin{aligned}\hat{u}(\hat{x} \to 0) = C_3 + \Delta\hat{T}\hat{x} + \sqrt{\frac{2\hat{x}\pi}{A}}\left(C_1 e^{-\frac{A}{\hat{x}}} + C_2 e^{\frac{A}{\hat{x}}}\right) + \\ \sqrt{\frac{2A\pi^2}{A}}\left(C_1\mathrm{erf}\sqrt{\frac{A}{\hat{x}}} - C_2\mathrm{erfi}\sqrt{\frac{A}{\hat{x}}}\right),\end{aligned} \tag{2.63}$$

where C_3 is an additional integration constant. When functions erfi and erf are developed in series, it is evident that in order to satisfy the partial wetting geometrical constraint (2.57), the constant C_2 has to be set to zero. For completeness the asymptotic relation for interface slope as $\hat{x} \to 0$ reads

$$\hat{u}(\hat{x} \to 0) = \theta_{micro} + \hat{x}\Delta\hat{T} + \frac{C_1}{A}e^{-\frac{A}{\hat{x}}}\hat{x}^{3/2}. \tag{2.64}$$

The result given by (2.62) clearly shows that the hydrodynamic contact line singularity at thermally controlled evaporation can be relaxed by using the Kelvin effect (dependence of saturation temperature on pressure). Indeed, the viscous stress (equal to Δp) is not only integrable but finite.

2.3.4 Various asymptotic solutions for $\Delta p(x \to 0)$

In this section three asymptotic solutions for pressure jump are presented.

Similarly to the previous section, one can add slip length or interface resistance to microregion problem (2.54 - 2.58) and obtain the asymptotic form of the pressure jump for $x \to 0$. One essentially follows the steps executed between Eqs. (2.59 - 2.61).

- Including interface resistance. For microregion model given by Eqs. (2.54 - 2.58) and (2.62) extended for interface resistance R^i term the asymptotic expression for pressure jump as $\hat{x} \to 0$ reads

$$\Delta\hat{p} - \Delta\hat{T} \sim C_1 x^{-3/4} \exp\sqrt{\frac{X_R}{\hat{x}}}, \tag{2.65}$$

  where $X_R = 12\mu T_{sat}/(\theta^3_{micro}\sigma R^i H \rho_L)$.

- Including slip length. For microregion model given by Eqs. (2.54 - 2.58) and (2.62) extended for slip length l_s the asymptotic expression for pressure jump as $\hat{x} \to 0$ reads

$$\Delta\hat{p} - \Delta\hat{T} \sim C_1 x^{-1/4} \exp\sqrt{\frac{X_s}{\hat{x}}}, \tag{2.66}$$

  where $X_s = 12\mu k_L T_{sat}/(\theta^3_{micro}\sigma l_s H \rho_L)$.

- Including slip length and interface resistance. For microregion model given by Eqs. (2.54 - 2.58) and (2.62) extended for both slip length and interface resistance terms, the asymptotic expression for pressure jump as $\tilde{x} \to 0$ reads

$$\Delta\hat{p} - \Delta\hat{T} \sim C_1 \hat{x}^{0.5(\sqrt{1+4X^s_R}-1)}, \tag{2.67}$$

  where $X^s_R = \mu T_{sat} H^2 \rho_L^2/(\theta^3_{micro} l_s R^i)$

2.3.5 Asymptotic solution for small superheating

In this section, the simplified microregion model given by Eqs. (2.54 - 2.58) and (2.62) is solved by regular perturbation about isothermal conditions. The following analysis was a contents of the publication [129].

We seek a solution by expanding the pressure jump $\Delta\hat{p}$ and shape $\hat{h}$ in a regular perturbation series in $\Delta\hat{T}$, which measures the deviation from isothermal conditions:

$$\begin{aligned} \Delta\hat{p} &= \Delta\hat{p}_0 + \varepsilon\Delta\hat{p}_1 + \cdots, \\ \hat{h} &= \hat{h}_0 + \varepsilon\hat{h}_1 + \cdots, \end{aligned} \tag{2.68}$$

where

$$\varepsilon \equiv \Delta\hat{T}.$$

If we substitute (2.68) in to Eqs. (2.54 - 2.58), (2.62) and collect terms of the same order in ε, we get at zero order $\Delta\hat{p}_0 = 0$ and $\hat{h}_0 = \theta_{micro}\hat{x}$.

At next order in ε, the following system of equations is obtained:

$$\hat{h}_0 \frac{d}{d\hat{x}}\left(\hat{h}_0^3 \frac{d\Delta\hat{p}_1}{d\hat{x}}\right) = A^2(\Delta\hat{p}_1 - 1), \tag{2.69}$$

$$\Delta\hat{p}_1 = \frac{d^2\hat{h}_1}{d\hat{x}^2}, \tag{2.70}$$

$$\hat{h}_1(\hat{x}=0) = 0, \qquad u(\hat{x}=0) = \theta_{micro}, \tag{2.71}$$

$$\Delta\hat{p}_1(\hat{x}\to\infty) = 0, \qquad \Delta\hat{p}_1(\hat{x}\to 0) = 1 \tag{2.72}$$

where $A = \sqrt{3N_l}/\theta_{micro}^2$. The solution of Eq. (2.69) is equivalent to Eq. (2.59)

$$\Delta\hat{p}_1(\hat{x}) = 1 + C_1\frac{K_1\left(A/\hat{x}\right)}{\hat{x}} + C_2\frac{I_1\left(A/\hat{x}\right)}{\hat{x}}. \tag{2.73}$$

Since I_1 diverges at infinity, the boundary condition (2.72b), requires $C_2 = 0$. The second constant C_1 is determined from (2.72a)

$$\Delta\hat{p}_1(\hat{x}) = 1 - \frac{A}{\hat{x}}K_1\left(\frac{A}{\hat{x}}\right), \tag{2.74}$$

and the full perturbation expansion in ε for $\Delta\hat{p}(\hat{x})$ is

$$\Delta\hat{p}(\hat{x},\varepsilon) = \varepsilon - \varepsilon\frac{A}{\hat{x}}K_1\left(\frac{A}{\hat{x}}\right). \tag{2.75}$$

The solution of Eq. (2.70) with boundary conditions (2.71) may be found by integrating twice $\Delta\hat{p}_1$. The first integration is the most important because it results in the slope u, the value of which at infinity corresponds to

$$\begin{aligned}\theta_{app} &= \theta_{micro} + \int_0^\infty \Delta\hat{p}(\hat{x},\varepsilon)d\hat{x}\\ &= \theta_{micro} + A\varepsilon\int_0^\infty\left[\frac{1}{z^2} - \frac{1}{z}K_1\left(z\right)\right]dz\\ &= \theta_{micro} + \frac{A\varepsilon\pi}{2}.\end{aligned} \tag{2.76}$$

The substitution $z = A/\hat{x}$ is used in Eq. (2.76) and the resulting integral is found with MATHEMATICA. The first order solution for interface slope $u(\hat{x})$ may also be found in terms of the generalized Meijer G-function:

$$u_1(\hat{x}) = \hat{x} + \frac{A}{4}G_{2,1}^{1,3}\left(\frac{A}{2\hat{x}},\frac{1}{2}\middle|\begin{array}{c}1\\ -\frac{1}{2},\frac{1}{2},0\end{array}\right). \tag{2.77}$$

The first order solution for $\hat{h}$ may be found also only in terms of the generalized Meijer G-function:

$$\hat{h}_1(\hat{x}) = \frac{\hat{x}^2}{2} + \frac{A\hat{x}}{8}G_{2,4}^{3,1}\left(\frac{A}{2\hat{x}},\frac{1}{2}\middle|\begin{array}{c}1,\frac{3}{2}\\ -\frac{1}{2},\frac{1}{2},\frac{1}{2},0\end{array}\right). \tag{2.78}$$

Another important quantity related to the microregion is the integrated heat flux $\hat{Q}$ defined by the expression $\hat{Q} = \int_0^{\hat{x}}\hat{q}_L^i d\hat{x}$. The first order solution for local heat flux at the liquid-vapor interface from the liquid side is

$$\hat{q}_L^i = \hat{q}_{L,1}^i = -\frac{\varepsilon}{\theta_{micro}}\frac{\Delta\hat{p}_1 - 1}{\hat{x}} = \frac{\varepsilon A}{\theta_{micro}}\frac{1}{\hat{x}^2}K_1\left(\frac{A}{\hat{x}}\right). \tag{2.79}$$

Note that $q_L^i(x\to\infty) = 0$. The integrated heat flux can be found by integration of (2.79)

$$\hat{Q}(\hat{x}) = \frac{\varepsilon}{\theta_{micro}}K_0\left(\frac{A}{\hat{x}}\right). \tag{2.80}$$

One can easily check that the Eq. (2.80) is logarithmically divergent at $\hat{x}\to\infty$. This is the artefact of the wedge geometry, where $h\to\infty$ for $x\to\infty$. Eq. (2.7) causes $q_L^i \sim 1/x$ and $Q(x)\sim\ln x$. At first order approximation for small superheat, this slope is given by θ_{micro}, for

full solution it is the apparent contact angle which defines the slope of the liquid-vapor interface for $x \to \infty$.

By returning to the dimensional variables, one obtains the apparent contact angle in terms of the microscopic contact angle within the first order approximation:

$$\theta_{app} = \theta_{micro} + \frac{\pi \Delta T}{2\sigma\theta_{micro}^2}\sqrt{\frac{3\mu k_L}{T_{sat}}}. \tag{2.81}$$

This expression shows the independence of the latent heat and a strong dependence on the microscopic contact angle. It also predicts the amplification of the flow effect at high pressures (near critical point) where σ strongly decreases.

In this section, a solution of the microregion simplified model given by Eqs. (2.54 - 2.58), (2.62) by regular perturbation about isothermal conditions was presented. The first order solutions for pressure jump (2.73), slope (2.77), shape (2.78) and local heat flux (2.79) are shown. In addition the expressions for the apparent contact angle (2.81) and integrated heat flux were obtained (2.80). The expression of the type (2.81) provides an important insight into the dependence of apparent contact angle on system parameters in the limit of small superheating. The calculated apparent angles for FC-72 at 0.04 MPa, water at 10 and 0.1 MPa are compared with the numerical solutions in Fig. 2.4b.

2.3.6 Physical scales governing the simplified microregion problem

The following section contains the original research work made in collaboration with B. Andreotti from PMMH, ESPCI.

First, the simplified microregion model described by Eqs. (2.54 - 2.58) is formulated in the form suitable for the analysis. Next, the important length scales and parameters of the problem are identified.

Eqs. (2.54 - 2.55) rewritten in a single equation in dimensional form

$$\overbrace{\frac{d}{dx}\left[\frac{h^3}{3}\frac{d(\sigma K)}{dx}\right]}^{L} = \overbrace{\frac{\mu k_L T_{sat}\sigma K}{h(H\rho_L)^2}}^{\mathrm{K}} - \overbrace{\frac{\mu k_L \Delta T}{hH\rho_L}}^{\mathrm{S}}, \tag{2.82}$$

where the terms L, K, S are called Laplace, Kelvin and Superheating terms. The variables x and h are to be scaled by characteristic scales X and Z. X and Z differ by the factor θ, $Z = \theta X$. The angle θ can be either θ_{micro} or θ_{app} (or in sec. 2.4, the Voinov angle θ_V). The characteristic scale of curvature is $[K] = Z/X^2$.

The dimensional prefactors of members in (2.82) are:

$$L: \quad \frac{\sigma\theta^4}{3}; \quad K: \frac{T_{sat}\mu k_L}{(\rho_L H)^2}\frac{\sigma}{X^2}; \quad S: \frac{\Delta T k_L \mu}{\theta X H \rho_L}. \tag{2.83}$$

The characteristic scale, which balances the two terms containing the interface pressure jump (Laplace and Kelvin terms) is:

$$X \equiv l_K = \frac{\sqrt{3\mu k_L T_{sat}}}{\theta^2 \rho_L H}. \tag{2.84}$$

Eq. (2.82) in the scaled variables (denoted by bar) then reads

$$\bar{h}\frac{d}{d\bar{x}}\left[\bar{h}^3\frac{d^3\bar{h}}{d\bar{x}^3}\right] = \frac{d^2\bar{h}}{d\bar{x}^2} - \varepsilon_\theta, \tag{2.85}$$

where

$$\varepsilon_\theta = \frac{\Delta T\sqrt{3T_{sat}\mu k_L}}{\theta^3\sigma T_{sat}} \tag{2.86}$$

is the modified superheating parameter. It is the only parameter characterizing the problem. Depending on chosen angle used to link the scales X and Z, ε_{micro} or ε_{app} for θ_{micro} or θ_{app}, respectively will be denoted. The chosen reference angle has an important impact on the boundary condition (which is the key aspect of the analysis below) for ε_{micro} the counterpart expressions to (2.71 - 2.72) are

$$\left.\frac{d\bar{h}}{d\bar{x}}\right|_{\bar{x}=0} = 1, \quad \bar{h}|_{\bar{x}=0} = 0, \quad \left.\frac{d^2\bar{h}}{d\bar{x}^2}\right|_{\bar{x}\to\infty} = 0, \quad \left.\frac{d^2\bar{h}}{d\bar{x}^2}\right|_{\bar{x}=0} = \varepsilon_{micro}. \tag{2.87}$$

Note that the reduced slope of the free interface for $\bar{x} \to \infty$ is $\theta_{app}/\theta_{micro}$. Within the present notation, (2.81) reduces to

$$\theta_{app} = \theta_{micro}\left(1 + \frac{\pi}{2}\,\varepsilon_{micro}\right). \tag{2.88}$$

If now θ_{app} is taken for θ, one obtains instead of (2.87) the following boundary conditions for Eq. (2.85)

$$\left.\frac{d\bar{h}}{d\bar{x}}\right|_{\bar{x}\to\infty} = 1, \quad \bar{h}|_{\bar{x}=0} = 0, \quad \left.\frac{d^2\bar{h}}{d\bar{x}^2}\right|_{\bar{x}\to\infty} = 0, \quad \left.\frac{d^2\bar{h}}{d\bar{x}^2}\right|_{\bar{x}=0} = \varepsilon_{app}. \tag{2.89}$$

Following the procedure shown in section 2.3.5 and solving the Eq. (2.85) for small ε_{app} one obtains the following full perturbation expansion in ε_{app} for $\Delta\bar{p}$

$$\Delta\bar{p} = \varepsilon_{app} - \frac{\varepsilon_{app}}{\bar{x}} K_1\left(\frac{1}{\bar{x}}\right), \tag{2.90}$$

where K_1 stands for the modified Bessel function of the first order. In the following step, the integration of the latter expression from $+\infty$ to 0 (cf. (2.76)) gives the following expression for the apparent contact angle

$$\theta_{micro} = \theta_{app}\left(1 - \frac{\pi}{2}\,\varepsilon_{app}\right). \tag{2.91}$$

The last approximate equation predicts that $\theta_{micro}/\theta_{app}$ vanishes (at large θ_{app}) as ε_{app} tends to a critical value $\varepsilon^c_{app} = 2/\pi$. The numerical solution shows that the exact ε^c_{app} is rather 0.3, see Fig. 2.3, where the numerical solution is also shown.

Note that $\varepsilon_{micro} = \varepsilon_{app}(\theta_{app}/\theta_{micro})^3$ and the expressions (2.88) and (2.91) can be combined into the following formula

$$\frac{\theta_{micro}}{\theta_{app}} = 1 - \frac{\pi}{2}\,\varepsilon_{micro}\left(\frac{\theta_{micro}}{\theta_{app}}\right)^3. \tag{2.92}$$

At small superheating, this expression conforms to the result (2.88). At large ε_{micro}, ε_{app} tends to $\varepsilon^c_{app} > 0$ so that one gets the scaling law $\theta_{app} = \theta_{micro}(\varepsilon_{micro}/\varepsilon^c_{app})^{1/3}$ that for dimensional parameters reads $\theta_{app} = \theta_{micro}(\Delta T\sqrt{3T_{sat}\mu k_L}/(\theta^3_{micro}\sigma T_{sat}\varepsilon^c_{app}))^{1/3}$.

2.3.7 Discussion

The main results obtained in the previous sections related to the asymptotic analysis of the microregion model are analyzed here.

In Fig. 2.3, the ratio of microscopic contact angle to apparent contact angle is plotted as a function of ε_{app}. The solid line represents the results obtained by solving the Eq. (2.82) numerically. The dashed line represents the solution (2.88). The lines coincide for $\varepsilon_{app} \to 0$. Note that the critical value of ε_{app} based on Eq. (2.88) slightly overestimates the numerically

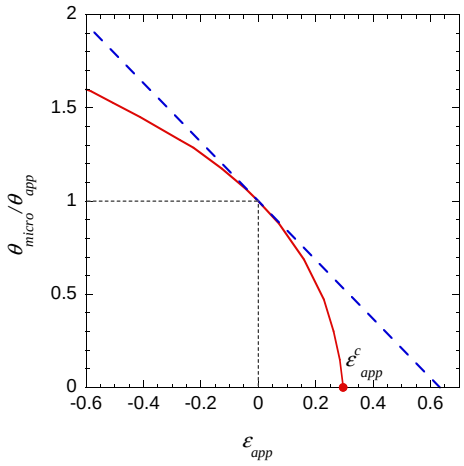

Figure 2.3: The ratio of microscopic contact angle and apparent contact angle is plotted vs. ε_{app}. The solid line is the numerical solution of Eq. (2.82), the dashed line is the solution given by Eq. (2.88). The critical value of $\varepsilon^c_{app} \sim 0.297$ is marked by the red point.

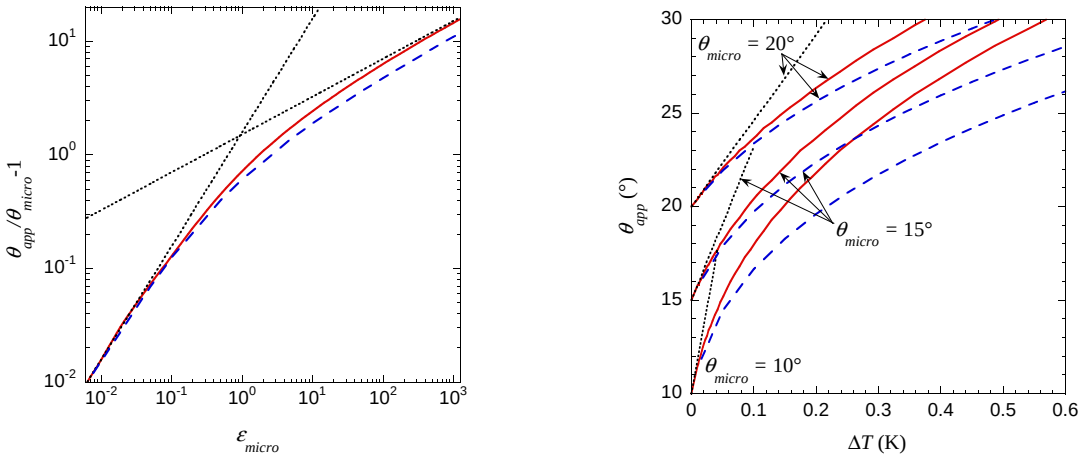

(a) (b)

Figure 2.4: a) $\theta_{app}/\theta_{micro} - 1$ plotted vs. ε_{micro}. The solid line is the numerical solution of Eq. (2.82), the dashed line is given by Eq. (2.92) and the dotted lines show the asymptotic slopes obtained from (2.92) for small and large ε_{app}, respectively. b) The numerical results for water at 10 MPa for several values of θ_{micro}.

obtained value of ε^c_{app} (by a factor of two). This is caused by the fact that asymptotic solutions (2.88 - 2.91) are only the first order solution of (2.82).

The same data as in Fig. 2.3 expressed however as a parameter $\theta_{app}/\theta_{micro} - 1$ are plotted vs. ε_{micro} in Fig. 2.4a. The dotted lines show two asymptotic slopes. The parameter $\theta_{app}/\theta_{micro} - 1$ varies for small ε_{micro} as $\pi/2\varepsilon_{micro}$ (cf. Eq. (2.88)) and for large ε_{micro} as $(\varepsilon_{micro}/\varepsilon^c_{app})^{1/3}$. The solid line represents the numerical solution of Eq. (2.82). Note its universality. All results calculated for various parameters (e.g. θ_{micro}, ΔT, etc.) collapse on this curve.

In Fig. 2.4b, some representative results calculated for water at 10 MPa and for three microscopic contact angles (10°, 15° and 20°) are shown. The apparent contact angle increases strongly with the imposed superheating ΔT. One can see that asymptotic solution (2.81) provides the slope of $\theta_{app}(\Delta T, \theta_{micro})$ curve at $\Delta T = 0$. For $\Delta T > 0$, the latter solution overestimates the apparent contact angle. This is obvious because the first order approximation for curvature

is based on a straight wedge with the angle θ_{micro}. The evaporation rate is thus overestimated which results in a large value of the apparent contact angle. The apparent contact angle based on (2.92) is lower than the actual value of θ_{app} calculated numerically, see Fig. 2.4.

2.3.8 Conclusion

The main finding of the previous sections related to asymptotic treatment of microregion model is that the Kelvin effect (dependence of saturation temperature on pressure) is sufficient by itself to relax the hydrodynamics contact line singularity [110, 111]. In principle other phenomena such as slip length or thermal interface resistance are not from the mathematical point of view essential to solve the problem. By relying on this fact, the minimal complexity microregion model is formulated (Eqs. (2.63 - 2.58)) and the missing boundary condition for its solution is obtained (2.31). At the next step, the minimum complexity model is solved analytically by using regular perturbation method. The first order solutions for pressure jump, interface slope, interface shape and evaporation rate along the liquid wedge are obtained. The most useful output from solving the minimal microregion model is the first order solution for the apparent contact angle (2.81) and integrated heat flux (2.80). Next, the governing length scale related to the Kelvin effect is identified. The length scale (along the x axes) is of the form[1] $l_K \sim 1/\theta_{micro}^2$. It means that for small microscopic contact angle this scale can be very large. For example, for FC-72 ($\theta_{micro} = 8°$), l_K 59.8 nm. This suggests that Kelvin effect imposes in many real systems the dominant scale. In this case the other phenomena such as interface thermal resistance or slip length would be of a secondary role. The latter scaling is used to find a universally valid law describing the apparent contact angle θ_{app}, which provides higher order approximation with respect to formula (2.81). The apparent contact angle calculated from Eqs. (2.81) and (2.92) are compared with the numerical solution of the minimal complexity microregion model.

[1] θ_{micro} is used as a reference angle as it is the relevant parameter at the limit $x \to 0$ of our interest.

2.4 Kelvin effect and contact line dynamics

The following section contains the original research work made in collaboration with B. Andreotti (PMMH, ESPCI). It was shown in the previous section that the Kelvin effect is sufficient by itself to regularize the hydrodynamic singularity for the immobile CL. Here the latter phenomena is used to relax the singularity appearing when the contact line moves. The multiscale nature of this phenomena is addressed. The following analysis is a contents of the preprint [110].

The contact line dynamics is a multiscale phenomenon as was already mentioned in the section 1.1. In Fig. 2.5 is shown schematically the structure of the flow close to the contact line for a slowly spreading drop on the solid surface. For the moment let us consider a macroscopically isothermal case (i.e., $\Delta T = 0$). Even for infinitesimal v_{CL} there exist following regions: 1) the macroregion (outer region) characterized by the length $L \sim 1$ mm, 2) the intermediate (mesoscopic) region where the diverging viscous stress is balanced by a gradient of capillary pressure, and 3) the microregion (inner region) where the microscopic processes, at a scale of ~ 10 nm, make the problem regular. The description of the flow in the intermediate region can be

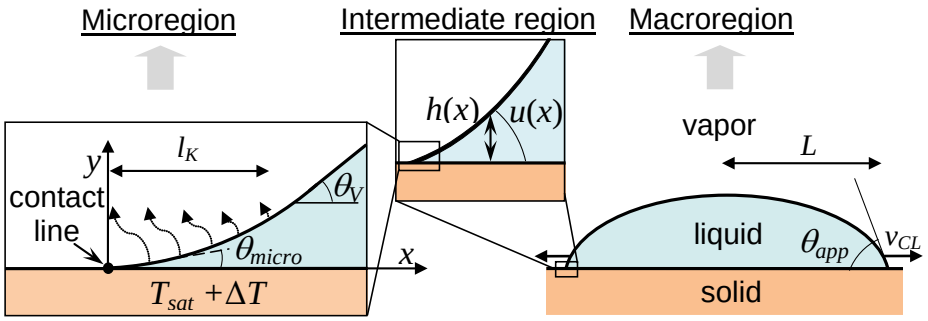

Figure 2.5: The illustrative figure shows a macroscopic liquid object at a different scales. The inner region, close to the moving contact line is controlled by evaporation. θ_{micro}, θ_V, θ_{app} and scales l_K, L are shown. Note that $v_{CL} > 0$ corresponds to advancing CL in this section.

made quantitative in the lubrication approximation. When all the terms related to microscopic scale are omitted, the following third order differential equation is valid in the intermediate region [8]:

$$\sigma \frac{d^3 h}{dx^3} = -\frac{3\mu v_{CL}}{h^2}. \tag{2.93}$$

This equation has an exact solution [133] that satisfies zero curvature boundary condition at infinity. It reduces to the asymptotic form proposed by Voinov [106]:

$$u(x)^3 = \theta_V^3 + 9Ca \ln\left(\frac{x}{l_V}\right), \tag{2.94}$$

where $u(x) = dh/dx$ and the capillary number $Ca = \mu v_{CL}/\sigma$. The Voinov angle θ_V and the Voinov length l_V are inherited from the inner region. The mesoscopic solution (2.94) must also be matched at the macroscopic scale L to an outer solution where liquid viscosity can usually be neglected. The apparent contact angle corresponds to the slope of interface at the matching of the mesoscopic and macroscopic regions, see Fig. 2.5.

The singular behavior of Eq. (2.93) for $x \to 0$ is frequently regularized by introducing the slip length, discussed in section 1.3.1.1. Note that in this case the inner region is dominated by the liquid slip. It was shown recently by Eggers [134] that when slip length is used and ($Ca \ll 1$) the Voinov angle is θ_{micro} and the length entering the (2.94) is $l_V = 3l_s/\mathrm{e}$, where $\mathrm{e} = 2.718\ldots$.

In the following the Kelvin effect is proposed to regularize the hydrodynamics singularity at the CL. First, the mixed situation will be considered ($\Delta T \neq 0$, $v_{CL} \neq 0$) and later we show that even for the macroscopically isothermal situation ($\Delta T = 0$, $v_{CL} \neq 0$) a completely regular solution is obtained. The derivations of the Voinov length l_V and of the Voinov angle θ_V as a function of the substrate temperature will be given.

The minimal complexity problem is extended for the contact line motion term. In practice it means that the term $\mu v_{CL} dh/dx$ is subtracted[2] from the the right hand side of Eq. (2.82). In this case the inner region will be evaporation/condensation dominated and the intermediate region CL motion dominated. The matching between these regions will be shown. The slope at the border or the inner and intermediate regions is associated with the Voinov angle θ_V. The Voinov angle is thus used as the reference angle. The equation (2.82) extended for the contact line motion term is reduced similarly as in the section 2.3.6 ($Z = \theta_V X$ and $[K] = Z/X^2$)

$$\bar{h}\frac{d}{d\bar{x}}\left[\bar{h}^3\frac{d^3\bar{h}}{d\bar{x}^3}\right] = \frac{d^2\bar{h}}{d\bar{x}^2} - \varepsilon_V - \delta\bar{h}\frac{d\bar{h}}{d\bar{x}}, \tag{2.95}$$

where $\delta = 3\mu v_{CL}/(\sigma\theta_V^3)$ is the modified capillary number, $\varepsilon_V = \sqrt{3\mu k_L T_{sat}}\Delta T/(\sigma T_{sat}\theta_V^3)$ the modified superheating. As previously the Kelvin length scale $l_{K,V} = \sqrt{3\mu k_L T_{sat}}/(\theta_V^2 \rho_L H)$ defines X. It includes θ_V instead of θ in l_K (2.84).

One can see indeed, that the outer region (large h) CL motion term is dominated, while it can be neglected at small h. The fourth order differential equation (2.95) must be complemented by appropriate boundary conditions. Two of them are geometrical (cf. Eqs. (2.27 - 2.28))

$$\bar{h}(\bar{x} = 0) = 0, \qquad \bar{u}(\bar{x} = 0) = \frac{\theta_{micro}}{\theta_V}. \tag{2.96}$$

The condition (2.31) reads

$$\Delta\bar{p}(\bar{x} = 0) = \varepsilon_V. \tag{2.97}$$

Finally, to make the problem compatible with the asymptotic expansion (2.94), one has to assume a vanishing curvature far from CL (cf. (2.29))

$$\Delta\bar{p}(\bar{x} \to \infty) \to 0. \tag{2.98}$$

By definition, θ_V is the interface slope far from the contact line in the limit $\delta = 0$. Note that for the case $\delta = 0$ the Voinov angle coincides with θ_{app}, in section 2.3.6 (the mesoscopic region described in Fig. 2.5 is absent in this case). However in this section the term apparent contact angle is strictly reserved for the slope at the scale the intermediate region is matched to the marcoregion. For the case ($\delta = 0$) Eq. (2.95) reduces the form of the equation (2.85), however with scaling based on θ_V and the finite slope of the free interface (corresponding to θ_V) for $\bar{x} \to \infty$ can be considered

$$\bar{u}(\bar{x} \to \infty) = 1. \tag{2.99}$$

The dash dotted line in Fig. 2.6a represents a typical solution obtained numerically for $\delta = 0$, cf. section 2.6.1. The cross-over from θ_{micro} to θ_V takes place for $\bar{x}$ of order unity. Similarly to the section 2.3.5, we perform a linear expansion of the solution in ε_V, writing $H = H_0 = \bar{x} + \varepsilon_V \bar{h}_{\varepsilon_V} + \mathcal{O}(\varepsilon_V^2)$. At this point it is convenient to make a link between this section and section 2.3.6. The solution H_0 of the problem is identical to the solution presented in the latter section, if θ_{app} is replaced by θ_V, c.f. see (2.90 - 2.91)

$$\frac{\theta_{micro}}{\theta_V} = 1 - \frac{\pi}{2}\varepsilon_V + \mathcal{O}(\varepsilon_V^2), \tag{2.100}$$

[2]The negative sign originates from the opposite orientation of v_{CL} in this section, cf. Figs. 2.5. $v_{CL} > 0$ corresponds to advancing CL, here.

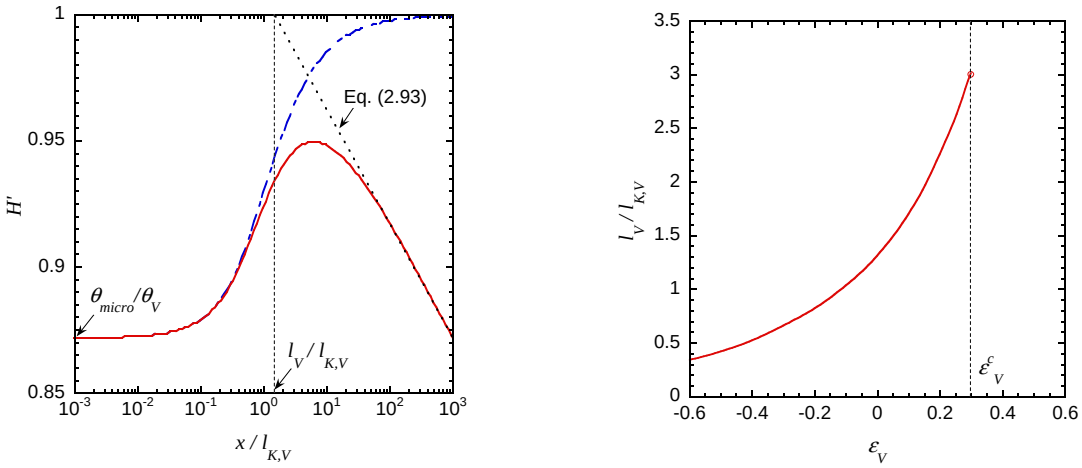

(a) (b)

Figure 2.6: a) Solution of the equations for an overheating $\varepsilon_V = 0.08$ and the receding contact line $\delta = -0.07$. The dash dotted line corresponds to the static case ($\delta = 0$). The dotted line corresponds to the Voinov outer asymptotics (2.94). These solutions allow one to extract the rescaled Voinov length l_V/l_K and the rescaled Voinov angle θ_V/θ_{micro}. b) Ratio of l_V to $l_{K,V}$.

Note the existence of a critical value $\varepsilon_V^c \simeq 0.297$ of the overheating parameter.

We now consider CL moving at a velocity v_{CL}. At distances much larger than l_V, one expects to recover the Voinov solution (2.94) at small capillary numbers. In scaled variables, one obtains from (2.94) at the first order in δ the asymptotic expansion

$$H'(\bar{x} \gg 1) \sim 1 - \delta \log(\bar{x}/l_V). \tag{2.101}$$

We linearize the governing equation around the solution H_0 obtained at vanishing δ by writing $H = H_0 + \delta H_\delta$:

$$3H_0^2 H_0''' H_\delta + H_0^3 H_\delta''' - Q_\delta = H_0 \tag{2.102}$$

$$Q_\delta' + \frac{H_0'' - \varepsilon_V}{H_0^2} H_\delta - \frac{H_\delta''}{H_0} = 0. \tag{2.103}$$

Note that Eqs. (2.102 - 2.103) are difficult to solve analytically. We thus solve the problem numerically. A typical solution for the scaled interface slope H' is shown in Fig. 2.6a (solid line) together with the asymptotic solutions for $\bar{x} \to 0$ (static solution obtained for $\delta = 0$ considered in section 2.3.5, dash dotted line) and $\bar{x} \to \infty$ (Voinov expansion (2.101), dotted line). The Voinov length l_V is obtained from the numerical results, as shown geometrically in Fig. 2.6a (intersection between the dashed line and the horizontal line $\bar{u}(\bar{x}) = 1$). θ_V is obtained from the solution for $\delta = 0$.

Figure 2.6b shows the dependence of l_V on the overheating. As expected from the dimensional analysis, l_V is of the order of the Kelvin length $l_{K,V}$. The ratio $l_V/l_{K,V}$ turns out to increase with the overheating, from $\simeq 1.32$ at $\varepsilon_V = 0$ to $\simeq 3.00$ at $\varepsilon_V = \varepsilon_V^c$. Note that matching the inner and the outer boundary conditions is possible only for $\varepsilon_V < \varepsilon_V^c$: the value ε_V^c is attained in the limit of large both ΔT and θ_V (see sec. 2.3.6).

In the remaining part of this section, the solution for $\varepsilon_V = 0$ (no heating) will be discussed. In this situation, the Voinov angle is equal to the microscopic contact angle $\theta_V = \theta_{micro}$. In Fig. 2.7a, a typical solution for two cases, $\delta = \pm 0.07$ is shown. The corresponding scaled curvature is shown in Fig. 2.7b. Note that the maximum of $|K|$ is attained at the scale l_K

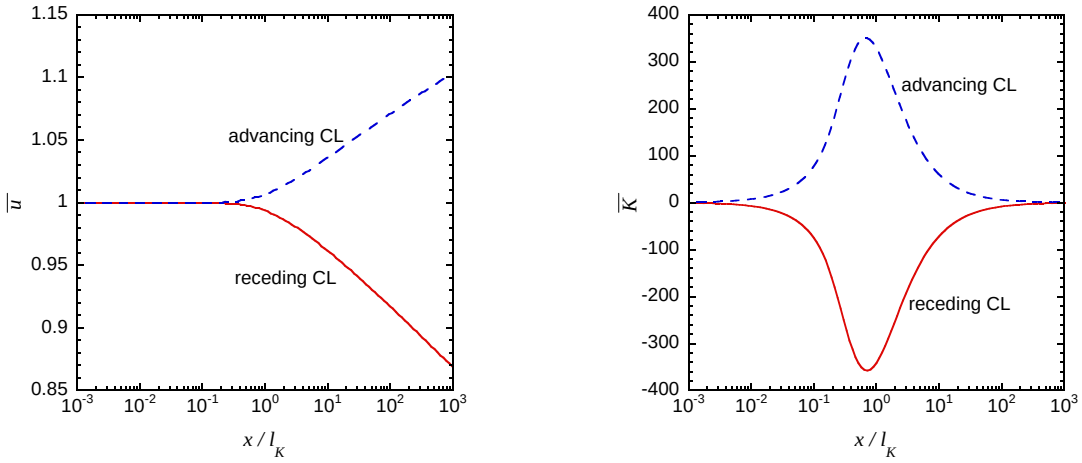

(a) (b)

Figure 2.7: Solution of the equation (2.95) for $\varepsilon_V = 0$ ($\theta_V = \theta_{micro}$) and $\delta = \pm 0.07$. a) Scaled interface slope, b) Interface curvature.

and is thus controlled by the Kelvin effect. The solution is perfectly regular, which confirms the result of section 2.3.2. Note that the no slip boundary condition is imposed at the solid-liquid interface: at a scale smaller than l_K, the interface advances by the curvature driven condensation (or recedes by evaporation).

In Table 2.1, the values of the length related to the Kelvin effect l_K are shown. The microscopic contact angle was chosen $\theta_{micro} = 8°$, which agrees with the experimental data for FC-72 on copper [4]. Note that l_K is inversely proportional to θ^2_{micro}; it means that for situation the contact angle is small, l_K is large. $l_V \sim l_K$ (for $\delta = 0$) and one can compare the equivalent value of l_V based on the slip length ($l_V = 3l_s/\mathrm{e}$, [134]) and the value of the Voinov length based on Kelvin effect.

	FC-72 (0.04 MPa)	Water (0.1 MPa)	Water (10 MPa)
l_K	59.8 nm	11 nm	25.2 nm

Table 2.1: Values of the scale related to the Kelvin effect l_K, based on $\theta_{micro} = 8°$.

2.4.1 Conclusion

The moving contact line problem and its multiscale nature were addressed in this section. The inner and outer (resp. intermediate) problems were defined: inner problem controlled by evaporation, and outer problem where the viscous stress is balanced by a gradient of capillary pressure. The asymptotic matching of the inner and outer regions was performed.

The main finding of this section is that the Kelvin effect relaxes the viscous stress singularity appearing when the contact line moves [110, 111]. In practice this means that in the model the liquid is allowed to evaporate or condensate as the saturation temperature of the liquid-vapor interface is linked through the Kelvin effect to the hydrodynamic pressure in the liquid phase. The condensation occurs during advancing contact line motion while the evaporation accompanies the contact line receding. The Kelvin effect singularity relaxation is compared to that of the hydrodynamic slip length. It is found that the length scale associated with the Kelvin effect is in many situations larger than the slip length and thus Kelvin effect is the dominant phenomenon for volatile fluids.

2.5 Impact of disjoining pressure on evaporation

In this section the extended microregion model including the disjoining pressure term is solved numerically. A specific disjoining pressure for partial wetting is presented. Next, a parametric study of the apparent contact angle on superheating and on the CL velocity is performed. The original study presented in this section corresponds to the research paper [135] and partly to the conference proceedings [136].

2.5.1 Disjoining pressure choice

A brief theoretical introduction to the theory of surface forces for the partial wetting is presented in section 1.3.1.4. Here the concrete disjoining pressure $\Pi(h)$ shape, used in Eq. (D.2) is proposed and discussed.

At h of the order of several nanometers, experiments [137] and also theoretical investigations [85, 86] suggest the existence of a maximum of $\Pi(h)$. The experimental data for h smaller than several nm are extremely rare and are unknown to us for the metal substrates of interest. One needs to choose a form compatible with experimental facts and with the partial wetting condition (1.18) that imposes a constraint to

$$P(h \to 0) \equiv \int_0^\infty \Pi(h) dh. \tag{2.104}$$

We choose here the simplest form that satisfies all these criteria,

$$\Pi(h) = \begin{cases} ah + b, & h \in (0, d_D) \\ A/(6\pi h^3), & h \in (d_D, \infty) \end{cases}, \tag{2.105}$$

where d_D is a length parameter defining the position of the maximum of the $\Pi(h)$ function. It is of the order of several nm. The coefficients a, b, once θ_Y, θ_{micro} are fixed can be found from Eqs. (1.18, 2.104) and from the condition of the continuity of $\Pi(h)$:

$$\begin{aligned} a &= \frac{A - 4\pi d_D^2 P(0)}{2\pi d_D^4}, \\ b &= \frac{6 d_D^2 \pi P(0) - A}{3\pi d_D^3}. \end{aligned}$$

The corresponding energy of the surface forces reads:

$$P(h) = \begin{cases} -\frac{ah^2}{2} - bh + P(0), & h \in (0, d_D) \\ \frac{A}{12h^2\pi} - \frac{A}{12\pi d_d^2} - bd_d - \frac{ad_d^2}{2} + P(0), & h \in (d_D, \infty) \end{cases}. \tag{2.106}$$

The resulting disjoining pressure shape is shown in Fig. 2.8 together with corresponding $P(h)$, which is a continuous and smooth function. The corresponding static shape of the liquid-vapor interface is schematized in Fig. 1.12; the numerically calculated static shape is shown in Fig. 2.9. The static liquid wedge $h(x)$ and its slope $u(h)$ including the disjoining pressure of the form (2.105) can however be obtained in an analytical form. Solution for $u(h)$ is shown in the following. The Young Laplace equation augmented for the disjoining pressure term (1.19) can be rearranged as (independent variable does not appear explicitly in (1.19)

$$-\sigma u(h) \frac{\partial u(h)}{\partial h} = \Pi = \begin{cases} ah + b, & h \in (0, d_D) \\ A/(6\pi h^3), & h \in (d_D, \infty) \end{cases}. \tag{2.107}$$

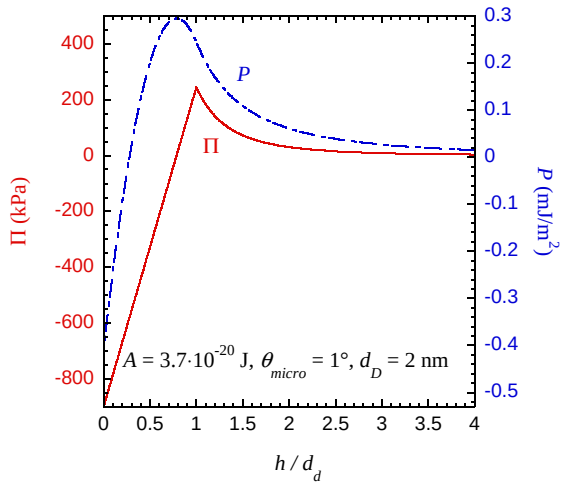

Figure 2.8: Shape of disjoining pressure (Eqs. (2.105)) and corresponding surface energy.

Eq. (2.107) may be solved for u analytically. The solution reads

$$u^2(h) = \begin{cases} -\frac{2bh+ah^2-2\sigma C_1}{\sigma}, & h \in (0, d_D) \\ \frac{A}{h^2 6\pi\sigma} + 2C_2, & h \in (d_D, \infty) \end{cases} . \tag{2.108}$$

The integration constants C_1, C_2 are to be determined from the boundary condition $u(0) = \theta_{micro}$ and matching of $u(h)$ at $h = d_D$.

The derivative of $\Pi(h)$, given by (2.105) is however discontinuous. It is a consequence of chosen shape of Π. We verified numerically by using a parabolic shape for the matching of straight line to (1.21) that the discontinuity does not influence the results (see Appendix C for smooth form of the disjoining pressure).

Note that the disjoining pressure can be calculated from the potential energy of the intermolecular interaction [84] with a mean-field approach. The h^{-3} dependence of $\Pi(h)$ appears due to the r^{-6} long range attraction term (r being the distance between the molecules). The r^{-6} attraction is only a part of the full interaction potential (e.g. that of Lennard-Jones) that has to contain also a short-range repulsion term (r^{-12} in the case of Lennard-Jones). The contribution to $\Pi(h)$ from this latter term is of the opposite sign and leads [117] to a maximum of $\Pi(h)$ at the nanometer scale (which conforms to Eq. (2.105)) but also to $\Pi(h \to 0) \to -\infty$ (which disagrees with Eq. (2.105)). Nevertheless, the Lennard-Jones potential may lead to the partial wetting [115, 120] in molecular dynamics calculations (which are more precise than the above mean-field approach). This means that for practical purposes, one has to use a $\Pi(h)$ curve with a finite negative $\Pi(h \to 0)$ as in Fig. 2.8.

2.5.2 Impact of surface forces on evaporation

The disjoining pressure shape proposed in the last section is used in the extended microregion model (introduced in Appendix D) and numerical results are presented below. The impact of surface forces (disjoining pressure Π) on the evaporation in the vicinity of the CL is studied here.

In order to avoid any confusion between θ_{micro}, θ_Y and θ_{app} the meaning of each of them is shortly reminded. The microscopic contact angle θ_{micro} is an angle imposed at the CL ($x = 0$). In case the surface forces are absent in the model (disjoining pressure term $\Pi = 0$) its value is automatically considered as a static contact angle given by its Young value $\theta_{micro} = \theta_Y$ for an ideally flat and homogeneous heater surface. When the effect of surface forces is included

via $\Pi \neq 0$, the system is described by two angles $\theta_{micro} \neq \theta_Y$, where θ_{micro} is related to the energy of surface forces, and θ_Y through the Eq. (1.18), for more details see section 1.3.1.4. The meaning of the apparent contact angle θ_{app} is throughout of this thesis unambiguous. It is an angle established far from CL at the scale the impact of CL is negligible. In case $v_{CL} \neq 0$ the apparent contact angle corresponds to the slope of liquid-vapor interface at the border of microregion and macroregion.

The numerical calculation is performed (unless mentioned specifically), for water at 10 MPa, $\theta_Y = 15°$, $l_s = 10$ nm. The parameters related to the disjoining pressure are $\theta_{micro} = 1°$, $d_D = 1$ nm and $A = 3.7 \cdot 10^{-20}$ J. The values of the dimensionless constants (see Appendix D for their definition) calculated for $\Delta T = 0.5$ K are $N_M = 9.4 \cdot 10^{-3}$, $N_p = 1.6$, $N_e = 5.1 \cdot 10^{-4}$, and $N_R = 0.2$. Since $N_R < 1$, l_s is larger than the length scale $l_R = k_L R^i$ associated with the interfacial resistance. The largest scale in the system is $N_p l_s$; it is associated with the Kelvin effect. However for $\Delta T \gtrsim 1$ K the largest scale is l_s. Examples of the computed shape of

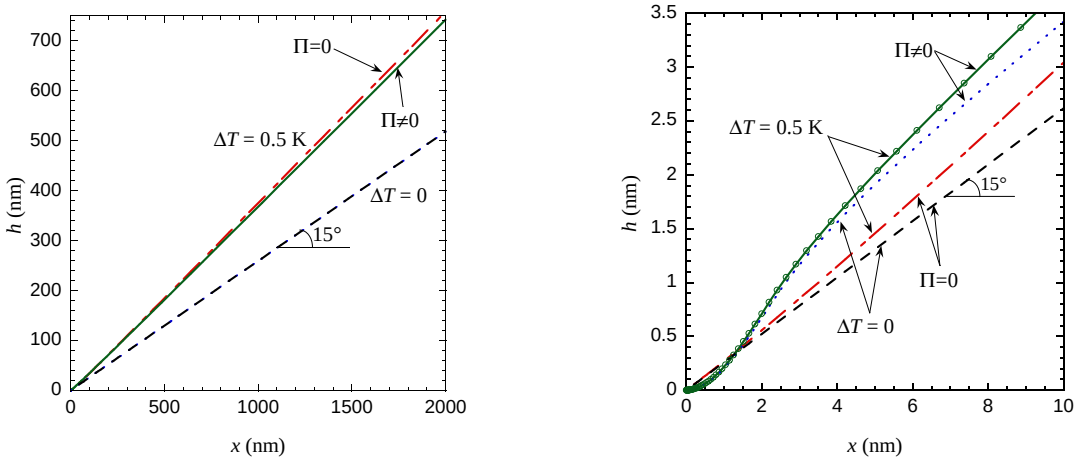

(a) (b)

Figure 2.9: Liquid-vapor interface computed for $\theta_Y = 15°$ with and without disjoining pressure implementation. (a) Large scale view. The curves corresponding to $\Pi = 0$ and $\Pi \neq 0$ are indistinguishable at this scale for $\Delta T = 0$. (b) Zoomed in vicinity of the contact line. The data points for $\Delta T = 0.5$ K, $\Pi \neq 0$ are indicated with circles to illustrate the increasingly dense meshing near the contact line. Note that θ_Y does not correspond to any actual slope when $\Pi \neq 0$ and $\Delta T \neq 0$.

the liquid-vapor interface with and without accounting for the disjoining pressure are shown in Fig. 2.9. One can see that the macroscopic shapes in Fig. 2.9a for the cases $\Pi = 0$ and $\Pi \neq 0$ are very close and almost indistinguishable at equilibrium. The contact line vicinity is zoomed in Fig. 2.9b. The solution for $\Delta T \neq 0$ is compared to the isothermal shape. In agreement with the previous asymptotic treatment of the simplified microregion model, heating results in an increase of θ_{app}.

The slope variation of the liquid-vapor interface is shown in Fig. 2.10a. The data which corresponds to $x < 1$ nm are not excluded from the graph in spite of the fact that the continuum approach is not physically justified there: they show that the solutions approach at $x \to 0$ the boundary conditions. For $\Pi \neq 0$, a strong variation of slope at nanometer scale is due to the effect of surface forces. A small slope θ_{micro} at the contact line is imposed in agreement with Eq. (2.28). At a scale comparable to l_s, an increase of slope is due to the fluid flow induced by evaporation.

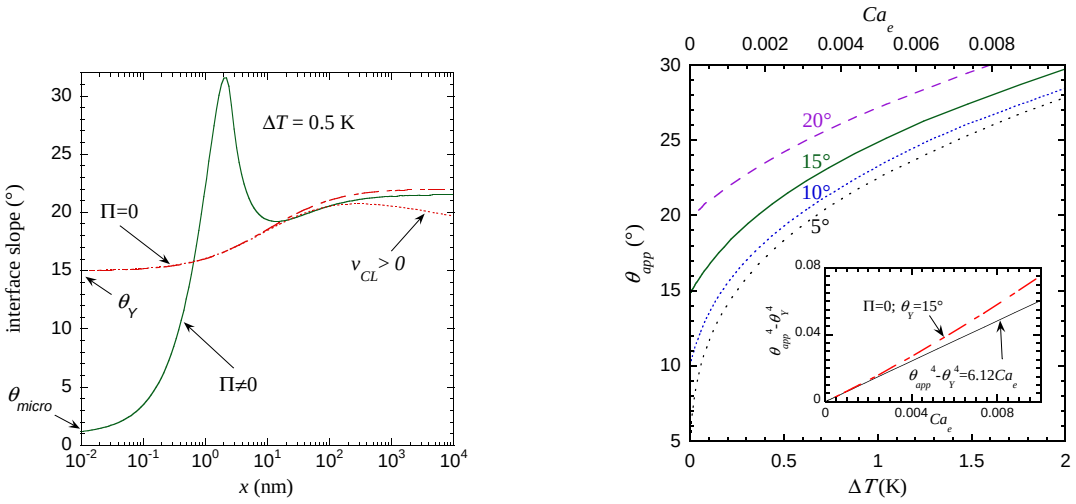

(a) (b)

Figure 2.10: a) Liquid-vapor interface slope variation computed for $\theta_Y = 15°$ and $\Delta T = 0.5$ K. The dotted line corresponds to $v_{CL} = 0.02$ m/s, $\Pi = 0$. The other curves are computed for $v_{CL} = 0$. b) Apparent contact angle θ_{app} as a function of ΔT for $\Pi \neq 0$ for different values of θ_Y.

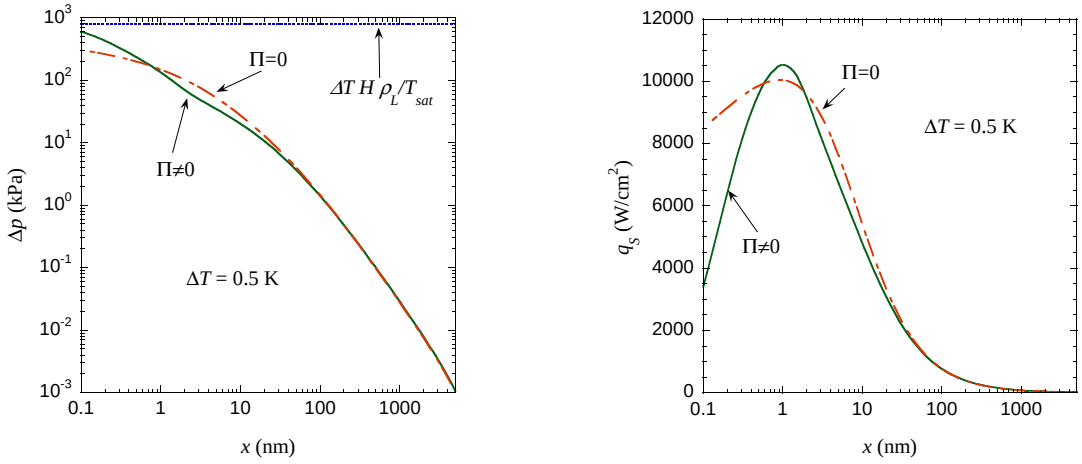

(a) (b)

Figure 2.11: Pressure difference and heat flux distribution for $\Delta T = 0.5$ K and $\theta_Y = 15°$ with and without disjoining pressure account for the immobile CL. (a) Pressure difference. The asymptotic value given by Eq. (D.6) is shown. (b) Heat flux.

The computed pressure jump and the heat flux are shown in Fig. 2.11 as functions of x for the immobile CL. A positive Δp value means that the flow is directed towards the CL. One can see that both the pressure and the flux limits (2.39, D.6), however the case including Π approaches the boundary conditions much faster. It is due to the smaller imposed slope (we considered $\theta_{micro} < \theta_Y$) of the free interface at CL.

Introduction of the disjoining pressure in the model results only in a small change of Δp, compared to the model without disjoining pressure. The peak of heat flux is slightly larger for $\Pi \neq 0$. The difference in the small scale behavior for the cases with or without disjoining pressure is related to the small-scale difference of the wedge shape (see Fig. 2.9b). Since the liquid layer thickness is smaller for $\Pi \neq 0$, the heat flux is larger. Note that the difference of the cases $\Pi \neq 0$

and $\Pi = 0$ concerns mainly very small scales.

The apparent contact angle θ_{app} is plotted versus ΔT for different θ_Y in Fig. 2.10b. It is evident that Young's contact angle θ_Y plays an important role, especially when small ΔT is considered. For small values of θ_Y, a rapid increase of θ_{app} occurs for low ΔT. For $\Delta T > 0.5$ K, the curves for all θ_Y grow with about the same rate. $\theta_{app} - \theta_Y$ can attain 25° (which is a quite a strong effect) for a small superheating of 2 K.

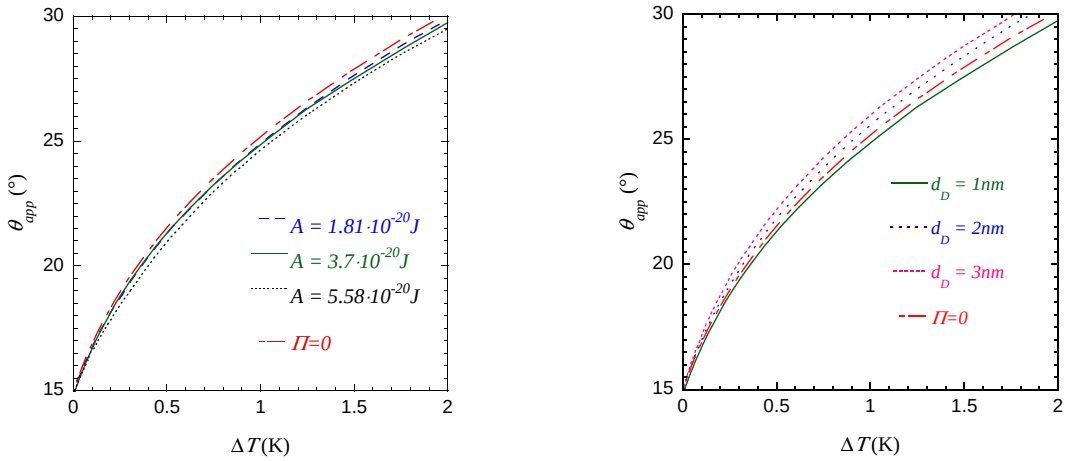

(a) (b)

Figure 2.12: Apparent contact angle θ_{app} versus ΔT for $\theta_Y = 15°$ and different parameters of disjoining pressure. The curve for $\Pi = 0$ is shown for comparison and coincides with curve prescribed to d_D . (a) Hamaker constant variation. (b) Dependence on the position d_D of the maximum of disjoining pressure.

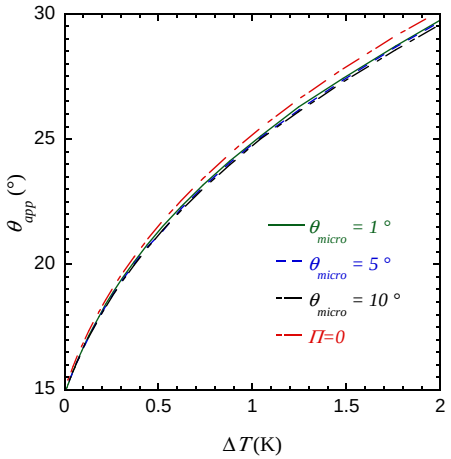

Figure 2.13: Apparent contact angle θ_{app} versus ΔT for $\theta_Y = 15°$ and different values of microscopic contact angle.

The sensitivity of the results to the parameters of disjoining pressure is analyzed in Fig. 2.12. This analysis is necessary because of the uncertainty of their experimental determination. It can be seen that the Hamaker constant variation does not notably affect θ_{app}. The maximum of disjoining pressure is lower for smaller A, the influence of Π is weaker, and the curves approach that for $\Pi = 0$. Note that for an oxidized metal surface, the Hamaker constant is an order of value smaller than the theoretically obtained values for pure metals [138], which leads to even

smaller difference comparing to the case $\Pi = 0$. In Fig. 2.13 the variation of θ_{micro} from 1° to 10° is shown. The impact of θ_{micro} on the apparent contact angle is even smaller than of A and d_D.

2.5.3 The moving CL case

The influence of surface forces on the solution of liquid evaporation and CL motion within the microregion is studied in the section. In the case of the moving CL (as was already mention in previous sections), the definition of θ_{app} becomes more difficult. This problem is well studied in the absence of evaporation where the Cox-Voinov law [83] shows that the slope diverges logarithmically if the infinite domain is considered. In the calculation x_{max} is chosen as obtained for the corresponding case for $v_{CL} = 0$, when using the proposed criteria (see section D.3). The apparent contact angle is thus here associated with the slope of the free interface at x_{max}.

For an example of calculated slope variation along the wedge see Fig. 2.10a. The logarithmic decrease of the slope at large x is visible.

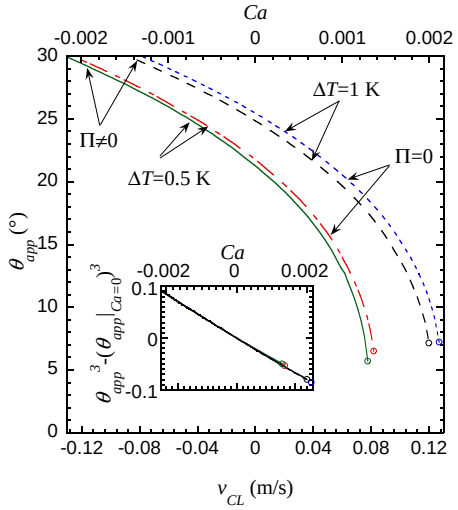

Figure 2.14: Dependence of apparent contact angle θ_{app} on the contact line velocity calculated with and without taking into the disjoining pressure for $\Delta T = 0.5$, 1 K.

The influence of the CL motion on θ_{app} is illustrated in Fig. 2.14, where the curves are calculated for the same x_{max}. The capillary number $Ca = \mu v_{CL}/\sigma$ is presented at the upper axis. The difference between the cases with and without disjoining pressure is not significant; the curves are just slightly shifted. The insert shows that the Cox-Voinov law is satisfied also for the case of evaporation: the curves for different ΔT collapse on the same straight line. This is not surprising as one knows that the evaporation (as well as Π) impacts only the microregion, while the contact line motion impacts the whole wedge; the angle $\theta_{app}(\Delta T, Ca = 0)$ thus provides the "inner" description while the Cox-Voinov formula solves the "outer" region.

No stationary solution with the triple CL can be found if the CL velocity exceeds a threshold. Such a situation is fully analogous to the case $\Delta T = 0$ where a transition [127] occurs to another stationary regime, in which CL is absent and the wedge is connected to a continuous liquid film (called Landau-Levich film). Such a transition is called the Landau-Levich or film entrainment transition. The thickness of such a film is controlled by a hydrodynamic effect and is usually micrometric, to be distinguished from the nanometric wetting films. Figure 2.14 shows that the transition velocity grows with ΔT.

2.5.4 Conclusion

A model describing hydrodynamics and heat flow in the vicinity of the contact line with the account of surface forces is shown in this section. The case of ideally smooth and homogeneous substrate is considered. It is shown that in case Π is considered the liquid meniscus is curved due to two effects: the surface forces and the hydrodynamic flow that appears because of evaporation and contact line motion. For the immobile CL, the meniscus slope saturates far from the contact line and defines the apparent contact angle θ_{app}. The latter rapidly increases with the superheating (difference between the substrate temperature and the saturation temperature) for low values of Young's contact angle. For stronger superheating the apparent contact angle growth rate is almost independent of the Young contact angle. The effect of the imposed contact line velocity on the apparent contact angle is significant. The general trend is similar to the isothermal contact line dynamics, where the film entrainment transition is detected at some velocity of the receding contact line.

The phenomena of the (equilibrium) contact angle and the disjoining pressure are intrinsically linked because they are both caused by the intermolecular forces. By introducing a particular form of the disjoining pressure into the model, one fixes a particular equilibrium contact angle value. However, a different form of disjoining pressure may result in the same equilibrium contact angle value. Our results show that the impacts of the disjoining pressure and the heating may be decoupled. The apparent contact angle created by heating depends mostly on the equilibrium contact angle value and is almost independent on the disjoining pressure details. This occurs because the length scales that describe the heating process are typically five to ten times larger than those of the disjoining pressure.

For the receding contact line, the film entrainment transition occurs at evaporation similarly to the isothermal case. The transition contact line velocity grows with the evaporation rate. Similarly to immobile CL evaporation case the impact of chosen disjoining pressure shape found to be negligible. Based on results of this study we suggest to used $\theta_{micro} = \theta_Y$ instead of introducing θ_Y with $\Pi(\theta_Y)$.

2.6 Parametric study revealing the influence of R^i, l_s and γ

In this section is presented a parametric study revealing the impact of various phenomena on evaporation in the contact line vicinity. First, the minimum complexity microregion model is numerically solved and system variables such as pressure jump, local heat flux, interface slope and shape along the liquid wedge are presented. Next, the latter model is extended to account for another phenomena that may influence the evaporation. In particular, the impact of the slip length, thermal resistance of vapor-liquid interface, slip length, and thermocapillary term are investigated. Presented results are calculated numerically for three sets of physical parameters; FC-72 at 0.04 MPa, water at 10 and 0.1 MPa. The impact of vapor recoil effect on evaporation in the vicinity of the contact line is studied in section 2.8.3 for microregion extended to the high slopes of interface.

2.6.1 Solution of simplified microregion model $l_s = R^i = \gamma = v_{CL} = 0$

In this section, the numerical solutions of the minimal complexity microregion model (including only the Kelvin effect) are presented. It serves here as the baseline model to which other results are compared below. The asymptotic analysis of this model has been carried out in section 2.3.3. The solution method is essentially the same (simplified for neglected terms) as described in the Appendix D. If not written explicitly, $\theta_{micro} = 15°$ is used.

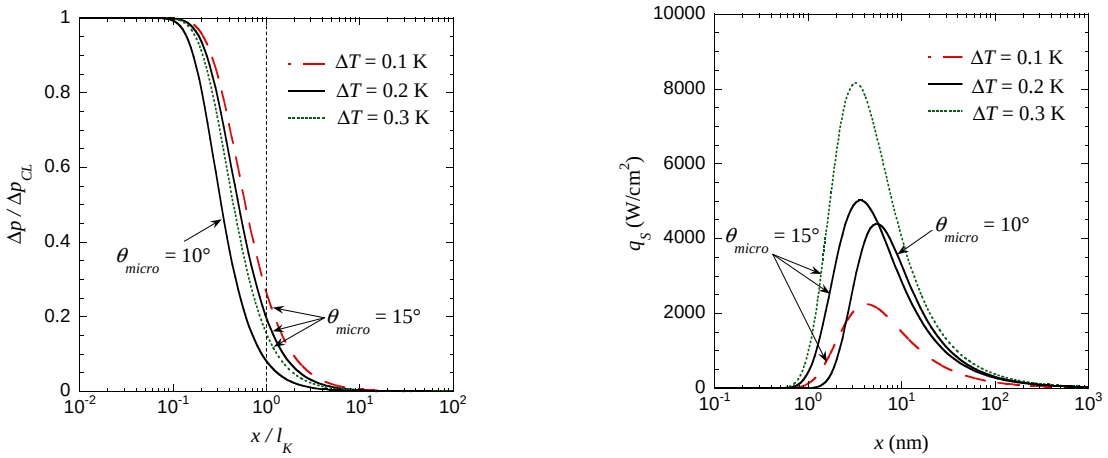

(a) (b)

Figure 2.15: Pressure and heat flux spatial variations obtained numerically for water at 10MPa, $\Delta T = 0.1$, 0.2 and 0.3 K, $\theta_{micro} = 10°$, 15°. The corresponding values of l_K for these two values of θ_{micro} are 16.1 and 7.16 nm. The curves obtained with either Eq. (2.62) or Eq. (D.14) are undistinguishable. (a) Pressure jump variation in scaled variables, Δp_{CL} corresponds to (2.31) and l_K to (2.84). (b) Heat flux variation.

Fig. 2.15a shows the scaled pressure jump $\Delta p/\Delta p_{CL}$ vs. x/l_K. The graph shows the monotonic growth of the pressure jump Δp as $x \to 0$. A positive value of pressure jump means that the flow is directed towards the CL. The x axis is extended to the nonphysically small values to show the asymptotic convergence of calculated $\Delta p(x)$ to the boundary condition (2.62). In the numerical treatment, Eq. (D.14) was used as boundary condition (instead of (2.62)). For comparison, the results for water at 10 MPa, $\Delta T = 0.2$ K obtained with boundary condition (2.62) and also with (D.14) are shown in Fig. 2.15 simultaneously. The curves are undistinguishable.

With decreasing microscopic contact angle, the distance from CL at which Δp (note that

$\Delta p/\sigma$ is the interface curvature) is negligible, increases. This means that $\Delta p \ll \Delta p_{CL}$ and the interface slope nearly does not change. This scale is defined by l_K (2.84), see Fig. 2.15 for its values. In Fig. 2.15b is shown the interface heat flux q_L^i variation along the liquid wedge in dimension units. The maximum of its value seems to be reached approximately at the scale where Δp attains an inflexion point. The heat flux vanishes as $x \to 0$. Such a behavior is similar to the complete wetting case, where the non evaporated liquid film persists at the left domain limit ($x \to -\infty$ in that case). A reduction of the steep heat flux variation near CL requires very fine meshing (see Fig. (2.17b)). However with the boundary condition (D.14) it is not mandatory in order to obtain the reliable θ_{app} results.

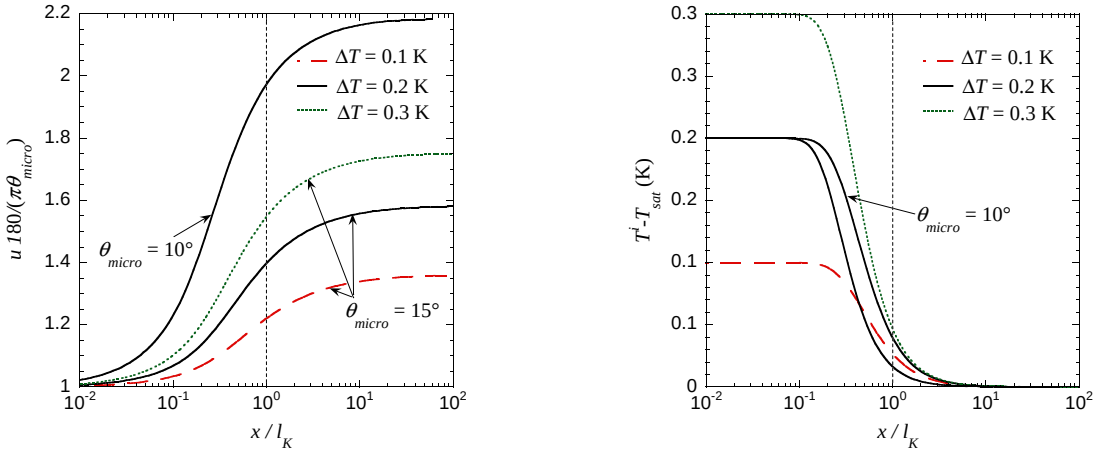

(a) (b)

Figure 2.16: Liquid-vapor interface slope and temperature variation computed for the parameters used in Fig. 2.15. (a) Interface slope variation. (b) Temperature along the liquid-vapor interface.

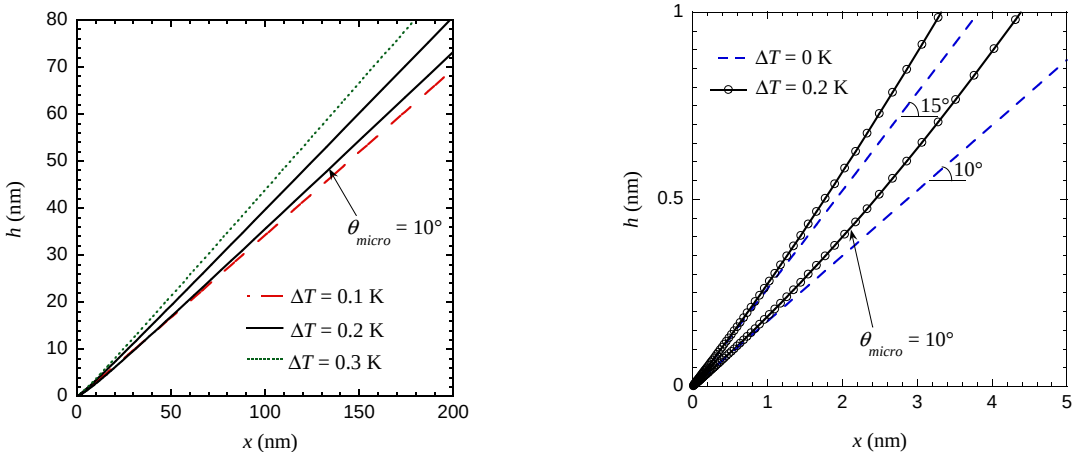

(a) (b)

Figure 2.17: Shape of the liquid-vapor interface calculated numerically for the parameters used in Fig. 2.15a. (a) Large scale view. (b) Zoomed in vicinity of the contact line. There only two curves are shown: water at 10 MPa, $\Delta T = 0.2$ K with microscopic contact angle $\theta_{micro} = 10°$, 15°.

The free interface slope variation is shown in Fig. 2.16a. The slope saturates at the scale l_K, shown by the vertical line. The parameter r_{app} at which $u(x)$ curves satisfy the criterion

($u(r_{app}) = 0.99\ \theta_{app}(x_{max})$) (see section D.3) is for presented cases $\sim$ 100 nm. This shows that the evaporation is very localized in the vicinity of the CL.

The liquid-vapor interface temperature variation along the wedge is plotted in Fig. 2.16b. As $x \to 0$, T^i matches the temperature of the solid heater. For the other limit $x \to \infty$, T^i matches the saturation temperature given by bulk vapor pressure. One can notice that $T^i(x) - T_{sat}$ curves are very similar to the pressure jump variation, see Fig. 2.15a. This is a direct consequence of the fact that both are linked through relation (2.4), the Kelvin effect.

The interface shape is shown in Figs. 2.17. At the scale of $\sim$ 100 nm the liquid-vapor interface is nearly straight (cf. Fig. 2.17a) and makes the apparent contact angle θ_{app} with the solid substrate. Fig. 2.17b shows the detail of CL region, where only two curves with different imposed microscopic contact angles are shown.

The apparent contact angle is the main result from the microregion calculation. Graph showing θ_{app} vs. ΔT (Fig. 2.4) is shown in section 2.3.7. The universally valid scaled apparent contact angle vs. ε_Y covering all possible combinations of parameters is presented in Fig. 2.4a.

2.6.2 Impact of the slip length

First, only the impact of slip length term on the solution of microregion model is studied. The slip length is introduced in section 1.3.1.1. The typical value of $l_s = 10$ nm (smooth and chemically homogeneous surface [71]) is taken here as a reference value. For $l_s > 0$ the pressure jump saturates at smaller distance from the CL, see Fig. 2.18a. This might complicate the numerical treatment of the problem.

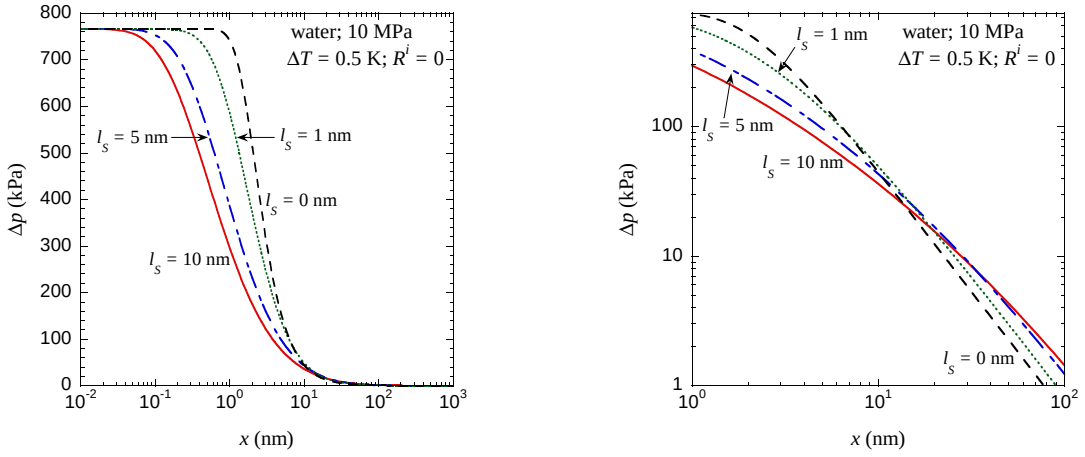

Figure 2.18: Pressure and heat flux spatial variations obtained numerically for water at 10 MPa, $\Delta T = 0.5$ K and $\theta_{micro} = 15°$ for four values of l_s. (a) Pressure jump variation. (b) Heat flux variation.

One can also argue that such a scale is below value that can be considered as physically reasonable for given system described in the frame of continuum approach. On the other hand, the slip is frequently used to remove the CL singularity for moving contact line, which however results in (logarithmically) divergent $\Delta p(x \to 0)$. In our model the pressure attains finite value at CL, which is physically coherent. If the slip length is considered, Δp decays slower along the wedge for $x \gtrsim l_s$ with respect to the case $l_s = 0$, see Fig. 2.18b. The apparent contact angle is thus established at larger scales.

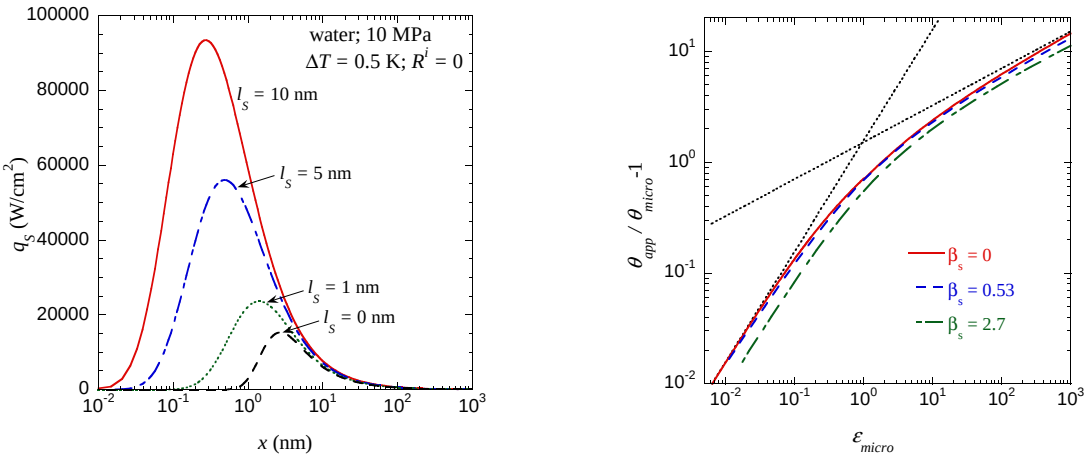

(a) (b)

Figure 2.19: (a) Heat flux spatial variations obtained numerically for water at 10 MPa, $\Delta T = 0.5$ K and $\theta_{micro} = 15°$ for four values of l_s. (b) Parameter $\theta_{app}/\theta_{micro} - 1$ vs. ε_{micro} for three values of modified slip length. Curve for $\beta_s = 0$, corresponds to results calculated from minimum complexity microregion model, from Fig. 2.4a.

The liquid-vapor interface heat flux variation along the liquid wedge is plotted in Fig. 2.19a. With larger value of slip length the maxima of the local heat flux are higher. This is due to the fact that pressure jump (and thus the interface temperature) saturates at very small scale when $l_s \neq 0$. At this scale the conductive thermal resistance is extremely small and this results in high heat flux maxima, which is shifted towards the contact line.

When using the same scaling (based on l_K, see sec. 2.3.6), the microregion model including the slip length and the Kelvin effect can be reduced in to the following form (cf. Eq. 2.85):

$$\bar{h}\frac{d}{d\bar{x}}\left[\left(\beta_s\bar{h}^2+\bar{h}^3\right)\frac{d^3\bar{h}}{d\bar{x}^3}\right]=\frac{d^2\bar{h}}{d\bar{x}^2}-\varepsilon_{micro}, \tag{2.109}$$

where the parameter $\beta_s = 3l_s/(l_K\theta_{micro})$ is the modified slip length, l_K is defined by Eq. (2.84) and ε_{micro} by Eq. (2.86). Note that β_s expresses the ratio of two length scales; l_s/θ_{micro} is related to the slip length, ε_{micro} and β_s are the only parameters defining the behavior of the system. In Fig. 2.19b the curves $\theta_{app}/\theta_{micro} - 1$ vs. ε_{micro} are compared for three values of β_s = 0, 0.53 and 2.7 (which corresponds to l_s = 0, 1 and 3.3 nm, for water at 10 MPa and θ_{micro} = 5°). It is evident that the apparent contact angle decreases with the slip length. The slopes of the curves for small and large ε_{micro} seem to be the same as for the case $\beta_s = 0$. It practically means that the asymptotic expressions for both small and large superheatings are of the same form as follows from Eq. (2.92) obtained for the case $l_s = 0$.

2.6.3 Impact of the interface thermal resistance

The impact of the interface thermal resistance R^i (see section 1.3.1.3) is studied here. The R^i term is characterized by the scale $l_R = R^i k_L$, which can be interpreted as an additional thickness of the liquid layer with the equivalent thermal resistance. l_R is usually of the order of several nm, e.g. l_R = 2 nm, when R^i is calculated from Eq. (1.13) for water at 10 MPa. In Figs. 2.20 is shown the impact of four different R^i values on the pressure jump and interface heat flux variations along the liquid wedge. Fig. 2.20b shows that because of the interface resistance the heat flux is considerably reduced. The length scale at which the maximum of q_S is attained,

remains nearly unaffected. The pressure jump variation attains the value given by Eq. (2.62) at a smaller distance from CL if $R^i \neq 0$. This explains why the apparent contact angle, proportional to $\int_0^\infty \Delta p(x)dx$ attains lower value for $R^i \neq 0$ (see Fig. 2.23a).

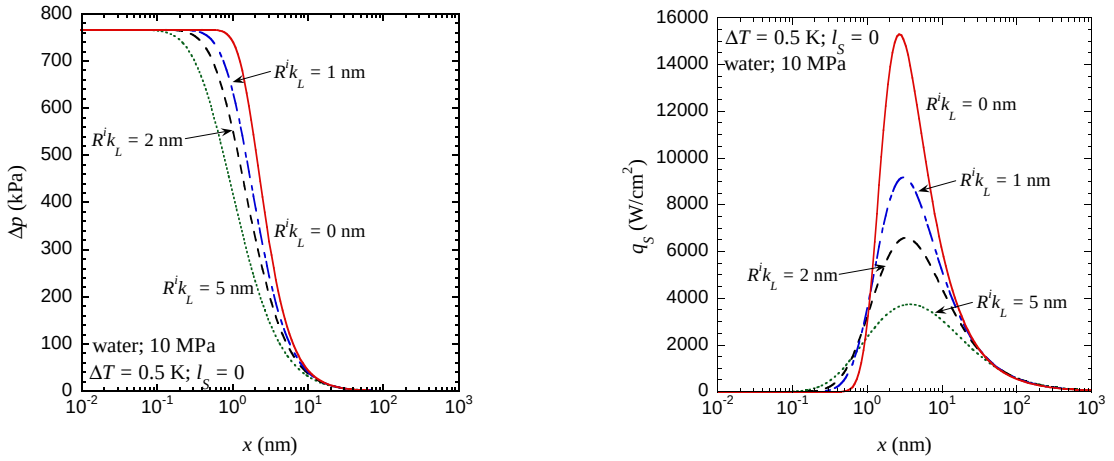

(a) (b)

Figure 2.20: Pressure and heat flux spatial variations obtained numerically for water at 10 MPa, $\Delta T = 0.5$ K and $\theta_{micro} = 15°$ for four values of R^i. (a) Pressure jump variation. (b) Heat flux variation.

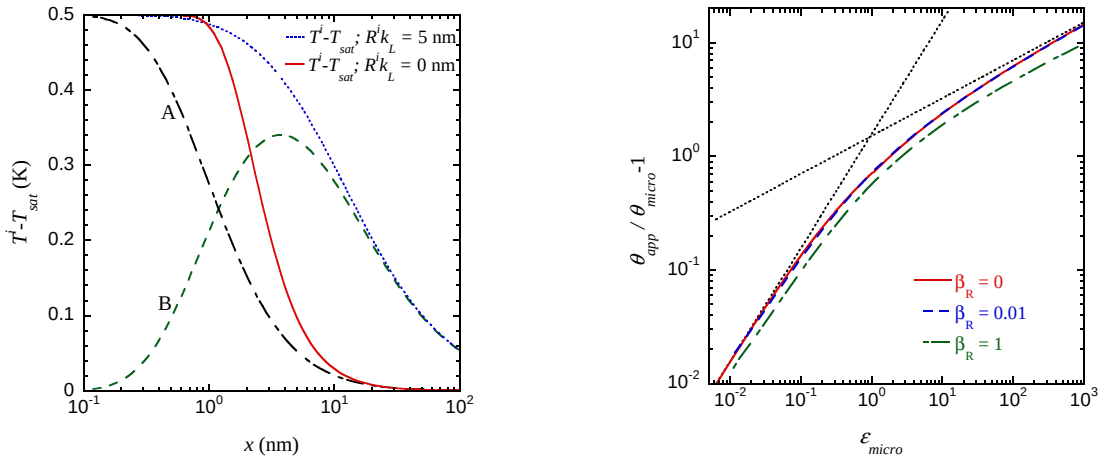

(a) (b)

Figure 2.21: (a) Variation of liquid-vapor interface temperature (respective $T^i - T_{sat}$)along the wedge obtained numerically for water at 10 MPa, $\Delta T = 0.5$ K, $\theta_{micro} = 15°$ for two cases $R^i k_L = 5$ nm and without interface resistance. The temperature terms A and B in Eq. (2.110) are shown. (b) Parameter $\theta_{app}/\theta_{micro} - 1$ vs. ε_{micro} for three values of modified interface thermal resistance. Curves for $\beta_R = 0$, correspond to results calculated from minimum complexity microregion model, see section 2.3.7.

The interface resistance term influences the liquid-vapor interface temperature through Eq. (2.4), (with neglected recoil term):

$$T^i - T_{sat} = \overbrace{\frac{\Delta p T_{sat}}{H \rho_L}}^{\text{A}} + \overbrace{R^i q_L^i}^{\text{B}}. \tag{2.110}$$

The term A represents contribution to $T^i - T_{sat}$ from hydrodynamics (Kelvin effect) and term B the contribution from the interfacial resistance. In Fig. 2.21a, the interface temperatures $T^i - T_{sat}$ for the simplified microregion model ($R^i = 0$) and for the case where the interface resistance is present ($R^i k_L = 5$ nm) are plotted together with the contributions A and B. It is clearly visible that when R^i is considered, the interface temperature decays much slower at large x. Note however that the two cases compared in Fig. 2.21 result in different θ_{app}, as the thermal resistance is given mainly by the thickness of the liquid layer. The maximum of the contribution B (c.f. Eq. (2.21)) is attained at the scale l_R. Such a finding will be important for the case where the thermocapillary effect is included into the microregion model, see below.

Similarly to the case with slip length, one can reduce the microregion model including the interface resistance into the following form:

$$(\bar{h} + \beta_R)\frac{d}{d\bar{x}}\left[\bar{h}^3\frac{d^3\bar{h}}{d\bar{x}^3}\right] = \frac{d^2\bar{h}}{d\bar{x}^2} - \varepsilon_{micro}, \tag{2.111}$$

where the parameter $\beta_R = l_R/(l_K\theta_{micro})$ is the modified interface thermal resistance, l_K is given by Eq. (2.84) and ε_{micro} by Eq. (2.86). Similarly to the previous section, β_R is a ratio of two characteristic length scales of the problem. One related to the interface resistance (l_R) and second to the Kelvin effect (l_K). The factor θ_{micro}^{-1} rescales l_R (characteristic scale in y direction) to x direction. The parameter ε_{micro} and β_R are the only parameters defining behavior of the system. In Fig. 2.21b is compared the parameter $\theta_{app}/\theta_{micro} - 1$ vs. ε_{micro} for three values of β_R = 0, 0.01 and 1 (which corresponds to $R^i k_L = 0$, 1 and 10 nm, for water at 10 MPa and $\theta_{micro} = 5°$). It is evident, that the apparent contact angle is lower for the $\beta_R \neq 0$ case. Similarly to the case with the slip length, the curves for $\beta_R = 0.01, 1$ are shifted with respect to the case $\beta_R = 0$. The slopes for small and large ε_{micro} seems to be the same form as follows from Eq. (2.92) for the case $R^i = 0$.

2.6.4 Combination of slip length and interface resistance term

The slip length and the interface thermal resistance are usually used together [103, 104]. In this case one can expect from comparison of asymptotic solutions for the pressure jump as $x \to 0$ (see section 2.3.4) a slower convergence of the pressure jump to its value given by Eq. (2.31). This may complicate numerical treatment as the first node of the microregion computational grid (see. Fig. D.2) is not exactly placed at $x = 0$ (or more precisely at $\zeta \to -\infty$) but at x_{min}. Here we study the impact of this parameter on the numerical solution. Note that this was meaningless for previous cases where either $l_s = 0$ or $R^i = 0$ because the pressure jump saturated to the value given by Eq. (2.31) at the nanometer distance from CL, see Figs. 2.18a, 2.20a. In Fig. 2.22a, the pressure jump variation for three different values of x_{min} is shown. One can see that the pressure jump approaches asymptotically the value given by Eq. (2.31) while the boundary condition used is (D.14). The corresponding calculated apparent contact angle is shown in Fig. 2.22b. The apparent contact angle practically does not change when $x_{min} < 10^{-2}$ nm.

Some parametric analysis of results for constant heat load ($\Delta T = 0.5$ K) is presented in Fig. 2.23a, where θ_{app} is plotted versus the slip length for varying interface resistance. Fig. 2.23a clearly demonstrates that nor the slip length neither the interface resistance is essential in the CL singularity relaxation: θ_{app} saturates as they tend to zero. θ_{app} as a function of superheating, calculated with physically reasonable values of R^i and l_s for water at 10 MPa ($R^i k_L = 2$ nm and $l_s = 10$ nm) is shown in Fig. 2.23b.

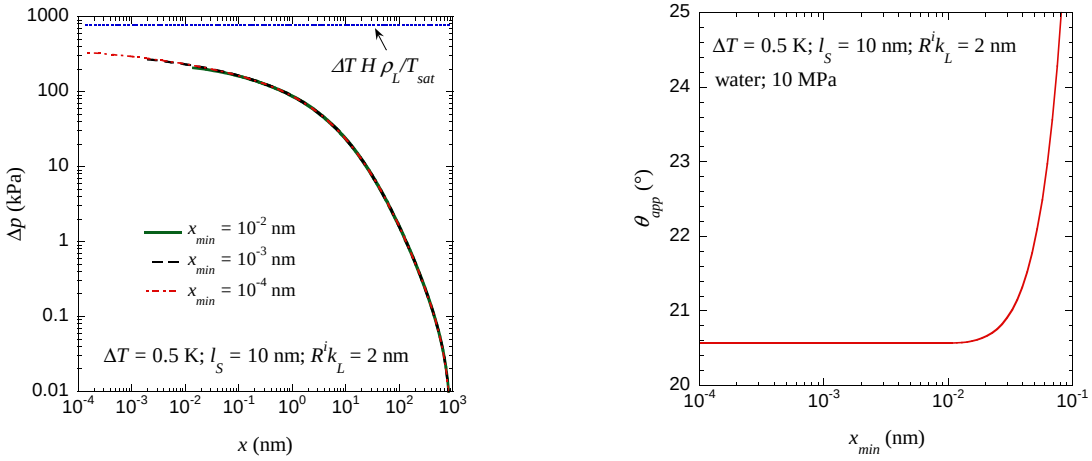

(a) (b)

Figure 2.22: Pressure jump and apparent contact angle for different x_{min}. Calculated for water at 10 MPa, $\Delta T = 0.5$ K and $\theta_{micro} = 15°$. (a) Pressure jump variation. (b) Apparent contact angle.

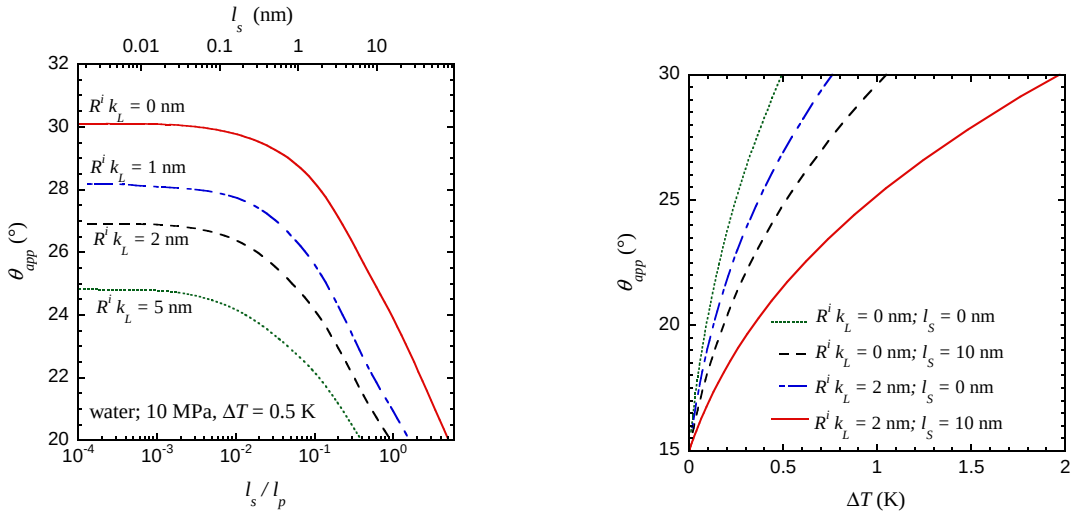

(a) (b)

Figure 2.23: Comparison of calculated θ_{app} for various values of R^i and l_s

2.6.5 Thermocapillary effect

This phenomena is addressed here because the liquid-vapor interface temperature (and surface tension $\sigma(T^i)$) spatially changes, cf. Fig. 2.21a. The gradient of surface tension induces a motion of the liquid through the thermocapillary stress. The value of γ (see Eq. (2.21)) is given by $-\partial\sigma/\partial T$ and thus its value is well defined if the temperature dependence of σ is known for the given fluid. The gradient of temperature along the interface can be expressed as

$$\frac{\partial T^i}{\partial x} = \frac{T_{sat}}{H\rho_L}\frac{\partial \Delta p}{\partial x} + R^i \frac{\partial q_L^i}{\partial x}, \tag{2.112}$$

where the vapor recoil contribution is neglected. From this expression, it is evident that including the R^i term directly impacts the strength of the thermocapillary effect (similarly to complete wetting situation [97]). In Fig. 2.24, the resulting apparent contact angle for FC-72 at 0.04 MPa is

plotted vs. superheating. The impact of the thermocapillary effect on θ_{app} is nearly absent when $R^i = 0$. The impact is however strong when the interface resistance is included (cf. Fig. 2.21a),

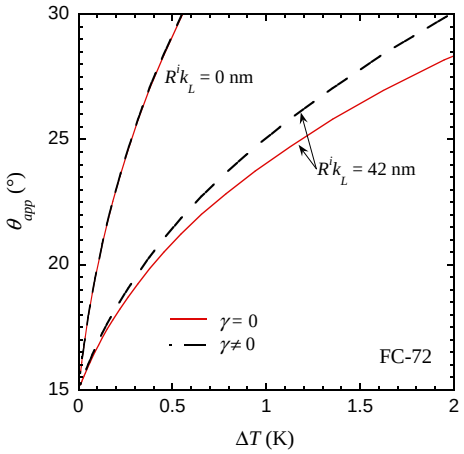

Figure 2.24: a) Comparison of θ_{app} vs. ΔT for FC-72 at 0.04 MPa, $\theta_{micro} = 15°$, $l_s = 0$ calculated for cases including thermocapillary effect and interface resistance.

see Fig. 2.24. For plotted values (FC-72 at 0.04 MPa, $\theta_{micro} = 15°$), $\Delta\theta_{max}/(\theta_{app} - \theta_{micro}) \approx 20$ %, where $\Delta\theta_{max}$ is the maximal difference between the cases $\gamma = 0$ and $\gamma \neq 0$.

2.6.6 Comparison to previous theoretical results

Hocking [103] derived an expression for the apparent contact angle that can be rewritten in the present notation as

$$\theta_{app}^4 - \theta_{micro}^4 = 12 Ca_e \log\left(\frac{\mathrm{e} l_R \theta_{micro}}{2 l_s \theta_{app}}\right), \tag{2.113}$$

where e is the base of the natural logarithm and $Ca_e = \Delta T \mu/(\rho_L \sigma H R^i) \equiv N_e/N_R$ is the "evaporation capillary number" introduced by Morris [5]. Note that ε of Hocking is the height to half-width ratio of the drop, which is equal to $\theta_{app}/2$. The expression of [5] obtained for the complete wetting case had a similar structure,

$$\theta_{app}^4 = 2.2 Ca_e. \tag{2.114}$$

Equations (2.113) and (2.114) can be compared if one assumes that in the latter case $\theta_{micro} = 0$.

Note that Eq. (2.113) cannot apply to the case $l_R < l_s$ which is the water at 10 MPa considered in most of the calculations. While $\theta_{app} > \theta_{micro}$ should hold, the argument of the logarithm turns out to be smaller than one. For this reason, this expression is not applied directly to our results. However, we perform a fit of our data to the equation

$$\theta_{app}^4 - \theta_{micro}^4 = B Ca_e \tag{2.115}$$

and we determine the constant $B \simeq 6$ (see the inset in Fig. 2.10b). This value is closer to that of Morris than to that of Hocking. It changes slightly with θ_{micro}. One can see that, generally, the fit (2.115) is applicable only for the superheating smaller than 100 mK. Note that Morris considered the experimental results of Wayner's group where the superheating was even weaker. Note that both expressions (2.113, 2.114) provide the scaling for apparent contact angle $\sim \Delta T^{1/4}$ which is different from our results (which suggests scaling $\sim \Delta T^{1/3}$), see section 2.3.7. The apparent contact angle calculated numerically from the model including R^i, l_s and γ is plotted vs. wall

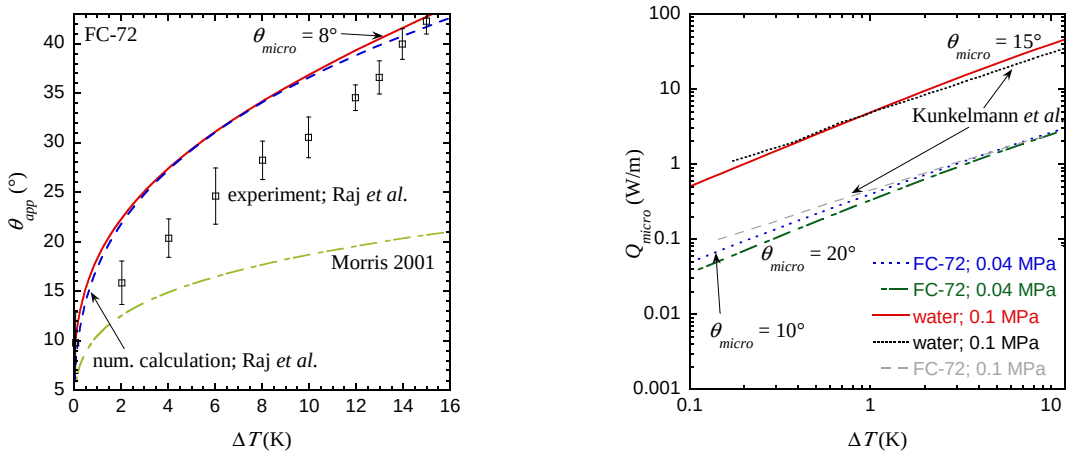

Figure 2.25: a) Apparent contact angle θ_{app} vs. wall superheat calculated for FC-72 at 0.04 MPa ($R^i k_L$ = 42 nm, l_s = 10 nm) and $\theta_{micro} = 10°$ compared with results of [4] and [5], Eq. (2.114) are compared. b) Integrated heat flux calculated from our microregion model for FC-72 at 0.04 MPa and water at 0.1 MPa for different θ_{micro} compared with numerical results of [40] obtained for complete wetting.

superheating in Fig. 2.25a for water at 10 MPa ($\theta_{micro} = 10, 20°$) and FC-72 ($\theta_{micro} = 8°$). The results for FC-72 are compared with those of another research group [1, 4]. The agreement is excellent with data obtained from microregion model [1][3], briefly summarized in introduction, section 1.3.2. Note that results of [4] were calculated with the complete wetting microregion model, where liquid-vapor interface smoothly meets the adsorbed liquid film ($\theta_{micro} = 0°$). In our calculation we used $\theta_{micro} = 8°$ as this value was measured[4] by the authors [4] for FC-72 when $\Delta T = 0K$. The theoretical result of [5],(2.114) is also added in the graph for comparison. The agreement between our results and that of [4] might be due to the fact that for low microscopic contact angle ($\theta_{micro} = 8°$) the length scale related to the Kelvin effect (included in our model and also in [4]) is large (l_K = 59.8 nm) and thus it is the most important phenomenon. Other microscopic phenomena such as slip length or interface thermal resistance are secondary.

Another important quantity is the total heat transferred through the microregion Q, called integrated heat flux. Calculated values of Q for FC-72 at 0.04 MPa (two values of θ_{micro}) and water at 0.1 MPa for θ_{micro} 15° are presented in Fig. 2.25b. These values are compared with results calculated for complete wetting [40]. The results are very close[5]. The integrated heat flux depends on the size of the microregion ($Q(x \to \infty) \to \infty$). In all our calculations, x_{max} = 1μm. We assume that the microregion in [40] is about the same size as it was not explicitly given. The integrated heat flux is higher for small θ_{micro}. The curves for Q vs. ΔT appear to be straight lines in log-log coordinates, see Fig. 2.25b. It means that the function $Q(\Delta T)$ is of the form $Q = a\Delta T^b$. Such a property was used [41] to fit the numerically obtained results.

[3] Numerically obtained results of [1] were fitted by following expression (calculated values were not explicitly shown in [4]) $\theta_{app} = 17.4\Delta T^{0.323}$

[4] This is in fact in contradiction with the model used and measured results as theoretical model considered complete wetting ($\theta_{micro} = 0°$); the authors measured $\theta_{micro} = 8°$. This issue was however not discussed by the authors.

[5] Our data for FC-72 and those of [40] are obtained for different values of pressure.

2.6.7 Conclusion

In this section, numerically calculated results from the minimal complexity microregion model and its extended version including slip length, interface thermal resistance, thermocapillary terms or their combination are presented.

Evaporation in the vicinity of the contact line induces strong liquid flow towards the contact line which causes a pressure drop and the interface curvature. As a consequence, the apparent contact angle increases. The pressure jump attains a maximum (given by (2.31)) at the contact line. The apparent contact angle is attained at a scale $\sim l_K$ (defined by (2.84)), which is the governing length scale for x coordinate. The thermocapillary term has a negligible impact for the minimal complexity microregion model where $l_s = 0$, $R^i = 0$.

With the slip length or interface thermal resistance, the pressure jump attains the asymptotic value at the contact line at a smaller scale comparing to the case $l_s = 0$ or $R^i = 0$. θ_{app} decreases with both l_s and R^i. The heat flux maximum is reduced when $R^i \neq 0$. Inclusion of R^i influences the interface temperature, its variation is shifted to the scales given by $\sim R^i k_L$. R^i influences the impact of the thermocapillary effect (similarly to complete wetting modeling [97]). The latter is quite strong when considered together with large value of R^i. For $\gamma > 0$ it causes an increase of the apparent contact angle.

The dimensionless parameters describing the behavior of the microregion model including l_s and R^i are identified. The asymptotic behavior of θ_{app} is checked numerically in the presence of l_s and R^i. The inclusion of l_s and R^i does not impact the asymptotic expressions for $\theta_{app}/\theta_{micro} - 1$ both for small and large superheatings. They are of the same form as given by Eq. (2.92) for the cases $l_s = R^i = 0$.

When both slip length and the interface thermal resistance are considered, the convergence of the pressure jump to its asymptotic value is slow and obeys the power law (instead of exponential law valid for the case where R^i or l_s is equal to zero, see section 2.3.4).

The apparent contact angle and integrated heat flux are compared to the results from microregion evaporation model for the complete wetting case. The agreement is excellent with the results with the numerical data from [4]. The available experimental data for apparent contact angle are compared also and show reasonably good agreement.

2.7 Extended microregion model

In this section, two extensions of the microregion model presented in section 2.2.4 are introduced: the influence of CL motion and the impact of solid substrate conductivity. Both studies are of importance with respect to the vapor bubble growth simulation. As the CL moves due to increase of the bubble volume (no CL pinning is considered), but also due to increase of the contact angle.

2.7.1 The moving CL case

The idea of extension of the microregion evaporation concept to the moving CL case is attractive for practical applications. The moving CL case was already discussed in sections 2.4 and 2.5.3. In the case of the evaporating liquid wedge is moving, the definition of θ_{app} becomes more difficult. One can expect that at some distance from the CL the impact of evaporation on interface slope is negligible [95]. The problem for $x \to \infty$ is thus equivalent to the case of absence of evaporation. In this case the so called Cox-Voinov law [83] shows that the slope diverges logarithmically if the infinite domain is considered (while the curvature for $x \to \infty$ vanishes). For this reason, the microregion is treated similarly as in sec. 2.5.3. We consider a microregion of a finite size (x_{micro} = 1 μm). Far from the contact line, we impose a finite value of Δp. This value is in practical applications given by the matching to the a macroscopic problem statement [98, 110, 111]. We postulate that Δp in macroregion is much smaller with respect to the characteristic curvature within the microregion Δp_0 and thus we impose $\Delta p(x = x_{micro}) = 0$. This simplifies a comparison of results as the impact of the macroscopic liquid object curvature is eliminated. The influence of CL motion on θ_{app} is illustrated in Fig. 2.26a. The capillary number $Ca = v_{CL}\mu/\sigma$ is presented at the upper axis. The apparent contact angle decreases with v_{CL} ($v_{CL} > 0$ corresponds to the

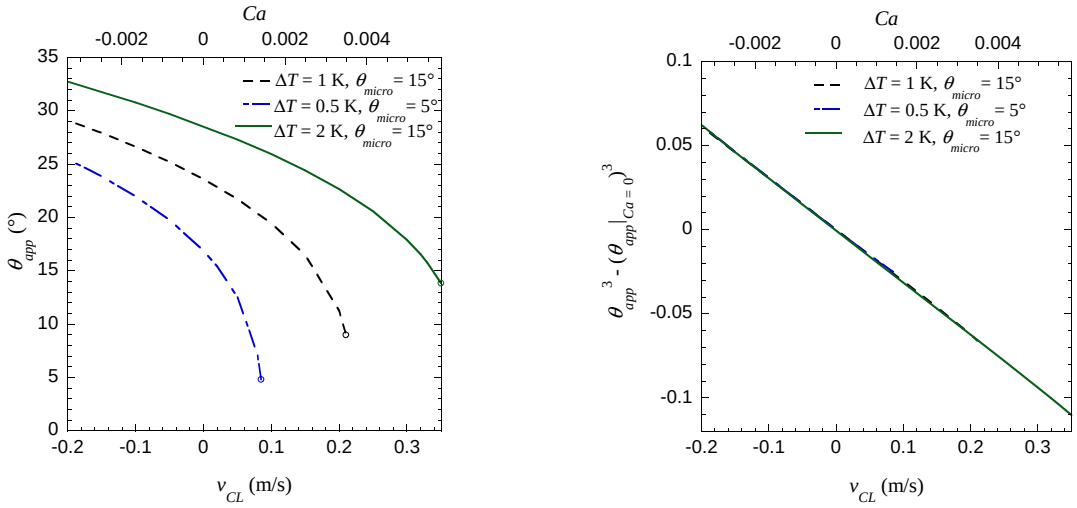

Figure 2.26: Dependencies on the contact line velocity calculated for water at 10 MPa, θ_{micro} = 5, 15°, ΔT = 0.5, 1, 2 K. (a) Apparent contact angle θ_{app} vs v_{CL}. (b) $\theta_{app}^3 - (\theta_{app}|_{Ca=0})^3$ vs v_{CL}.

receding contact line). The apparent contact angle can not be calculated when v_{CL} is above a threshold marked by the circles in Fig. 2.26a. The threshold corresponds to the Landau-Levich (entrainment) transition, which occurs (for isothermal situation [127]) at a finite $v_{CL} > 0$ and a finite θ_{app}. This means that there is no CL stationary solution for larger velocities (and smaller θ_{app}); a continuous liquid film forms behind the receding liquid meniscus. The curves in Fig. 2.26a are very similar to the isothermal case. This evokes the idea to plot data as

$\theta_{app}^3 - (\theta_{app}|_{Ca=0})^3$ vs. Ca (or v_{CL}). Fig. 2.26b shows that all data presented in Fig. 2.26a collapse to a single master curve which is in fact the Cox-Voinov law. The linear fit of data of the form $\theta_{app}^3 - (\theta_{app}|_{Ca=0})^3 = ACa$ results in $A = -18.8$. This value is given by the size of the microregion domain chosen and the Voinov scale, see section 2.4. The latter expression thus provides a very good approximation for apparent contact angle $\theta_{app}(v_{CL})$.

In many systems (e.g. growth of vapor bubble during boiling) the total heat transferred through the microregion

$$Q_{micro} = \int_0^{x_{max}} q_L^i(v_{CL}, \Delta T, x)dx \tag{2.116}$$

is also an important parameter. One can expect that such a quantity will be also strongly influenced by the contact line motion. It was shown in [5] that the major contribution to Q_{micro} is from the part of the microregion, where θ_{app} is nearly[6] established. Note that this scale is for the simplified microregion model (see sec. 2.3.6) defined by l_K. In Fig. 2.27a, Q_{tot} is plotted as a function of the contact line velocity. It is evident that for the CL receding ($\theta_{app}(\Delta T, v_{CL}) < \theta_{app}(\Delta T, 0)$), the total heat transferred through the microregion increases due to a smaller thickness of the liquid layer. The situation is more pronounced for small θ_{micro}, see Fig. 2.27a. In the following, we propose an approximate expression for Q_{micro} which can be used

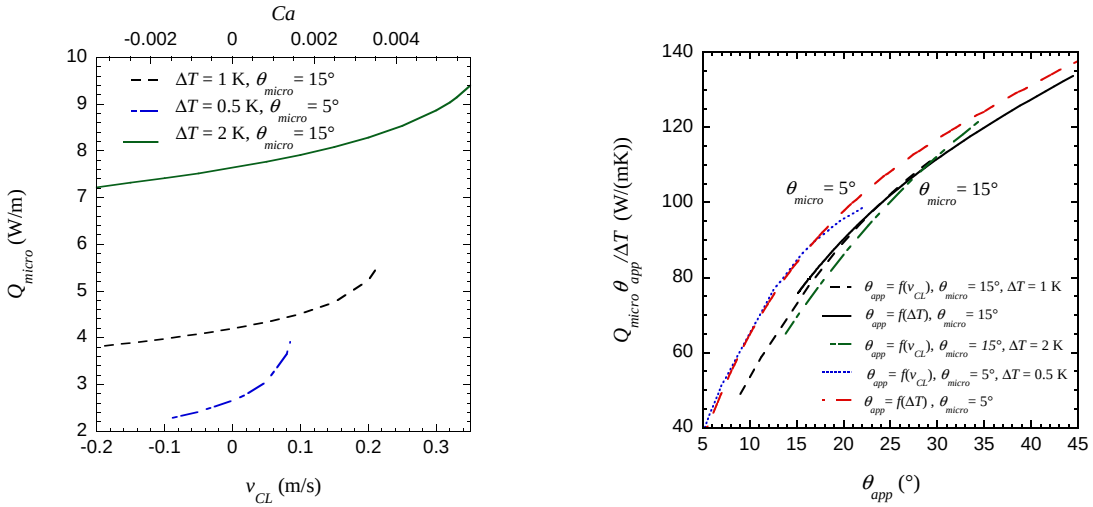

(a) (b)

Figure 2.27: Dependencies on the contact line velocity calculated for water at 10 MPa, $\theta_{micro} = 5, 15°$, $\Delta T = 0.5, 1, 2$ K. (a) Total heat transferred through the microregion Q_{micro} vs v_{CL}. (b) $Q_{micrio}\theta_{app}/\Delta T$ vs v_{CL}.

to estimate quantitatively Q_{micro} for $v_{CL} \neq 0$.

The total heat transferred through the microregion is given by Eq. (2.116) where, for large x, $q_L^i \sim k_L \Delta T/(\theta_{app} x)$. We postulate that the main contribution to Q_{micro} is obtained by integration of the last expression[7] $Q \sim \int_x^{x_{max}} k_L \Delta T/(\theta_{app} x)dx$. The $\Delta T/\theta_{app}$ term is constant and is thus factored out from the integral. In the following step, we say that when Q_{micro} is rescaled by $\Delta T/\theta_{app}$ the data should fall into a master curve. $Q_{micro}\theta_{app}/\Delta T$ as a function of θ_{app} is plotted in Fig. 2.27b, including the values calculated for $v_{CL} = 0$ (e.g. from Fig.

[6] The idea is based on the scale separation and cutting the wedge into inner and outer regions. θ_{app} was determined within the inner region contributing a negligible fraction of total evaporation, while the total transferred heat is mainly given by its contribution at larger scales.

[7] Note that the expression for $q_L^i(x \to \infty)$ is divergent for $x \to 0$ in the nonintegrable manner.

2.25). For small values of superheating (e.g. for water at 10 MPa, $\theta_{micro} = 15°$, $\Delta T = 1$ K) the quantity $Q_{micro}\theta_{app}/\Delta T$ is presented in Fig. 2.27b from calculated values of θ_{app} and Q_{micro} for $v_{CL} = 0$ nearly coincides. Providing thus θ_{app} and Q_{micro} vs. ΔT (e.g. tabulated values) and the slope of the curve in Fig. 2.26b one can get approximative expression for $\theta_{app}(\Delta T, v_{CL})$ and $Q_{tot}(\Delta T, v_{CL})$.

2.7.2 Impact of solid substrate conductivity

In this section, we are interested in the impact of the heater conductivity. For this purpose, the microregion model presented in section 2.2.4 needs to be modified. Instead of the constant temperature of the solid heater, a 2D stationary heat conduction problem in the solid is considered. First, the existence of solution of such a problem is shown. Next, the problem is solved numerically and some representative results are shown and discussed.

The equation

$$\nabla^2 T = 0, \tag{2.117}$$

inside the infinite (along x axis) solid heater of thickness D is solved for the temperature $T = T(x, y)$, see Fig. 2.28. The temperature $T_{sat} + \Delta T$ is imposed at the bottom side of the heater $y = -D$. The second boundary condition is given by (2.7) and relates the temperature T_S and the heat flux q_S at the top of the heater $y = 0$ for $x > 0$. At $x < 0$, zero heat flux condition (2.6) is applied. The boundary conditions at $x \to \pm\infty$ and any $y \in (-D, 0)$ are given by the equation

$$T(x \to \pm\infty, y) = T_{sat} + \Delta T - \frac{q_S(x)}{k_S}(y + D), \tag{2.118}$$

because the temperature is not perturbed by the presence of the contact line. The temperature of the solid-liquid surface of the heater T_S is a function of x coordinate $T_S = T_{sat} + \Delta T(x)$.

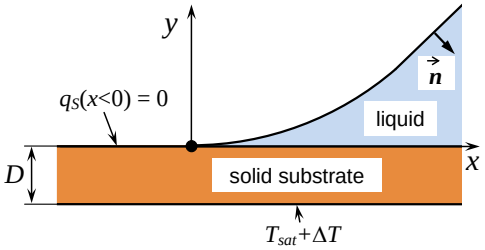

Figure 2.28: Geometry of the solid domain for 2D heat stationary conduction in the solid substrate.

Before solving the solid domain thermal problem numerically, it is necessary to verify if its solution exists. The existence of the solution can be proved by checking the integrability of the Green function $G(x, y)$ that describes a temperature distribution created by a localized heat sink. Indeed, for constant temperature boundary conditions, the solution involves an integral of the Green function [139]. The heat is consumed mainly in the CL vicinity, so that one may perform the analysis by assuming a point heat sink placed at the CL position (Fig. 2.28) and consider only the solid domain. This problem is equivalent that of the 2D Green function $G(x, y)$ for an infinitely long stripe $x \in (-\infty, \infty)$, $y \in (-D, 0)$ with the boundary conditions, at $y = -D$ (imposed temperature),

$$G = 0, \tag{2.119}$$

and at $y = 0$ (imposed heat flux),

$$\frac{\partial G}{\partial y} = 0. \tag{2.120}$$

Such a Green function problem is equivalent to that for an infinitely long stripe $x \in (-\infty, \infty)$, $y \in (-D, D)$ with the boundary conditions $G(y = \pm D) = 0$. When the heat sink is placed at the symmetry plane $y = 0$, the condition (2.120) is satisfied at $y = 0$ automatically. At the upper side of the solid substrate it reads [139]

$$G(x, 0) = \frac{1}{2\pi} \log \left| \frac{\exp(\pi x/2D) - 1}{\exp(\pi x/2D) + 1} \right| \simeq -\frac{1}{\pi} \exp\left(-\frac{\pi x}{2D}\right). \tag{2.121}$$

This function is obviously integrable at $x \to \infty$ and proves the existence of the stationary heat conduction solution.

Note that such a reasoning leads also to the correct answer for the half space domain $y < 0$ ($D \to \infty$ limit of the above problem). The 2D Green function for the infinite space $G(x, 0) = \log(x)$ is not integrable when $x \to \infty$, which signifies the absence of a stationary solution for $D \to \infty$.

When considering the conductive heater, the numerical treatment of the microregion model (see Appendix D) needs to be changed. The constant element Boundary Element Method (BEM) (see Appendix F for short introduction to the method) is used to solve the heat conduction problem in solid. The BEM mesh at the $y = 0$ line is consistent with the liquid domain meshing. The total number of elements for the BEM mesh is $N_f = 500$. The heat conduction problem is converted with BEM to a set of N_f linear equations for the nodal values of temperatures and heat fluxes. These equations are solved simultaneously with the set of discretized Eqs. (D.9 - D.10), where constant ΔT is replaced by $\Delta T(x)$. Note that now the reduced solid temperature is not unity but $(\tilde{T}_S(\tilde{x}) - T_{sat})/\Delta T = \Delta\tilde{T}(\tilde{x})$. For the purpose of numerical calculation a finite x size of the solid domain needs to be used, $20 \cdot D$ was found to be sufficient. Note that for a realistic thickness of the solid heater, e.g. a thin 10 μm metallic foil used in [37], the computational domain is rather large with respect to the microregion characteristic scales e.g. $R^i k_L \sim 2$ nm.

In the following, the conductive substrate (Eqs. (2.117 - 2.118)) is considered, some representative numerical results are presented and the assumption of isothermal heater is evaluated. Two heater materials frequently used in industrial applications are considered: copper (Cu) and stainless steel (ss). In reality, the heat conduction in the heater during the bubble growth is never stationary. In order to avoid solving the transient heat transfer problem, the heater of finite "effective" thickness D_h is chosen. D_h is based on thermal diffusion length, that depends on chosen characteristic time. Such a length can be associated with the thickness of the thermal boundary layer in solid substrate when CL moves. Here we address only the impact of substrate conductivity on the results and for this reason the time scale is arbitrarily chosen as 1 μs , which generates corresponding thickness of the heater ($D_h = D_{Cu} = 10.6$ μm or $D_h = D_{Ss} = 1.94$ μm). The solutions for the same $D = D_{Cu}$ but different conductivities are calculated. The results for the isothermal, copper and stainless steel heaters are compared in Fig. 2.29. θ_{app} calculated for isothermal and cooper heaters are very close. The conductivity of the heater causes a decrease of the apparent contact angle. The relative surface temperatures of the solid heater are compared in Fig. 2.29b. The temperature of cooper heater is nearly unaffected by the intensive evaporation in the vicinity of CL at $x = 0$ (this trend holds even for larger values od D). The temperature variation is steeper along the dry solid surface ($x < 0$). Notice significant decrease of temperature close to CL for thick stainless steel heater (up to 50% of its value far from CL). From the insert in Fig. 2.29b it is evident that the temperature varies at a scale much larger

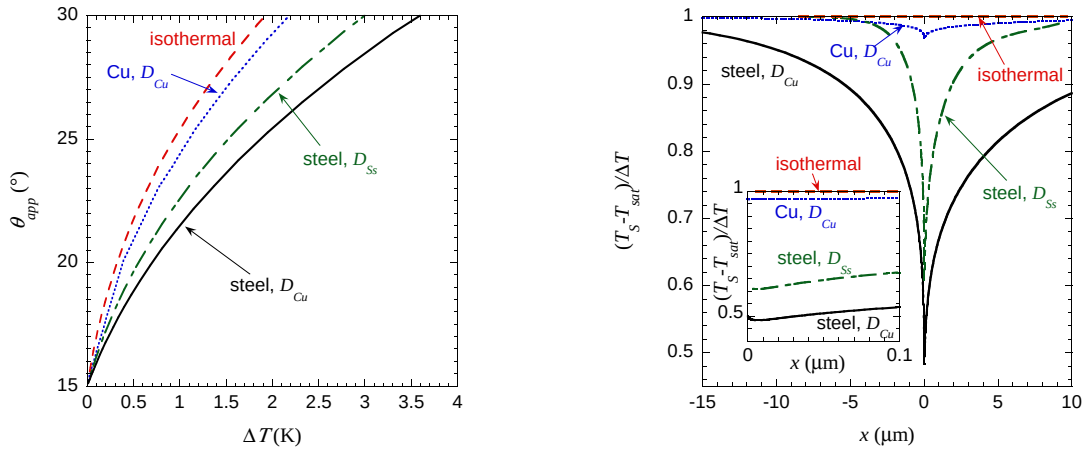

Figure 2.29: Calculated results for isothermal heater, copper heater with $D = D_{Cu}$, stainless steel heater with $D = D_{Ss}$ and $D = D_{Cu}$ wall, water at 10 MPa with $\theta_{micro} = 15°$. a) θ_{app} vs. ΔT a) θ_{app} vs. ΔT. b) Dimensionless temperature along the solid heater for $\Delta T = 2.5$ K.

than the characteristic scales of microregion like l_K. The isothermal heater consideration is thus a good approximation for metal heaters. Similar conclusion was made e.g. by Morris [95] who performed an analogous study for the complete wetting microregion model. He states that when $k_L/k_S \ll 1$ (for water at 10 MPa $k_L/k_{Cu} = 0.0015$ and $k_L/k_{ss} = 0.037$), the isothermal heater is a good approximation. The temperature variation along the heater is resolved at large scale in [140].

2.7.3 Conclusion

First, we studied the impact of the CL motion on the apparent contact angle and the integrated heat flux. We demonstrated that the evaporation is a phenomenon localized at the CL. The general tendencies of θ_{app} observed for the moving CL in isothermal systems remain the same for the evaporation case. The apparent contact angle can be well approximated by the Cox-Voinov law: $\theta_{app}^3 = (\theta_{app}|_{Ca=0})^3 + ACa$, where A is constant for the given fluid and size of the microregion. An approximative expression for the integrated heat flux leads to a convergence of the results to a mastercurve. For moderate Ca and superheating values the proposed approximation for Q_{micro} provides a good approximation.

In the second part of this section, the impact of solid heater conductivity is discussed. The model extended for conductive heater is solved numerically. The results were calculated for water at 10 MPa and two material parameters (copper, stainless steel). The representative results are shown, however the author is aware that more systematic study of this problem needs to be preformed in order to provide more general conclusion related to this problem. The results are however consistent with those of [95]. The apparent contact angle grows with the heater conductivity because of the decrease of the heater thermal resistance.

2.8 High slopes of the interface

In this chapter the microregion model is extended to high slopes of interface. Such a feature is needed in order to apply the microregion model to the vapor bubble simulation presented in chapter 3. In the following, the equations describing the microregion are rederived for high slopes. Some representative results are exposed at the end of this section.

2.8.1 Extension of lubrication theory to account for high interface slopes

A correction to the lubrication theory of evaporating meniscus has been derived by Mathieu [45] and follows the original idea of Voinov [106] used by Boender *et al.* [141] applied to the isothermal CL dynamics. The theory introduced in [141] was rederived recently [142]. The approach is based on the analytical solution of the 2D Stokes flow problem in the straight wedge with the liquid sink U placed at its apex (CL position), see Appendix E. The wedge opening angle is ϕ. The boundary conditions mimic the real CL evaporation free-interface problem statement evaluated far from CL, where the slope is large. The evaporation is assumed to be localized at small scales and is modeled by the liquid sink. The flow is directed to CL where the liquid is evaporated. The boundary conditions reflect (i) the impermeability of the solid substrate $y = 0$, with no hydrodynamic slip, (ii) the impermeability of the liquid-gas interface with zero tangential stress at it. The solution to such a problem in terms of the stream function is described in Appendix E.3. The corresponding solution for the liquid pressure at the interface reads

$$\frac{dp_L}{dr} = U\frac{\mu}{r^3}\frac{4}{\phi\cos 2\phi - \cos\phi\sin\phi}, \tag{2.122}$$

where r is the distance to the wedge apex.

Consider now the curved interface with a small curvature. The main assumption [141] is that the local liquid flow is equivalent to that of the straight wedge with the opening angle corresponding to the local slope ϕ of the interface (see Fig. 2.30). The local pressure variation

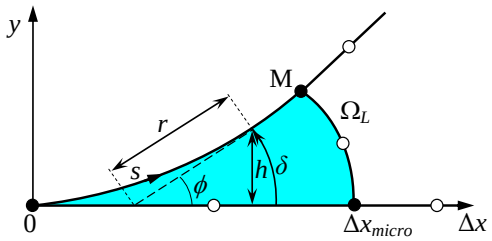

Figure 2.30: A sketch of the liquid part of the microregion (colored). The BEM nodes (see chapter 3) at the boundaries with macroregion are shown with the open circles. The arc length δ, meniscus height h, local wedge coordinate r and local slope angle ϕ are shown for the point M.

dp_L/ds at the liquid-gas interface can be obtained from Eq. (2.122) where ϕ is now a function of s. The identity $r = \delta/\phi$ leads to the expression

$$\frac{dp_L}{ds} = -U\mu\frac{3}{\delta^3}G, \tag{2.123}$$

where

$$G = -\frac{\phi^3}{3}\frac{4}{\phi\cos 2\phi - \cos\phi\sin\phi} \tag{2.124}$$

is the correction to the conventional lubrication approximation. Indeed, $G(\phi \to 0) = 1$. Rather than using the liquid layer height h as the main variable (conventional in the standard lubrication approximation) we operate with the arc length δ. This replacement is based on the fact that such a substitution itself (with $G = 1$) provides more precise results[8] in the wedge shaped domains (for slopes higher than $\sim 35°$, which is the validity limit conventionally accepted in the standard lubrication approximation) in the domains of the wedge shape. Such a theory results in the following final expression for the volume flux $U(s)$ flowing through the section of the liquid film confined between the heated substrate and the gas-liquid interface,

$$\mu G(\phi) U = \frac{d\sigma}{ds}\left(\frac{\delta^2}{2} + \delta l_s\right) + \left(\frac{\delta^3}{3} + \delta^2 l_s\right)\frac{d\Delta p}{ds}, \tag{2.125}$$

where the identity $d\Delta p/ds = -dp_L/ds$ was used and the CL is assumed to be immobile. Similarly to Delon *et al.* [127], the slip length was added to Eq. (2.125) without modifying G. We added the thermocapillary effect to Eq. (2.125) also without modifying (2.124). An attempt to obtain the correction of the thermocapillary term similar to (2.124) was made, see Appendix E. However, an extended study is needed to finalize such a task (e.g. to perform a similar to [45] comparison with 2D calculation of the liquid flow in the wedge).

Similarly to the section 2.2.2, the following steps are performed. By using the fluid mass conservation law, U can also be expressed via the mass evaporation flux J at the gas-liquid interface (assumed positive at evaporation),

$$U = -\frac{1}{\rho_L}\int_0^s J ds, \tag{2.126}$$

which can be rewritten as

$$\frac{dU}{ds} = -\frac{J}{\rho_L}, \tag{2.127}$$

where J is obtained from the heat transfer part of the microregion problem discussed later in this section.

The gas-liquid interface shape in the microregion is defined by Eq. (2.22) where $\Pi = 0$. The curvature expression comes from its geometrical definition

$$K = \frac{d\phi}{ds} \tag{2.128}$$

while another differential equation links δ and ϕ,

$$\frac{dh}{ds} = \sin\phi, \quad h = \delta\frac{\sin\phi}{\phi}. \tag{2.129}$$

Similarly to microregion model presented in Appendix D, the "one-sided" [77] approximation is considered. The relation for the liquid-vapor interface temperature is based on the linearized Clausius-Clapeyron relation enhanced for the interfacial resistance R^i (Eq. (2.4) where the vapor recoil contribution is neglected). The heat conduction in microregion is considered to be stationary due to the small thermal inertia of the microregion liquid wedge. The temperature distribution is postulated to be linear along the arc length δ (see Fig. 2.30) as suggested by the rigorous thermal analysis of the straight wedge [100],

$$q_L^i = k_L\frac{T_{sat} + \Delta T - T^i}{\delta}. \tag{2.130}$$

[8] For the detailed derivation and comparison with numerical simulations see [45].

Like in [1, 2, 43], the variation of the heater temperature in the vicinity of the CL is neglected and ΔT is a parameter.

Since the vapor heat conductivity is neglected, the interfacial heat balance reads $q_L^i = HJ$. By combining it with Eqs. (2.4, 2.130), one obtains

$$J = \frac{k_L}{H}\frac{\Delta T - \Delta p T_{sat}/(H\rho_L)}{R^i k_L + \delta}, \tag{2.131}$$

which closes the system of Eqs. (2.22, 2.125, 2.127 - 2.129).

This set of ODE's is of the fourth order and requires thus four boundary conditions. In the partial wetting case considered here, two of them are geometrical constraints defined at the CL,

$$\begin{aligned} \delta(s \to 0) &= 0, \\ \phi(s \to 0) &= \theta_{micro}. \end{aligned} \tag{2.132}$$

The third is the matching of the microregion pressure jump at $s = s_M$ with its macroregion value, as demonstrated by the bubble growth case discussed in the next chapter (see Fig. 3.1b). By using the fact that the pressure jump in the macroregion σ/R is usually negligibly small with respect to its value in the vicinity of CL, the condition

$$\Delta p(s_M) = 0 \tag{2.133}$$

is applied. The microregion size $\Delta x_{micro} \simeq s_M$ (cf. Fig. 2.30) is determined by the criterion that its influence on the apparent contact angle $\theta_{app} = \arctan u(s_M)$ is negligible (within the given precision). This criterion can always be satisfied because the the meniscus slope tends to θ_{app} as $s \to \infty$.

The fourth boundary condition is the finite pressure at CL that follows from (2.31) and its equivalent formulation in s coordinate is

$$\Delta p(s \to 0) = \frac{H\rho_L \Delta T}{T_{sat}}. \tag{2.134}$$

In practice, the following equivalent condition (cf. Eqs. (2.38, D.14)), is used instead:

$$s\frac{d\Delta p}{ds}\bigg|_{s\to 0} = 0. \tag{2.135}$$

2.8.2 Model reduction

Similarly to the Appendix D, l_s, σ/l_s and ΔT are used to make lengths, pressures and temperatures non-dimensional. By combining Eqs. (2.24, 2.125, 2.127 - 2.129) the following three differential and one algebraic equations can be written

$$\frac{\partial}{\partial \tilde{s}}\left\{-\frac{N_R N_M}{G(\phi)}\left(\frac{\tilde{\delta}^2}{2}+\tilde{\delta}\right)\frac{\partial \tilde{J}}{\partial \tilde{s}} + \left[\frac{\tilde{\delta}^3}{3} + \tilde{\delta}^2\left(1 - \frac{N_p N_M}{2}\right) - N_p N_M \tilde{\delta}\right]\frac{1}{G(\phi)}\frac{\partial \Delta\tilde{p}}{\partial \tilde{s}}\right\} = -N_e \tilde{J}, \tag{2.136}$$

$$\frac{\partial \phi}{\partial \tilde{s}} = \Delta\tilde{p} + N_r \tilde{J}^2, \tag{2.137}$$

$$\frac{d\tilde{h}}{d\tilde{s}} = \sin\phi \tag{2.138}$$

where

$$\tilde{J} = \frac{1 - \Delta\tilde{p} N_p}{N_R + \tilde{\delta}}, \quad \tilde{h} = \tilde{\delta}\frac{\sin\phi}{\phi}$$

is the dimensionless evaporation mass flux and the relation that links h with δ (note that $\partial\tilde{s}/\partial\tilde{x} = 1/\cos\phi$). The tilde is used here to denote the reduced variables.

For convenience of the reader the definition of the dimensionless parameters are repeated here, but in principle they are the same as in the Appendix D. $N_r = q_l^2 l_s/(\rho_V H^2\sigma)$ is the parameter that measures the impact of the recoil force, $N_M = \gamma\Delta T/\sigma$ is the Marangoni number, $N_e = \mu k_L \Delta T/(\rho_L \sigma H l_s)$ characterizes the influence of evaporation on the interface shape, and $N_R = R^i k_L/l_s$ is the dimensionless interfacial resistance. The parameter $N_p = \sigma T_{sat}/(\Delta T H \rho_L l_s)$ can be seen as a ratio of two characteristic pressure scales: a capillary pressure scale σ/l_s and the pressure $\Delta T H \rho_L/T_{sat}$ that measures the strength of the Kelvin effect. For completeness, the boundary conditions (2.132 - 2.133) and (2.135) are rewritten here for the dimensionless variables

$$\tilde{\delta}|_{\tilde{s}\to 0} = 0, \tag{2.139}$$

$$\phi|_{\tilde{s}\to 0} = \theta_{micro}, \tag{2.140}$$

$$\Delta\tilde{p}|_{\tilde{s}=\tilde{s}_M} = 0, \tag{2.141}$$

$$\tilde{s}\frac{\partial\Delta\tilde{p}}{\partial\tilde{s}}|_{\tilde{s}\to 0} = 0. \tag{2.142}$$

Similarly to the microregion model presented in section 2.2.4, solving Eqs. (2.136 - 2.142) in the present form would lead to difficulities[9] related to the smallness of coefficients at the highest derivatives. In order to avoid (or at least reduce) this difficulty the variable change (D.7 - D.8) was used, see the following section. The numerical implementation is thus very similar to treatment of microregion model discussed in Appendix D. The constant size of the microregion was chosen by keeping $s_M = 1$ μm throughout the calculation. This is sufficient to find θ_{app} within $1-2$ % accuracy.

Eqs. (2.136) and (2.142) are rewritten here in a form used in the computational code. The equations (2.136) and (2.142) were rewritten in terms of $\tilde{h}$ and x and thus the variable change (D.7 - D.8) was used

$$\tilde{J}\left(N_R + \frac{\phi\chi e^{\zeta}}{\sin\phi}\right) + N_p\Delta\tilde{p} = 1, \tag{2.143}$$

$$\frac{\partial}{\partial\zeta}\left(e^{\zeta}\frac{\partial\chi}{\partial\zeta}\right) = e^{2\zeta}(\Delta\tilde{p} + N_r\tilde{J}^2)\left[1 + \left(\chi + \frac{\partial\chi}{\partial\zeta}\right)^2\right]^{3/2}, \tag{2.144}$$

$$\frac{\partial}{\partial\zeta}\left(B\frac{\partial\Delta\tilde{p}}{\partial\zeta} - A\frac{\partial\tilde{J}}{\partial\zeta}\right) = -N_e\tilde{J}\frac{e^{\zeta}}{\cos\phi}, \tag{2.145}$$

where

$$B = [\chi^2 e^{2\zeta}\phi^2/(3\sin^2\phi) + \chi e^{\zeta}\phi(1 - N_p N_M/2)/\sin\phi - N_p N_M]\chi\phi/(\sin\phi G(\phi)),$$
$$A = \chi N_R N_M[\chi e^{\zeta}\phi^2/(2\sin\phi) + \phi]/(G(\phi)\tan\phi),$$

and $\tan\phi = \partial h/\partial x$. The boundary conditions are

$$\left.\frac{\partial\chi}{\partial\zeta}\right|_{\zeta\to-\infty} = 0, \quad \chi|_{\zeta\to-\infty} = \theta_{micro}, \tag{2.146}$$

$$\left.\frac{d\Delta\tilde{p}}{d\zeta}\right|_{\zeta\to-\infty} = 0, \quad \Delta\tilde{p}|_{\zeta=\zeta_M} = 0, \tag{2.147}$$

[9] The matrix generated after discretization would contain small diagonal elements, cf. Eq. (2.139).

The equations (2.143 - 2.145) are discretized in the same way as in Appendix D and for this reason the procedure is not repeated here. The only difference lies in the implementation of boundary condition (2.147b). The size of microregion in ζ units (the boundary condition (2.147b) is implemented at ζ_M) is calculated iteratively in order to keep $s_M = 1$ μm. The simplest Newton-Raphson iterative method was used, four iteration give 0.5 % accuracy for ζ_M.

2.8.3 Results for high interface slopes

A numerical results from microregion CL model extended for high interface slopes are presented and discussed in this section.

In most of the calculated cases the material parameters for water at 10 MPa and FC-72 at 0.04 MPa are used. Unless mentioned specifically, $l_s = 10$ nm and interface resistance R^i is calculated from Eq. (1.13) for the corresponding fluid.

In order to reach high values of apparent contact angle, high heat load (imposed superheating ΔT) is needed. Under such conditions several assumptions introduced at the beginning of this chapter might be violated (e.g. one sided approach, constant temperature of solid within the microregion, etc.). For this reason one has to put a reserve on the results for $\theta_{app} > 40°$, which can be also interpreted as the robust extrapolation of the small θ_{app} data. The results are however coherent with those of another research group [4, 40] for $\theta_{app} < 40°$, see Fig. 2.32a.

The pressure jump variation along the liquid wedge (along s coordinate, see Fig. 2.30) is shown in Fig. 2.31a for two superheatings, $\Delta T = 10$ and 25 K. Such heat loads result in corresponding apparent contact angles 50° and 74° respectively. The pressure jump variation

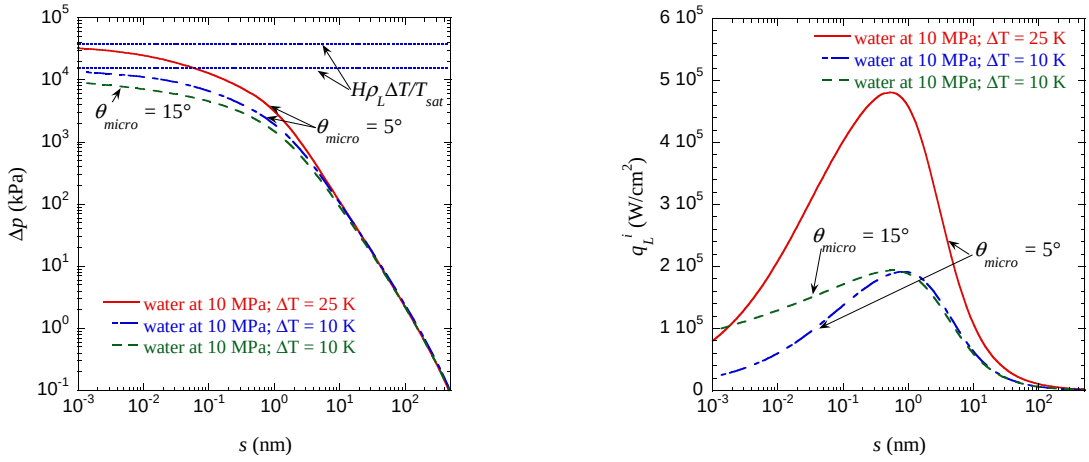

(a) (b)

Figure 2.31: Pressure jump and heat flux variation along the liquid-vapor interface for water at 10 MPa and two microscopic contact angles $\theta_{micro} = 5°$ and 15°. (a) Pressure jump variation. (b) Heat flux variation.

along the wedge shows the saturation of pressure for $x \to 0$ to the asymptotic value given by Eq. 2.134 (shown by blue dotted lines). The pressure jump saturates slower with increase of θ_{micro}. This behavior also explains a slower decrease[10] of the local heat flux at the liquid-vapor interface in Fig. 2.31b as $x \to 0$ for $\theta_{micro} = 15°$ with respect to the curve for $\theta_{micro} = 5°$. We verified that the apparent contact angle does not change if x_{min} is chosen to be smaller (by two orders) then the smallest physical scale of the problem (l_R, l_s or l_l). When increasing this value, a similar to

[10] The local heat flux (as well as mass evaporation flux J) goes to zero when Δp attains a value given by Eq. (2.134).

Fig. 2.22 behavior is obtained. Even for a small value of microscopic contact angle (e.g. θ_{micro} = 5°), the microregion model calculation is robust enough to calculate apparent contact angles close to 90° (more precisely, $\leq$ 89.5°).

The apparent contact angle θ_{app} and the integrated heat flux Q_{micro} are plotted vs. superheating in Fig. 2.32. The presented results are used in bubble growth numerical simulation in chapter 3. The data of another group [4] calculated and measured for FC-72, are included for comparison. The agreement is excellent. One can notice that for the same value of superheating, the total heat transferred through microregion is nearly one order higher than for FC-72. This is in agreement with results of [40] and [41] (see Fig. 2.25b for comparison). Physically the high value of the latent heat is responsible for such a difference. Smaller microregion contact angle results in higher value of Q. This is caused by smaller thermal resistance of liquid layer near CL (where θ_{micro} is imposed).

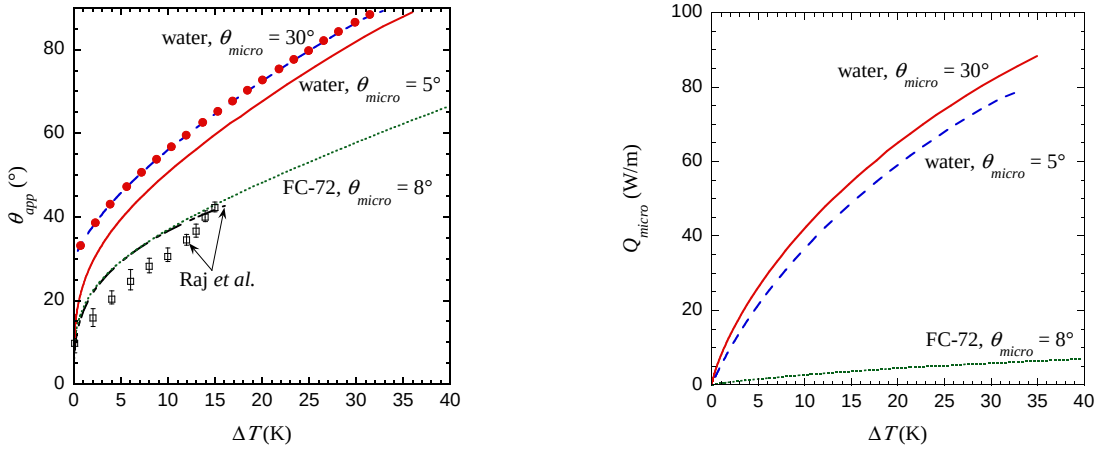

(a) (b)

Figure 2.32: Results for water at 10 MPa and two values of θ_{micro}. The curve for FC-72 at 0.04 MPa and θ_{micro} = 8° is compared to the results [4, 40]. (a) Apparent contact angle, (b) Total heat transferred through the microregion for s_M = 1 μm.

Important question is related to the significance of the vapor recoil effect as the local heat flux is expected to be very high. The vapor recoil effect impacts the microregion through two aspects. First, it may influence the liquid vapor interface temperature (see Eq. 2.4) and second, the vapor recoil term is present in the interface pressure balance (2.137). The impact of the vapor recoil term in the expression of the interface temperature is checked to be negligible. Note that the second term in the right side of Eq. (2.9) (appearing because of the vapor recoil) is proportional to H^{-4} so as expected from dimensional analysis its contribution is negligible. The demonstrative calculation including this term for water at 10 MPa, θ_{micro} = 30° is shown in Fig. 2.32a (the red points). The curve coincides with the blue dashed line calculated without this term. Such a result was observed for all calculations (water, FC-72).

The study of the impact of the vapor recoil term on the interface pressure balance is presented next. The vapor recoil contribution represents the second term in the right side of Eq. (2.137). The increase of apparent contact angle can be expressed as

$$\Delta\theta = \theta_{app} - \theta_{micro} = \overbrace{\int_0^{s_{max}} \Delta\tilde{p} ds}^{\text{A}} + \overbrace{\int_0^{s_{max}} N_r \tilde{J}^2 ds}^{\text{B}}, \tag{2.148}$$

where the first term A represents the integral contribution that results from hydrodynamics and

the second term B the contribution due to vapor recoil. The term A is a linear functional of J while the term B contains J^2. This suggests that with the increasing heat load the relative contribution of B increases. In Fig. 2.33, B/$\Delta\theta$ as a function of ΔT is plotted. With increas-

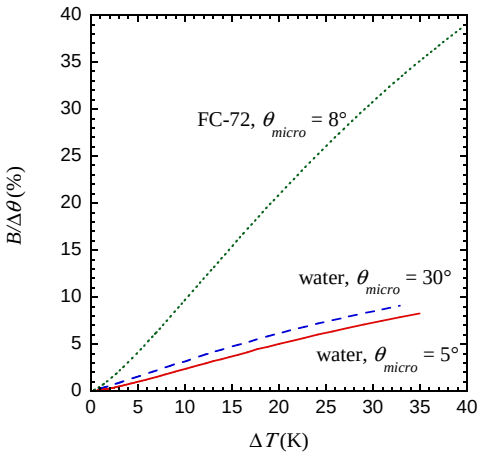

Figure 2.33: Contribution of vapor recoil to θ_{app}.

ing ΔT the importance of B contribution indeed increases. The significant difference in the B contribution is found between water and FC-72. This is caused by large difference between the values of latent heat of water and FC-72. Note that the parameter N_r which characterizes the impact of the vapor recoil is inversely proportional to H^2, cf. Eq. (D.2).

It was found that the impact of vapor recoil pressure on interface temperature is insignificant. However, the vapor recoil term included in the force balance equation (2.137) at the interface is important. By comparing results for water and FC-72, a higher importance of this therm for liquids with smaller value of latent heat was shown.

2.8.4 Conclusion

In this section the microregion model based on the lubrication theory, extended for large interface slopes was presented. Such an approach was already used in the microregion model for the complete wetting case by Mathieu [45]. Here, the version for the partial wetting case is presented. The algorithm is robust and even for small imposed microscopic contact angle, the calculation of apparent contact angle up to nearly 90° turns out to be possible.

Chapter 3

Vapor bubble growth during boiling

Contents

In this chapter, a two dimensional numerical simulation of the growing vapor bubble during boiling is presented and discussed. The purpose of this chapter is to show continuity with the research approach presented in [54] and overcome some of its limitations. In the latter publication, a numerical study of the vapor bubble growth illustrated in Fig. 3.1 was presented. The study relied on the hypothesis that the vapor recoil is the only mechanism of the apparent angle formation. The hydrodynamics was absent and the liquid vapor interface was isothermal at T_{sat}. In other words, the microregion was absent and only a macroregion simulation has been performed. The local heat flux was calculated from the transient heat conduction problem in the solid and liquid domains. Heat was produced by the volume source in the solid. The local heat flux (and thus the vapor recoil pressure as well, cf. Eq. (1.24)) at the vapor bubble foot was divergent. In order to make the total force exerted by the vapor recoil effect finite, the local heat flux was limited by the maximum theoretical heat flux resulting from the molecular kinetics theory [22]. The spreading of a vapor bubble induced purely by the vapor recoil effect was observed. The gravity vas absent. The apparent contact angle increased due to vapor recoil which scales as q_{local}^2. The vapor bubble size growth scales like q so that at some threshold heat load (associated with q_{CHF}) the vapor recoil caused the bubble spreading. The objective of this chapter is to couple a realistic model developed above with a macroregion numerical simulation in order to check if the same vapor bubble spreading tendency is detected. The microregion model presented in the section 2.8.1 is used in this simulation. The primary interest of such a calculation is to show the impact of the intensive evaporation near CL on the bubble growth dynamics. The triggering mechanisms of the boiling crises under high pressure due to bubble spreading is proposed and the critical heat flux (CHF) is analyzed as a function of the gravity

level and of the contact angle. One of the important problems is the bubble departure criterion. This issue is addressed in the section 3.3.

3.1 Problem statement

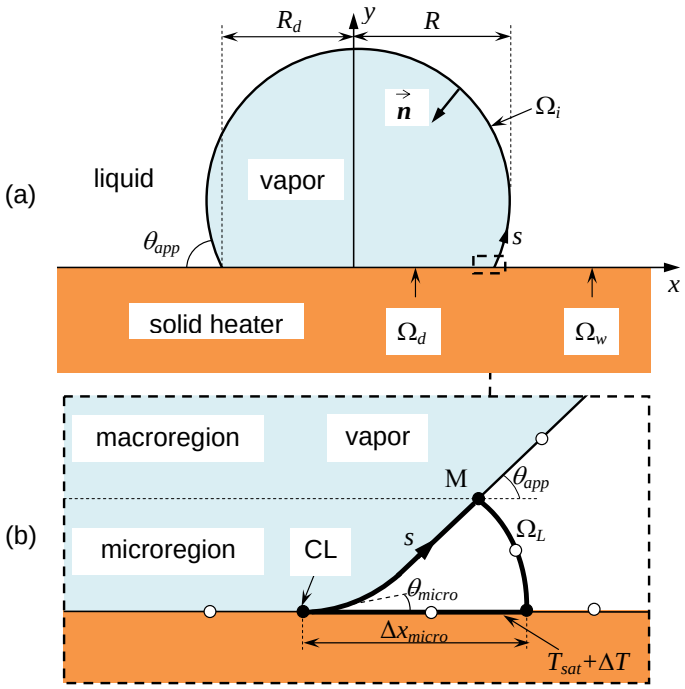

Figure 3.1: Vapor bubble on the heater surrounded by liquid. The macroregion (a) and the microregion (b) are shown.

The shape of the vapor bubble (and the dry spot formed on the heater underneath) depends on its apparent contact angle, i.e. that defined at a scale comparable to the bubble size. This scale is called hereafter "macroscopic" to distinguish it from the microscopic scale of the contact line (CL) phenomena. The apparent contact angle is well known (see chapter 2) to grow with the heater temperature. The boiling crisis scenario developed here can be outlined as follows. At low heat fluxes the apparent angle is low, the bubble grows and departs. At some heat flux the apparent contact angle may attain 90° during the bubble growth. From theoretical considerations, this event is very important for several reasons. First, the dry area attains its maximum value with respect to the bubble size which leads to the heater temperature rise. Second, the bubble adhesion to the heater increases which facilitates the bubble coalescence. Third, and the most important, the dry areas under bubbles coalesce at the very moment of bubble coalescence, which leads to the fast heater temperature increase. All these reasons suggest that the triggering of BC occurs when θ_{app} becomes to be close to 90° before bubble departs. Therefore we postulate that CHF corresponds to a situation where θ_{app} attains 90° at the moment of the bubble departure. The CHF will be determined from this criterion by simulation under some assumptions and its dependence on the system parameters will be studied.

In order to demonstrate and qualitatively describe such a phenomenon, a numerical simulation of a single bubble growth at boiling is performed. The difficulty of such a task is its multiscale nature: the scales ranging from mm (bubble size) to nm (microscopic scale of the CL phenomena) need to be solved. Following [1], the computational domain is decomposed into two parts: (i)

the macroscopic domain (bubble scale) called macroregion and (ii) a region of vapor and liquid in the vicinity of the bubble CL called microregion. The problems in these two regions are solved separately and coupled with an iterative procedure.

3.1.1 Macroregion

We consider the growth of a vapor bubble with free interface attached to the semi-infinite ($y < 0$) solid heater in the semi-infinite ($y > 0$) liquid domain in 2D, see Fig. 3.1. Since the bubble is symmetrical, only a half of the whole domain at $x > 0$ may be considered.

3.1.1.1 Thermal part of the problem

The heat transfer due to convection and radiation is neglected in this model problem; only the heat conduction in the liquid is accounted for. This corresponds to the slow bubble growth at high pressures and at low gravity level. It allows us using the BEM which simplifies this problem *a priori* complicated because of the free bubble interface. The vapor is assumed to be nonconducting. Because of the absence of the hydrodynamic motion in the macroregion, the pressure is uniform both in the vapor and in the liquid. In the macroregion, the bubble interface is isothermal at T_{sat}.

A spatially homogeneous inside the solid volume heating (e.g. by the electric current) is considered. The transient heat conduction equations for the solid and liquid domains,

$$\frac{\partial T_S}{\partial t} = \alpha_S \nabla^2 T_S + \frac{\alpha_S}{k_S} j(t), \quad y < 0 \tag{3.1}$$

$$\frac{\partial T_L}{\partial t} = \alpha_L \nabla^2 T_L, \quad y > 0 \tag{3.2}$$

will be solved. The boundary and initial conditions are like in [54]:

$$T_L|_{t=0} = T_{sat}, \tag{3.3}$$

$$T_L|_{\Omega_i} = T_{sat}, \tag{3.4}$$

$$q_S = -k_S \frac{\partial T_S}{\partial y}|_{y=0} = \begin{cases} -k_L \frac{\partial T_L}{\partial y} & \text{at } \Omega_w \\ 0 & \text{at } \Omega_d \end{cases}, \tag{3.5}$$

$$T_S|_{\Omega_w} = T_L|_{y=0}, \tag{3.6}$$

$$T_S|_{t=0} = T_{sat}. \tag{3.7}$$

A case of saturated boiling is considered, which means that the temperature in the liquid far from the heater is T_{sat}, the saturation temperature for the given system pressure. The homogeneous initial temperature T_{sat} is assumed both in the solid and in the liquid. The temperature and heat flux continuity boundary conditions are imposed at the remaining macroregion boundaries. They include the macroregion part of the solid-liquid interface and two parts of the boundary with the microregion. The temperature $T_{sat} + \Delta T$ and the heat flux are matched at the solid-liquid portion of the boundary with the microregion (cf. Fig. 3.1). The heat flux integrated over this portion is equal to Q_{micro}, cf. Eq. (3.29) below.

Following [54], the volume heat supply in the solid phase is chosen in the form $j(t) \sim t^{-1/2}$, which results in the time constant heat flux $q(x \to \infty, y = 0)$ denoted q_0 hereafter. This particular

choice will allow us avoiding the influence of the varying heat flux on the bubble growth; q_0 can be used as the control parameter. It can be shown that

$$T_S(x \to \infty, y = 0) = T_{sat} + \frac{2q_0}{k_L}\sqrt{\frac{\alpha_L t}{\pi}}, \tag{3.8}$$

see Appendix G, which contains full analytical solution for temperatures $T_S(x \to \infty, y)$ and $T_L(x \to \infty, y)$.

3.1.1.2 Vapor bubble dynamics

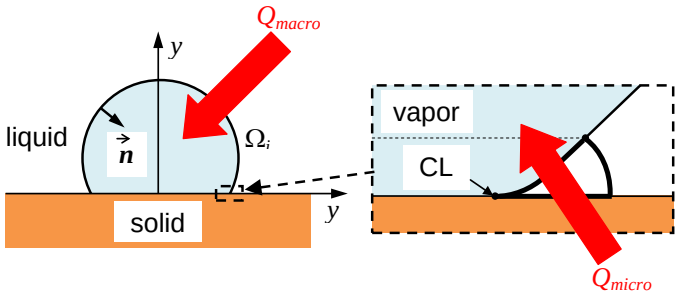

Figure 3.2: Vapor bubble on the heater surrounded by liquid with indicated two considered heat flux contributions Q_{macro} and Q_{micro}.

The bubble growth is controlled by the supplied to it heat

$$H\rho_L \frac{dV}{dt} = Q_{macro} + Q_{micro}, \tag{3.9}$$

where $Q_{macro} = \int_{\Omega_i} q_L^i d\Omega$; $q_L^i = -k_L \partial T_L/\partial \vec{n} \equiv -k_L \vec{n} \cdot \nabla T_L$ is the local heat flux defined at the macroregion part Ω_i of the gas-liquid interface, see Fig. 3.2.

The bubble interface is free and is defined at each time moment by the normal interface stress balance Eq. (2.22), to which the buoyancy force needs to be added and disjoining pressure excluded since the length scale under consideration is large now,

$$K\sigma = (\rho_L - \rho_V)gy + \Delta p. \tag{3.10}$$

In the macroregion the liquid flow and the vapor recoil force are both neglected, which corresponds to the quasi-static approximation [54]; thus the value of Δp is constant. This value is obtained by using the bubble volume given by Eq. (3.9). To solve Eq. (3.10), θ_{app} needs to be prescribed. This value comes from the microregion calculation.

It is assumed that a small vapor bubble of a radius R_0 is initially nucleated at the solid heater. The bubble departure takes place when the lift-off forces acting on the bubble overcome its adhesion to the heater, see more detailed discussion of this issue in section 3.3 and associated article [39]. The departure occurs when the contact pressure force (i.e., the reaction force of the solid, $2R_d\Delta p$ in the 2D case) becomes zero. In the most interesting for us case $\theta_{app} \lesssim 90°$ and in 2D, the condition $\Delta p = 0$ is attained earlier (i.e., for smaller V) then $R_d = 0$. Thus the bubble departure criterion is $\Delta p = 0$. Within the present quasistatic macroregion model, the condition $\theta_{app} = 90°$ is equivalent to the condition $R_d = R$. In other words, a concave bubble profile (that corresponds to $\Delta p < 0$) is impossible for $\theta_{app} \leq 90°$ because the departure occurs when Δp attains zero. In reality, just before the departure, the bubble becomes unstable and R_d rapidly shrinks to zero; the bubble exhibits transiently concave "bottleneck" profiles.

Since the heat flux influences the bubble shape only through θ_{app}, the value of which is known a priori at the boiling crisis (90°), the bubble shape departure where $\Delta p = 0$ for the given gravity level can be checked independently by directly calculating it from Eq. (3.10) with $\Delta p = 0$ (see Fig. 3.5b below and the associated discussion).

3.1.2 Microregion

As was already discussed in previous chapter, the intensive evaporation induces significant liquid flow towards the CL [1, 4, 104, 143] (this means that p_L decreases near CL and thus Δp increases) and the curvature strongly increases near the CL, which means that $\theta_{app} > \theta_{micro}$, cf. Fig. 2.32a. In order to describe such a phenomenon, it is necessary to solve full hydrodynamic and heat exchange problems in the liquid phase. The microregion model used in the vapor bubble growth simulation was presented and discussed in section 3.1.2 of the previous chapter.

3.2 Coupling of micro and macro regions

The microregion model is implemented as a subgrid scale model within the BEM macroregion problem. Similarly to [1], the microregion is coupled to macroregion by matching locally the marcoregion mesh to the geometrical data (coordinates of the point M, see Figs. 2.30, 3.1). In the following, the parameters exchanged between micro and macroregion are listed:

1. superheating of the solid substrate ΔT in the microregion, cf. Eq. (2.131),
2. θ_{app} (see Fig. 3.1) and
3. heat power supplied from part of the heater located underneath the microregion to the bubble Q_{micro},

$$Q_{micro} = \int_{s=0}^{s_M} q_L^i ds, \tag{3.11}$$

where q_L^i is the local heat flux at the liquid-vapor interface from the liquid side in microregion, coordinate s is shown in Fig. 3.1. This value is important to the macroregion heat transfer problem for two reasons. First, its contribution to the bubble volume is large, cf. Eq. (3.9). Second, as mentioned above, this value defines the heat flux boundary condition at the microregion part of the solid-liquid interface. These quantities are important to be matched accurately between both regions by an iterative procedure. Since θ_{app} and Q_{micro} depend only on ΔT (besides the fixed system parameters), it is possible to tabulate them and use a fitting procedure instead of recalculating them at each iteration.

3.3 Bubble departure criterion

In this section the bubble departure from the heater is discussed. The description is based on the original work by Nikolayev and Janeček [39]. It is an important phenomenon which impacts crucially the heat transfer during the nucleate boiling and CHF criterion. It needs to be clarified before used in the vapor bubble growth simulation presented in this chapter.

Numerous studies deal with the bubble departure, see e.g. [23, 144, 145]. The bubble departure occurs when the lift-off forces (like buoyancy F_g) overcome the adhesion forces. One of the most important adhesion forces is the capillary adhesion force $F_\sigma = \Gamma\sigma \sin\theta$, see Fig. 3.3. While reading studies on the bubble departure, one feels an ambiguity that concerns the value

of the contact angle that needs to be used in the above expression. In the theoretical studies [23, 145] it is derived from the force balance at the contact line, from which it is evident that the Young static contact angle θ_{micro} needs to be used for θ. In the experiment-oriented studies [4, 144], the apparent contact angle θ_{app} is used. It is taken from bubble shape snapshots[1] and may vary with the bubble growth conditions. Such a substitution usually results in a good agreement with experiments [4] and simulations [43, 146]. The ambiguity becomes striking when the notion of the capillary adhesion force is applied to the case of complete wetting [4] where the solid is covered by the continuous liquid film and the contact line is absent at all. We aim to clarify this issue and bridge these two approaches.

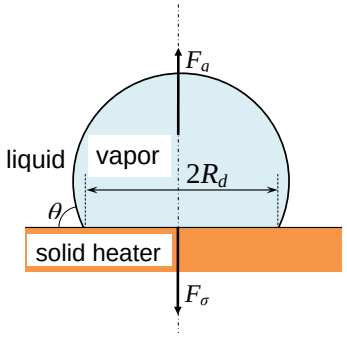

Figure 3.3: Schematic of the vapor bubble attached to the solid heater and two main forces considered: buoyancy force F_g and capillary adhesion force F_σ.

Consider a vapor bubble attached to the horizontal solid heater (Fig. 3.4). The bubble grows due to evaporation of the surrounding liquid. For simplicity and without the loss of generality, the hydrodynamic stresses at the liquid-vapor interface caused by the large-scale fluid convection and the bubble growth are omitted here. The normal stress balance at the bubble interface is given by Eq. (3.10). The capillary (Laplace) pressure is balanced by the hydrostatic pressure, the interfacial pressure jump and the differential vapor recoil. While the macroscopic effect of the liquid motion is neglected, it is essential in the vicinity of the actual line Γ of the triple (gas-liquid-solid) contact where the evaporation is strongly localized, see section 2.6 or [4, 104]. The size of this vicinity is of the order of 1 μm and in coherence with other chapters in this thesis is called microregion. Note however, that in this chapter the microregion includes also the vapor part of the bubble cf. Fig. 3.4. The rest of the fluid is called hereafter macroregion.

As was already shown in chapter 2 in the liquid part of the microregion, the strong flow of liquid is directed towards the contact line. The resulting viscous pressure drop (that corresponds to the spatial variation of Δp) increases near the contact line and results according to Eq. (3.10) in a strong bubble interface curvature. Since (by its geometrical definition) the curvature is the spatial slope change, the interface slope changes strongly in the microregion leading to a large difference between the slopes at the contact line (i.e., θ_{micro}) and some distance from CL (at the boundary Γ_{app} with the macroregion). The slope variation is much weaker in the macroregion because the flow is relatively small here (for the sake of simplicity it is completely neglected here). For this reason the slope at the boundary with the macroregion is measured experimentally, and its value is associated with the apparent contact angle θ_{app}.

To obtain the vertical components of the forces that act on the bubble, the balance of the normal to the interface forces (3.10) is multiplied by the vertical component of $\vec{n}$ and integrated

[1] Note that the measurement of the contact angle in the presence of a temperature gradient is not accurate when done with simple flash photography. This is because there is an index of refraction gradient within the thermal boundary layer which creates a parallax effect [33].

over the whole gas-liquid interface A. The surface integrals can be reduced easily if one breaks A into two parts A_u and A_l (upper and lover part of the bubble cup) depending on the sign of n_y, negative for A_u and positive for A_l, see Fig. 3.4. One mentions next that $|n_y|dA = dS$ is the projection of dA to the horizontal plane. For any function G, one obtains that

$$\int\limits_{(A)} G n_y dA = \int\limits_{(S_l)} G_l dS - \int\limits_{(S_u)} G_u dS, \tag{3.12}$$

where S_u and S_l are the projections of A_u and A_l to the horizontal plane, and G_u and G_l are the values of G at A_u and A_l, respectively.

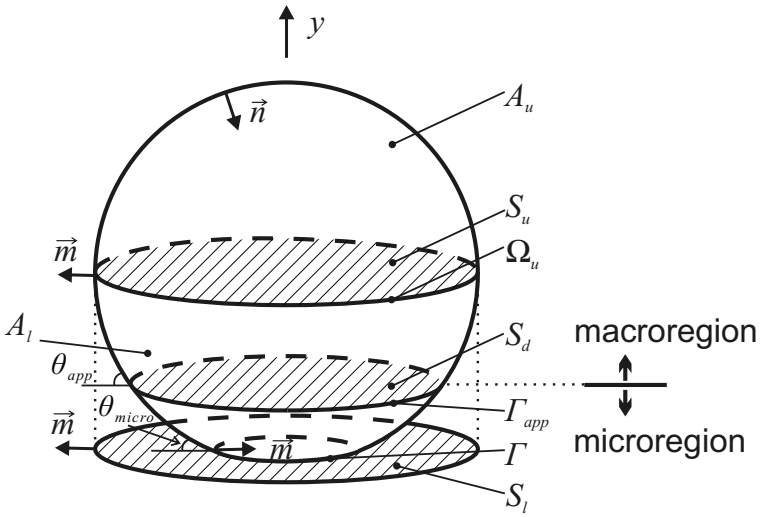

Figure 3.4: Vapor bubble on a heater. The relative size of microregion is exaggerated.

The interface curvature can be expressed as $K = -\mathrm{div}\,\vec{n}$ and the Gauss theorem can be applied,

$$\int\limits_{(S_u)} \mathrm{div}\,\vec{n} dS = \oint\limits_{(\Omega_u)} \vec{n}\cdot\vec{m} d\Omega = -\Omega_u, \tag{3.13}$$

where $\vec{m}$ is a horizontal unit vector normal to the contour and external to the integration area, Ω_u is a contour separating A_u and A_l; $\vec{m} = -\vec{n}$ at Ω_u. Since the angle between $\vec{m}$ and $\vec{n}$ is $\pi/2 - \theta_{micro}$ at Γ,

$$\int\limits_{(S_l)} \mathrm{div}\,\vec{n} dS = \oint\limits_{(\Omega_u \cup \Gamma)} \vec{n}\cdot\vec{m} d\Omega = -\Omega_u + \Gamma \sin\theta_{micro}. \tag{3.14}$$

It is evident that the integration in Eq. (3.12) with $G = -y$ yields the bubble volume V. The integration of Eq. (3.10) results in

$$\begin{aligned} \sigma\Gamma\sin\theta_{micro} = (\rho_L - \rho_V)Vg - \int\limits_{(A\setminus A_{micro})} \Delta p_{macro} n_y dA \\ - \int\limits_{(A)} p_r n_y dA - \int\limits_{(A_{micro})} \Delta p n_y dA, \end{aligned} \tag{3.15}$$

where A_{micro} is the microregion part of A and constant Δp_{macro} is the Δp value in the macroregion.

By using Eq. (3.12), one obtains the equation

$$\int\limits_{(A\setminus A_{micro})} \Delta p_{macro} n_y dA = -\int\limits_{(S_d)} \Delta p_{macro} dS = -\Delta p_{macro} S_d \tag{3.16}$$

where S_d is the area inside Γ_{app}, see Fig. 3.4.

Since p_r is neglected in macroregion, its integration in Eq. (3.15) is limited only to the microregion. The bubble force balance thus reads

$$\begin{aligned}\Delta p_{macro} S_d = \sigma\Gamma \sin\theta_{micro} - (\rho_L - \rho_V)Vg \\ + \int\limits_{(A_{micro})} \Delta p n_y dA + \int\limits_{(A_{micro})} p_r n_y dA.\end{aligned} \tag{3.17}$$

The first term on the right hand side is the capillary adhesion force and the second is the buoyancy force. If the flow in the microregion was neglected, the balance of these two terms would provide the condition of the bubble departure. In other words, the criterion of bubble departure is the equality to zero of the pressure force

$$\Delta p_{macro} S_d = 0. \tag{3.18}$$

It occurs when $\Delta p_{macro} = 0$ or for vanishing S_d. The microregion-related terms of Eq. (3.15) however modify the force balance. We aim to show how it is modified.

By reducing the third term on the right hand side of Eq. (3.17) with Eq. (3.10) (where the gravity term is negligible in the microregion because of its small volume) one obtains

$$\int\limits_{(A_{micro})} \Delta p n_y dA = \sigma \int\limits_{(S_{micro})} K dS - \int\limits_{(A_{micro})} p_r n_y dA, \tag{3.19}$$

where S_{micro} is the projection of A_{micro} to the horizontal plane. It has a ring shape similar to that of S_l (cf. Fig. 3.4). By applying again the Gauss theorem to the curvature integration (cf. Eq. (3.14)), one obtains

$$\int\limits_{(S_{micro})} K dS = \Gamma_{app} \sin\theta_{app} - \Gamma \sin\theta_{micro}, \tag{3.20}$$

where Γ_{app} is the length of the apparent CL where the angle between $\vec{n}$ and $\vec{m}$ is $\pi/2 + \theta_{app}$. One can interpret this additional adhesion term easily. Since the fluid flow is directed towards the CL, the pressure in the microregion is lower than the pressure in the macroregion. This means that a non-compensated force presses A_{micro} (and thus the bubble) downward.

Finally, the vertical force balance becomes

$$\Delta p_{macro} S_d = -(\rho_L - \rho_V)Vg + \sigma\Gamma_{app} \sin\theta_{app}. \tag{3.21}$$

This expression means that the departure occurs when the buoyancy becomes to be equal to the effective capillary adhesion force that involves the macroregion parameters only. The presence of the apparent contact angle instead of its microscopic value (cf. Eq. (3.15)) is an important feature. Note that Eq. (3.21) can be applied for the case of the complete wetting where the actual capillary adhesion force is zero.

It was shown here, by applying force balance on the growing vapor bubble attached to the horizontal heater how the microregion influences the associated forces acting on the bubble.

The liquid flow induced by the intensive evaporation at the CL vicinity due to small thermal resistance of the microregion liquid layer results in an additional adhesion force acting on the bubble. The impact of such a force can be equivalently considered when the apparent contact angle is used for calculating the effective capillary adhesion force. Such a result is applicable also in the case of complete wetting, resulting in frequently used bubble departure criteria given by Eqs. (3.18) and (3.21) (see eg. [4]). The discussed bubble departure criterion (3.18) and (3.21) is used in the vapor bubble growth simulation presented in the rest of this chapter.

3.4 Bubble growth simulation

3.4.1 Macroregion

Characteristic dimensional parameters related to the macroregion bubble growth problem are listed in Table 3.1.

Microregion characteristic dimensional parameters		
length	R_0	initial radius of the spherical bubble
pressure	$\Delta p_{init} = \sigma/R_0$	initial pressure jump of the vapor bubble
temperature	T_{sat} $q_0 R_0/k_L$	saturation temperature for given vapor pressure
time	Δt	time step
heat flux	q_0	time constant heat flux at the solid liquid interface (for volume heat supply in the form $j(t) \propto t^{-1/2}$)

Table 3.1: List of important dimensional quantities associated to the macroregion problem.

By introducing characteristic scales for time (Δt, time step), length (R_0), heat flux (q_0), and pressure (σ/R_0), all other variables can be made dimensionless. The conductivity of liquid is used to make k_S dimensionless. The solution for temperature for $x \to \infty$, $T_{S,L}^{inf} \equiv T_{S,L}(x \to \infty, y, t)$, derived in Appendix G can be used to reformulate the problem in terms of reduced temperatures $\psi_{S,L} = (T_{S,L} - T_{S,L}^{\inf})k_L/(q_0 R_0)$.

The dimensionless heat transfer problem statement is (the tilde means the corresponding dimensionless quantity, different from section D.1 and chapter 2:

$$\frac{\partial \psi_{L,S}}{\partial t} = \mathrm{Fo}_{L,S} \nabla^2 \psi_{L,S}, \tag{3.22}$$

$$\psi_{L,S}|_{t=0} = 0, \tag{3.23}$$

$$\psi_L|_{\Omega_i} = -\bar{T}_L^{inf}(\bar{y}, \bar{t}), \tag{3.24}$$

$$\zeta_L|_{\Omega_w} = \zeta_S|_{\Omega_w}, \tag{3.25}$$

$$\zeta_L|_{\Omega_d} = -1, \tag{3.26}$$

where $\zeta_L = \partial \psi_L/\partial \vec{n}$, $\zeta_S = \bar{k}\, \partial \psi_S/\partial \vec{n}$, and

$$\bar{T}_L^{inf}(\bar{y}, \bar{t}) = 2\sqrt{\frac{\mathrm{Fo}_L \bar{t}}{\pi}} \exp\left(-\frac{\bar{y}^2}{4\mathrm{Fo}_L \bar{t}}\right) - \bar{y}\, \mathrm{erfc}\left(\frac{\bar{y}}{2\sqrt{\mathrm{Fo}_L \bar{t}}}\right). \tag{3.27}$$

ψ attains the zero value at infinity. In addition one can verify that Eqs. (3.1, 3.2) rewritten for ψ are both in the form of a linear diffusion problem (the source term from Eq. (3.1) was eliminated). Both these properties are necessary for the application of BEM, see Appendix F.

The boundary conditions at the boundaries with microregion (cf. Fig. 3.1) are defined as follows,

$$\psi^{LM} = \psi_L|_{\Omega_L} = \Delta\bar{T}\bar{y}/\bar{y}_M - \bar{T}_L^{inf}(\bar{y},\bar{t}), \tag{3.28}$$

$$\zeta^{SM} = \zeta_S|_{y=0} = \bar{Q}_{micro}/\Delta\bar{x}_{micro} - 1. \tag{3.29}$$

The bubble volume equation (3.9) in the dimensionless form reads

$$\frac{d\bar{V}}{d\bar{t}} = \mathrm{Fo}_L \cdot \mathrm{Ja} \cdot \bar{Q}_{micro} + \mathrm{Fo}_L \cdot \mathrm{Ja} \int\limits_{(\Omega_i)} (\zeta_{inf} - \zeta_L)\, d\Omega, \tag{3.30}$$

where $\zeta_{inf} = n^y \mathrm{erfc}\left[\bar{y}/\left(2\sqrt{\mathrm{Fo}_L\bar{t}}\right)\right]$. The non-dimensional groups that appears in the Eqs. (3.22 - 3.30) are listed below

$$\mathrm{Fo}_{S,L} = \frac{\alpha_{S,L}\Delta t}{R_0^2} - \text{Fourier number}, \tag{3.31}$$

$$\mathrm{Ja} = \frac{q_0 R_0}{\alpha_L H \rho_V} - \text{Jakob number}, \tag{3.32}$$

$$\mathrm{Bo} = \frac{g(\rho_L - \rho_V)R_0^2}{\sigma} - \text{Bond number}. \tag{3.33}$$

By following [54], the bubble shape equation (3.10) is written in the parametric form by choosing s as an independent variable, see Fig. 3.1. The dimensionless coordinates $(\bar{x},\bar{y})$ for a given point on the bubble interface are then functions of $\xi = s/L$ that varies along the bubble half-contour from 0 to 1, $\xi = 0$ and $\xi = 1$ corresponding to the point M of matching of the micro and macro regions and to the topmost point of the bubble, respectively. Eq. (3.10) is thus equivalent to the set of ordinary differential equations

$$\frac{d\breve{x}}{d\xi} = \cos\phi, \tag{3.34}$$

$$\frac{d\breve{y}}{d\xi} = \sin\phi, \tag{3.35}$$

$$\frac{d\phi}{d\xi} = \bar{L}(\Delta\bar{p} + Bo\,\bar{y}), \tag{3.36}$$

where the rescaled with $\bar{L}$ variables $\breve{x} = x/L$, $\breve{y} = y/L$ are introduced. The boundary conditions for Eqs. (3.34 - 3.36) are

$$\bar{x}|_{\xi=1} = 0, \quad \phi|_{\xi=1} = \pi, \quad \bar{y}|_{\xi=0} = 0, \quad \phi|_{\xi=0} = \theta_{app}. \tag{3.37}$$

It was checked that the error introduced by the replacement of $\bar{y}_M$ by zero in the third boundary condition is negligible. Only three boundary conditions are necessary to solve Eqs. (3.34-3.36). The fourth is needed to find $\bar{L}$, *a priori* unknown. The value of $\Delta\bar{p}$ is independent of ξ and is determined from known $\bar{V}_{macro} = \bar{V} - \bar{V}_{micro}$ which is compared to the expression for the bubble volume in terms of $\bar{x},\bar{y}$ derived below. Since $\bar{V}_{micro} \simeq (\bar{R}_d + 0.5\Delta\bar{x}_{micro}\cos\theta_{app})\Delta\bar{x}_{micro}\sin\theta_{app} \ll \bar{V}_{macro}$, $\bar{V} \simeq \bar{V}_{macro}$.

The equation for $\bar{V}_{macro}$ is slightly modified with respect to that of [54]. By using the identity $\mathrm{div}(x\vec{e}^{\,x}) = 1$ (which is evident corollary the divergence definition, $\vec{e}$ is the unit vector directed along an axes), the bubble volume can be written as

$$V_{macro} = \int\limits_{(V_{macro})} dV = \int\limits_{(V_{macro})} \mathrm{div}(x\vec{e}^{\,x})dV. \tag{3.38}$$

Application of the Gauss integral theorem yields the expression

$$V_{macro} = -\int\limits_{(\Omega_i \cup \Omega_d)} x n^x d\Omega. \tag{3.39}$$

Since $n^x = 0$ on Ω_d, one obtains finally

$$\bar{V}_{macro} = \bar{L}^2 \int\limits_0^1 \breve{x}\breve{y}' d\xi, \tag{3.40}$$

To obtain $\Delta\bar{p}$, the direct application of Eq. (3.40) would require an additional iteration loop. To avoid it, we follow an idea outlined in [147]. By integrating Eq. (3.36) along the bubble contour, the pressure jump is obtained directly,

$$\Delta\bar{p} = \frac{\pi - \theta_{app}}{\bar{L}} - \mathrm{Bo} \int\limits_0^1 \bar{y} d\xi, \tag{3.41}$$

where the bubble half length is expressed with Eq. (3.40).

The macroscopic heat transfer problem (3.22 - 3.29) is solved as in [148] by the constant element BEM well suitable to the free interface problems[2]. This approach is highly advantageous in our case due to vanishing values of ψ, ζ at infinity which eliminates the necessity of integration over liquid and solid domains at infinity. The discretization of the integration subcontours Ω_w, Ω_d, and Ω_i (cf. Fig. 3.1a) follows the exponential law with the smallest element size ($\approx \Delta x_{micro}\theta_{app}$) located in the vicinity of the boundary Ω_L (cf. Fig. 2.30). In principle, the integration domain Ω_w continues to infinity. In the numerical treatment its finite size has to be adopted. One can verify that growing vapor bubble perturbs the temperature field described by $T_{S,L}(x \to \infty, y, t)$ only locally and thus the maximum size of Ω_w is considered to grow in time as $4\sqrt{\alpha_S t}$ based on the largest of the thermal diffusivities. It was verified that the increase of Ω_w beyond this value does not influence the results. Both the part of the solid-liquid interface which corresponds to the microregion and Ω_L (cf. Fig. 3.1b) are taken as single (straight) elements. The heat flux at Ω_L is checked to be always $\ll Q_{micro}/\Delta x_{micro}$ and its contribution is added to Q_{micro} in Eq. (3.30), to satisfy the global energy balance. A discretized equations (3.22) and schematic drawing of the computational grid are presented in Appendix F.

3.4.2 General algorithm

The problem is nonlinear because of nonlinear terms and especially because of the free boundary. Initially it is assumed that a circular bubble of radius R_0 is nucleated at the solid surface and the temperature of both the solid and the liquid domains is uniform and equal to T_{sat}. The following iteration algorithm is needed to determine the bubble shape and the thermal field at each time step:

1. The interface bubble shape, the bubble interface velocity (needed for the BEM calculation, see Appendix F for details) and Q_{micro} are guessed to be the same as at the previous time step;

2. Remeshing of the contours Ω_w, Ω_d and Ω_i is performed if needed;

[2] A brief introduction to BEM is presented in Appendix F.

3. Temperatures and fluxes on the contours Ω_w, Ω_d and Ω_i are found by solving Eqs. (3.22 - 3.29) by BEM for $\psi_{L,S}$, $\zeta_{L,S}$; the value of ΔT is obtained;

4. Based on ΔT, the microregion calculation is performed and new values for $\bar{Q}_{micro}$, θ_{app} are obtained;

5. New $\bar{V}$ is calculated from Eq. (3.30) with the trapezoidal rule;

6. Bubble shape is determined using the values of $\bar{y}$ and $\bar{L}$ from previous iteration. First, $\Delta\bar{p}$ is determined with Eq. (3.41). Next, Eq. (3.36) is solved for ϕ. The latter is used to integrate Eqs. (3.34, 3.35). Finally, $\bar{L}$ is updated with Eq. (3.40), and $\bar{x} = \bar{L}\breve{x}$, $\bar{y} = \bar{L}\breve{y}$ are recalculated.

7. The interface velocity is calculated, and steps 2-7 are repeated until the required accuracy of θ_{app}, R_d and V is attained.

As a rule, four iterations give 0.2% accuracy. In order to reduce the calculation time at the step 4, the precalculated values of $\theta_{app}(\Delta T)$ and $Q_{micro}(\Delta T)$ are interpolated by cubic splines. By performing full micro-macro coupling procedure, we checked that this shortcut does not influence the results. There is one more reason in using the tabulation of the microregion values for parameters Q_{micro} and θ_{app}. The described microregion model cannot provide the data for $\theta_{app} = 90°$; the maximum attainable value is $\sim 89.8°$. Both θ_{app} and Q_{micro} are extrapolated up to 90° by using a power law $\theta_{app} \propto \Delta T^{\alpha}$, $Q_{micro} \propto \Delta T^{\beta}$, cf. Fig. 2.25b. We verified that increasing the time step from 1 to 50 ms is minimally influencing the calculation accuracy without impacting the numerical stability; this is an intrinsic property of BEM. The time step $\Delta t = 20\,\mu$s was used in most simulations.

3.5 Results

3.5.1 Bubble growth numerical simulation

In order to demonstrate the employment of the macroregion model for high slopes of the interface some results from 2D bubble growth numerical simulation are presented in this section. The aim of the bubble growth numerical simulation is also to demonstrate that the increase of the apparent contact angle may significantly prolongate the vapor bubble residence at the solid heater. This means that the total area of dry spots is high and the temperature necessarily strongly vary along the heater. Depending on the heat load, two bubble growth regimes can be distinguished. At low heat loads (Fig. 3.5a) the bubble volume increases until the buoyancy force becomes to be equal to the capillary adhesion force, which corresponds to the bubble departure. In the beginning of growth, the dry spot size increases. At some point of growth R_d nearly saturates while both the bubble volume and the visible from the top bubble radius R keep growing. Therefore the quotient R_d/R decreases at the end of the bubble evolution, see the lower curve in Fig. 3.7a. This regime is called hereafter "bubble departure regime". At high heat loads (Fig. 3.5b), we postulate that when the condition $\theta_{app} = 90°$ is attained while the bubble is attached to the heater, the boiling crises arises (the bubble spreads over the heater). This is the "bubble spreading regime" that corresponds to the BC triggering. It is possible that θ_{app} grows beyond 90° in reality while the bubble remains attached. However the present microregion model cannot describe such an event so that the simulation is stopped as soon as $\theta_{app} = 90°$. Within the present quasistatic macroregion approach, the latter condition is equivalent to $R_d = R$ (cf. sec. 3.3, or 3.1.1.2).

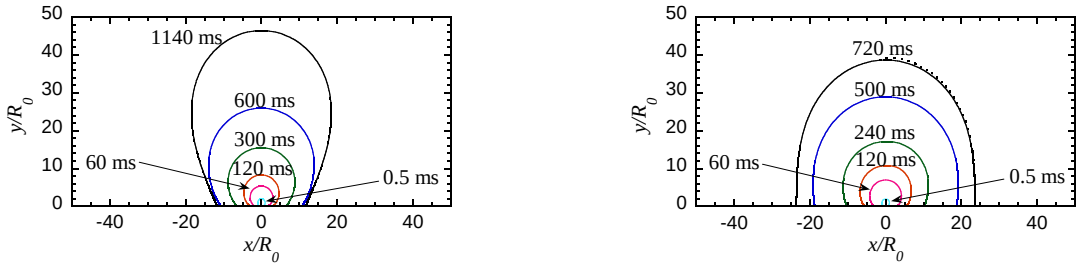

(a) (b)

Figure 3.5: Bubble shape evolution shown for $\theta_{micro} = 15°$. (a) $q_0 = 0.05$ MW/m^2. The 1140 ms profile corresponds to the bubble departure. (b) $q_0 = 0.1$ MW/m^2. The 720 ms profile corresponds to the BC triggering.

The value of the ratio R_d/R at the moment of bubble departure is plotted vs. imposed heat load (q_0) in Fig 3.6. In other words, each point of these curves corresponds to the terminal point of a curve of Fig. 3.7a that marked with an open circle. One can see that the ratio R_d^{dep}/R^{dep} grows with the heat flux. The postulated BC criterion is satisfied when R_d^{dep}/R^{dep} attains unity.

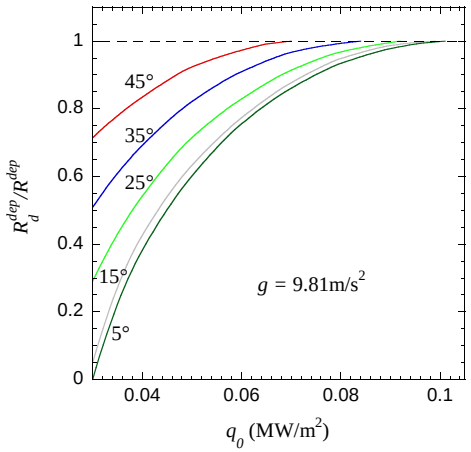

Figure 3.6: The quotient of the dry spot radius and the bubble radius at the moment of bubble departure as a function of heat flux for different values of θ_{micro}.

The accuracy of the vapor bubble shape at CHF calculation can be easily checked by an independent test. Indeed, since the conditions $\theta_{app} = 90°$ and $\Delta p = 0$ (cf. sec. 3.3) are both satisfied at the CHF, the bubble shape depends only on the Bond number and can be calculated independently from the heat exchange calculation. The shape calculation carried out by the standard Runge-Kutta method is shown by the (half-contour at $x > 0$) dotted line in Fig. 3.5b. It nearly coincides with its counterpart calculated for the moment of departure ($t = 720$ ms) with the general algorithm, which proves its accuracy.

Our simulation enables the temperature distribution within the solid and liquid domain to be rigorously calculated. The full temperature fields of the vicinity of growing bubble are shown in Fig. 3.8 for the case of bubble departure regime and in Fig. 3.9 for the bubble spreading regime (parameters as in Fig. 3.5).

The heater surface temperature is shown in Fig. 3.10, which corresponds to the bubble profiles of Fig. 3.5. Far from the bubble, the surface temperature increases in time independently of x and follows the square root law (3.8). When approaching the CL, it decreases to the temperature $T_S = T_{sat} + \Delta T$ as shown in the insert of Fig. 3.10a due to the intensive latent heat consumption

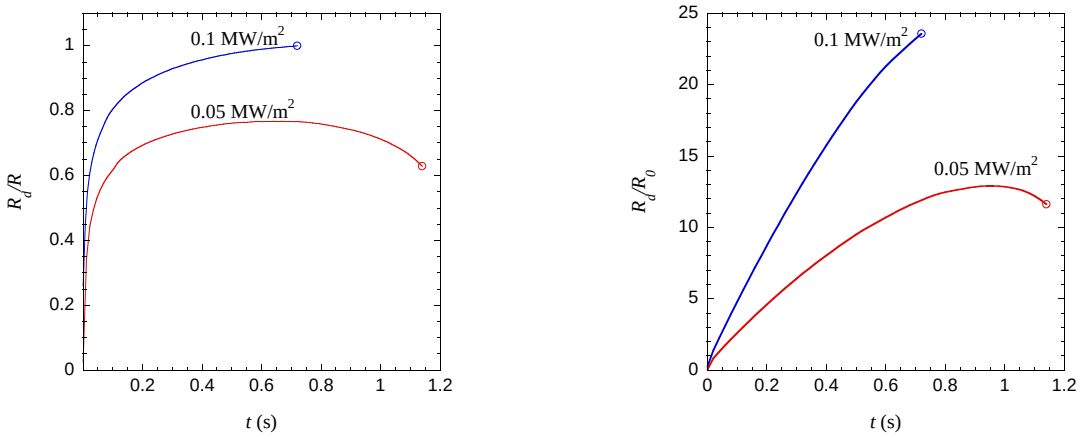

(a) (b)

Figure 3.7: Vapor bubble growth shape results for $\theta_{micro} = 15°$ and two different values of q_0. The bubble departure points are indicated with open circles. (a) The temporal evolution of R_d/R (see Fig. 3.1 for their definition). (b) The temporal evolution of R_d.

during evaporation in the microregion. This feature agrees with experimental observations (see Fig. 1.5) and numerical simulations, see section 1.2.2. Inside the dry spot, T_S increases with time because the heat transfer through the dry spot is blocked. Note that in the bubble departure regime (Fig. 3.10a) inside the dry spot temperature is lower than that far from the bubble. At the CHF (Fig. 3.10b) the dry spot becomes to be hotter than the rest of the heater. This temperature increase leads eventually to the burnout of the heater observed during the BC.

A parametric CHF study for different gravity levels and contact angles can be carried out. The microregion model is developed for the partial wetting conditions characterized by the constant microscopic contact angle. The calculation, enables to provide a qualitative results which characterize the impact of this undoubtedly important parameter on the bubble growth, spreading and departure. Fig. 3.6 shows the ratio R_d/R at departure for several values of the contact angle. The difference between the curves for $\theta_{micro} = 5°$ and $15°$ is very small with respect to the pair $35°$ and $45°$ where the difference is striking. With increasing heat load R_d^{dep}/R^{dep} increases and attains unity at the CHF. The unique value of $R_d^{dep} = R^{dep}$ depends only on the surface tension and gravity within the present force balance model; for water at 10 MPa and $g = 9.81$ m/s^2 this value is 1.18 mm. Note that it is important to account for the actual (non-circular) shape of the bubble. If the circular shape was imposed, an essentially different value of 1.57 mm would result from the force balance at departure. This is expected because under the gravity the bubble extends in the vertical direction (Fig. 3.5a) so that its size in the perpendicular direction is smaller than that calculated from the circular approximation.

The impact of θ_{micro} on the critical heat flux is illustrated in Fig. 3.12a for two values of g. For decreasing θ_{micro}, q_{CHF} tends to saturate at a value corresponding to the complete wetting case. This tendency is in agreement with the small difference between results for $\theta_{micro} = 5°$ and $15°$ in Fig. 3.6.

CHF decreases with the contact angle (Fig. 3.12a) in agreement with the experimental results [25, 57]. The experimental data for small contact angles usually show a somewhat steeper change than that of Fig. 3.12a. The experimental dependencies on the contact angle should however be considered with caution because it is difficult to isolate the effect of the contact angle: other material properties often change with its change. It is also important to note that the large measured experimentally values of equilibrium contact angle are often due to the CL pinning on

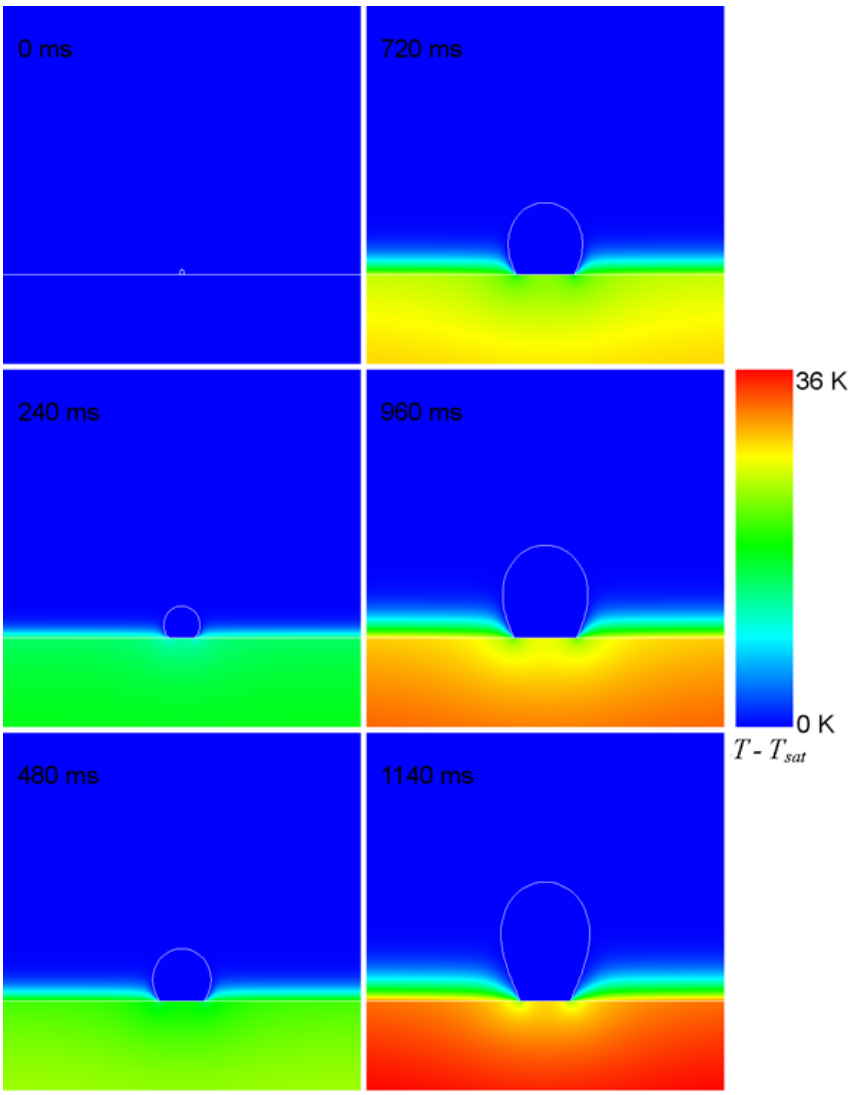

Figure 3.8: Temperature fields for six different times shown for $\theta_{micro} = 15°$, $q_0 = 0.05$ MW/m^2.

the heater surface heterogeneities (responsible for the wetting hysteresis, see [149]) rather than to the surface energy effect that influences the CL dynamics considered here. The equilibrium contact angle values remain small for most clean and smooth substrates.

The impact of gravity on the critical heat flux is analyzed in Fig. 3.11b. The CHF is an increasing function of gravity in agreement with experimental observations [56]. The gravity dependence is well fitted by a power law with the exponent $\simeq 0.44$ which is larger than that predicted by Zuber-Kutateladze expression (1.1).

To obtain all the above data on the boiling crisis within a relatively simple numerical approach, the hydrodynamic flows in the macroregion have been neglected. Their account would require the use of a DNS code with an efficient management of the moving gas-liquid interfaces with phase exchange (like Trio_U code [150]). Therefore this work should be considered as a preparation step for such a study necessary to have the benchmark and the understanding of main features of the BC. It is difficult to require the quantitative agreement with the experiment within the present modeling; for this reason we discussed above only the qualitative features of the BC triggering.

The boiling crisis is not an instantaneous phenomenon, it develops progressively. Once its

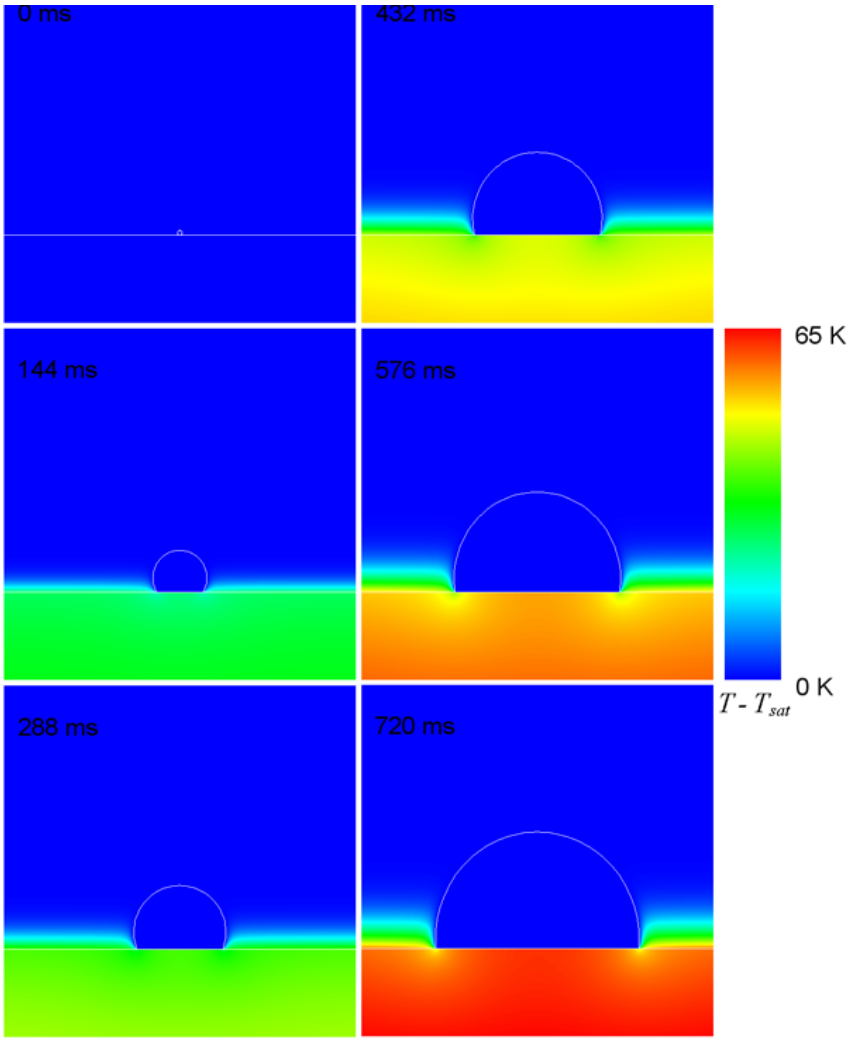

Figure 3.9: Temperature fields for six different times shown for $\theta_{micro} = 15°$, $q_0 = 0.1$ MW/m^2.

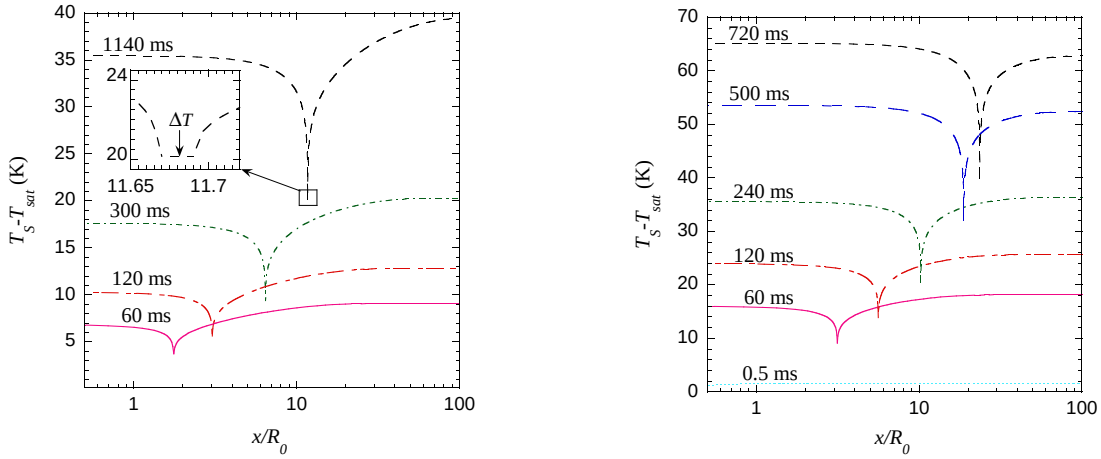

(a) (b)

Figure 3.10: Variation of the temperature along the heater surface different growth times (corresponding to those of Fig. 3.5) for $\theta_{micro} = 15°$ and for (a) $q_0 = 0.05$ MW/m^2 (b) $q_0 = 0.1$ MW/m^2.

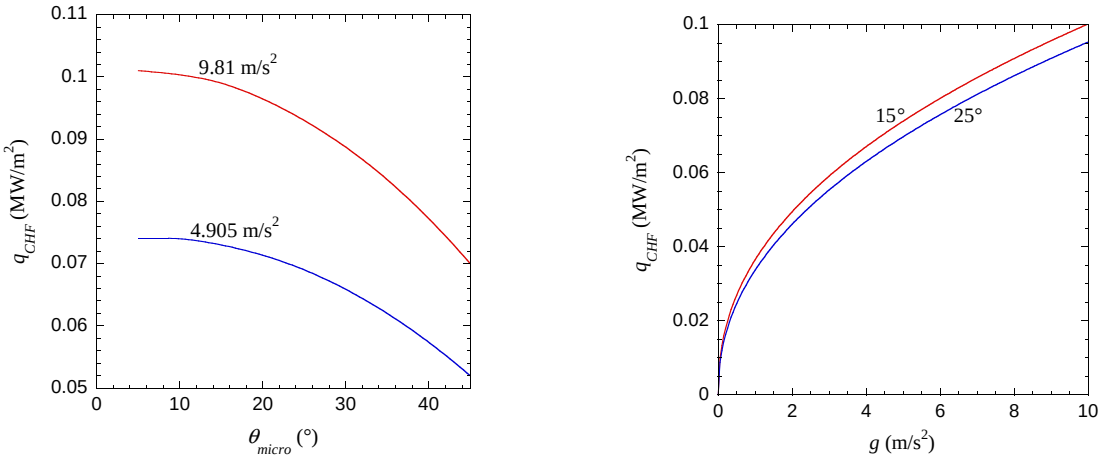

Figure 3.11: (a) The critical heat flux q_{CHF} as a function of (a) microscopic contact angle for two different values of g. (b) The critical heat flux q_{CHF} as a function of the contact angle for two different values of g.

triggering occurs, its dynamics (and thus duration) is controlled by several processes. First, it is the bubble spreading studied here. Next, the bubble interaction should be considered. The bubbles may interact both temporally and spatially. The temporal interaction manifests itself through the thermal history of a particular nucleation site that becomes more and more hot after each bubble growth and departure cycle. The spatial interaction occurs both through coalescence of neighboring bubbles that causes further extension of the dry heater area and through the heat diffusion inside the heater that controls the general heater temperature rise during BC. These processes are yet to be studied.

3.5.2 Influence of the CL velocity during the initial bubble growth phase

The initial vapor bubble growth dynamics ($t < 1$ ms) is qualitatively different from that presented in the previous section for long simulation times. The initial bubble growth evolution is specific due to the small initial vapor bubble size (in our numerical simulation $R_0 = 0.05$ mm), which results in a very large initial velocity of the moving CL. This is caused by the increase of vapor bubble volume due to evaporation but also by increase of the apparent contact angle due to intensive evaporation within microregion. Note that in principle (when bubble growth described by classical physics), for $q_0 > 0$ the CL velocity diverges as $R_0 \to 0$. In reality such a situation never appears as the bubble nucleation size is finite. In order to avoid such problems in bubble growth numerical simulations a somewhat larger value of initial vapor bubble radius is usually imposed ([32] (0.25 mm);[1] (0.125 mm); [41] (0.1 mm)).

In the following, the results from the numerical simulation for water at 10MPa, $\theta_{micro} = 5°$ of vapor bubble growth are presented. The apparent contact angle and integrated heat flux are considered not only as functions of local CL superheating ΔT but also of CL velocity v_{CL}. This is implemented by using the data from section 2.7.1 (Figs. 2.26b, 2.27a). Relatively small heat load $q_0 = 0.02$ MW/m^2 was chosen for the calculation because of two reasons: 1) additional variable that is coupled (v_{CL}) introduces significant nonlinearity, difficult to treat by iterative procedure for high heat loads, 2) high imposed heat load would result in a large value of v_{CL} for which using the approximate expressions from sec. 2.7.1, $\theta_{app}(\Delta T, v_{CL})$, $\Delta Q_{micro}(\Delta T, v_{CL})$ might be out of validity.

In Fig. 3.12a is plotted the apparent contact angle vs. time for three cases which differ by number of dependent variables considered in expressions for apparent contact angle and integrated heat flux. First case is when both θ_{app} and Q_{micro} are considered as functions of

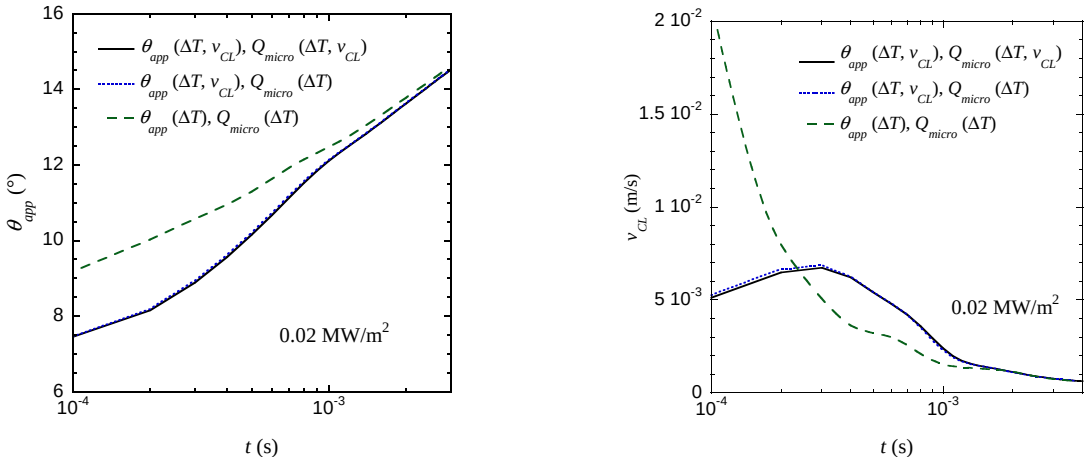

(a) (b)

Figure 3.12: Vapor bubble growth evolution results for $\theta_{micro} = 5°$ and $q_0 = 0.02\text{MW/m}^2$. (a) The temporal evolution of θ_{app}. (b) The temporal evolution of v_{CL}.

superheating ΔT and CL velocity v_{CL}. Second case is when the apparent contact angle depends on both ΔT, v_{CL} but integrated heat flux depends only on superheating: $Q_{micro} = f(\Delta T)$. The last case is when both θ_{app} and Q_{micro} depend only on ΔT (such a situation coincides with that from section 3.5.1). One can see from Fig. 3.12a that there is a strong difference between θ_{app} evolution in time for the cases where the apparent contact angle is taken as a function of both ΔT and v_{CL} and when it is taken as a function of only superheating ΔT. For the case where v_{CL} is included into the consideration, the apparent contact angle is lower (receding CL)[3]. It turned out to be not important whether Q_{micro} is considered to be a function of v_{CL}. The explanation for this behavior is a small heat load used here and also the fact that $v_{CL} > 0$ (receding CL) causes an increase of Q_{micro} value, but at the same time the higher heat sucked from the heater results in decrease of local temperature (ΔT decreases), which means θ_{app} decreases and v_{CL} as well. Due to this, the error following from neglecting dependence of Q_{micro} on v_{CL} is small. In Fig. 3.12b is shown the velocity of the CL vs. time.

The calculation for an initial stage of bubble growth using the approximate expressions $\theta_{app}(\Delta T, v_{CL})$ and $Q_{micro}(\Delta T v_{CL})$ derived in section 2.7.2 was presented. Account of the v_{CL} influence leads to the slowing down at the beginning of the dry spot growth. The error caused by neglecting dependence of integrated microregion heat flux on contact line velocity is small. This is due to the fact that Q_{micro} increases when $v_{CL} > 0$. It means that larger portion of heat is evacuated from the solid heater, which causes decrease of ΔT.

3.6 Conclusion

A quasistatic numerical simulation of the single vapor bubble growth on a massive (semi-infinite) heater has been performed in order to study the triggering of the boiling crisis. It is shown that

[3]Note that such a behavior is similar to results from the numerical simulation of evaporating liquid drop [104], where the apparent contact angle increase is limited by receding CL dynamics.

phenomena acting in the vicinity of the triple contact line (the microregion) have a strong impact on the vapor bubble dynamics. The microregion has been modeled for the case of partial wetting where the microscopic contact angle is an input parameter. Several quantities are determined from the microregion model including the apparent contact angle and integrated heat flux. Coupling of the microregion to the macroregion was performed.

Two regimes of bubble growth have been identified. The first regime is the conventional bubble growth-and-departure at small heat fluxes. The second, "bubble spreading" regime occurs when the superheating is strong enough to cause a strong increase of the apparent contact angle that, in its turn, causes an increase of the dry area under the bubble. The radius of the dry area becomes equal to the bubble radius when the apparent contact angle attains 90°. Such a value is an important threshold for several reasons. (i) Dry area growth causes the heater temperature rise that should lead to the increase of the apparent contact angle of neighboring bubbles. (ii) Strong adhesion to the heater caused by the large apparent contact angle should favor the coalescence of bubbles attached to the heater. (iii) Coalescence of the dry areas under the bubbles occurs during the bubble coalescence, which causes the heater temperature rise favoring the spreading of neighboring bubbles and therefore coalescence of the newly formed bubble with its neighbors. Therefore, the bubble spreading is considered to be the triggering mechanism of the boiling crisis. The corresponding heat flux is associated with the CHF. It has been studied as a function of gravity and of the contact angle. The results correspond at least qualitatively to the available experimental data. To obtain the quantitative agreement with the experiments, a more realistic model of the macroregion (accounting for the fluid motion in it) needs to be implemented. A simulation of growth of the multiple bubbles and their interaction need to be carried out to describe the dynamics of the boiling crisis.

Chapter 4

Summary and conclusions

The evaporation in the vicinity of the triple gas-liquid-solid contact line is of high importance in many natural and technological processes (e.g. boiling, drying of paint, etc.). While this phenomenon was intensively studied last decades, many questions still remain unsolved. The main issue that complicates understanding of the heat and mass transport processes lies in their strong localization in the vicinity of the contact line. This complicates on one hand experimental measurements and on the other, the mathematical and numerical modeling. Indeed, one has to deal with a system exhibiting singular-like behavior of various macroscopic quantities (e.g. shear rate, local heat flux etc.). One also has to mention that although the transport processes occur at a scale smaller than several hundreds of nm (microregion) it is necessary to consider also a coupling with the macroscopic problem (macroregion). The multiscale nature of the problem reveals the necessity of new studies and approaches to treat the transport processes in the vicinity of the contact line, in order to elucidate the physics of various macroscopic problems (e.g. boiling phenomenon or oscillating heat pipe).

In my thesis, I studied theoretically the transport processes in the vicinity of the triple gas-liquid-solid contact line and their impact on macroscopic evaporation. I focused on the description of partial wetting system, for which, under isothermal conditions, the liquid-vapor interface meets the solid surface at a finite slope that defines the microscopic contact angle assumed to be defined by the Young formula. The evaporation to the atmosphere of the pure vapor is assumed to be driven by the substrate heating. Such a regime is met in many technological applications like boiling heat exchangers or heat pipes.

First, the important question of singularity relaxation is addressed. The main finding of the thesis is that the Kelvin effect (dependence of saturation temperature on pressure) is sufficient by itself to relax the hydrodynamic contact line singularity [110, 111]. By relying on this fact, the minimal complexity microregion model, describing thermal and hydrodynamic aspects of the evaporation in the contact line vicinity in the limit of small interface slopes is formulated. The asymptotic analysis of this model is performed in order to obtain an asymptotic behavior of the system variables in the vicinity of contact line. This analysis provides the missing boundary conditions for its solution. At the next step, the minimum complexity model is solved numerically but also analytically by using regular perturbation method. The governing length scales of the problem are identified and used to find a universally valid law describing the apparent contact angle (angle at the matching point between microregion and macroregion).

It is found that the Kelvin effect relaxes the viscous stress singularity appearing when contact line moves [110, 111]. In practice this means that in the model the liquid is allowed to evaporate or condensate as the saturation temperature of the liquid-vapor interface is linked through the Kelvin effect to the hydrodynamic pressure in the liquid phase. The relaxation by Kelvin effect holds even for the macroscopically isothermal system: the thermal gradients caused by

evaporation/condensation appear only in the contact line vicinity. The condensation occurs during advancing contact line motion while the evaporation accompanies the contact line receding. The Kelvin effect on the singularity relaxation is compared to that of the hydrodynamic slip length. It is found that length scale associated with the Kelvin effect is in many situations larger than the slip length and thus Kelvin effect should be the dominant phenomenon for volatile fluids.

The moving contact line problem and its multiscale nature were addressed in a separate section (sec. 2.4). The inner and outer problems were defined: inner problem controlled by evaporation, and outer problem where the viscous stress is balanced by a gradient of capillary pressure. The asymptotic matching of the inner and outer regions is performed.

Next, the minimum complexity microregion model is extended to account for other phenomena that may influence the evaporation. In particular, the thermal resistance of vapor-liquid interface, slip length, thermocapillary term have been considered. I perform a parametric study revealing the influence of each of these phenomena. The impact of solid wall conductivity is also studied by adding a conductive heater directly to the microregion problem. Such a model is numerically solved by combining the Finite Volume method (liquid domain) and the Boundary Element method (solid domain). The increase of the apparent contact angle caused by evaporation is analyzed.

The influence of surfaces force on evaporation was studied (sec. 2.5) under the regime of partial wetting (sec. 2.5.1). The impact on the apparent contact angle was found to be weak.

In the last part of the chapter related to the microregion modeling, an extension of the lubrication approximation to high slopes of the gas-liquid interface at evaporation is discussed (sec. 3.1.2). The latter extension is necessary in order to use the microregion model in the vapor bubble growth macroscopic modeling of nucleate boiling phenomenon. The increase of the apparent contact angle caused by the evaporation is analyzed. The algorithm is robust and even for small microscopic contact angle the calculation of apparent contact angle up to nearly 90° is possible. It was found that the impact of vapor recoil on interface temperature is tiny. The vapor recoil term in the force balance at the liquid-vapor interface is however important. The impact of vapor recoil force is strong for liquids with small latent heat of vaporization (like freons). The impact of the vapor recoil on the apparent contact angle was analyzed.

In the second part of the thesis, the previously established microregion model was coupled to the macroregion bubble dynamics described within a quasistatic approximation. A vapor bubble growth problem is solved numerically in 2D with the Boundary Element method. The purpose is to simulate the boiling under high heat loads, for which the evaporation in the vicinity of contact line might play an important role, influencing the vapor bubble dynamics and through it, the overall boiling dynamics.

First, the bubble departure from the heater at boiling was studied. The growing vapor bubbles during boiling are attached to the solid heater due to the adhesion provided in particular by the capillarity. I showed in the thesis that the apparent contact angle that should be used in the expression for the capillary adhesion force instead of the much smaller Young contact angle (sec. 3.3). This finding agrees with the existing experimental data. Second, it was found that under high heat loads, the increase of the apparent contact angle causes the vapor bubble to spread over the heater. Such a behavior is proposed as the triggering mechanism of the dryout

of heater at the boiling crisis (sudden drop of the heat transfer rate in boiling causing the heater destruction if the heating is not cut).

Two regimes of bubble growth have been identified. The first regime is the conventional bubble growth-and-departure regime of small heat fluxes. The second, "bubble spreading" regime occurs when the superheating is strong enough to cause a strong increase of the apparent contact angle that, in its turn, causes increase of the dry area under the bubble. The radius of the dry area becomes equal to the bubble radius when the apparent contact angle attains 90°. Such a value is an important threshold. It was proposed that the critical heat flux of the boiling crisis corresponds to the situation where the apparent angle of 90° is attained at the moment of bubble departure. The CHF derived from this criterion is calculated as a function of gravity and the microscopic contact angle.

Such a phenomenon was already observed, in particular for the systems near the liquid-gas critical point. The results correspond at least qualitatively to the available experimental data. To obtain the quantitative agreement with the experiments, a more realistic model of the macroregion (accounting for the fluid motion in it) needs to be implemented. A simulation of growth of the multiple bubbles and their interaction needs to be carried out to describe the dynamics of the boiling crisis.

Appendix A

DECLIC experiment

The boiling crisis investigation is one of the main objectives of the French-US research project called DECLIC (DEvice for the study of Critical Liquids and Crystallization Dispositif pour l'Etude de la Croissance et des LIquides). This project is managed by CNES and NASA respectively. The DECLIC apparatus is a high precision microgravity instrument that allows the advanced methods of optical diagnostics (direct observation, interferometry, grid shadow observation, microscopy, light scattering) to be used for heat transfer studies of near-critical fluids. The boiling crisis is studied by using ALI (ALICE-Like Insert) which is a development of the ALICE apparatus that functioned on board the Mir space station. However the ALICE cells have been designed for other purposes and did not allow any quantitative information to be obtained. ALI contains two different 2 cm^3 cells filled with extra-pure SF6: direct observation and interferometry cells [151]. Both cells are cylindrical, with sapphire transparent bases for the optical observation and copper lateral walls that serve to regulate the temperature of the fluid bulk within 15 μK precision required near the critical point.

The direct observation cell, allows observing the spreading of a single vapor bubble through the transparent cell bases. A transparent conducting film deposed onto one of the bases is used as a heater. The experiment is designed in a way to allow the direct observation of the contact line motion. This cell allows measuring only the evolution of the dry spot but does not allow measuring the shape of the bubble.

This is exactly the purpose of the interferometry cell that gives a unique opportunity to measure both the shape of a single growing bubble and the temperature in the bulk of the fluid by interferometry. A flat controlled heater perpendicular to the observation direction is located inside the cell allowing for the sidewise bubble observation.

a) 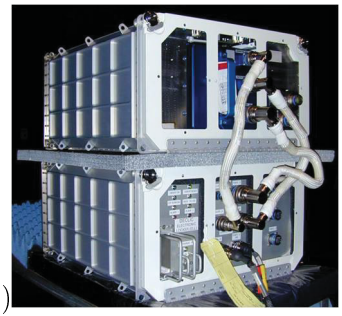 b) 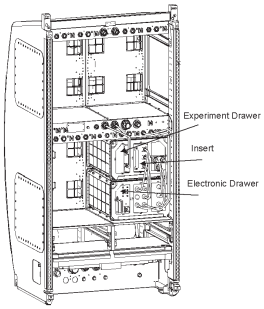

Figure A.1: a) Flight model of DECLIC, b) DECLIC integrated into Express Rack.

Appendix B

Material properties

Material parameter	Water (10 MPa)	Water (0.1 MPa)	FC-72 [2] (0.04 MPa)
T_{sat}, [K]	584.18	372.73	305.15
ρ_L, [kg/m^3]	688.63	958.66	1656.48
ρ_V, [kg/m^3]	55.48	0.59	5.688
H, [J/kg]	$1.312{\cdot}10^6$	$2.258{\cdot}10^6$	$88{\cdot}10^3$
$c_{p,L}$, [J/(kg· K)]	$6.124\ {\cdot}10^3$	$4.216\ {\cdot}10^3$	$1.064{\cdot}10^3$
k_L, [W/(m·K)]	0.55	0.679	0.056
M, [(g/mol)]	18.02	18.02	338.04
T_c, [K]	647.14	647.14	449
σ, [N/m][1]	$12.04{\cdot}10^{-3}$	$61.126{\cdot}10^{-3}$	$9.6{\cdot}10^{-3}$
μ, [Pa·s][4]	$0.2{\cdot}10^{-3}$	$0.284{\cdot}10^{-3}$	$0.563{\cdot}10^{-3}$
γ, [N/(m·K)][3]	$2.26{\cdot}10^{-4}$	$1.477{\cdot}10^{-4}$	$7.5{\cdot}10^{-5}$

Table B.1: Fluid properties used in the simulations. If not marked otherwise, the material properties are taken from [152]. Liquid and vapor properties are taken at saturation conditions.

Material	cooper (Cu)	stainless steel (ss)
ρ_S, [kg/m^3]	8894	8000
$c_{p,S}$, [J/(kg· K)]	415.2	500
k_S, [W/(m·K)]	380.1	15

Table B.2: Material parameters of the solid substrate used in the simulations [152].

.

[1] Surface tension for water at 10MPa taken from [153]; for water at 0.1 MPa taken from [22], p. 54, Eq. (2.57); FC-72 from [4]

[2] Material properties taken from 3M Product Information sheet

[3] Marangoni coefficient for water at 10MPa taken from [153]; for water at 0.1 MPa taken from [22], p. 55; FC-72 from [4]

[4] For water at 10MPa, the viscosity value used for calculation and presented in the table is larger than the correct value $82{\cdot}10^{-6}$ Ps· s found later in the literature [154]

Appendix C

Disjoining pressure

C.1 Smooth disjoining pressure shape

In order to avoid discontinuity of derivative of Π of the simplest Π form, (2.105) has to be modified. One of the simplest possibilities is to use smooth parabolic matching for $h = d_D$. The disjoining pressure is then described by three functions

$$\Pi(h) = \begin{cases} ah + b, & h \in (0, d_1) \\ ch^2 + dh + e, & h \in (d_1, d_2) \\ A/(6\pi h^3), & h \in (d_2, \infty) \end{cases} . \tag{C.1}$$

The constants d_1 and d_2 are coordinates at which the three parts of Π are connected. The constants a, b, c, d and e, once θ_Y, θ_{micro} are fixed can be found from Eqs. (1.18, 2.104) and from the condition of the continuity of $\Pi(h)$ and its derivative. The constants are: $a = 2dd_1 + \phi_2 - 2cd_2$, $b = \phi_1 - cd_1^2 - \phi_2 d_2 + cd_2^2$, $c = 3\alpha/(d_2^3 - d_1^3)$, $d = \phi_2 - 2cd_2$, $e = \phi_1 - \phi_2 d_2 + cd_2^2$ where $\phi_1 = -3A/(6\pi d_2^4)$, $\phi_2 = A/(6\pi d_2^3)$ and $\alpha = -P(0) - A/(12\pi d_2^2) + \phi_2 d_2^2/2 - \phi_1 d_2$. This disjoining pressure shape is fully described by four constants $P(0)$ (calculated from θ_Y, θ_{micro}), A (Hamaker constant) and two parameters d_1, d_2 for which one can hardly assign physically justified values. Such a type of disjoining pressure thus served only for verification of negligible impact of sharp disjoining pressure matching (2.105) on results in numerical solution. The disjoining pressure (C.1) is plotted in Fig. C.1 together with (2.105).

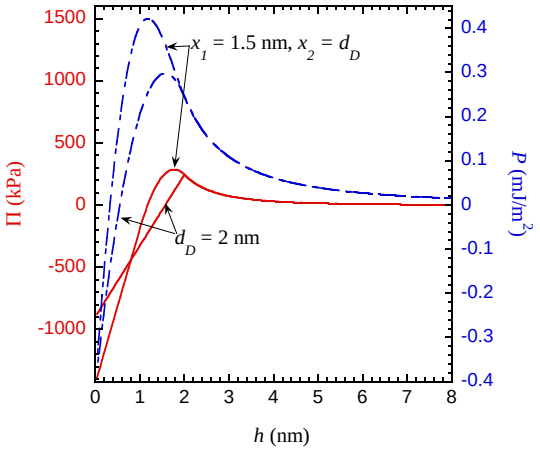

Figure C.1: The two shapes of disjoining pressure (Eqs. (2.106) and Eqs. (C.1)) and corresponding surface energies for water at 10 MPa, $\theta_Y = 15°$, $\theta_{micro} = 1°$ and $A = 3.7 \cdot 10^{-20}$ J.

Appendix D

Solution procedure of the contact line model

In the following section, the solving procedure of the microregion model given by Eqs. (2.24 - 2.29, 2.31) is discussed. First, the dimensionless version of the model used for numerical treatment is presented. The presence of CL and thus vanishing $h(x \to 0)$ complicates the numerical treatment and the problem needs to be solved differently from standard solving procedures [155]. Here the method proposed in [104] is used. The variable change suitable for the given problem is briefly shown. Next, the general algorithm and solving procedure are discussed. A criterion, based on which the size of the microregion domain for the case $v_{CL} = 0$ may be determined, is proposed. At the end, the governing equations in the discretized form are presented.

D.1 Reduction to dimensionless form

In the following, l_s, σ/l_s and ΔT are used to make lengths, pressures and temperatures non-dimensional. Other important scales related to the problem are listed in Table. D.1.

By combining Eqs. (2.9, 2.19) and (2.22) the following two differential equations can be written,

$$\frac{\partial}{\partial \tilde{x}}\left\{-N_R N_M\left(\frac{\tilde{h}^2}{2}+\tilde{h}\right)\frac{\partial \tilde{J}}{\partial \tilde{x}}+\left[\frac{\tilde{h}^3}{3}+\tilde{h}^2\left(1-\frac{N_p N_M}{2}\right)-N_p N_M \tilde{h}\right]\frac{\partial \Delta\tilde{p}}{\partial \tilde{x}}\right\}= Ca\frac{\partial \tilde{h}}{\partial \tilde{x}}-N_e\tilde{J}, \tag{D.1}$$

$$\frac{\partial^2 \tilde{h}}{\partial \tilde{x}^2}=\Delta\tilde{p}-\tilde{\Pi}+\tilde{p}_r, \tag{D.2}$$

where

$$\tilde{J}=\frac{1-\Delta\tilde{p}N_p}{N_R+\tilde{h}}$$

is the dimensionless evaporation mass flux. Note that in principle one can reduce the system of equations (D.1 - D.2) to one single differential equation of the forth order in $\tilde{h}$ as it is presented in e.g. [6, 103, 156]. We however prefer to present the two equations separately (similarly to [5]) as it is useful for the analytical but also for numerical treatment.

Here $N_M = \gamma\Delta T/\sigma$ is the Marangoni number, $N_e = \mu k_L \Delta T/(\rho_L \sigma H l_s)$ characterizes the influence of evaporation on the interface shape, $Ca = v_{CL}\mu/\sigma$ is the capillary number and $N_R = R^i k_L/l_s$ is the dimensionless interfacial resistance. The parameter $N_p = \sigma T_{sat}/(\Delta T H \rho_L l_s)$ can be seen as a ratio of two characteristic pressure scales: a capillary pressure scale σ/l_s and the pressure $\Delta T H \rho_L/T_{sat}$ that measures the strength of the Kelvin effect. The latter pressure scale is usually used [5] to make the pressure dimensionless in the complete wetting case. For completeness, the

boundary conditions (2.27 - 2.29) and (2.31) are rewritten here in the dimensionless form

$$\tilde{h}|_{\tilde{x}=0} = 0, \tag{D.3}$$
$$u|_{\tilde{h}=0} = \theta_{micro}, \tag{D.4}$$
$$\Delta\tilde{p}|_{\tilde{x}\to\infty} = 0, \tag{D.5}$$
$$\Delta\tilde{p}|_{\tilde{x}\to 0} = \frac{1}{N_p}\left[1 + N_R\tilde{J}(\tilde{x}\to 0)\right]. \tag{D.6}$$

Note that the equation (D.1) and boundary condition (2.31) are presented here without the vapor recoil term. Its contribution is negligible (see section 2.8.3) and in all calculations (except those of section 2.8.3) this term is not considered.

Microregion characteristic dimensional parameters		
length	$l_K = \frac{\sqrt{3\mu k_L T_{sat}}}{\theta^2 \rho_L H}$	Kelvin length, see section 2.3.6
	l_V	Voinov length, see section 2.4
	$l_R = R^i k_L$	interface thermal resistance length scale
	$l_h = \sigma/(H\rho_L)$	length scale related to the latent heat
	$l_p = \sigma T_{sat}/(\Delta T H \rho_L)$	length scale related to the Kelvin efect
	$l_e = \mu k_L \Delta T/(\rho_L \sigma H)$	length scale related to the evaporation
	$l_a = \sqrt{A/(6\pi\sigma)}$	molecular scale [83] based on (1.21)
	$h_{ad} = (\rho_L H \Delta T/A)^{-1/3}$	thickness of the adsorbed liquid film at, scale relevant to complete or pseudo-partial wetting
	d_D	thickness of the liquid film that corresponds to the maximum of Π
	$D_m = \sqrt{\alpha\tau}$	thermal diffusion length, m is either Cu - copper or ss - stainless steel, τ is a characteristic time
	D_h	thickness to the solid heater
pressure	Δp_{CL}	pressure jump at the CL, defined by Eq. (2.31)
	$p_K = H\rho_L \Delta T/T_{sat}$	pressure related to the Kelvin effect (for $v_{CL} = 0, p_K = \Delta p_{CL}$)
	$p_\sigma = \sigma/l$	pressure scale related to the surface tension, l represents any characteristic length scale of the problem
	$p_d = \mu v/l$	pressure related to the viscosity, l again represents any length scale of the problem, v is any characteristic velocity of the system
temperature	T_{sat}	saturation temperature for given vapor pressure
	ΔT	imposed superheating
velocity	v_{CL}	contact line velocity
	$v_c = \Delta T/(\rho_L H R^i)$	velocity scale related to the liquid flow normal to the interface (it was introduced in [5])

Table D.1: List of important dimensional quantities associated to the microregion problem.

D.2 Change of variables

The applied variable change used to solve the microregion CL problem given by Eqs. (D.1 - D.6) is briefly outlined in the following.

The terms of Eq. (D.1) containing the derivatives are proportional to $\tilde{h}$. This may cause a loss of accuracy near the CL (at small $\tilde{h}$) related to the poor determination of the matrix (i.e., smallness of its diagonal elements) generated after discretization. In order to avoid this difficulty, the following change of variables [104]

$$\tilde{x} = \exp(\zeta), \tag{D.7}$$

$$\tilde{h} = \chi \exp(\zeta), \tag{D.8}$$

is applied. The point $\tilde{x} = 0$ corresponds to $\zeta \to -\infty$. Eqs. (D.1) and (D.2) reduce to

$$\frac{\partial}{\partial\zeta}\left\{-N_R N_M\left(\frac{\chi e^{\zeta}}{2}+1\right)\chi\frac{\partial\tilde{J}}{\partial\zeta}+\left[\frac{\chi^2 e^{2\zeta}}{3}+\chi e^{\zeta}\left(1-\frac{N_p N_M}{2}\right)-N_p N_M\right]\chi\frac{\partial\Delta\tilde{p}}{\partial\zeta}\right\} = e^{\zeta}\left[Ca\left(\chi+\frac{\partial\chi}{\partial\zeta}\right)-N_e\tilde{J}\right], \tag{D.9}$$

$$\frac{\partial}{\partial\zeta}\left(e^{\zeta}\frac{\partial\chi}{\partial\zeta}\right) = e^{2\zeta}(\Delta\tilde{p}-\tilde{\Pi}+\tilde{p}_r), \tag{D.10}$$

where

$$\tilde{J} = \frac{1-\Delta\tilde{p}N_p}{N_R+\chi e^{\zeta}}.$$

The boundary conditions (D.3 - D.5) read

$$\left.\frac{\partial\chi}{\partial\zeta}\right|_{\zeta\to-\infty} = 0, \tag{D.11}$$

$$\chi|_{\zeta\to-\infty} = \theta_{micro}, \tag{D.12}$$

$$\Delta\tilde{p}|_{\zeta\to\infty} = 0. \tag{D.13}$$

The fourth BC (D.6) is replaced in numerical treatment by

$$\left.\frac{d\Delta\tilde{p}}{d\zeta}\right|_{\zeta\to-\infty} = 0, \tag{D.14}$$

valid at $\zeta \to -\infty$. It follows from Eq. (D.7) if one mentions that $d\Delta p/d\zeta = x d\Delta p/dx$ and that $d\Delta p/dx$ is bounded, see Eq. (2.29).

D.3 Numerical implementation

For a numerical calculation, $\zeta = \zeta_{min}$ needs to be used for the left domain boundary instead of $-\infty$; the value $\zeta_{min} = -10$ is found to be sufficiently small. A study of x_{min} dependence is shown in Fig. 2.22b.

The solution method is similar to that used in [104]. An equidistant mesh of 250 elements is used for the domain $\zeta \in (\zeta_{min}, \zeta_{max})$, where $\zeta_{max} = \log(x_{max}/l_s)$. In the x domain, such a mesh is increasingly dense when $x \to 0$, see Fig. 2.17b. The choice of x_{max} is important because it corresponds to the size of microregion. In general, the latter is defined as a distance where the effects related to the CL can be neglected so that the matching with the macroregion can be performed. From the macroscopic point of view, the microregion is a geometrical point where θ_{app} boundary condition is imposed. To avoid an error related to the macroscopic interface curvature (e.g. for boiling applications, it is defined by the bubble radius), the microregion needs to be as small as possible. We propose a definition of the size of the microregion for immobile

CL ($v_{CL} = 0$), as a distance r_{app} where the curvature induced by the CL effects can be neglected with the given accuracy (which needs to be smaller than the macroscopic curvature). In practice, r_{app} is determined as a distance at which the interface slope approaches the slope at $x = x_{max}$ with a criterion $x_{max} \simeq 2r_{app}$ and within an imposed accuracy that is chosen to be 10^{-3}, see Fig. D.1. For most of the calculations the size of the domain $x_{max} = 1$ μm was found to be large enough to calculate θ_{app} with 0.5% accuracy.

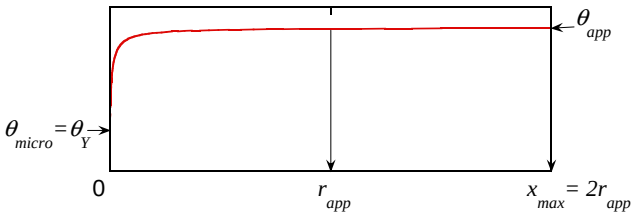

Figure D.1: Schematic graph of interface slope along the liquid wedge domain. r_{app} and x_{max} distances are marked.

The variables are supposed to be constant on each element. The nodes ζ_i are chosen in the centers of the elements, see Fig. D.2. The values of variables $\tilde{J}, \chi, \Delta\tilde{p}$ at i-th node are denoted $\tilde{J}_i, \chi_i$ and $\Delta\tilde{p}_i$ respectively.

The pair of equations (D.9 - D.10) is nonlinear. However the nonlinearity is not strong and the iteration method can be applied; nonlinear terms are replaced by their respective values from the previous iteration.

The finite volume method (FVM) [155] is used to discretize Eqs. (D.9, D.10), see below. Such an approach provides a sufficient numerical stability that allows us to calculate $h(x)$ for at least six decades of x variation on a PC.

D.4 Discretized microregion equations

In this section the descritized equations (D.9) and (D.14) are presented.

Eqs. (D.9 - D.14) are rewritten here in the form they were implemented in the numerical treatment. The equation for $J(x)$ is written separately. This is not in principle necessary. In case where the heat conduction in solid substrate is solved together with the microregion problem, $\tilde{J}_i$ (or more precisely $\tilde{q}_{S,i}$) are unknowns and equation (D.15) needs to be written separately. We thus solve it separately even when the microregion alone is solved, it is just a matter of convenience and unification.

$$\tilde{J}(N_R + \chi e^{\zeta}) + N_p \Delta\tilde{p} = 1, \tag{D.15}$$

$$\frac{\partial}{\partial\zeta}\left(e^{\zeta}\frac{\partial\chi}{\partial\zeta}\right) = e^{2\zeta}(\Delta\tilde{p} - \tilde{\Pi} + \tilde{p}_r), \tag{D.16}$$

$$\frac{\partial}{\partial\zeta}\left(B\frac{\partial\Delta\tilde{p}}{\partial\zeta} - A\frac{\partial\tilde{J}}{\partial\zeta}\right) = e^{\zeta}\left[Ca\left(\chi + \frac{\partial\chi}{\partial\zeta}\right) - N_e\tilde{J}\right], \tag{D.17}$$

where $B = (\chi^2 e^{2\zeta}/3 + \chi e^{\zeta}(1 - N_p N_M/2) - N_p N_M)\chi$ and $A = N_R N_M(\chi e^{\zeta}/2 + 1)\chi$. The boundary conditions

$$\left.\frac{\partial\chi}{\partial\zeta}\right|_{\zeta\to-\infty} = 0, \quad \chi|_{\zeta\to-\infty} = \theta_{micro}, \tag{D.18}$$

$$\left.\frac{d\Delta\tilde{p}}{d\zeta}\right|_{\zeta\to-\infty} = 0, \quad \Delta\tilde{p}|_{\zeta\to\infty} = 0, \tag{D.19}$$

The vector of unknowns $\vec{Z}$ is defined as follows:

Z_m	m
$J_{i=1}$	1
:	:
$J_{i=N_{tot}}$	i
$\chi_{i=2}$	$N_{tot}+1$
:	:
χ_i	$N_{tot}+i-1$
:	:
$\chi_{i=N_{tot}}$	$2N_{tot}-1$
$\Delta p_{i=1}$	$2N_{tot}$
:	:
Δp_i	$i+2N_{tot}-1$
:	:
$\Delta p_{N_{tot}-1}$	$i=3N_{tot}-2$

The index i is the number of element ($i = 1...N_{tot}$) and m is the number of unknown in the vector $\vec{Z}$ ($m = 1...N_{max} = 2N_{tot} - N_c$). The nonlinearity is treated by iteration procedure. The

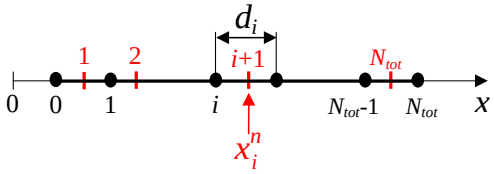

Figure D.2: Computational 1D grid: Microregion. The node coordinate is shown $x_i^n = e^{\zeta_i^n}$.

variables taken from previous iteration are marked by superscript, e.g. χ^{prev}. For initialization, the isothermal straight wedge profile is used. In the case of the sequence of calculations with e.g. increasing ΔT at each calculation, the variables are initialized with the respective values from the previous calculation. The discretized equations are described below.

D.4.1 Discretized Equations for $\tilde{J}$

- For $i = 1 \dots N_{tot} - 1$ ($m = i$)

$$N_p Z_{i+2N_{tot}-1} + Z_i(N_R + \chi_i^{prev} x_i^n) = 1, \tag{D.20}$$

- for $i = N_{tot}$ ($m = i$)

$$Z_i(N_R + \chi_i^{prev} x_i^n) = 1. \tag{D.21}$$

D.4.2 Discretized equation for χ

The FVM [155] was used to discreteze Eq. (D.16)

- $i = 1$ ($m = N_{tot} + 1$)

$$x_0^{-1} \frac{Z_{N_{tot}+1}}{\zeta_2^n - \zeta_1^n} - d_1 Z_{2N_{tot}} = x_0^{-1} \frac{\chi_1}{\zeta_2^n - \zeta_1^n} + d_1(-\tilde{\Pi}_1^{prev} + \tilde{p}_{r,1}^{prev}), \tag{D.22}$$

- $i = 2$ $(m = N_{tot} + 2)$

$$x_1^{-1}\frac{Z_{N_{tot}+2} - Z_{N_{tot}+1}}{\zeta_3^n - \zeta_2^n} - x_2^{-1}\frac{Z_{N_{tot}+1}}{\zeta_2^n - \zeta_1^n} - d_2 Z_{2N_{tot}+1} = -x_2^{-1}\frac{\chi_1}{\zeta_2^n - \zeta_1^n} + d_2(-\tilde{\Pi}_2 + \tilde{p}_{r,2}^{prev}), \tag{D.23}$$

- $i = 3 \ldots N_{tot} - 1$ $(m = N_{tot} + i)$

$$x_{i-1}^{-1}\frac{Z_{N_{tot}+1} - Z_{N_{tot}+i-1}}{\zeta_{i+1}^n - \zeta_i^n} - x_i^{-1}\frac{Z_{N_{tot}+i-1} - Z_{N_{tot}+i-2}}{\zeta_i^n - \zeta_{i-1}^n} - d_i Z_{2N_{tot}+i-1} = d_i(-\tilde{\Pi}_i + \tilde{p}_{r,i}^{prev}). \tag{D.24}$$

D.4.3 Discretized equation for $\Delta\tilde{p}$

The FVM [155] was used to discreteze Eq. (D.17)

- $i = 1$ $(m = 2N_{tot})$

$$\beta_1(Z_{2N_{tot}+1} - Z_{2N_{tot}}) - \alpha_1(Z_2 - Z_1) = d_1 x_1^n (Ca\theta_{micro} - Z_1 N_e), \tag{D.25}$$

- $i = 2....N_{tot} - 2$ $(m = 2N_{tot} + i - 1)$

$$\begin{aligned}\beta_i(Z_{2N_{tot}+i} - Z_{2N_{tot}+i-1}) - \beta_{i-1}(Z_{2N_{tot}+i-1} - Z_{2N_{tot}+i-2}) - \alpha_i(Z_{i+1} - Z_i) + \\ \alpha_{i-1}(Z_i - Z_{i-1}) = d_i x_i^n \left[Ca\left(\chi_i + \frac{\chi_i - \chi_{i-1}}{\zeta_i^n - \zeta_{i-1}^n}\right)^{prev} - Z_i N_e\right],\end{aligned} \tag{D.26}$$

- $i = N_{tot} - 1$ $(m = 3N_{tot} - 2)$

$$\begin{aligned}-\beta_{N_{tot}-1} Z_{3N_{tot}-2} - \beta_{N_{tot}-2}(Z_{3N_{tot}-2} - Z_{3N_{tot}-3}) - \alpha_{N_{tot}-1}(Z_{N_{tot}} - Z_{N_{tot}-1}) + \\ \alpha_{N_{tot}-2}(Z_{N_{tot}-1} - Z_{N_{tot}-2}) + d_{N_{tot}-1} x_{N_{tot}-1}^n Z_{N_{tot}-1} N_e = \\ d_{N_{tot}-1} x_{N_{tot}-1}^n Ca\left(\chi_{N_{tot}-1} + \frac{\chi_{N_{tot}-1} - \chi_{N_{tot}-1}}{\zeta_{N_{tot}-1}^n - \zeta_{N_{tot}-1}^n}\right)^{prev},\end{aligned} \tag{D.27}$$

where $\gamma_i = d_i/(2B_i)$, $\delta_i = d_i/(A_i 2)$, $\beta_i = 1/(\gamma_i + \gamma_{i+1})$ and $\alpha_i = 1/(\delta_i + \delta_{i+1})$.

The numerical treatment of the microregion problem was presented in this section. In some sections (2.6.1, 2.7.2, or 2.8.3) the discretized form of equations is different from (D.20 - D.27) due to modifications of employed equations. The comment on corresponding differences from the general description presented here is made at each section.

Appendix E

Stokes flow in a wedge

In the following, the simplified form of Navier-Stokes equations called Stokes approximation (or creeping flow) is discussed. Stokes flow is a type of fluid flow where advective inertial forces are small compared with viscous forces. A Stokes flow has no dependence on time other than through time-dependent boundary conditions. This means that, given the boundary conditions of a Stokes flow, the flow can be found without knowledge of the flow at any other time. When advection and external force terms are neglected, the Eqs. (2.2) reduce to

$$\nabla p = \mu \nabla^2 \vec{u}. \tag{E.1}$$

The Stokes flow approximation is valid for Reynolds number $Re = VL\rho/\mu << 1$ (good agreement with real flow properties when $Re < 0.1$), where V is a characteristic fluid velocity and L a characteristic length scale associated with the problem. In 2D we obtain a set of two *linear* equations:

$$\frac{\partial p}{\partial x} = \mu \left(\frac{\partial^2 u}{\partial x^2} + \frac{\partial^2 u}{\partial y^2} \right), \tag{E.2}$$

$$\frac{\partial p}{\partial y} = \mu \left(\frac{\partial^2 v}{\partial x^2} + \frac{\partial^2 v}{\partial y^2} \right). \tag{E.3}$$

Equation (E.1) is a function of both pressure and velocity, which is not very convenient. It can be converted into two other forms, which are each a function of the pressure field or the velocity only.

Taking divergence of the (E.1)

$$\nabla \cdot \nabla p = \nabla \cdot \mu \nabla^2 \vec{u}, \tag{E.4}$$

and considering that right side of (E.4) can be written as $\mu \nabla^2 (\nabla \cdot \vec{u})$ which is zero because of the (incompressibility consideration) continuity equation (2.1). The left side can be rewritten as

$$\nabla^2 p = 0. \tag{E.5}$$

This form of Stokes equation might be useful in case the boundary conditions are specified only in terms of pressure, which is not the case of contact line problems considered in this thesis.

The other form of Stokes equation is obtained by eliminating pressure by taking curl of equation (E.1)

$$\nabla \times \nabla p = \nabla \times \mu \nabla^2 \vec{u}. \tag{E.6}$$

The curl of the pressure gradient is 0 and using identity $\nabla \times \nabla^2 \vec{u} = \nabla^2 (\nabla \times \vec{u})$, the final expression is

$$\nabla^2 (\nabla \times \vec{u}) = \nabla^2 (\vec{\omega}), \tag{E.7}$$

where was used definition of vorticity $\nabla \times \vec{u} = \vec{\omega}$. Note that for 2D case ω_z obeys Laplace equation. Equation (E.1) can be also written in terms of the stream function Ψ ($u = \frac{\partial \Psi}{\partial y}$, $v = -\frac{\partial \Psi}{\partial x}$) than instead of two equations to solve (E.1) and Laplace equation we obtain single

equation for Ψ (incompressible continuity equation is satisfied automatically by the properties of the stream function) that needs to be solved

$$\nabla^4\Psi = \nabla^2(\nabla\Psi) = 0. \tag{E.8}$$

This equation is called biharmonic equation and ∇^4 biharmonic operator. This equation is useful in case boundary conditions are expressed in terms of velocity. It is of the 4^{th} order in derivatives.

For cylindrical coordinate system (see Fig. E.1), the stream function is $\Psi(\varphi, r)$ and components of the velocity (incompressible and two-dimensional flow) are obtained as

$$v_\varphi = \frac{\partial\Psi}{\partial r}, v_r = \frac{1}{r}\frac{\partial\Psi}{\partial\varphi}, \tag{E.9}$$

where v_r is a velocity in the radial direction and v_φ is a velocity in the tangential direction.

E.1 Steady contact line movement

Let us consider steady movement of a triple solid-liquid-gas CL with velocity v_{CL}, see Fig. E.1. $v_{CL} > 0$ corresponds to the displacement of the substrate to the left in Fig. E.1 (i.e., to the substrate drying). The liquid-vapor interface is treated as straight wedge (e.g. for $\sigma \to \infty$), making angle ϕ with the solid substrate. It was shown that such a solution gives the dominant component of the flow even for a curved interface [141, 142]. The problem requires to solve (E.8)

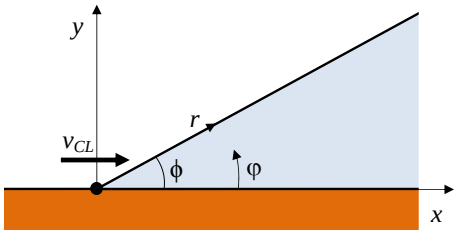

Figure E.1: Geometry of the problem: contact line movement.

with following boundary conditions:

- Kinematic conditions: vanishing normal component of the velocity at the solid surface as well as liquid/liquid interface

$$0 = \Psi \begin{cases} \varphi = 0 & \text{and } r \geq 0 \\ \varphi = \phi & \text{and } r \geq 0 \end{cases} . \tag{E.10}$$

- Kinematic condition: no slip of the liquid along the solid surface $v_{CL} = v_r$

$$-\frac{1}{r}\frac{\partial\Psi}{\partial\varphi} = v_{CL};\ \varphi = 0 \quad \text{and } r > 0\ . \tag{E.11}$$

- Dynamic condition: No tangential stress at the liquid-gas interface $\tau_{Br\varphi} = 0$

$$\mu\frac{\partial^2\Psi}{\partial\varphi^2} = 0;\ \varphi = \phi \quad \text{and } r > 0\ . \tag{E.12}$$

The general solution of biharmonic equation (E.8) in polar coordinates has been known since 1899 [157], in the form

$$\Psi(r,\varphi) = r^{\lambda} f_{\lambda}(\varphi), \tag{E.13}$$

where λ is conveniently called [158] the exponent of the corresponding solution. General form of the function $f_{\lambda}(\varphi)$, is

$$f(r,\varphi) = C_1 \sin\lambda\varphi + C_2 \cos\lambda\varphi + C_3\varphi \sin\left[(\lambda-2)\varphi\right] + C_4\varphi\cos\left[(\lambda-2)\varphi\right], \tag{E.14}$$

for particular cases $\lambda = 2$ and 1,

$$\Psi(r,\varphi) = r^2(C_1\cos 2\varphi + C_2 \sin 2\varphi + C_3\varphi + C_4), \tag{E.15}$$

$$\Psi(r,\varphi) = r(C_1\sin\varphi + C_2\cos\varphi + C_3\varphi\sin\varphi + C_4\varphi\cos\varphi), \tag{E.16}$$

where C_1, C_2, C_3 and C_4 are unknown constants. For the case of steady contact line movement the Eq. (E.16) is employed and following [69], unknown constants are determined from specified boundary conditions (E.10 - E.12) and

$$\Psi(r,\varphi) = \frac{r v_{CL}}{\sin\phi\cos\phi - \phi}\left[(\varphi-\phi)\sin\varphi - \varphi\sin(\varphi-\phi)\cos\phi\right]. \tag{E.17}$$

The expression for radial velocity is

$$v_r(\varphi) = \frac{1}{r}\frac{\partial\Psi}{\partial\varphi} = \frac{v_{CL}}{\sin\phi\cos\phi-\phi}\left[\sin\varphi + \varphi\cos\varphi - \phi\cos\varphi - \sin(\varphi-\phi)\cos\phi - \varphi\cos(\varphi-\phi)\cos\phi\right], \tag{E.18}$$

and thus for the radial velocity at $\varphi = \phi$

$$v_r(\phi) = v_{CL}\frac{\sin\phi - \phi\cos\phi}{\sin\phi\cos\phi - \phi}. \tag{E.19}$$

The expression for axial component of velocity is

$$v_{\varphi} = \frac{\partial\Psi}{\partial r} = U\frac{(\varphi-\phi)\sin\varphi - \varphi\sin(\varphi-\phi)\cos\phi}{\sin\phi\cos\phi-\phi}, \tag{E.20}$$

the axial component of velocity for $\varphi = \phi$ is $v_{\varphi} = 0$ (which was imposed by boundary condition (E.10a).

The expression for the pressure variation along the free interface ($\varphi = \phi$)

$$P(r) = -\frac{U\mu}{r}\frac{2\sin\phi}{\phi - \sin\phi\cos\phi}, \tag{E.21}$$

and the expression representing pressure variation is

$$\frac{\partial P}{\partial r} = \frac{v_{CL}\mu}{r^2}\frac{2\sin\phi}{\phi-\sin\phi\cos\phi} = \frac{v_{CL}\mu A(\phi)}{r^2}, \tag{E.22}$$

where $A(\phi) = (2\sin\phi)/(\phi - \sin\phi\cos\phi)$, which is identical to the result obtained in [141] and in [142].

Note that the solution for the straight wedge [69], (E.21) is in fact not correct with respect to the real CL problem (see nice discussion on this [130]) as the solution does not satisfy the normal stress boundary condition. The solution of the problem when the normal stress boundary condition is implemented properly was shown in [159]. However in this case, the solution became a bit cumbersome.

E.2 Steady evaporation from the vicinity of the CL

Let us consider that the evaporation mass flux at the liquid-vapor interface is known and is of the form $J(r) \propto r^{\kappa}$. The velocity of liquid at the interface is thus $v_{\Psi} = Ar^{\kappa}$. It was shown in [10] that for slow evaporation of the drop controlled by the diffusive transport of the liquid vapor in to the gas (air) environment, the mass evaporation flux is $J \propto (r)^{\kappa}$, where $\kappa = (\pi - 2\theta_{micro})/(2\pi - 2\theta_{micro})$. The problem requires to solve (E.8) with following boundary

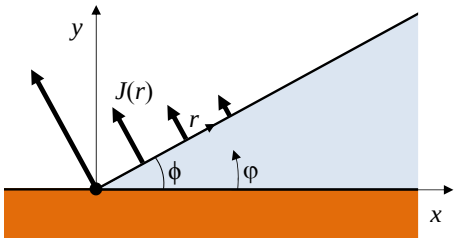

Figure E.2: Geometry of the problem: movement of liquid induced by evaporation in the vicinity of the CL.

conditions:

- Kinematic conditions: vanishing normal component of the velocity and no slip of liquid at the solid surface

$$-\frac{1}{r}\frac{\partial \Psi}{\partial \varphi} = 0; \;\; \varphi = 0 \quad \text{and } r > 0 \;, \tag{E.23}$$

$$\frac{\partial \Psi}{\partial r} = 0; \;\; \varphi = 0 \quad \text{and } r > 0 \;. \tag{E.24}$$

- Kinematic conditions: prescribed velocity of the liquid at the liquid gas interface (given by $J(r)$)

$$Ar^{\kappa} = Ar^{\lambda - 1} = \frac{J(r)}{\rho_L} = \frac{\partial \Psi}{\partial r}; \;\; \varphi = \phi \quad \text{and } r > 0 \;, \tag{E.25}$$

  where $\lambda = \kappa + 1$.

- Dynamic condition: No tangential stress at the liquid gas interface $\tau_{r\varphi} = 0$

$$\tau_{r\varphi}(r, \phi) = \mu \left[r \frac{\partial}{\partial r} \left(\frac{1}{r} \frac{\partial \Psi}{\partial r} \right) - \frac{1}{r^2} \frac{\partial^2 \Psi}{\partial \varphi^2} \right] = 0; \;\; \varphi = \phi \quad \text{and } r > 0 \;, \tag{E.26}$$

The solution of the evaporation problem Eqs. (E.8, E.23 - E.26) for $\lambda \neq 0, 1, 2$ is given by Eqs. (E.13, E.14) with the following constants:

$$C_1 = A \frac{(-2 - \lambda)(-\sin[(\lambda - 2)\varphi] + \sin[\lambda \varphi])}{2(\lambda \cos(\lambda \varphi) \sin[(\lambda - 2)\varphi] - C_5)}, \qquad C_3 = -C_1, \tag{E.27}$$

$$C_2 = A \frac{(\lambda - 2)((\lambda - 2)\cos[(\lambda - 2)\phi] - \lambda \cos(\lambda \phi))}{2\lambda(\lambda \cos(\lambda \phi) \sin[(\lambda - 2)\phi] - C_5)}, \tag{E.28}$$

$$C_4 = -A \frac{((\lambda - 2)\cos[(\lambda - 2)\phi] - \lambda \cos(\lambda \phi))}{2(\lambda \cos(\lambda \phi) \sin[(\lambda - 2)\phi] - C_5)}, \tag{E.29}$$

where $C_5 = (\lambda - 2)\cos[(\lambda - 2)\phi] \sin(\lambda \phi)$.

For the case $\lambda = 1$ ($\kappa = 0$) the general solution of (E.8) is (E.16) and four unknown constants are

$$C_1 = 0, \qquad C_3 = A\frac{\cos\phi}{\phi - \cos\phi\sin\phi}, \tag{E.30}$$

$$C_2 = A\frac{2\cos\phi}{-2\phi + \sin(2\phi)} \qquad C_4 = C_3\frac{\sin\phi}{\cos\phi}. \tag{E.31}$$

$$\tag{E.32}$$

The stream function in this case reduces to a rather simple form

$$\Psi(\varphi, r) = \frac{2Ar[\cos\phi(\varphi\cos\varphi - \sin\phi) + \varphi\sin\phi\sin\varphi]}{2\phi - \sin 2\phi}. \tag{E.33}$$

For the case $\lambda = 2$ ($\kappa = 1$) the general solution of (E.8) is (E.15) and four unknown constants are

$$C_1 = A\frac{\sin 2\phi}{4\phi\cos 2\phi - 2\sin 2\phi}, \qquad C_3 = C_1\frac{2\cos 2\phi}{\sin 2\phi}, \tag{E.34}$$

$$C_2 = \frac{C_3}{2} \qquad C_4 = -C_1. \tag{E.35}$$

$$\tag{E.36}$$

And the stream function is

$$\Psi(\varphi, r) = \frac{Ar^2(\varphi\cos(2\phi) - \cos(2\phi - \varphi)\sin\varphi)}{2\phi\cos(2\phi) - \sin(2\phi)}. \tag{E.37}$$

Note that the results presented here were also obtained in [160].

E.3 Steady evaporation induced by substrate superheating

In this section are presented results obtained by Mathieu [45]. The results are used in the section 3.1.2 where the microregion model is extended to high interface slopes .

We wish to obtain expression in analytical form for a straight wedge solving the heat conduction problem in the liquid domain for constant temperature of the solid heater ($T_S = T_{sat} + \Delta T$) and liquid-vapor interface (T_{sat}). The problem coincides with the case discussed in section E.2 for $\kappa = -1$ ($\lambda = 0$). One can verify that the solution for such a case is not easy to obtain (e.g. the solution to biharmonic equation (E.8) $\Psi = A + B\varphi + C\varphi^2 + D\varphi^3$, proposed by [158] is not valid[1]).

Another concept to such a problem was found by Mathieu [45]. The intensive evaporation in the vicinity of the CL was associated with the source (or sink) of liquid at CL, Fig. E.3. The problem requires to solve (E.8) with following four boundary conditions:

- Kinematic conditions: vanishing normal component of the velocity and no slip of liquid at the solid surface

$$-\frac{1}{r}\frac{\partial\Psi}{\partial\varphi} = 0; \quad \varphi = 0 \quad \text{and } r > 0\ , \tag{E.38}$$

$$\frac{\partial\Psi}{\partial r} = 0; \quad \varphi = 0 \quad \text{and } r > 0\ . \tag{E.39}$$

[1] It is necessary to note that H. K. Moffatt realized this and in the version of his paper [158], posted on his web `http://www.igf.fuw.edu.pl/KB/HKM/` this solution is crossed by the pen.

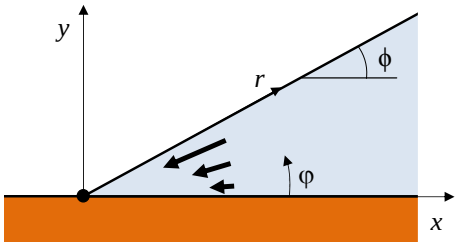

Figure E.3: Geometry of the problem: evaporation driven by substrate heating, situation modeled by liquid sing placed at CL.

- Kinematic conditions: prescribed zero tangential liquid velocity at the liquid-vapor interface

$$\frac{\partial \Psi}{\partial r} = 0; \quad \varphi = \phi \quad \text{and } r > 0 \ . \tag{E.40}$$

- Dynamic condition: No tangential stress at the liquid gas interface

$$-\mu \frac{1}{r^2} \frac{\partial^2 \Psi}{\partial \varphi^2} = 0; \quad \varphi = \phi \quad \text{and } r > 0 \ . \tag{E.41}$$

By choosing the solution in the form

$$\Psi(\varphi) = C_1 \varphi + C_2 \sin(2\varphi) + C_3 \cos(2\varphi) \tag{E.42}$$

(no dependence on r) the boundary conditions (E.39 - E.40) will be satisfied automatically. The Eqs. (E.38 - E.41) will serve for determining two constants in (E.42) and the third constant will be determined from mass conservation law $U = \int_0^{\phi} v_r(\varphi) r d\varphi$. The detailed discussion related to this problem can be found in [45]. The final expression for the stream function is

$$\Psi(\varphi) = -U \frac{\sin(2\phi - 2\varphi) + 2\varphi \cos(2\phi)}{2\phi \cos(2\phi) - \sin(2\phi)}. \tag{E.43}$$

The expression for the pressure variation along the free interface ($\varphi = \phi$)

$$P(r) = \frac{U\mu}{r^2} \frac{4}{2\phi \cos(2\phi) - \sin(2\phi)}, \tag{E.44}$$

and for variation of $\partial P/\partial r$ along the free interface

$$\frac{\partial P(r)}{\partial r} = -\frac{U\mu}{r^3} \frac{4}{2\phi \cos(2\phi) - \sin(2\phi)}. \tag{E.45}$$

E.4 Steady movement of liquid induced by gradient of surface tension

The results presented in this section are the original results of the author. The gradient of surface tension (e.g. due to variation of chemical composition of an interface [9, 83] or temperature gradients along the interface [161]) induces motion of the liquid. In the following, a general surface tension gradient along the straight liquid-vapor interface of the form $\partial\sigma/\partial r = Mr^{\lambda}$ is assumed, where M, λ are constants. The results presented here can be used to derive a similar correction to lubrication approximation (for the problem schematized in Fig. E.4) as was obtained in [45] for the evaporation case or for the contact line dynamics case [141, 142].

The problem requires to solve (E.8) with following boundary conditions:

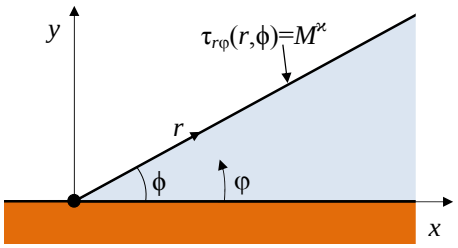

Figure E.4: Geometry of the problem: movement of liquid induced by gradient of surface tension.

- Kinematic conditions: vanishing normal component of the velocity and no slip of liquid at the solid surface

$$-\frac{1}{r}\frac{\partial \Psi}{\partial \varphi} = 0; \quad \varphi = 0 \quad \text{and } r > 0 \ , \tag{E.46}$$

$$\frac{\partial \Psi}{\partial r} = 0; \quad \varphi = 0 \quad \text{and } r > 0 \ . \tag{E.47}$$

- Kinematic conditions: vanishing normal component of the velocity at the liquid gas interface

$$\frac{\partial \Psi}{\partial r} = 0; \quad \varphi = \phi \quad \text{and } r > 0 \ . \tag{E.48}$$

- Dynamic condition: Prescribed tangential stress along the free liquid-vapor interface

$$\tau_{r\varphi}(r,\phi) = \mu\left[r\frac{\partial}{\partial r}\left(\frac{1}{r}\frac{\partial \Psi}{\partial r}\right) - \frac{1}{r^2}\frac{\partial^2 \Psi}{\partial \varphi^2}\right] = \dot{M}r^{\kappa} = Mr^{\lambda-2}, \tag{E.49}$$

where the first stress member is due to Eq. (E.47) zero and (E.49) reduces to

$$\tau_{r\varphi}(r,\phi) = \frac{1}{r^2}\frac{\partial^2 \Psi}{\partial \varphi^2} = Mr^{\lambda-2}, \tag{E.50}$$

where $M = -\dot{M}/\mu$ and $\lambda = \kappa + 2$

The solution of the problem Eqs. (E.8, E.46 - E.50) for $\lambda \neq 0, 1, 2$ is given by Eqs. (E.13, E.14) with the following constants:

$$C_1 = M((\lambda-2)\sin(\lambda\phi) - \lambda\sin(\lambda\phi - 2\phi)), \qquad C_3 = -C_1, \tag{E.51}$$

$$C_2 = M(\lambda-2)(\cos(\phi\lambda - 2\phi) - \cos(\phi\lambda)), \quad C_4 = -\frac{C_2}{\lambda-2}, \tag{E.52}$$

where $C_5 = 1/(4(\lambda-1)[\lambda\cos(\lambda\phi)\sin(\phi\lambda - 2\phi) - (\lambda-2)\cos(\phi\lambda - 2\phi)\sin(\phi\lambda)])$.

Special case arise for $\lambda = 1$ ($\kappa = -1$), the general solution of (E.8) is (E.16) and four unknown constants are

$$C_1 = 0, \quad C_3 = \frac{M\phi\sin(\phi)}{-2\phi + \sin(2\phi)}, \quad C_2 = -C_3, \quad C_4 = \frac{M(\phi\cos\phi - \sin\phi)}{2\phi - \sin(2\phi)}. \tag{E.53}$$

Another special case arise for $\lambda = 2$ ($\kappa = 0$), the general solution of (E.8) is (E.15) and four unknown constants are

$$C_1 = \frac{C_2(\sin(2\phi) - 2\phi)}{2\sin^2\phi}, \qquad C_3 = -2C_2, \tag{E.54}$$

$$C_2 = \frac{M\sin^2\phi}{4\phi\cos(2\phi) - 2\sin(2\phi)} \qquad C_4 = \frac{C_2(\phi - \cos\phi\sin\phi)}{\sin^2\phi}. \tag{E.55}$$

$$\tag{E.56}$$

The latter case ($\kappa = 0$) corresponds to linear temperature profile along the interface and the linear dependance of surface tension on temperature.

The last case corresponds to situation with $\lambda = 0$ ($\kappa = -2$). In this case the solution (E.42) with boundary conditions (E.46, E.50) are used together with mass conservation condition $U = \int_0^\phi v_r(\varphi, r) r d\varphi = 0$. The three unknown constants in (E.42) are:

$$C_1 = -2C_2, \quad C_3 = \frac{C_2}{2} \frac{-2\phi + \sin(2\phi)}{\sin^2 \phi}, \quad C_2 = \frac{M \sin^2 \phi}{4\phi \cos(2\phi) - 2\sin(2\phi)}. \tag{E.57}$$

Appendix F

Boundary Element Method

The boundary element method (BEM) is a numerical computational method of solving partial differential equations which have been formulated as integral equations (i.e., in boundary integral form). Apart from the *domain* methods as Finite Element Method (FEM) and the Finite Difference Method (FDM), the BEM is classified as *boundary* method, essentially meaning that the numerical discretization in performed at reduced spatial dimensions (e.g. for 2D problem the discretization is performed on the boundary contour only). Such a discretized problem leads to smaller linear system of equations which of course reduces computational costs. Here, the general background of the BEM is briefly shown on the example of Laplace's equation with mentioning the addaptations of BEM for solving the problems involving nonstationary diffusion problem with moving interface. Detailed description of BEM in general can be found in text books (e.g. [139, 162]) while a more detailed description of the BEM implementation to moving interfaces can be found in [148, 163, 164]. The historical evolution of BEM is well summarized by [165].

F.1 Solving the two dimensional Laplace's equation with BEM

In this section the principle of BEM on the two-dimensional Laplace's equation (written for Cartesian coordinate system) is explained. The goal is to find the solution of the following equation

$$\frac{\partial^2 \psi}{\partial x^2} + \frac{\partial^2 \psi}{\partial y^2} = 0, \tag{F.1}$$

in the interior of the two-dimensional region D bounded by the closed curve Ω and satisfying the appropriate boundary conditions:

- Dirichlet boundary condition:

$$\psi = f_1(x, y) \quad \text{on} \quad \Omega_1, \tag{F.2}$$

- Neumann boundary condition:

$$\frac{\partial \psi}{\partial \vec{n}} = f_2(x, y) \quad \text{on} \quad \Omega_2, \tag{F.3}$$

(the mixed boundary conditions are not for simplicity considered here). The vector $\vec{n}$ is the unit normal to the contour Ω pointing to the exterior of the domain D and $\Omega = \Omega_1 \cup \Omega_2$.

Now the problem to be solved is described by the equations. In order to use BEM for the numerical solution of the interior boundary value problem defined by Eqs. (F.1 - F.3) the Eq. (F.1) needs to be expressed in its integral form. The boundary equation can be deduced by means of several considerations: weighted residuals [162], reciprocal theorem [148], Green's third identity or fundamental principles such as virtual work.

In the following, the Green's third identity will be used. In order to solve the problem let us introduce the Green function G that satisfies the following problem

$$\nabla^2 G(\vec{r'}; \vec{r}) = \delta(|\vec{r'} - \vec{r}|), \tag{F.4}$$

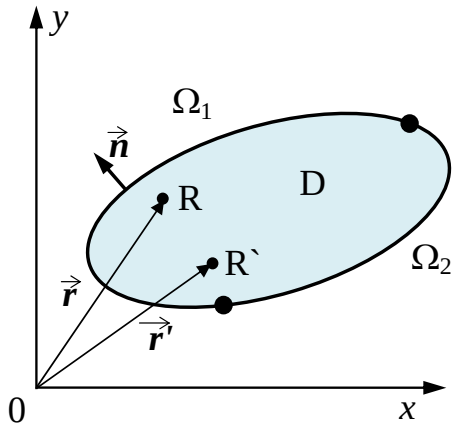

Figure F.1: Geometry

where δ is a dirac delta function at point R′ and R is a position of the source (see Fig. F.1) and $G(|\vec{r'}-\vec{r}|) \to \infty$ when $|\vec{r'}-\vec{r}| \doteq \sqrt{(x_{R'}-x_R)^2+(y_{R'}-y_R)^2} \to 0$. The Green's function that solves for the Eq. (F.4) is well known and for 2D problem is

$$G(\vec{r'};\vec{r}) = \frac{1}{2\pi}\ln|\vec{r'}-\vec{r}|. \tag{F.5}$$

The Green's function (F.5) allows us to find integral formulation of the initial problem (F.1). When using the second identity of Green one can show that the integral over the Laplace's equation is equal to zero:

$$\int_D \psi\nabla^2 G(\vec{r'};\vec{r})dD - \int_\Omega \frac{\partial G(\vec{r'};\vec{r})}{\partial\vec{n}}\psi d\Omega + \int_\Omega \frac{\partial\psi}{\partial\vec{n}}G(\vec{r'};\vec{r})d\Omega = 0. \tag{F.6}$$

Now the it can be shown (e.g. [148, 164]) that

$$\int_\Omega \frac{\partial G(\vec{r'};\vec{r})}{\partial\vec{n'}}\psi d_r\Omega - \int_\Omega \frac{\partial\psi}{\partial\vec{n'}}G(\vec{r'};\vec{r})d_r\Omega = \begin{cases} \psi(R'), & R'\in D/\Omega \\ \psi(R')/2, & R'\in\Omega \\ 0, & R'\notin\Omega \end{cases}. \tag{F.7}$$

Note that the last equation involves quantities only on the domain boundary.

F.2 Boundary element techniques applied to bubble growth problem

The transient heat conduction problem [163] (Eqs. (3.22) and (3.23)) is equivalent to the set of two integral equations, written for solid and liquid (Ω_S and Ω_L) domains [54]

$$\int_0^{t_F} \mathrm{d}t \int_{(\Omega_{L,S})} \left[G^{L,S}(\vec{r'},t_F;\vec{r},t)\left(\mathrm{Fo}_{L,S}\frac{\zeta(\vec{r},t)}{k_{L,S}} + \psi(\vec{r},t)v^n(\vec{r},t)\right) - \mathrm{Fo}_{L,S}\,\psi(\vec{r},t)\frac{\partial_r G^{L,S}(\vec{r'},t_F;\vec{r},t)}{\partial\vec{n}}\right] \mathrm{d}_r\Omega = \frac{1}{2}\psi(\vec{r'},t_F), \tag{F.8}$$

where $\vec{r'}$ is the evaluation point and t_F is the evaluation time. The integration is performed over the closed contours Ω_L and Ω_S that surround the liquid and solid domains and Ω_S, vector $\vec{n}$ being external to them. v^n is the projection of the local velocity of the possibly moving integration contour on the vector $\vec{n}$. Since the points $\vec{r'}$ and $\vec{r}$ belong to these contours, the BEM formulation does not require the values of ψ and ζ to be calculated in the internal points of the domains. The functions $G^{L,S}$ are the Green functions associated with Eqs. (3.22) [166]:

$$G^{L,S}(\vec{r'}, t_F; \vec{r}, t) = \frac{1}{4\pi \mathrm{Fo}_{L,S}(t_F - t)} \exp\left[-\frac{|\vec{r'} - \vec{r}|^2}{4\,\mathrm{Fo}_{L,S}(t_F - t)}\right]. \tag{F.9}$$

The indices L and S will be dropped in the following. ζ and ψ were assumed to be constant during any time step and on any element (constant element BEM), their values on the element being associated with the values on the node at the center of the element. The uniform mash in time was used, i.e. $t_f = f$, where f is the dimensionless time $(t/\Delta t)$. Therefore, the values of ζ and ψ on the element j at time f can be denoted by ζ_{fj} and ψ_{fj}. Each of the integral equations (F.8) reduces to the system of linear equations

$$\sum_{f=1}^{F} \sum_{j=1}^{2N_{tot}} [(\zeta_{fj}/k + \psi_{fj} v^n_{fj}/\mathrm{Fo}) G^{Ff}_{ij} - \psi_{fj} H^{Ff}_{ij}] = \psi_{Fi}/2, \tag{F.10}$$

where N_{tot} is the number of elements on one half of the integration contour at time step f, see Fig. F.2. F_{max} is the maximum number of time steps for the problem; $i = 1 \ldots 2N_{tot}$ and $F = 1 \ldots F_{max}$. The analytical expressions for coefficients of influence ($H_{i=j}$ and $G_{i=j}$) [167] were used. For all other cases the coefficient H_{ij} can be expressed analytically [167] through G_{ij}. G_{ij} was however calculated numerically. The system (F.10) can be simplified due to axial symmetry of the problem ($\psi_{fj} = \psi_{f(2N_{tot}-j)}$, etc.):

$$\sum_{f=1}^{F} \sum_{j=1}^{N_{tot}} [(\zeta_{fj}/k + \psi_{fj} v^n_{fj}/\mathrm{Fo}) \tilde{G}^{Ff}_{ij} - \psi_{fj} \tilde{H}^{Ff}_{ij}] = \psi_{Fi}/2, \tag{F.11}$$

where $i = 1 \ldots N_{tot}$, $F = 1 \ldots F_{max}$, $\tilde{G}^{Ff}_{ij} = G^{Ff}_{ij} + G^{Ff}_{i(2N-j)}$ and $\tilde{H}^{Ff}_{ij} = H^{Ff}_{ij} + H^{Ff}_{i(2N-j)}$. The discretized BEM equations for the solid and liquid domain are presented in the following section.

F.2.1 Numerical implementation to bubble growth

The vector of unknowns $\vec{Z}$ is as follows:

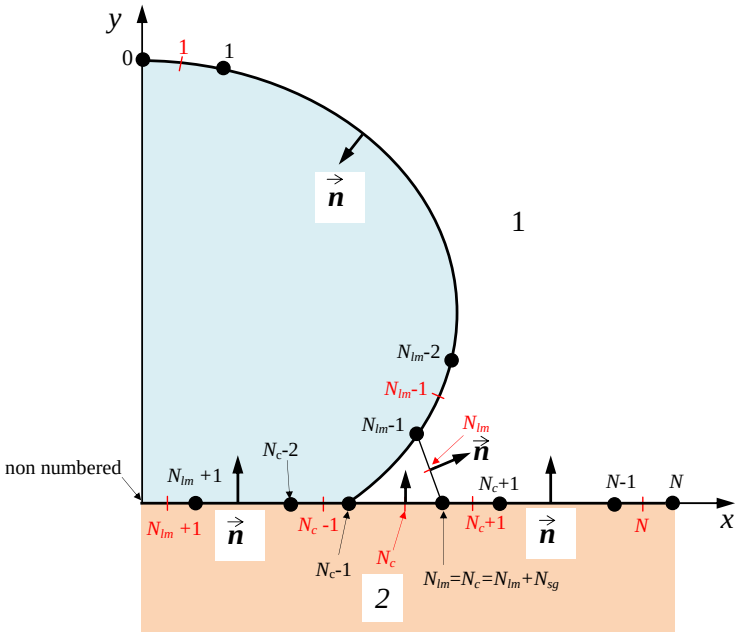

Figure F.2: Computational grid: Bubble growth.

Z_n	m
$\zeta^L_{i=1}$	1
:	:
$\zeta^L_{i=N_{lm}-1}$	i
$\zeta^L_{i=N_{lm}}$	i
$\psi^S_{i=N_{lm}+1}$	i
:	:
$\psi^S_{i=N_{lm}+N_{sg}-1}$	i
$\psi^S_{i=N_{lm}+N_{sg}=N_c}$	i
$\psi_{i=N_c+1}$	i
:	:
$\psi^S_{i=N_{tot}}$	$i = N_{tot}$
$\zeta^L_{i=N_c+1}$	$i = N_{tot} + 1$
:	:
ζ_i	$i - N_c + N_{tot}$
:	:
$\zeta^L_{i=N_{tot}}$	$N_{max} = 2N_{tot} - N_c$

The index i is the number of element ($i = 1...N_{tot}$) and n is the number of unknown in vector $\vec{Z}$ ($m = 1...N_{max} = 2N_{tot} - N_c$). The normal velocity of interface v^n_{Fi} at the time F and at node i is calculated using the expression

$$v^n_{Fi} = (x_{Fi} - x_{(F-1)j})n^x_{(F-1)j} + (y_{Fi} - y_{(F-1)j})n^y_{(F-1)j}, \tag{F.12}$$

where x_{Fi} is the coordinate of the node i at time F, and j is the number of the node (at time $F-1$) geometrically closest to (x_{Fi}, y_{Fi}).

F.2.1.1 BEM Equations for liquid domain

The BEM coefficients of influence H and G are calculated with Fo_L.

$$\begin{aligned}
&\sum_{f=1}^{F}\Bigg\{\sum_{j=1}^{N_{lm}-1}\left[\left(Z_{fj}+\frac{\psi_f^{iL}v_{fj}^n}{\mathrm{Fo}_L}\right)G_{ij}^{Ff;L}-\psi_f^{iL}H_{ij}^{Ff;L}\right]\\
&\quad-\left[\left(Z_{fj}+\frac{\psi_f^{LM}v_{fj}^n}{\mathrm{Fo}_L}\right)G_{ij}^{Ff;L}-\psi_f^{LM}H_{ij}^{Ff;L}\right]^{j=N_{lm}}\\
&-\sum_{j=N_{lm}+N_{sg}+1}^{N_{tot}}\left[Z_{f(j-N_{lm}-N_{sg}+N_{tot})}G_{ij}^{Ff;L}-Z_{fj}H_{ij}^{Ff;L}\right]\Bigg\}\\
&=\frac{1}{2}\begin{cases}\psi_F^{iL}, & i=1\ldots N_{lm}-1, \quad m=i\\ \psi_F^{LM}, & i=N_{lm}, \quad m=i\\ Z_{Fi}, & i=N_c+1\ldots N_{tot}, \quad m=i-N_c+N_{tot}\end{cases},
\end{aligned}\tag{F.13}$$

where $\psi_f^{iL}=(T_{sat}-T_L^{inf}(y,t))k_L/(q_0R_0)$, for ψ_f^{LM} see Eq. (3.28).

F.2.1.2 BEM Equations for solid domain

The BEM coefficients of influence H and G are calculated with Fo_S.

$$\begin{aligned}
&-\sum_{f=1}^{F}\Bigg\{\sum_{j=N_{lm}+1}^{N_{lm}+N_{sg}-1}-Z_{fj}H_{ij}^{Ff;S}+\left[\frac{\zeta^{SM}}{\tilde{k}}G_{ij}^{Ff;S}-Z_{fj}H_{ij}^{Ff;S}\right]^{j=N_{lm}+N_{sg}}\\
&\quad+\sum_{j=N_{lm}+N_{sg}+1}^{N_{tot}}\left[\frac{Z_{fj}}{\tilde{k}}G_{i(j-N_{lm}-N_{sg}+N_{tot})}^{Ff;L}-Z_{fj}H_{ij}^{Ff;S}\right]\Bigg\}\\
&=\frac{1}{2}\begin{cases}Z_{Fi}, & i=N_{lm}+1\ldots N_{lm}+N_{sg}-1, \quad m=i\\ Z_{Fi}, & i=N_{lm}+N_{sg}, \quad m=i\\ Z_{Fi}, & i=N_{lm}+N_{sg}+1\ldots N_{tot}, \quad m=i\end{cases},
\end{aligned}\tag{F.14}$$

where ζ^{SM} is defined by Eq. (3.29).

Appendix G

Some analytical solutions of heat transfer problem

G.1 Solution at infinity for heat source inside the heater

In the following, we deal with the problem given by Eqs. (3.1, 3.2) and BC (3.3 - 3.5a) and (3.6 - 3.7) representing the macroscopic problem statement (far from growing vapor bubble) from section 3.1.1.1. In this case the dependence on x ($x \to \infty$) is eliminated. The separate solutions for $y \geq 0$ and $y \leq 0$ can be found using the known Green function for the semi-infinite space [54, 168]

$$T_L^{\infty} = T_{sat} + \frac{\sqrt{\alpha_L}}{k_L\sqrt{\pi}} \int_0^t \frac{q_0(t-\tau)}{\sqrt{\tau}} \exp\left(-\frac{y^2}{4\alpha_L t}\right) d\tau, \quad y \geq 0, \tag{G.1}$$

$$T_S^{\infty} = T_{sat} + \frac{\alpha_S}{k_S} \int_0^t j(\tau) d\tau - \frac{\sqrt{\alpha_S}}{k_S\sqrt{\pi}} \int_0^t \frac{q_0(t-\tau)}{\sqrt{\tau}} \exp\left(-\frac{y^2}{4\alpha_S t}\right) d\tau, \quad y \leq 0. \tag{G.2}$$

The unknown heat flux from the heater, $q_0(t)$, can be found for arbitrary $j(t)$ out of the integral equation that results from equality of Eqs. (G.1) and (G.2) at $y = 0$. If $j \propto t^{-1/2}$, a constant q_0 satisfies this integral equation. This means that in the bubble growth problem (Chapter 3) with this choice of $j(t)$ the heat flux from the heater would be remain constant at least far from the growing bubble. This choice will allow us to avoid the influence of varying heat flux in time on the bubble growth. The solution in analytical form [54] is

$$j(t) = C/\sqrt{t},$$

$$q_0 = C\sqrt{\pi}\alpha_S k_L/(k_S\sqrt{\alpha_L} + k_L\sqrt{\alpha_S}), \tag{G.3}$$

$$T_S^{inf} = T_{sat} + \frac{2\alpha_S}{k_S} C\sqrt{t} - \frac{q_0}{k_S}\left[\sqrt{\frac{4\alpha_S t}{\pi}} \exp\left(-\frac{y^2}{4\alpha_S t}\right) + y\,\mathrm{erfc}\left(-\frac{y}{2\sqrt{\alpha_S t}}\right)\right], y \leq 0, \tag{G.4}$$

$$T_L^{inf} = T_{sat} + T_{inf}(y,t), \quad y \geq 0, \tag{G.5}$$

where

$$T_{inf}(y,t) = \frac{q_0}{k_L}\left[\sqrt{\frac{4\alpha_L t}{\pi}} \exp\left(-\frac{y^2}{4\alpha_L t}\right) - y\,\mathrm{erfc}\left(\frac{y}{2\sqrt{\alpha_L t}}\right)\right], \tag{G.6}$$

$\mathrm{erfc}(z)$ being the complementary error function [169] and C, q_0 are constant.

G.2 Steady temperature in semi-infinite medium: "dry spot"

Let us consider the following problem, which mimics and demonstrates the impact of dry spot on the thermal part of the problem in three dimensional space. The constant positive heat flux is considered at the solid liquid interface (e.g. by means of volumetric heat generation, see problem in G.1). One can exactly compensate the heat at the circular area of the diameter $2R_D$. In

other words it means that superposition of two elementary heat transfer problems is considered (imposed constant negative heat flux $-q_0$ along the solid surface and positive heat flux q_0 imposed at the circular area of the diameter $2R_D$), the resulting case is equivalent to the dry spot problem where the dry spot is considered to be thermally isolated. The cylindrical coordinate system is considered, see Fig. G.1. For the solving purposes it is convenient in addition to subtract the value q_0 and solve following equivalent heat transfer problem, see Fig. G.1. The constant heat

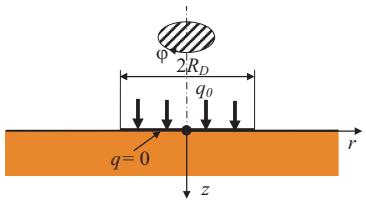

Figure G.1: Heat transfer problem "dry spot".

flux $-q_0$ is imposed for $z = 0$, $r < R_D$ for $\phi \in \langle 0, 2\pi)$ and zero heat flux for $z = 0$, $r > R_D$ for $\phi \in \langle 0, 2\pi)$. By using the Hankel transformation the temperature distribution is given by [168]

$$T_S = T^\infty + \frac{q_0 R_D}{k_S} \int_0^\infty \frac{\exp(-\lambda z) \mathrm{J}_0(\lambda r) \mathrm{J}_1(\lambda R_D)}{\lambda} d\lambda, \tag{G.7}$$

where T^∞ is a temperature given far from the dry spot ($r \to \infty$). The solution of the integral in (G.7), for $z = 0$ (solid liquid interface) can be found in [170] and

$$T_S^D(r) = T^\infty + \frac{2}{\pi} \frac{q_0 R_D}{k_S} \mathrm{E}\left(\frac{r}{R_D}\right), \quad \text{for } r < R_D, \tag{G.8}$$

$$T_S^D(r) = T^\infty + \frac{2}{\pi} \frac{q_0 R_D}{k_S} \left[\mathrm{E}\left(\frac{R_D}{r}\right) - \left(1 - \frac{R_D^2}{r^2}\right) \mathrm{K}\left(\frac{R_D}{r}\right)\right], \quad \text{for } r > R_D, \tag{G.9}$$

where K and E are the complete elliptic integrals of the first and second kinds respectively.

Notice that temperature of the solid surface at the center of the dry spot ($r = 0$) is $T = T^\infty + \frac{q_0 R_D}{k_S}$, an average temperature over $0 < r < R_D$ on the solid surface is $T = T^\infty + \frac{8 q_0 R_D}{3\pi k_S}$ and temperature at $r = R_D$ on the solid surface $T = T^\infty + \frac{2}{\pi} \frac{q_0 R_D}{k_S}$.

G.3 Steady temperature in semi-infinite medium: "contact line circle"

Another situation, demonstrating the impact of intensive evaporation in the vicinity of the CL is shown in Fig. G.2. The cylindrical coordinate system is considered. The constant heat flux is

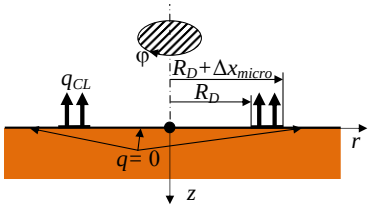

Figure G.2: Heat transfer problem "Contact line circle".

imposed for $z = 0$ and $R_D < r < R_2 = R_D + \Delta x_{micro}$ and similarly to previous case the constant

positive heat flux is considered at the solid liquid interface (e.g. by means of volumetric heat generation, see problem in G.1). The solution of such a problem can be find by superposition of two elementary solutions. The final expression for temperature is

$$T_S^{CL} = T^\infty + \frac{q_{CL} R_D}{k_S} \int_0^\infty \frac{\exp(-\lambda z) \mathrm{J}_0(\lambda r) \mathrm{J}_1(\lambda R_D)}{\lambda} d\lambda - \frac{q_{CL} R_2}{k_S} \int_0^\infty \frac{\exp(-\lambda z) \mathrm{J}_0(\lambda r) \mathrm{J}_1(\lambda R_2)}{\lambda} d\lambda. \tag{G.10}$$

The analytical expression for at the solid liquid interface can be easily deduced in analogy with the previous case (see section G.2), c.f. (G.8, G.9). The average temperature in the region $R_D < r < R_2$ is

$$\bar{T}_S^{CL} - T^\infty = -\frac{8 q_{CL}}{3\pi k_S} \frac{R_D^2 + R_D R_2 + R_2^2}{R_D + R_2} = -\frac{8 q_{CL}}{3\pi k_S} \frac{R_D^3 + 3 R_D \Delta x_{micro} + \Delta x_{micro}^2}{2 R_D + \Delta x_{micro}}. \tag{G.11}$$

Bibliography

[1] P. Stephan and J. Hammer, "A new model for nucleate boiling heat transfer," Heat Mass Transfer **30**, 119 – 125 (1994). 3, 10, 14, 15, 17, 18, 19, 24, 26, 27, 29, 63, 72, 78, 81, 93

[2] P. C. Wayner, Y. K. Kao, and L. V. LaCroix, "The interline heat-transfer coefficient of an evaporating wetting film," Int. J. Heat Mass Transfer **19**, 487 – 492 (1976). 3, 17, 18, 24, 29, 31, 33, 72

[3] S. Moosman and G. M. Homsy, "Evaporating menisci of wetting fluids," J. Colloid Interface Sci. **73**, 212 – 223 (1980). 3, 14, 17, 18, 25

[4] R. Raj, C. Kunkelmann, P. Stephan, J. Plawsky, and J. Kim, "Contact line behavior for a highly wetting fluid under superheated conditions," Int. J. Heat Mass Transfer **55**, 2664 – 2675 (2012). 19, 26, 27, 47, 63, 64, 74, 75, 81, 82, 85, 103

[5] S. J. S. Morris, "Contact angles for evaporating liquids predicted and compared with existing experiments," J. Fluid Mech. **432**, 1 – 30 (2001). 14, 17, 19, 25, 62, 63, 66, 107, 108

[6] A. Y. Rednikov and P. Colinet, "Truncated versus extended microfilms at a vapor-liquid contact line on a heated substrate," Langmuir **27**, 1758 – 1769 (2011). 14, 16, 19, 20, 107

[7] V. S. Ajaev, T. Gambaryan-Roisman, and P. Stephan, "Static and dynamic contact angles of evaporating liquids on heated surfaces," J. Colloid Interface Sci. **342**, 550 – 558 (2010). 3, 20, 25, 31

[8] D. Bonn, J. Eggers, J. Indekeu, J. Meunier, and E. Rolley, "Wetting and spreading," Rev. Mod. Phys. **81**, 739–805 (2009). 4, 20, 21, 44

[9] H. Y. Erbil, "Evaporation of pure liquid sessile and spherical suspended drops: A review," Advances in Colloid and Interface Science **170**, 67 – 86 (2012). 4, 118

[10] R. D. Deegan, O. Bakajin, T. F. Dupont, G. Huber, S. R. Nagel, and T. A. Witten, "Capillary flow as the cause of ring stains from dried liquid drops," Nature **389**, 827–829 (1997). 4, 116

[11] H. Masoud and J. D. Felske, "Analytical solution for stokes flow inside an evaporating sessile drop: Spherical and cylindrical cap shapes," Physics of Fluids **21**, 042102 (2009). 4

[12] J. Eggers and L. M. Pismen, "Nonlocal description of evaporating drops," Physics of Fluids **22**, 112101 (2010). 4

[13] G. Jing, H. Bodiguel, F. Doumenc, E. Sultan, and B. Guerrier, "Drying of colloidal suspensions and polymer solutions near the contact line: Deposit thickness at low capillary number," Langmuir **26**, 2288–2293 (2010). PMID: 19839602. 4

[14] F. Doumenc and B. Guerrier, "A model coupling the liquid and gas phases for a totally wetting evaporative meniscus," Eur. Phys. J. Special Topics **197**, 281–293 (2011). 4

[15] C.-T. Pham, G. Berteloot, F. Lequeux, and L. Limat, "Dynamics of complete wetting liquid under evaporation," Europhys. Lett. **92**, 54005 (2010). 4, 19

[16] G. Berteloot, C.-T. P. A. Daerr, F. Lequeux, and L. Limat, "Evaporation-induced flow near a contact line: Consequences on coating and contact angle," Europhys. Lett. **83**, 14003 (2008).

[17] E. Rio, A. Daerr, F. Lequeux, and L. Limat, "Moving contact lines of a colloidal suspension in the presence of drying," Langmuir **22**, 3186–3191 (2006). 4

[18] L. L. Vasiliev, "Heat pipes in modern heat exchangers," Applied Thermal Engineering **25**, 1 – 19 (2005). 5

[19] F. L. J. B. S. Khandekar, P. K. Panigrahi, "Local hydrodynamics of flow in a pulsating heat pipe: a review," Frontiers in Heat Pipes **1**, 1–20 (2010). 5

[20] J. Stuckert, M. Große, U. Stegmaier, and M. Steinbrück, "Results of severe fuel damage experiment QUENCH-15 with ZIRLOTM cladding tubes," Tech. rep., Karlsruhe Institute of Technology (2011). 6

[21] S. Nukiyama, "The maximum and minimum values of the heat Q transmitted from metal to boiling water under atmospheric pressure." J. Soc. Mech. Eng. Jpn. **37**, 367–374. (1934). 6

[22] V. P. Carey, *Liquid - vapor phase - change phenomena* (Hemisphere Publishing Corporation, 1992). 6, 8, 14, 28, 77, 103

[23] J. F. Klausner, R. A. Mei, D. M. Bernhard, and L. Z. Zeng, "Vapor bubble departure in forced convection boiling," Int. J. Heat Mass Transfer **36**, 651 – 662 (1993). 7, 81, 82

[24] P. Lloveras, F. Salvat-Pujol, L. Truskinovsky, and E. Vives, "Boiling crisis as a critical phenomenon," Phys. Rev. Lett. **108**, 215701 (2012). 7

[25] V. K. Dhir, "Boiling heat transfer," Ann. Rev. Fluid Mech. **30**, 365 – 401 (1998). 8, 10, 90

[26] R. M. Manglik, "On the advancements in boiling, two-phase flow heat transfer, and interfacial phenomena," J. Heat Transfer **128**, 1237 – 1242 (2006). 8

[27] C. Y. Han and P. Griffith, "The mechanism of heat transfer in nucleate pool boiling," Technical report 7673-19, Massachusetts Institute of Technology (1962). 8

[28] M. G. Cooper and A. J. P. Lloyd, "The microlayer in nucleate pool boiling," Int. J. Heat Mass Transfer **12**, 895 – 913 (1969). 8

[29] N. R. Snyder and D. K. Edwards, *Summary of Conference on Bubble Dynamics and Boiling Heat Transfer Held at the Jet Propulsion Laboratory*, Memo 20-137 (Jet Propulsion Laboratory, California Institute of Technology, 1956). 8

[30] B. B. Mikic and W. M. Rohsenow, "A new correlation of pool-boiling data including the effect of heating surface characteristics," Journal of Heat Transfer **91**, 245–250 (1969). 8

[31] J. Kim, "Review of nucleate pool boiling bubble heat transfer mechanisms," Int. J. Multiphase Flow **35**, 1067 – 1076 (2009). 8, 9

[32] A. Mukherjee and V. K. Dhir, "Study of lateral merger of vapor bubbles during nucleate pool boiling," J. Heat Transfer **126**, 1023–1039 (2004). 8, 9, 10, 93

[33] M. Cooper and T. Chandratilleke, "Growth of diffusion-controlled vapour bubbles at a wall in a known temperature gradient," Int. J. Heat Mass Transfer **24**, 1475 – 1492 (1981). 9, 82

[34] H. T. Phan, N. Caney, P. Marty, S. Colasson, and J. Gavillet, "Surface wettability control by nanocoating: The effects on pool boiling heat transfer and nucleation mechanism," Int. J. Heat Mass Transfer **52**, 5459 – 5471 (2009). 9

[35] G. Son, N. Ramanujapu, and V. K. Dhir, "Numerical simulation of bubble merger process on a single nucleation site during pool nucleate boiling," Journal of Heat Transfer **124**, 51–62 (2002). 9

[36] C. Sodtke, J. Kern, N. Schweizer, and P. Stephan, "High resolution measurements of wall temperature distribution underneath a single vapour bubble under low gravity conditions," International Journal of Heat and Mass Transfer **49**, 1100 – 1106 (2006). 9

[37] K. Ibrahem, M. A. Rabbo, T. Gambaryan-Roisman, and P. Stephan, "Experimental investigation of evaporative heat transfer characteristics at the 3-phase contact line," Exp. Therm Fluid Sci. **34**, 1036 – 1041 (2010). 9, 27, 68

[38] N. Schweizer, "Numerical modeling and investigation of boiling phenomena," Ph.D. thesis, TU Darmstadt (2010). 9

[39] V. S. Nikolayev and V. Janeček, "Impact of the apparent contact angle on the bubble departure at boiling," Int. J. Heat Mass Transfer **55**, 7352 – 7354 (2012). 9, 80, 81

[40] C. Kunkelmann and P. Stephan, "CFD simulation of boiling flows using the volume-of-fluid method within OpenFOAM," Numer. Heat Transfer, Part A **56**, 631 – 646 (2009). 10, 63, 74, 75

[41] C. Kunkelmann, "Numerical modeling and investigation of boiling phenomena," Ph.D. thesis, TU Darmstadt (2011). 10, 14, 63, 75, 93

[42] G. Son and V. K. Dhir, "Numerical simulation of nucleate boiling on a horizontal surface at high heat fluxes," Int. J. Heat Mass Transfer **51**, 2566 – 2582 (2008). 10

[43] G. Son, V. K. Dhir, and N. Ramanujapu, "Dynamics and heat transfer associated with a single bubble during nucleate boiling on a horizontal surface," J. Heat Transfer **121**, 623 – 631 (1999). 29, 31, 72, 82

[44] T. Fuchs, J. Kern, and P. Stephan, "A transient nucleate boiling model including microscale effects and wall heat transfer," J. Heat Transfer **128**, 1257 – 1265 (2006).

[45] B. Mathieu, "Etudes physiques, expérimentale et numérique des mécanismes de base intervenant dans les écoulements diphasiques," Ph.D. thesis, Polytech Marseille, Université de Provence, CNRS - UMR 6595, Marseille (2003). 29, 70, 71, 76, 117, 118

[46] Y. Chen and M. Groll, "Dynamics and shape of bubbles on heating surfaces: A simulation study," Int. J. Heat Mass Transfer **49**, 1115 – 1128 (2006).

[47] A. Markus and G. Hazi, "On pool boiling at microscale level: The effect of a cavity and heat conduction in the heated wall," Nuclear Engineering and Design **248**, 238 – 247 (2012). 10

[48] Y. Katto, "Critical heat flux," International Journal of Multiphase Flow **20, Supplement 1**, 53 – 90 (1994). 10

[49] Y. A. Buyevich, "Towards a unified theory of pool boiling – the case of ideally smooth heated wall," Int. J. Fluid Mech. Res. **26**, 189 – 223 (1999). 10

[50] T. Theofanous, J. Tu, A. Dinh, and T. Dinh, "The boiling crisis phenomenon: Part i: nucleation and nucleate boiling heat transfer," Experimental Thermal and Fluid Science **26**, 775 – 792 (2002). 10

[51] N. Zuber, "On the stability of boiling heat transfer," ASME J. Heat Transfer **80**, 711–720 (1958). 10

[52] A. Sakurai, "Mechanisms of transitions to film boiling at chfs in subcooled and pressurized liquids due to steady and increasing heat inputs," Nuclear Engineering and Design **197**, 301 – 356 (2000). 10

[53] V. S. Nikolayev and D. A. Beysens, "Boiling crisis and non-equilibrium drying transition," Europhys. Lett. **47**, 345 – 351 (1999). 10, 11, 17

[54] V. S. Nikolayev, D. A. Beysens, G.-L. Lagier, and J. Hegseth, "Growth of a dry spot under a vapor bubble at high heat flux and high pressure," Int. J. Heat Mass Transfer **44**, 3499 – 3511 (2001). 10, 28, 77, 79, 80, 86, 122, 127

[55] T. G. Theofanous, T. N. Dinh, J. P. Tu, and A. T. Dinh, "The boiling crisis phenomenon. Part II: Dryout dynamics and burnout," Exp. Thermal Fluid Sci. **26**, 793 – 810 (2002). 10

[56] J. Kim, J. F. Benton, and D. Wisniewski, "Pool boiling heat transfer on small heaters: effect of gravity and subcooling," Int. J. Heat Mass Transfer **45**, 3919 – 3932 (2002). 10, 91

[57] S. G. Kandlikar, "A theoretical model to predict pool boiling CHF incorporating effects of contact angle and orientation," J. Heat Transfer **123**, 1071 – 1079 (2001). 10, 90

[58] P. Bricard, P. Péturaud, and J.-M. Delhaye, "Understanding and modeling DNB in forced convective boiling: Modeling of a mechanism based on nucleation site dryout," Multiphase Sci. Techn. **9**, 329 – 379 (1997). 11

[59] D. B. R. Kenning and V. H. D. Valle, "Fully-developed nucleate boiling: Overlap of areas of influence and interference between bubble sites," Int. J. Heat Mass Transfer **24**, 1025 – 1032 (1981). 11

[60] K. O. Pasamehmetoglu and R. A. Nelson, "Cavity-to-cavity interaction in nucleate boiling: the effect of heat conduction within the heater," AIChE Symp. Ser. **87**, 342 – 351 (1991). 11

[61] S. G. Y. and R. H. Davis, "Close approach and deformation of two viscous drops due to gravity and van der Waals forces," J. Colloid Interface Sci. **144**, 412 – 433 (1991). 11

[62] S. Chatpun, M. Watanabe, and M. Shoji, "Nucleation site interaction in pool nucleate boiling on a heated surface with triple artificial cavities," Int. J. Heat Mass Transfer **47**, 3583 – 3587 (2004). 11

[63] I. Golobic, J. Petkovsek, H. Gjerkes, and D. B. R. Kenning, "Horizontal chain coalescence of bubbles in saturated pool boiling on a thin foil," Int. J. Heat Mass Transfer **54**, 5517 – 5526 (2011). 11

[64] H. J. Chung and H. C. No, "Simultaneous visualization of dry spots and bubbles for pool boiling of R-113 on a horizontal heater," Int. J. Heat Mass Transfer **46**, 2239 – 2251 (2003). 11

[65] S. G. Kandlikar and M. E. Steinke, "Contact angles and interface behavior during rapid evaporation of liquid on a heated surface," Int. J. Heat Mass Transfer **45**, 3771 – 3780 (2002). 11

[66] V. S. Nikolayev, D. Chatain, and D. Beysens, "Bubble spreading during the boiling crisis: modeling and experimenting in microgravity," in "Proc. 6th Int. Conf. on Boiling Heat Transfer," (Spoleto, Italy, 2006). 11

[67] V. S. Nikolayev, D. Chatain, Y. Garrabos, and D. Beysens, "Experimental evidence of the vapor recoil mechanism in the boiling crisis," Phys. Rev. Lett. **97**, 184503 (2006). 11

[68] V. Nikolayev, Y. Garrabos, C. Lecoutre, T. Charignon, D. Chatain, V. Janecek, D. Hitz, and D. Beysens, "Critical point as a tool to study boiling mechanisms," in "Seventh International Symposium on TWO-PHASE SYSTEMS FOR GROUND AND SPACE APPLICATIONS," (Beijing, China, 2012). 11

[69] C. Huh and L. E. Scriven, "Hydrodynamic model of steady movement of a solid/liquid/fluid contact line," J. Colloid Interf. Sci. **35**, 85 – 101 (1971). 12, 21, 115

[70] R. Pit, H. Hervet, and L. Léger, "Direct experimental evidence of slip in hexadecane: Solid interfaces," Phys. Rev. Lett. **85**, 980–983 (2000). 12

[71] E. Lauga, M. P. Brenner, and H. A. Stone, "Microfluidics: The no-slip boundary condition," in "Springer Handbook of Experimental Fluid Dynamics," , C. Tropea, A. Yarin, and J. Foss, eds. (Springer, New York, 2007), chap. 19, pp. 1217 – 1240. 12, 13, 21, 29, 57

[72] C. I. Bouzigues, P. Tabeling, and L. Bocquet, "Nanofluidics in the debye layer at hydrophilic and hydrophobic surfaces," Phys. Rev. Lett. **101**, 114503 (2008). 12

[73] P. A. Thompson and S. M. Troian, "A general boundary condition for liquid flow at solid surfaces," Nature **389**, 714–721 (1997). 13

[74] J. Koplik and J. R. Banavar, "Continuum deductions from molecular hydrodynamics," Annual Review of Fluid Mechanics **27**, 257–292 (1995). 13, 26

[75] J. M. Delhaye, *Thermohydraulics of two-phase systems for industrial design and nuclear engineering* (McGraw-Hill, 1981). 13

[76] L. D. Landau and E. M. Lifshitz, *Statistical physics* (Pergamon Press, Oxford, 1980). 13

[77] J. P. Burelbach, S. G. Bankoff, and S. H. Davis, "Nonlinear stability of evaporating/condensing liquid films," Journal of Fluid Mechanics **195**, 463–494 (1988). 14, 71

[78] R. W. Schrage, *A Theoretical study of interphase mass transfer* (Columbia University Press, 1953). 14

[79] J. W. Rose, "Accurate approximate equations for intensive sub-sonic evaporation," Int. J. Heat Mass Transfer **43**, 3869 – 3875 (2000). 14

[80] R. Meland, A. Frezzotti, T. Ytrehus, and B. Hafskjold, "Nonequilibrium molecular-dynamics simulation of net evaporation and net condensation, and evaluation of the gas-kinetic boundary condition at the interphase," Physics of Fluids **16**, 223–243 (2004). 14

[81] H. Wang, S. V. Garimella, and J. Y. Murthy, "Characteristics of an evaporating thin film in a microchannel," Int. J. Heat Mass Transfer **50**, 3933 – 3942 (2007). 14

[82] R. Marek and J. Straub, "Analysis of the evaporation coefficient and the condensation coefficient of water," Int. J. Heat Mass Transfer **44**, 39 – 53 (2001). 15

[83] P.-G. de Gennes, F. Brochard-Wyart, and D. Quéré, *Capillarity and Wetting Phenomena: Drops, Bubbles, Pearls, Waves* (Springer, New York, 2004). 15, 20, 26, 53, 65, 108, 118

[84] J. N. Israelachvili, *Intermolecular and Surface Forces* (Academic Press, London, 1992), 2nd ed. 15, 16, 26, 49

[85] F. Brochard-Wyart, D. M. J.-M., D. Quéré, and P.-G. de Gennes, "Spreading of nonvolatile liquids in a continuum picture," Langmuir **7**, 335 – 338 (1991). 15, 20, 48

[86] E. K. Yeh, J. Newman, and C. J. Radke, "Equilibrium configurations of liquid droplets on solid surfaces under the influence of thin-film forces: Part I. Thermodynamics," Colloids Surf., A **156**, 137 – 144 (1999). 15, 48

[87] E. K. Yeh, J. Newman, and C. J. Radke, "Equilibrium configurations of liquid droplets on solid surfaces under the influence of thin-film forces: Part II. Shape calculations," Colloids Surf., A **156**, 525 – 546 (1999). 15

[88] C. Miller and E. Ruckenstein, "The origin of flow during wetting of solids," Journal of Colloid and Interface Science **48**, 368 – 373 (1974). 16

[89] L. M. Hocking, "The influence of intermolecular forces on thin fluid layers," Physics of Fluids A: Fluid Dynamics **5**, 793–799 (1993). 19

[90] J. H. Snoeijer and B. Andreotti, "A microscopic view on contact angle selection," Phys. Fluids **20**, 057101 (2008). 16

[91] P.-G. de Gennes, "Wetting: statics and dynamics," Rev. Mod. Phys. **57**, 827 – 863 (1985). 16, 19, 20, 21

[92] M. Ishii and T. Hibiki, *Thermo-fluid Dynamics of Two-Phase Flow* (Springer, 2006). 17

[93] D. M. Anderson, P. Cermelli, E. Fried, M. E. Gurtin, and G. B. McFadden, "General dynamical sharp-interface conditions for phase transformations in viscous heat-conducting fluids," J. Fluid Mech. **581**, 323 – 370 (2007). 17, 28

[94] M. Potash and P. Wayner, "Evaporation from a two-dimensional extended meniscus," Int. J. Heat Mass Transfer **15**, 1851 – 1863 (1972). 17

[95] S. J. S. Morris, "A phenomenological model for the contact region of an evaporating meniscus on a superheated slab," J. Fluid Mech. **411**, 59 – 89 (2000). 19, 28, 29, 65, 69

[96] I. Y. Kim, "An optical study of the heat transfer characteristics of an evaporating thin liquid film," Ph.D. thesis, Rensselaer Polytechnic Institute, Troy, New York (1994). 19

[97] A. Y. Rednikov, S. Rossomme, and P. Colinet, "Steady microstructure of a contact line for a liquid on a heated surface overlaid with its pure vapor: parametric study for a classical model," Multiphase Sci. Techn. **21**, 213 – 248 (2009). 19, 25, 29, 61, 64

[98] P. Colinet and A. Rednikov, "On integrable singularities and apparent contact angles within a classical paradigm," Eur. Phys. J. Special Topics **197**, 89 – 113 (2011). 19, 20, 65

[99] A. Y. Rednikov and P. Colinet, "Evaporation-driven contact angles in a pure-vapor atmosphere : the effect of vapor pressure non-uniformity," Mathematical Modelling of Natural Phenomena **7**, 53–63 (2012). 20

[100] D. M. Anderson and S. H. Davis, "Local fluid and heat flow near contact lines," J. Fluid Mech. **268**, 231 – 265 (1994). 20, 21, 27, 28, 71

[101] D. M. Anderson and S. H. Davis, "The spreading of volatile liquid droplets on heated surfaces," Phys. Fluids **7**, 248 – 265 (1995). 20, 21, 27, 28, 29

[102] S. S. Panchamgam, A. Chatterjee, J. L. Plawsky, and P. C. W. Jr., "Comprehensive experimental and theoretical study of fluid flow and heat transfer in a microscopic evaporating meniscus in a miniature heat exchanger," International Journal of Heat and Mass Transfer **51**, 5368 – 5379 (2008). 20

[103] L. M. Hocking, "On contact angles in evaporating liquids," Phys. Fluids **7**, 2950 – 2955 (1995). 21, 27, 28, 29, 31, 60, 62, 107

[104] V. S. Nikolayev, "Dynamics of the triple contact line on a nonisothermal heater at partial wetting," Phys. Fluids **22**, 082105 (2010). 21, 31, 60, 81, 82, 94, 107, 109

[105] L. M. Hocking, "The spreading of a thin drop by gravity and capillarity," The Quarterly Journal of Mechanics and Applied Mathematics **36**, 55–69 (1983). 21

[106] O. V. Voinov, "Hydrodynamics of wetting," Fluid Dynamics **11**, 714–721 (1976). 21, 44, 70

[107] J. Eggers, "Hydrodynamic theory of forced dewetting," Phys. Rev. Lett. **93**, 094502 (2004). 21

[108] V. E. B. Dussan, "The moving contact line: the slip boundary condition," Journal of Fluid Mechanics **77**, 665–684 (1976). 21

[109] J. Eggers, "Contact line motion for partially wetting fluids," Phys. Rev. E **72**, 061605 (2005). 21

[110] V. Janeček, B. Andreotti, D. Pražák, T. Bárta, and V. S. Nikolayev, "Moving contact line of a volatile fluid," arXiv:1212.3717 [physics.flu-dyn] (2012). 21, 43, 44, 47, 65, 97

[111] A. Rednikov and P. Colinet, "Moving contact lines in a pure-vapor atmosphere: a singularity-free description in the sole framework of classical physics," arXiv:1202.0273 [physics.flu-dyn] (2012). During the thesis defence preparatory period, the author became aware of this independent work discussing the regularization of the dynamic contact line singularity by Kelvin effect. 21, 43, 47, 65, 97

[112] C. Andrieu, D. A. Beysens, V. S. Nikolayev, and Y. Pomeau, "Coalescence of sessile drops," J. Fluid Mech. **453**, 427 – 438 (2002). 21

[113] Y. Pomeau, "Contact line moving on a solid," Eur. Phys. J. Special Topics **197**, 15–31 (2011). 21

[114] I. G. Currie, *Fundamental Mechanics of Fluids* (Marcel Dekker, Inc, 2003). 24

[115] S. Maruyama, T. Kimura, and M.-C. Lu, "Molecular scale aspects of liquid contact on a solid surface," Therm. Sci. Eng. **10**, 23 – 29 (2002). 26, 49

[116] S. Maruyama and T. Kimura, "A molecular dynamics simulation of a bubble nucleation on solid surface," Int. J. Heat Technology **18, supplement 1**, 69 – 74 (2000).

[117] S. C. Maroo and J. Chung, "Molecular dynamic simulation of platinum heater and associated nano-scale liquid argon film evaporation and colloidal adsorption characteristics," J. Colloid Interface Sci. **328**, 134 – 146 (2008). 49

[118] S. C. Maroo and J. Chung, "Heat transfer characteristics and pressure variation in a nanoscale evaporating meniscus," Int. J. Heat Mass Transfer **53**, 3335 – 3345 (2010).

[119] T. Kimura and S. Maruyama, "Molecular dynamics simulation of heterogeneous nucleation of a liquid droplet on a solid surface," Microscale Thermophys. Eng. **6**, 3 – 13 (2002).

[120] B. Shi and V. K. Dhir, "Molecular dynamics simulation of the contact angle of liquids on solid surfaces," J. Chem. Phys. **130**, 034705 (2009). 49

[121] D. Zhiqiang, L. Weizhong, and S. Yongchen, "A numerical investigation of bubble growth on and departure from a superheated wall by lattice Boltzmann method," Int. J. Heat Mass Transfer **53**, 4908 – 4916 (2010). 26

[122] P. C. Wayner, "Intermolecular forces in phase-change heat transfer: 1998 Kern award review," AIChE Journal **45**, 2055–2068 (1999). 26

[123] E. van den Akker, A. Frijns, C. Kunkelmann, P. Hilbers, P. Stephan, and A. van Steenhoven, "Molecular dynamics simulation of the microregion," International Journal of Thermal Sciences **59**, 21 – 28 (2012). 26

[124] A. Y. Çengel, *Heat Transfer : A Practical Approach* (McGraw-Hill, 2003). 27

[125] N. P. Petroff, "Friction in machines and the effect of lubricant," Inzhenernyj Zhurnal, Sankt-Peterburg **1-4**, 71 – 140, 228 – 279, 377 – 436 and 535 – 564 (1883). Published in four issues, in Russian. 29

[126] O. Reynolds, "On the theory of lubrication and its application to Mr Beauchamp Tower's experiments, including an experimental determination of viscosity of olive oil," Phil. Trans. R. Soc. Lond. **177**, 157 – 234 (1886). 29

[127] G. Delon, M. Fermigier, J. H. Snoeijer, and B. Andreotti, "Relaxation of a dewetting contact line. Part 2: Experiments," J. Fluid Mech. **604**, 55 – 75 (2008). 31, 53, 65, 71

[128] V. S. Nikolayev, S. L. Gavrilyuk, and H. Gouin, "Modeling of the moving deformed triple contact line: Influence of the fluid inertia," J. Colloid Interface Sci. **302**, 605 – 612 (2006). 31

[129] V. Janeček and V. S. Nikolayev, "Contact line singularity at partial wetting during evaporation driven by substrate heating," Europhys. Lett. **100**, 14003 (2012). 32, 36, 38

[130] L. Pismen, "Some singular errors near the contact line singularity, and ways to resolve both," Eur. Phys. J. Special Topics **197**, 33–36 (2011). 34, 115

[131] R. Reyes and J. P. C. Wayner, "A Kelvin–Clapeyron adsorption model for spreading on a heated plate," J. Heat Transfer **118**, 822 – 830 (1996). 34

[132] G. Doetsch, *Handbuch der Laplace-Transformation I.* (Bitkhäuser, 1980). Satz 3.6.1. 36

[133] B. R. Duffy and S. K. Wilson, "A third-order differential equation arising in thin-film flows and relevant to tanner's law," Appl. Math. Lett. **10**, 63 (1997). 44

[134] J. Eggers, "Existence of receding and advancing contact lines," Phys. Fluids **17**, 082106 (2005). 44, 47

[135] V. Janeček and V. S. Nikolayev, "Apparent contact angle model at partial wetting and evaporation: impact of surface forces," Phys. Rev. E (2013). Accepted for publication. 48

[136] V. Janeček and V. S. Nikolayev, "Influence of the surface forces on the apparent contact angle at partial wetting and in the presence of heat and mass transfer," in "2nd Eu. Conf. on Microfluidics," (Toulouse, 2010). Paper 212. 48

[137] B. V. Derjaguin and N. V. Churaev, "Structural component of disjoining pressure," J. Colloid Interface Sci. **49**, 249 – 255 (1974). 48

[138] K. M. Andersson and L. Bergström, "DLVO interactions of tungsten oxide and cobalt oxide surfaces measured with the colloidal probe technique," J. Colloid Interf. Sci. **246**, 309 – 315 (2002). 52

[139] W. T. Ang, *A Beginner's Course in Boundary Element Methods* (Universal Publishers, Boca Raton, 2007). 67, 68, 121

[140] M. Mann, K. Stephan, and P. Stephan, "Influence of heat conduction in the wall on nucleate boiling heat transfer," Int. J. Heat Mass Transfer **43**, 2193 – 2203 (2000). 69

[141] W. Boender, A. K. Chesters, and A. J. J. van der Zanden, "An approximate analytical solution of the hydrodynamic problem associated with an advancing liquid-gas contact line," Int. J. Multiphase Flow **17**, 661 – 676 (1991). 70, 114, 115, 118

[142] J. H. Snoeijer, "Free-surface flows with large slopes: Beyond lubrication theory," Phys. Fluids **18**, 021701 (2006). 70, 114, 115, 118

[143] X. Xinpeng and Q. Tiezheng, "Thermal singularity and droplet motion in one-component fluids on solid substrates with thermal gradients," Phys. Rev. E **85**, 061603 (2012). 81

[144] G. Duhar and C. Colin, "Dynamics of bubble growth and detachment in a viscous shear flow," Phys. Fluids **18** (2006). 81, 82

[145] W. G. J. van Helden, C. W. M. van der Geld, and P. G. M. Boot, "Forces on bubbles growing and detaching in flow along a vertical wall," Int. J. Heat Mass Transfer **38**, 2075 – 2088 (1995). 81, 82

[146] J. Kern and P. Stephan, "Theoretical model for nucleate boiling heat and mass transfer of binary mixtures," J. Heat Transfer **125**, 1106 – 1115 (2003). 82

[147] K. P. Polevikov, "Methods for numerical modeling of two-dimensional capillary surfaces," Comput. Meth. Appl. Math. **4**, 66 – 93 (2001). 87

[148] V. S. Nikolayev and D. A. Beysens, "2D BEM modeling of a singular thermal diffusion free boundary problem with phase change," in "Boundary elements XXIV (Incorporating meshless solutions)," , vol. 13 of *Int. Series on Advances in Boundary Elements*, C. A. Brebbia, A. Tadeu, and V. Popov, eds. (WIT Press, Southampton, 2002), pp. 501 – 525. 87, 121, 122

[149] V. S. Nikolayev, "Dynamics and depinning of the triple contact line in the presence of periodic surface defects," J. Phys. Cond. Matt. **17**, 2111 – 2119 (2005). 91

[150] U. Bieder and E. Graffard, "Qualification of the CFD code Trio_U for full scale reactor applications," Nuclear Engineering and Design **238**, 671 – 679 (2008). 91

[151] Y. Garrabos, C. Lecoutre, D. Beysens, V. Nikolayev, S. Barde, G. Pont, and B. Zappoli, "Transparent heater for study of the boiling crisis near the vapor-liquid critical point," Acta Astronautica **66**, 760 – 768 (2010). 101

[152] D. R. Lide, ed., *Handbook of chemistry and physics* (CRC Press, 1998). 103

[153] N. B. Vargaftik, B. N. Volkov, and L. D. Voljak, "International tabels of the surface tension of water," J. Phy **12** (1983). 103

[154] J. T. R. Watson, R. S. Basu, and J. V. Sengers, "An improved representative equation for the dynamics viscosity of water substance," J. Phys. Chem. Ref. Data **9** (1980). 103

[155] S. V. Patankar, *Numerical heat transfer and fluid flow* (Hemisphere, Washington, 1980). 107, 110, 111, 112

[156] V. S. Ajaev, "Spreading of thin volatile liquid droplets on uniformly heated surfaces," J. Fluid Mech. **528**, 279 – 296 (2005). 107

[157] J. H. Michell, "On the Direct Determination of Stress in an Elastic Solid, with application to the Theory of Plates," Proc. London Math. Coc. **s1-31**, 100–124 (1899). 115

[158] H. J. Moffatt, "Viscous and resistive eddies near a sharp corner," Journal of Fluid Mechanics **18**, 1–18 (1964). 115, 117

[159] L. M. Pismen and A. Nir, "Motion of a contact line," Physics of Fluids **25**, 3–7 (1982). 115

[160] H. Gelderblom, O. Bloemen, and J. H. Snoeijer, "Stokes flow near the contact line of an evaporating drop," J. Fluid Mech. **709**, 69–84 (2012). 117

[161] H. Hu and R. G. Larson, "Marangoni effect reverses coffee-ring depositions," The Journal of Physical Chemistry B **110**, 7090–7094 (2006). 118

[162] C. A. Brebbia and J. Dominguez, *Boundary Elements - An Introductory Course* (WIT Press Publishing, 1992). 121

[163] W. D.-S. Jr and L. Wrobel, "A front-tracking BEM formulation for one-phase solidification/melting problems," Engineering Analysis with Boundary Elements **16**, 171 – 182 (1995). 121, 122

[164] M. Bonnet, *Equations intégrales et éléments de frontière* (CNRS Editions / Editions EYROLLES, 1995). 121, 122

[165] A. H. D. Cheng and D. T. Cheng, "Heritage and early history of the boundary element method," Engineering Analysis with Boundary Elements **29**, 268 – 302 (2005). 121

[166] H. L. G. P. na and J. L. M. Fernandes, *Topics in Boundary Element Research: Basic principles and applications* (Springer-Verlag, 1984), vol. 1, chap. Applications in Transient Heat Conduction. 123

[167] G.-L. Lagier, "Application of the boundary element method to multidimensional inverse heat conduction problems," Ph.D. thesis, Thése de l'Institut National Polytechnique de Grenoble (1999). 123

[168] H. S. Carslaw and J. C. Jaeger, *Conduction of Heat in Solids* (Clarendon Press, Oxford, 1959), 2nd ed. 127, 128

[169] M. Abramowitz and I. A. Stegun, *Handbook of Mathematical Functions with Formulas, Graphs, and Mathematical Tables* (Dover, New York, 1964), ninth dover printing, tenth gpo printing ed. 127

[170] P. H. Thomas, "Some conduction problems in the heating of small areas on large solids," The Quarterly Journal of Mechanics and Applied Mathematics **10**, 482–493 (1957). 128

Evaporation at microscopic scale and at high heat flux

Abstract: This thesis theoretically investigates the transport processes in the vicinity of the triple gas-liquid-solid contact line and its impact on macroscopic evaporation. In the first part of the thesis, the hydrodynamics close to the contact line at partial wetting is studied. Specifically, evaporation into the atmosphere of pure vapor driven by heating of the substrate is considered. The question of singularity relaxation is addressed. The main finding of the thesis is that the Kelvin effect (dependence of saturation temperature on pressure) is sufficient by itself to relax the hydrodynamic contact line singularity. The proposed microregion (the contact line vicinity) model for small interface slopes is solved numerically. Asymptotic solutions are found for some specific cases. The governing length scales of the problem are identified and the multiscale nature of the phenomenon is addressed. Parametric studies revealing the role of the thermal resistance of vapor-liquid interface, slip length, thermocapillary term, the vapor recoil and surface forces are also performed. An extension of the lubrication approximation for high slopes of the gas-liquid interface at evaporation is discussed.

In the second part of the thesis, the previously established microregion model is coupled to a simplified single vapor bubble growth numerical simulation. The bubble departure from the heater at boiling is also studied. It was proposed in the thesis, that under high heat loads, the increase of the apparent contact angle causes the vapor bubble to spread over the heated substrate. Such a behavior may cause the heater dry-out that occurs during the boiling crisis.
Keywords: contact line, evaporation, partial wetting, contact angle, singularity, boiling crisis

---

Evaporation à l'échelle microscopique et à haut flux thermique

Résumé: Cette thèse étudie théoriquement les processus de transport au voisinage de la ligne triple de contact liquide-gaz-solide et leur impact sur l'évaporation macroscopique. Dans la première partie de la thèse, l'hydrodynamique au voisinage de la ligne de contact est étudiée sous les conditions de mouillage partiel. L'évaporation induite par le chauffage du substrat dans l'atmosphère de vapeur du même fluide est considérée. La relaxation de la singularité hydrodynamique de la ligne triple est considérée. La principale conclusion de la thèse est que l'effet Kelvin (dépendance de la température de saturation de la pression) est suffisant en soi, pour faire disparaitre la singularité des variables hydrodynamiques. La microrégion (le voisinage de la ligne de contact) est résolue numériquement et analytiquement pour de faibles pentes de l'interface liquide-vapeur. Les échelles de longueur caractéristiques du problème sont identifiées et la nature multi-échelle du phénomène est prise en compte. Les études paramétriques effectuées révèlent le rôle de la résistance thermique de l'interface vapeur-liquide, de la longueur de glissement, du terme thermocapillaire, du recul de vapeur et ainsi que des forces de surface. Une extension de l'approximation de lubrification pour de pentes élevées de l'interface gaz-liquide à l'évaporation est discutée.

Dans la seconde partie de la thèse, le modèle précédemment établi pour la microrégion est couplé à des simulations numériques de la croissance d'une bulle de vapeur. Le départ de la bulle de vapeur de la paroi chauffante pendant l'ébullition a également été étudiée. Il a été proposé dans la thèse, que sous des charges thermiques élevées, l'augmentation de l'angle de contact apparent provoque l'étalement de la bulle de vapeur sur la paroi chauffante. Ce phénomène peut conduire, au séchage de la paroi observé pendant la crise d'ébullition.
Mots-clefs: ligne de contact, évaporation, mouillage partial, angle de contact, crise d'ébullition